



ATLAS NOTE

ATL-COM-PHYS-2016-1747

15th June 2017



Draft version 1.1

Modelling Studies for the Standard Model $VH, H \rightarrow b\bar{b}$

Ahmadov, Faig^y, Argyropoulos, Spyridon^r, Arnold, Hannah^k, Amaral Coutinho, Yara^p, Sanchez Pineda, Arturo Rodolfo^q, Bell, Andrew Stuart^f, Benitez, Jose^r, Buzatu, Adrian^h, Calderini, Giovanni^v, Chan, Stephen Kam-wah^e, Chen, Chunhui^t, Buckley, Andrew^o, Buscher, Daniel^k, Delporte, Charles^l, De Lorenzi, Francesco^t, De Vivie De Regie, Jean-Baptiste^l, Dao, Valerio^a, Enari, Yuji^g, Francavilla, Paolo^v, Gargiulo, Simona^k, Gaycken, Goetzⁿ, Gray, Chloe^o, Grivaz, Jean-Francois^l, Hays, Jonathan Michael^j, Hesketh, Gavin Grant^f, Hobbs, John^a, Huth, John^e, Ishijima, Naoki^u, Kado, Marumi^l, Kato, Chikuma^g, Li, Changqiao^b, Li, Haifeng^a, Liu, Yanwen^b, Marchiori, Giovanni^v, Ma, Lianliangⁱ, Ma, Yanhuiⁱ, Mario Jose da Cunha Sargedas de Sousa^x, Masubuchi, Tatsuya^g, Mallik, Usha^r, Mehta, Andrew^s, Montalbano, Alyssa^a, Morange, Nicolas^l, Moser, Brian^k, Pandini, Carlo Enrico^d, Piacquadio, Giacinto^a, Prell, Soeren^t, Robson, Aidan^o, Scanlon, Tim^f, Schopf, Elisabethⁿ, Sekula, Stephen^w, Thompson, Paul^m, Tsbychev, Dmitri^a, Vergel Infante, Carlos Miguel^t, Wang, Song-Ming^h, Wang, Wei^{h,z}, Weiser, Christian^k, Yamaguchi, Yohei^c, Yang, Siqi^r, Yu, Jie^t

^a*Stony Brook University*

^b*University of Science and Technology of China*

^c*Tokyo Institute of Technology*

^d*INFN Pisa and Universita' di Pisa, Dipartimento di Fisica*

^e*Harvard University*

^f*Department of Physics and Astronomy, University College London*

^g*International Center for Elementary Particle Physics and Department of Physics, The University of Tokyo*

^h*Academia Sinica, Taipei*

ⁱ*Shandong University (CN)*

^j*Queen Mary University of London*

^k*Albert-Ludwigs-Universitaet Freiburg*

^l*LAL, Univ. Paris-Sud, IN2P3/CNRS, Universite Paris-Saclay*

^m*University of Birmingham*

ⁿ*University of Bonn*

^o*University of Glasgow, SUPA - School of Physics and Astronomy*

^p*Universidade Federal do Rio De Janeiro, COPPE/EE/IF*

^q*INFN Gruppo Collegato di Udine and Universita' di Udine, Dipartimento di Chimica, Fisica e Ambiente*

^r*University of Iowa*

^s*University of Liverpool*

^t*Iowa State University*

^u*Osaka University*

^v*LPNHE, UPMC, Universite Paris-Diderot, CNRS/IN2P3*

^w*Southern Methodist University, Department of Physics*

^x*LIP and FCUL*

^y*JINR*

^z*Nanjing University, Department of Physics*

42

Abstract

43

This note describes the signal and background models and their associated uncertainties used
44 in the standard model VH , $H \rightarrow bb$ 2015+2016 publication analysis. The backgrounds
45 considered are those coming from vector boson plus jets, top (pair and single), dibosons and
46 1-lepton multijet processes.

Not reviewed, for internal circulation only

© 2017 CERN for the benefit of the ATLAS Collaboration.

47 Reproduction of this article or parts of it is allowed as specified in the CC-BY-3.0 license.

48 Contents

49	1 Introduction	6
50	2 SM Signal Characterisation	7
51	2.1 SM VH Nominal Monte Carlo Simulation	7
52	2.2 Update of nominal Predictions	7
53	2.3 Alternative Monte Carlo Samples	10
54	2.4 Cross-Section	10
55	2.5 NLO Electroweak Corrections	11
56	2.6 Systematic Uncertainties	11
57	2.6.1 Inclusive cross section uncertainties	11
58	2.6.2 Analysis specific uncertainties	13
59	3 Backgrounds	21
60	3.1 Vector Boson+Jets Production	22
61	3.1.1 Nominal Monte Carlo Prediction	22
62	3.1.2 Alternative Monte Carlo Samples	25
63	3.1.3 Cross-Section	27
64	3.1.4 V+jets Systematic Uncertainties	28
65	3.1.5 W+jets uncertainties	29
66	3.1.6 Z+jets uncertainties	34
67	3.2 Top-Pair Production	40
68	3.2.1 Cross-Section	41
69	3.2.2 Alternative Samples	41
70	3.2.3 $t\bar{t}$ Systematic Uncertainties	42
71	3.2.4 Assignment of systematic variations on the $t\bar{t}$ background	43
72	3.3 Single-Top Production	52
73	3.3.1 Cross-Section	52
74	3.3.2 Alternative Samples	53
75	3.3.3 Single-top Systematic Uncertainties	54
76	3.4 Diboson Production	59
77	3.4.1 Nominal Monte Carlo Simulation	59
78	3.4.2 Update of Nominal Predictions	59
79	3.4.3 Cross-Sections	60
80	3.4.4 Alternative Monte Carlo Samples	60
81	3.4.5 Diboson Systematic Uncertainties	62
82	3.5 Multi Jet Production	67
83	3.5.1 1-lepton channel	67
84	Appendix	81
85	A Particle-Level Analysis Definition	81
86	A.1 Standard Model VH Analysis	81
87	B Additional material for SM VH modelling systematics	83
88	B.1 PS/UE	83

89	B.2 Scale uncertainties	87
90	B.3 PDF+ α_s	91
91	C Additional material for $t\bar{t}$ modeling systematics	94
92	C.1 Normalisation uncertainties	94
93	C.1.1 0-lepton	94
94	C.1.2 1-lepton	94
95	C.1.3 ttbar: 1lepton+0lepton	95
96	C.1.4 bc/bb ratio	95
97	C.1.5 ttbar: 2lepton	96
98	C.2 Fits for shape uncertainties	99
99	C.2.1 0-lepton fits	99
100	C.2.2 1-lepton fits	101
101	C.2.3 2-lepton fits	103
102	C.3 Residual shape effects across regions	105
103	D Additional material for single top modeling systematics	107
104	D.1 2-lepton modeling check	107
105	E Additional material for diboson modeling systematics	109
106	E.1 Breakdown of PS/UE uncertainties	109
107	E.1.1 0L	109
108	E.1.2 1L	109
109	E.1.3 2L	109
110	E.1.4 V p_T shape	112
111	E.1.5 m_{bb} shape	117
112	E.2 Breakdown of scale variations	122
113	E.2.1 0L	122
114	E.2.2 1L	122
115	E.2.3 2L	122
116	E.2.4 V p_T shape	124
117	E.2.5 m_{bb} shape	125
118	E.3 Sherpa vs Powheg	126
119	E.4 Miscellanea	128
120	F Additional material for W+jets modeling systematics	129
121	F.1 Breakdown of normalisation/extrapolation uncertainties	129
122	F.1.1 njet extrapolation	129
123	F.1.2 CR-SR extrapolation	129
124	F.1.3 0Lepton-1Lepton extrapolation	130
125	F.1.4 flavour composition	131
126	F.2 Single variation shape fit	133
127	F.3 Residual shape effects across regions	137
128	F.4 Rivet-Reco comparison	138
129	F.5 Data/MC plots	138
130	G Additional material for Z+jets modeling systematics	139

131	G.1 Breakdown of normalisation/extrapolation uncertainties	139
132	G.1.1 2-3 jet extrapolation	139
133	G.1.2 0 to 2 Lepton extrapolation	139
134	G.1.3 flavour composition	140
135	H Additional material for 1 lepton multijet modeling	143

[Not reviewed, for internal circulation only]

136 1. Introduction

137 This supporting document describes the signal and background processes and the Monte Carlo (MC)
138 generators used in the Standard Model $V(H \rightarrow b\bar{b})$ search with Run 2 ATLAS data. The purpose of
139 this supporting note is to give a complete overview of the setup of the MC generators used to estimate
140 signal and backgrounds, their normalisation including cross-section, filter efficiencies and when needed
141 higher-order k -factors. In the case of the multijet background, the techniques used to estimate the multijet
142 background from data are described. In addition, we provide a detailed description of the studies per-
143 formed to estimate modelling systematic uncertainties for the different processes.

144

145 ***Status of this version of the supporting document***

146 *This note has been updated with the latest V+jet, ttbar, single-top, diboson, multijet and signal modelling*
147 *for the winter 2017 analysis. This version contains the final signal and diboson modelling uncertainties*
148 *which will be incorporated into the analysis for the Higgs group approval.*

149 2. SM Signal Characterisation

150 This section details the signal samples used for the modelling of Standard Model Higgs associated
 151 production processes (VH). These samples are used to estimate the signal prediction for the search for a
 152 SM Higgs boson in VH production.

153 2.1. SM VH Nominal Monte Carlo Simulation

154 The VH signals include three main Higgs production modes: $ZH \rightarrow vvbb\bar{b}$, $ZH \rightarrow llbb\bar{b}$ and $WH \rightarrow lvbb\bar{b}$,
 155 where $l = e, \mu, \tau$. The ZH production modes are furthermore split into two contributions depending on
 156 the partonic initial state: $q\bar{q} \rightarrow ZH$ and $gg \rightarrow ZH$.

157 All $q\bar{q}$ -initiated production processes are simulated using the Powheg generator with the MiNLO (Multiscale
 158 Improved NLO) procedure applied [1], interfaced to the Pythia 8 [2] MC generator applying the AZNLO
 159 tune [3] with the NNPDF3.0 PDF [4] set, while for the gg -initiated ZH contribution we rely on the
 160 Powheg prediction interfaced with Pythia 8 for the modelling of parton shower, underlying event and
 161 multiple parton interactions, applying the AZNLO tune [3] with the NNPDF3.0 PDF [5] for both the
 162 matrix-element (ME) and the parton shower.

163 All VH signal processes are listed in Table 1, along with the statistics of the generated samples. The cross
 164 sections used for the normalisation of these samples are detailed in Section 2.4.

DS ID	Process	Generator	Events
<i>qq</i> -initiated (nominal)			
345053	$qq \rightarrow W^+H \rightarrow l^+vvbb$	Powheg +MiNLO+Pythia 8	3999950
345054	$qq \rightarrow W^-H \rightarrow l^-vvbb$	Powheg +MiNLO+Pythia 8	3999950
345055	$qq \rightarrow ZH \rightarrow llbb\bar{b}$	Powheg +MiNLO+Pythia 8	3000000
345056	$qq \rightarrow ZH \rightarrow vvbb\bar{b}$	Powheg +MiNLO+Pythia 8	2000000
<i>qq</i> -initiated (alternative)			
343608	$qq \rightarrow WH \rightarrow lvbb$	MADGRAPH 5_aMC@NLO+Pythia 8	1000000
343619	$qq \rightarrow ZH \rightarrow llbb\bar{b}$	MADGRAPH 5_aMC@NLO+Pythia 8	1000000
343629	$qq \rightarrow ZH \rightarrow vvbb\bar{b}$	MADGRAPH 5_aMC@NLO+Pythia 8	1000000
<i>gg</i> -initiated (nominal)			
345057	$gg \rightarrow ZH \rightarrow llbb\bar{b}$	Powheg +Pythia 8	
345058	$gg \rightarrow ZH \rightarrow vvbb\bar{b}(*)$	Powheg +Pythia 8	

Table 1: Standard Model VH samples used in the analyses including alternative samples to assess the systematic uncertainties. The dataset ID, MC generator, and total number of generated events are shown. (*) The sample is currently being re-generated due to a configuration problem.

165 2.2. Update of nominal Predictions

166 In the ICHEP version of the analysis, the nominal predictions for $q\bar{q}$ -initiated production processes were
 167 simulated using the Pythia 8 [2] MC generator applying the A14 tune [6] with the NNPDF2.3LO PDF [5]
 168 set. The nominal predictions for these processes have now been updated to a NLO prediction generated
 169 using Powheg +MiNLO+Pythia 8. This new samples has better statistics with respect to the sample used
 170 for ICHEP. The m_{bb} and p_T^V shapes were compared between Pythia 8 and Powheg +MiNLO+Pythia 8
 171 and are shown in Figures 1 and 2 respectively. The shape difference between the p_T^V distributions is shown

172 to be negligible whereas shape differences can be seen in the m_{bb} distributions. These are not used as a
 173 systematic uncertainty, they are purely to document the changes between the sample.

Not reviewed, for internal circulation only

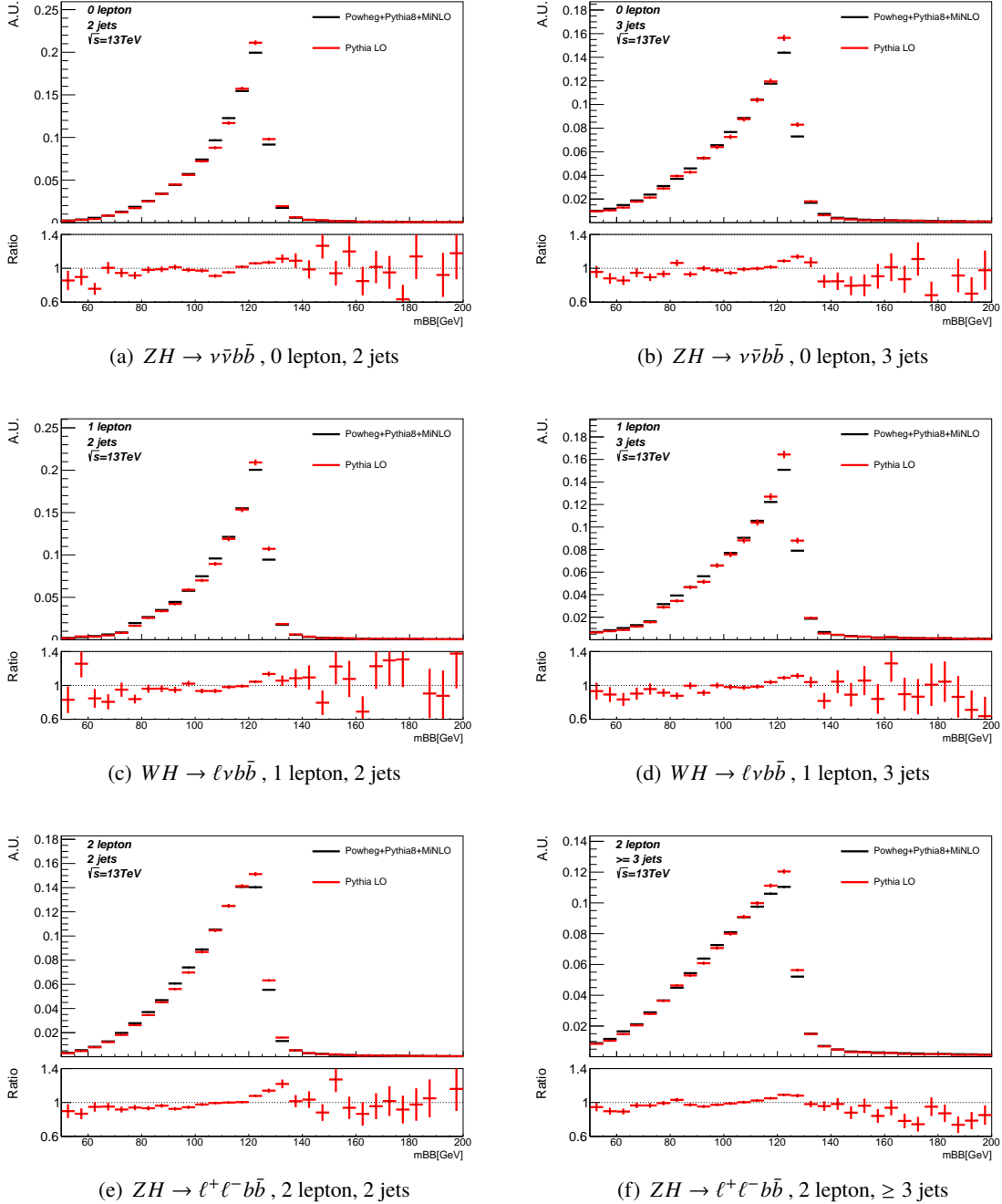


Figure 1: Shape comparison of the m_{bb} distributions for each VH process, i.e. lepton channel and each number of jets category, inclusive in p_T^V . Shown is a comparison between PYTHIA 8 (red) and POWHEG +MiNLO+PYTHIA 8 (black). The ratio between the two samples is shown in the lower panel of the plot.

Not reviewed, for internal circulation only

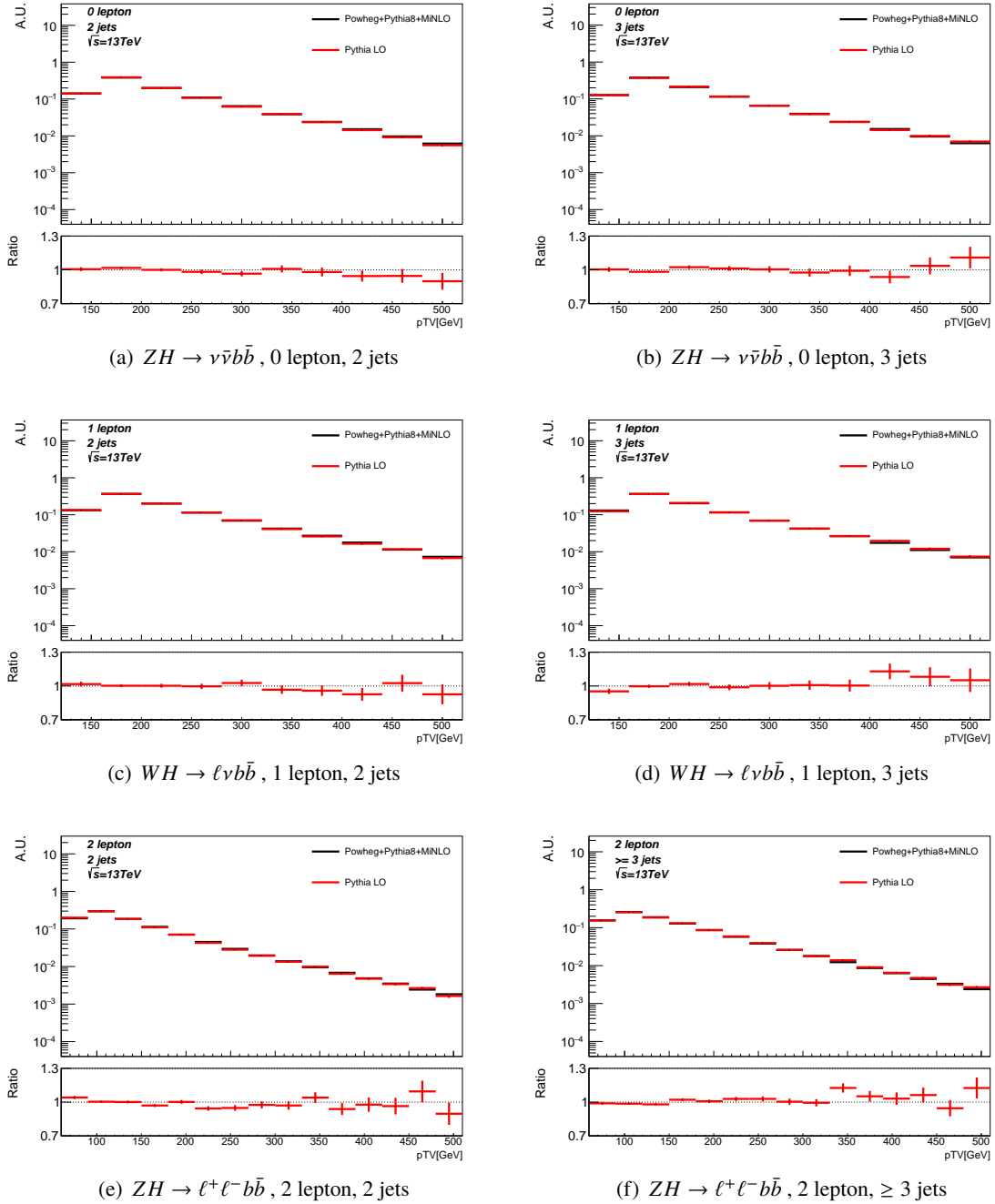


Figure 2: Shape comparison of the p_T^V distributions for each VH process, i.e. lepton channel and each number of jets category, inclusive in p_T^V . Shown is a comparison between PYTHIA 8 (red) and POWHEG +MiNLO+PYTHIA 8 (black). The ratio between the two samples is shown in the lower panel of the plot.

174 2.3. Alternative Monte Carlo Samples

175 In order to cross check the signal modelling and study uncertainties, `MADGRAPH 5_aMC@NLO+PYTHIA 8`
 176 samples were used. These samples are produced using `MADGRAPH 5_aMC@NLO` [7] for the hard scattering
 177 generation and `PYTHIA 8` for the PS, hadronisation, UE and MPI simulation. Following the PDF4LHC
 178 prescription [8] the NNPDF2.3 5f FFN [5] PDF sets with the A14 tune [6] were used. In addition to
 179 the nominal `MADGRAPH 5_aMC@NLO+PYTHIA 8` samples also `MADGRAPH 5_aMC@NLO+PYTHIA 8`
 180 samples with various variations are available. To assess the analysis specific systematic uncertainties the
 181 following samples are considered:

- 182 • `MADGRAPH 5_aMC@NLO+PYTHIA 8` nominal description
- 183 • `MADGRAPH 5_aMC@NLO+PYTHIA 8` with parton shower and underlying event variations: By
 184 comparing these samples to the nominal `MADGRAPH 5_aMC@NLO+PYTHIA 8` samples effects
 185 from the parton showering and underlying event may be assessed. These samples were generated
 186 using 5 tunes of the A14 tune each with an up and a down variation [6].

187 In addition to these samples, `POWHEG +MiNLO+HERWIG 7` samples were used to asses the systematic
 188 uncertainties associated with using a different parton shower model.

189 Contrary to the ICHEP analysis, the nominal signal samples generated with `POWHEG +MiNLO+PYTHIA 8`
 190 include systematic variations which are stored as alternative event weights. The available samples contain
 191 weights which allow the following to be applied:

- 192 • Variations of renormalisation μ_R and factorisation μ_F scales. Both scales are varied by a factor of
 193 0.5 or 2 in a correlated and independent way, leading to 6 possible variations
- 194 • 30 PDF and 2 α_s variations from the PDF4LHC15_30 set [4, 9–14] allowing the computation of
 195 uncertainties following the updated PDF4LHC prescription [9].

196 The presence of internal weights allows the effect of systematic uncertainties on the fully simulated events
 197 to be assessed without having to rely on a particle-based truth selection.

198 2.4. Cross-Section

199 All samples are normalised to the best theoretical prediction of the cross section for the different processes.
 200 The cross sections for WH and ZH are calculated at NNLO in QCD [15] [16] and NLO in EW [17] and
 201 the next-order ($\mathcal{O}(\alpha_S^3)$) contribution to the gluon-induced heavy-quark loop mediate subprocess for ZH
 202 has been calculated in the limit of infinite top-quark and vanishing bottom-quark masses [18]. The cross
 203 section calculation also takes photon-induced contributions into account which are in the order of $\mathcal{O}(5\%)$
 204 for WH and $\mathcal{O}(1\%)$ for ZH . The WH signal samples are normalised to the production cross section
 205 of 1.37 pb; the W^+H production channel contributes with $\sigma_{W^+H} = 0.84$ pb and the W^-H production
 206 channel with $\sigma_{W^-H} = 0.53$ pb to the total cross section. The ZH signal samples are normalised as
 207 follows: the $gg \rightarrow ZH$ samples use their cross section calculated from NLO+NNL QCD corrections
 $\sigma_{gg \rightarrow ZH}^{NLO(QCD)} = 0.12$ pb; the $qq \rightarrow ZH$ samples cross section is obtained from the difference between the
 208 total ZH production cross section and the $gg \rightarrow ZH$ cross section which corresponds to $\sigma_{gg \rightarrow ZH}^{NLO(QCD)} =$
 209 0.76 pb. This is done to avoid double counting when merging $qq \rightarrow ZH$ and $gg \rightarrow ZH$ samples together.
 210 The total cross section for the ZH production corresponds to $\sigma_{ZH}^{NNLO(QCD)+NLO(EW)} = 0.88^{+0.04}_{-0.03}$ pb.
 211 The given uncertainties here take into account QCD scale, PDF and α_s uncertainties which were added
 212

in quadrature but are given as separate nuisance parameters to the fit. They are discussed in detail in section 2.6. All cross section numbers are obtained from the LHC Higgs Cross Section Working Group prescriptions for a Higgs boson mass of $m_H = 125\text{GeV}$. The inclusive cross section for the various signal processes are summarised in Table 2.

Process	order	cross section (pb)
WH	NNLO(QCD)+NLO(EW)	1.37 ± 0.04
W^+H	NNLO(QCD)+NLO(EW)	0.84
W^-H	NNLO(QCD)+NLO(EW)	0.53
ZH	NNLO(QCD)+NLO(EW)	$0.88^{+0.04}_{-0.03}$
$gg \rightarrow ZH$	NLO+NNL(QCD)	0.12
$qq \rightarrow ZH$		0.76

Table 2: Inclusive cross section for the signal processes.

2.5. NLO Electroweak Corrections

Although the total VH cross section used to normalise these samples is computed at NLO (EW), we expect the EW NLO corrections to have a sizeable impact on the shape of the p_T^V distributions (transverse momentum of the Higgs boson), which is not accounted for in the total higher order cross section (and it's not included in the MC prediction from Powheg or Pythia 8). The VH differential cross section will therefore be computed at NLO EW using the HAWK MC software as a function of p_T^V to extract a correction function $k_{EW}^{NLO}(p_T^V) = 1 + \delta_{EW}$. Figure 3 shows δ_{EW} in dependence of p_T^V for $(W^- \rightarrow l^-\bar{\nu})H$, $(W^+ \rightarrow l^+\nu)H$, $(Z \rightarrow l^+l^-)H$ and $(Z \rightarrow \nu\bar{\nu})H$. Note that this is applied only to the $qqVH$ processes and is not applied to $ggZH$.

2.6. Systematic Uncertainties

2.6.1. Inclusive cross section uncertainties

The first set of systematics are overall normalisation uncertainties that stem from uncertainties on the calculation of the VH cross section and the $H \rightarrow b\bar{b}$ branching ratio for a nominal Higgs boson mass of $m_H = 125$ GeV. They follow the recommendations of the LHC Higgs working group [19] and [20] and are summarised in table 3.

The QCD scale uncertainties on the overall VH cross section were obtained by varying the renormalisation scale μ_R and factorisation scale μ_F independently in a range of 1/3 of their original value and 3 times their original value.. The PDF and α_s uncertainty on the overall VH cross section is given combined and was calculated from the 68% CL interval using the PDF4LHC15_nnlo_mc PDF set. Since the latest LHC Higgs working group recommendations [19] do not separate between uncertainties for $qq \rightarrow ZH$ and $gg \rightarrow ZH$ and only gives them for the overall ZH production two different approaches were chosen to separate these two cases. To obtain the QCD scale uncertainties separately for $qq \rightarrow ZH$ and $gg \rightarrow ZH$ it was assumed that the QCD scale uncertainty on $qq \rightarrow ZH$ is identical to the QCD scale uncertainty on WH . The $gg \rightarrow ZH$ uncertainty is then derived such that the sum in quadrature of the $qq \rightarrow ZH$ and $gg \rightarrow ZH$ uncertainties considering their respective production cross sections amounts to the QCD scale uncertainty for the overall ZH production given in [20]. Since the PDF+ α_s uncertainties are larger for WH than

Not reviewed, for internal circulation only

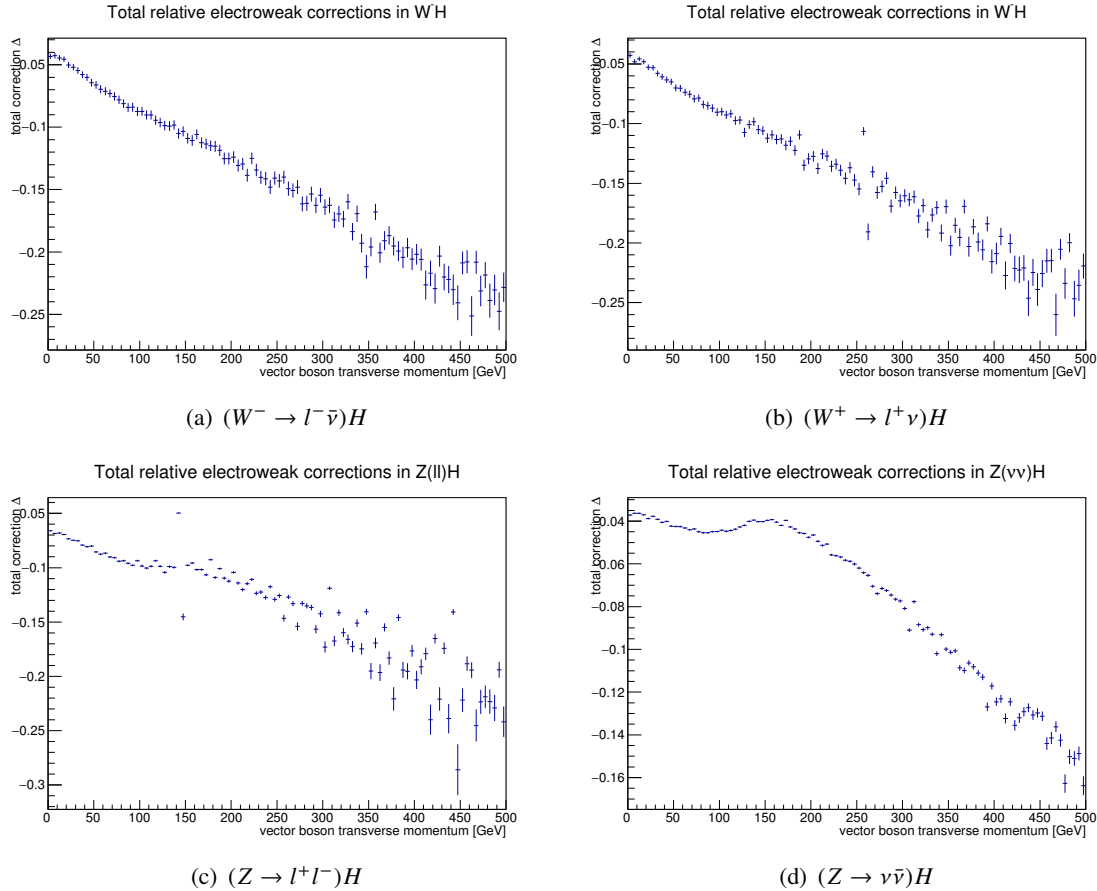


Figure 3: $[\delta_{\text{EW}}$ distribution in dependence of p_T^V for the $(W^- \rightarrow l^- \bar{\nu})H$, $(W^+ \rightarrow l^+ \nu)H$, $(Z \rightarrow l^+ l^-)H$ and $(Z \rightarrow \nu \bar{\nu})H$ process.

243 ZH production the method used for the QCD scale uncertainty cannot be exploited for this uncertainty.
 244 Therefore the uncertainty for the $gg \rightarrow ZH$ production was taken from previous recommendations [19]
 245 while the $qq \rightarrow ZH$ PDF+ α_s uncertainty was taken from the latest recommendation [20] under the
 246 assumption that the $gg \rightarrow ZH$ uncertainty has no large contribution to the overall uncertainty and
 247 therefore the overall ZH uncertainty corresponds to the $qq \rightarrow ZH$ uncertainty.

248 Another systematic uncertainty on the overall VH cross section originates from unaccounted higher order
 249 electro-weak effects and it is determined in the following way:

$$250 \quad \Delta_{\text{EW}} = \max\{1\%, \delta_{\text{EW}}^2, \Delta_\gamma\}$$

251 with the maximum of the generic size of the neglected NNLO EW effects 1%, the relative NLO EW
 252 correction δ_{EW} and the uncertainty of the photon induced cross section relative to the total $(W/Z)H$ cross
 253 section. The systematic uncertainty on the $H \rightarrow b\bar{b}$ branching ratio is 1.7% following the recommendations
 254 of the LHC Higgs working group. This uncertainty takes into account missing higher order effects in
 255 QCD and EW theory calculation as well as uncertainties on the b -quark mass and α_s .

Sys Name	source	Norm. effect	applied to
ATLAS_BR_bb	$H \rightarrow b\bar{b}$ decay uncertainties (HO effects, m_b , α_s)	1.7%	all VH processes
ATLAS_QCDscale_VH	QCD scale uncertainty	0.7%	$qq \rightarrow VH$ processes
ATLAS_QCDscale_ggZH	QCD scale uncertainty	27%	$gg \rightarrow ZH$
ATLAS_pdf_Higgs_VH	PDF+ α_s uncertainty	1.9% 1.6%	$qq \rightarrow WH$ $qq \rightarrow ZH$
ATLAS_pdf_Higgs_ggZH	PDF+ α_s uncertainty	5.0%	$gg \rightarrow ZH$

Table 3: Summary of all systematic uncertainties on the VH cross section including their value, source and the corresponding nuisance parameter name.

256 2.6.2. Analysis specific uncertainties

257 To assess analysis specific systematic uncertainties, a combination of the nominal samples with internal
 258 variation weights applied and the **MADGRAPH 5_aMC@NLO+PYTHIA 8** samples as described in sec-
 259 tion 2.3, were utilised. Most of the samples were studied on particle level using Rivet but in the case of
 260 the PDF uncertainties the reco-level distributions were studied. The Rivet analysis was implemented to
 261 mirror the $V(H \rightarrow b\bar{b})$ analysis as close as possible and the object and event selections are described in
 262 appendix A. For each variation two different set of systematics were determined: acceptance uncertainties
 263 for the analysis categories and shape uncertainties for the p_T^V and $m_{b\bar{b}}$ shape. These two distributions
 264 were chosen since Run 1 experience shows that they are sufficiently decorrelated, the most important input
 265 variables for the BDTs and uncertainties on those two variables cover sufficiently shape uncertainties in
 266 the other input variables. For all comparisons the samples were normalised to the same cross section to
 267 only assess acceptance uncertainties. For the shape uncertainties all distributions were also normalised to
 268 the same area since acceptance uncertainties are already accounted for.

269 In all cases the uncertainties for $ZH \rightarrow \nu\bar{\nu}b\bar{b}$ were derived using the 0 lepton selection, the uncertainties
 270 for $WH \rightarrow \ell\nu b\bar{b}$ using the 1 lepton selection and for $ZH \rightarrow \ell^+\ell^- b\bar{b}$ using the 2 lepton selection.

271 PS and UE variations

272 For the PS and UE variations, acceptance and shape uncertainties were derived. Two different approaches
 273 were used for this: nominal **MADGRAPH 5_aMC@NLO+PYTHIA 8** samples were compared to those
 274 generated with the varied A14 tunes and the nominal **POWHEG +MiNLO+PYTHIA 8** was compared to
 275 **POWHEG +MiNLO+HERWIG 7** to assess the effects of using a different parton shower model. The first set
 276 of systematics are acceptance uncertainties for the 2 jet and 3(3p) jet categories of each VH channel,
 277 i.e. lepton channel, given by the ratio of each variation and the nominal. To derive the final PS/UE
 278 uncertainty the maximum was taken between the absolute value of the up variation and the absolute value
 279 of the down variation for each tune and then the uncertainties of all tunes were added in quadrature.
 280 Following the recommendation from the Physics Modelling Group, the final uncertainty comes from taking
 281 the envelope between this quadrature sum and the uncertainty from the parton shower model comparison.
 282 The uncertainty on the 2-jet acceptance was taken as the final acceptance uncertainty and an additional
 283 systematic uncertainty was derived to control the ratio between the 2 jet and 3(3p) jet categories calculating
 284 double ratios for each variation:

$$\frac{\text{Acceptance}[\text{Category}_A(\text{nominal MC})]}{\text{Acceptance}[\text{Category}_B(\text{nominal MC})]} \left| \frac{\text{Acceptance}[\text{Category}_A(\text{alternative MC})]}{\text{Acceptance}[\text{Category}_B(\text{alternative MC})]} \right| \quad (1)$$

285 The combination of all tunes for this 2 jet to 3(3p) jet ratio was done in the same way as was done for the 2
 286 jet and 3(3p) jet category, described above. All acceptance uncertainties for the 2 lepton channel are calcu-

lated inclusive in p_T^V and additional p_T^V shape uncertainties were derived. The values of these acceptance uncertainties are summarised in table 4 and uncertainties with the same nuisance parameter name are correlated in the fit. Based on Run 1 experience, for the ZH channels the same uncertainties are used for the $gg \rightarrow ZH$ production channel and are correlated to the uncertainties for the $qq \rightarrow ZH$ production channel.

To derive the shape uncertainties from A14 tune variations for p_T^V and $m_{b\bar{b}}$, the deviation between each variation and the nominal MADGRAPH 5_aMC@NLO+PYTHIA 8 description was parametrised by a linear fit for p_T^V and a second order polynominal for $m_{b\bar{b}}$, which is shown in figure 4 and 5 respectively. For both the p_T^V and $m_{b\bar{b}}$ distributions, the up and down variation of each tune was fitted. The shapes were considered separately for the 2-jet and 3-jet channels in each case. From Figure 4 it can be seen that the p_T^V shape deviations are small and similar in the 2-jet and 3(3p)-jet regions therefore the same shape uncertainty was used for both. The $p_T V^V$ shapes seen from the comparison between nominal POWHEG +MiNLO+PYTHIA 8 and the POWHEG +MiNLO+HERWIG 7 sample were found to be smaller than those seen for the A14 tunes, therefore no uncertainty was assigned from this. For the $m_{b\bar{b}}$ distributions, the strongest shape deviations were seen from the parton shower model comparison, shown in Figure 6. These shapes were similar across all analysis regions. The shapes are complex and as a result were difficult to fit, therefore the histogram showing the largest deviation was used as the shape uncertainty. For the ZH channels the same uncertainties are used for the $gg \rightarrow ZH$ production channel and are correlated to the uncertainties for the $qq \rightarrow ZH$ production channel.

NP name	0L: $ZH \rightarrow v\bar{v}bb$		1L: $WH \rightarrow \ell vbb$		2L: $ZH \rightarrow \ell^+\ell^-bb$	
	2j	3j	2j	3j	2j	$\geq 3j$
ATLAS_UEPS_VH_hbb	10.0%	10.0%	12.1%	12.1%	13.9%	13.9%
ATLAS_UEPS_VH_hbb_32JR	—	13.0%	—	12.9%	—	13.4%
ATLAS_UEPS_VH_hbb_VPT	shape only				shape+norm	
ATLAS_UEPS_VH_hbb_MBB	shape only					

Table 4: Summary of the effects of parton shower and underlying event variations on the VH acceptance in each analysis region and on the p_T^V and $m_{b\bar{b}}$ shapes, including their nuisance parameter name.

Not reviewed, for internal circulation only

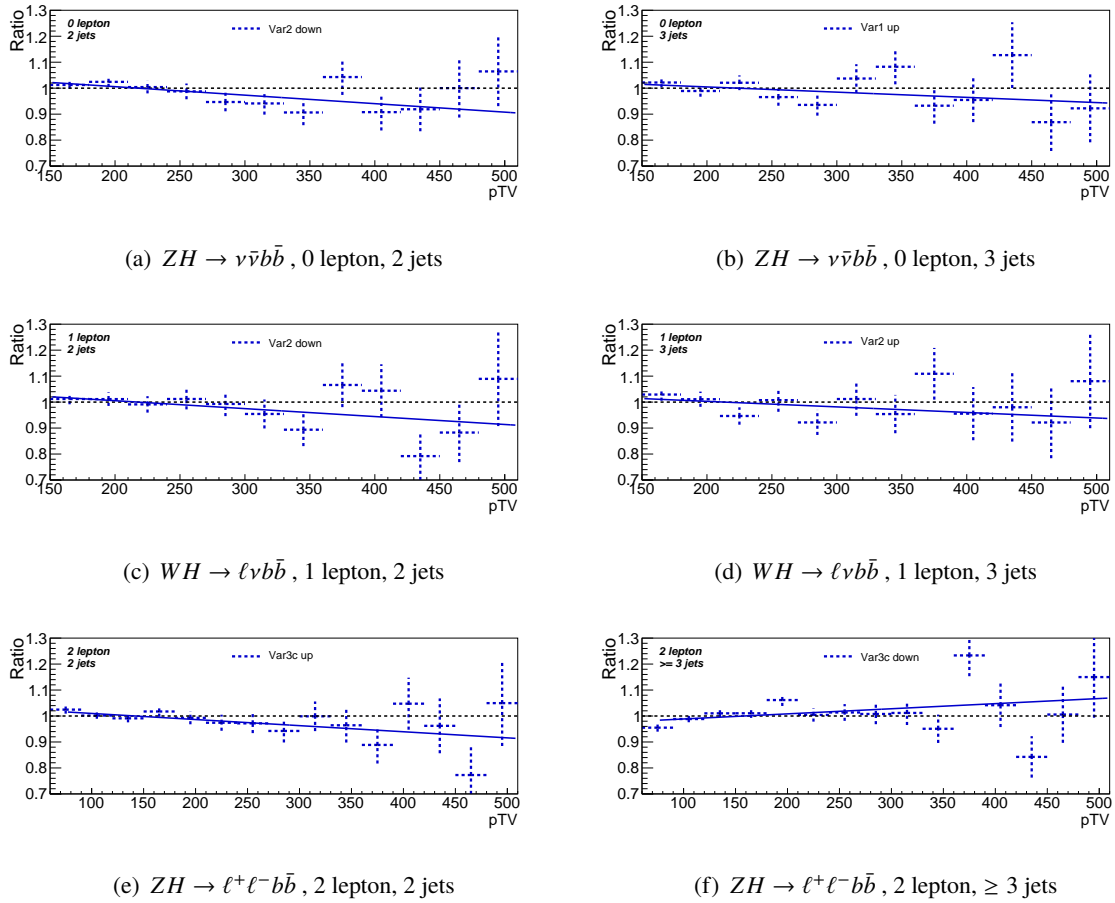


Figure 4: p_T^V : for each VH process, i.e. lepton channel, the PS/UE variation is shown that has a significant slope and the largest deviation to the nominal. The fit through these deviations were used as systematic uncertainties.

Not reviewed, for internal circulation only

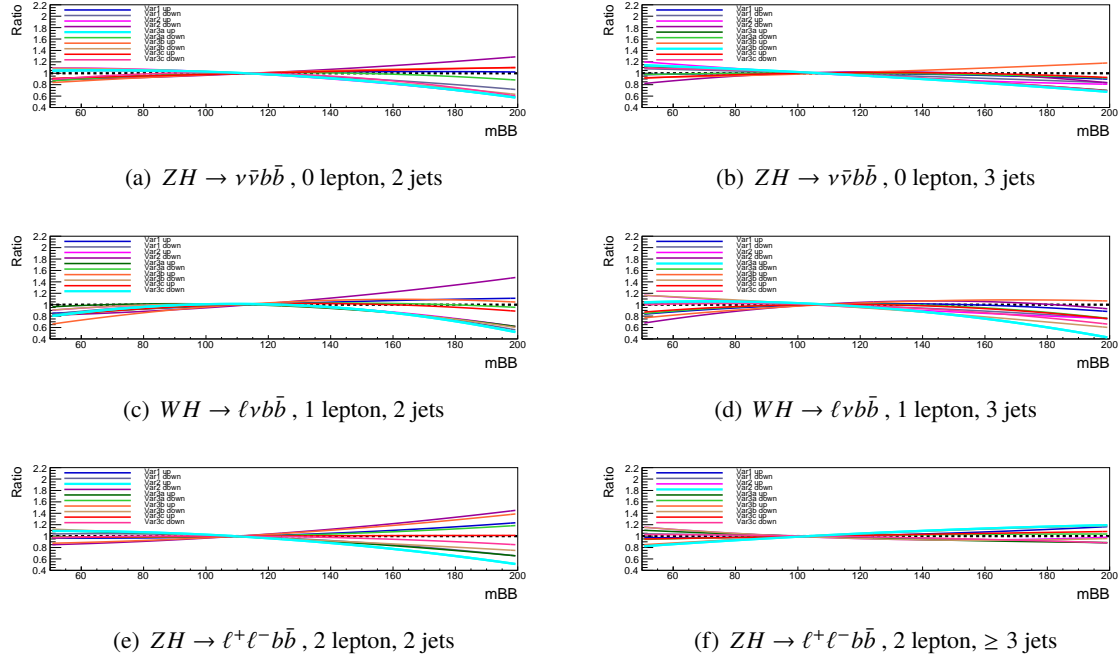


Figure 5: Shape comparison of the $m_{b\bar{b}}$ distributions for each VH process, i.e. lepton channel, and each number of jets category. Shown is the fit through the up and down variation of each tune where the maximum fit is highlighted by the cyan line. The latter was used as a shape uncertainty.

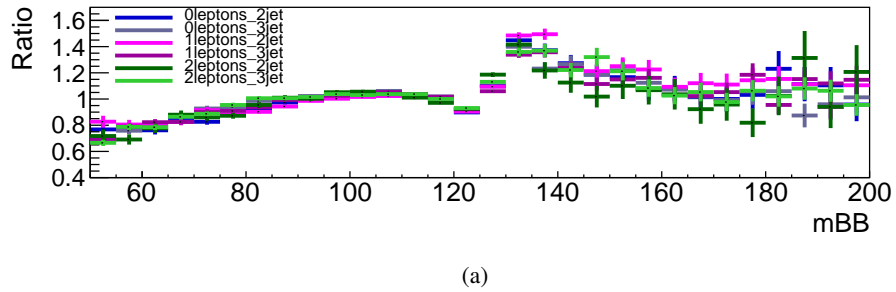


Figure 6: Shape comparison of the $m_{b\bar{b}}$ distributions for each VH process, i.e. lepton channel, and each number of jets category after comparing the POWHEG +MiNLO+PYTHIA 8 and POWHEG +MiNLO+HERWIG 7 sample.

306 **Scale variations**

307 For the scale variations acceptance and shape uncertainties were derived. To derive those the nominal
 308 **POWHEG +MiNLO+PYTHIA 8** samples were compared to those generated with weights corresponding to
 309 varied factorisation and renormalisation scales applied. The first set of systematics are acceptance
 310 uncertainties for the 2 jet and 3(3p) jet categories of each lepton channel. For the 0 and 1 lepton channel
 311 an additional acceptance uncertainty was assigned to the 3 jet category that accounts for the fact that events
 312 with 4 jets are vetoed in the analysis. To derive the uncertainties the envelope of the various combinations
 313 of μ_R and μ_F was taken and the final uncertainties were derived using the Stewart-Tackmann-method (ST
 314 method) [21]. All acceptance uncertainties for the 2 lepton channel are calculated inclusive in p_T^V and
 315 additional p_T^V shape uncertainties were derived. For the ZH channels the same uncertainties are used for
 316 the $gg \rightarrow ZH$ production channel but are de-correlated to the uncertainties for the $qq \rightarrow ZH$ production
 317 channel since Run 1 experience showed a difference between the uncertainties for these two production
 318 channels. The values of these acceptance uncertainties are summarised in table 5.
 319 To derive the shape uncertainties for $m_{b\bar{b}}$ and p_T^V the deviation between each variation and the nominal
 320 description was parametrised by a linear fit for p_T^V and a second order polynomial for $m_{b\bar{b}}$ which is shown
 321 in figure 7 and 8 respectively. For both variables, the shapes were considered separately for the 2 jet
 322 and 3 jet category. From Figure 7 it can be seen that the p_T^V shapes are very similar across all regions
 323 therefore the largest variation was considered as correlated across all channels. For the ZH channels the
 324 same uncertainties are used for the $gg \rightarrow ZH$ production channel and are correlated to the uncertainties
 325 for the $qq \rightarrow ZH$ production channel.

NP name	0L: $ZH \rightarrow v\bar{v}bb$		1L: $WH \rightarrow \ell v\bar{v}bb$		2L: $ZH \rightarrow \ell^+\ell^-bb$	
	2j	3j	2j	3j	2j	$\geq 3j$
QCDscale_VH_ANA_hbb_J2	6.9%	–	8.8%	–	3.3%	–
QCDscale_VH_ANA_hbb_J3	-7%	+5%	-8.6%	+6.8%	-3.2%	+3.9%
QCDscale_VH_ANA_hbb_JVeto	–	-2.5%	–	3.8%	–	–
QCDscale_VH_ANA_hbb_VPT	shape only				shape+norm	
QCDscale_VH_ANA_hbb_MBB	shape only					

Table 5: Summary of the systematic uncertainties on the VH acceptance in each analysis region and on the p_T^V and $m_{b\bar{b}}$ shapes originating from altering the QCD scale, including their nuisance parameter name.

Not reviewed, for internal circulation only

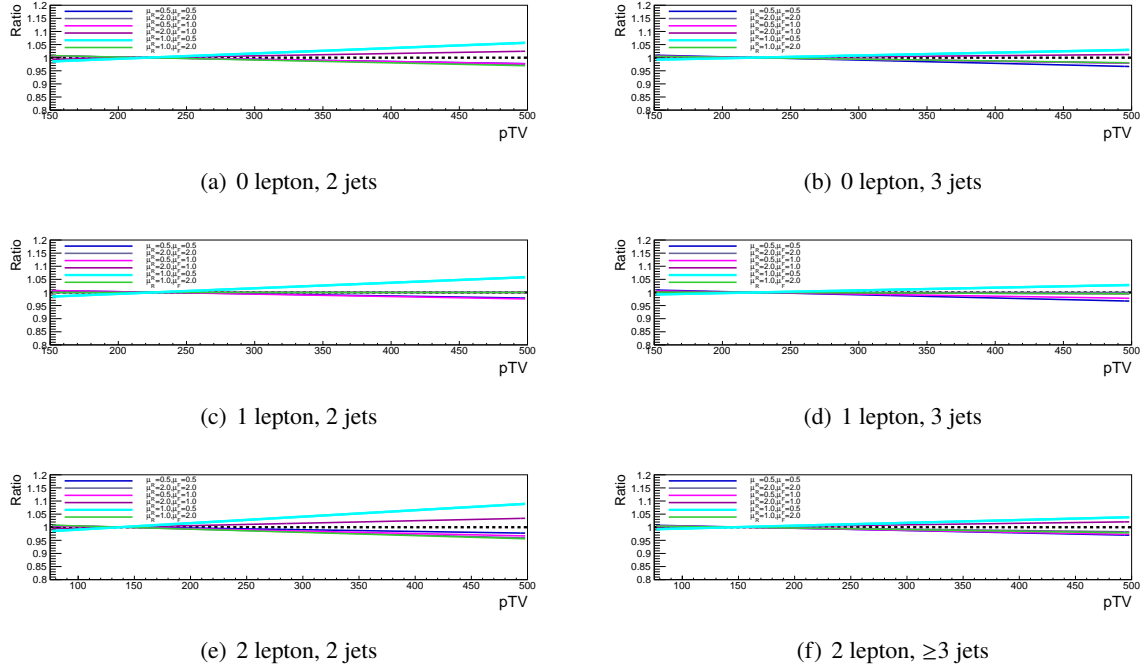


Figure 7: p_T^V : Fits through the deviations originating from each scale variation for each VH process, i.e. lepton channel, split into the 2 jet and 3(3p) jet category. The cyan line shows the envelope of those variations and was chosen as a systematic uncertainty for the p_T^V shape.

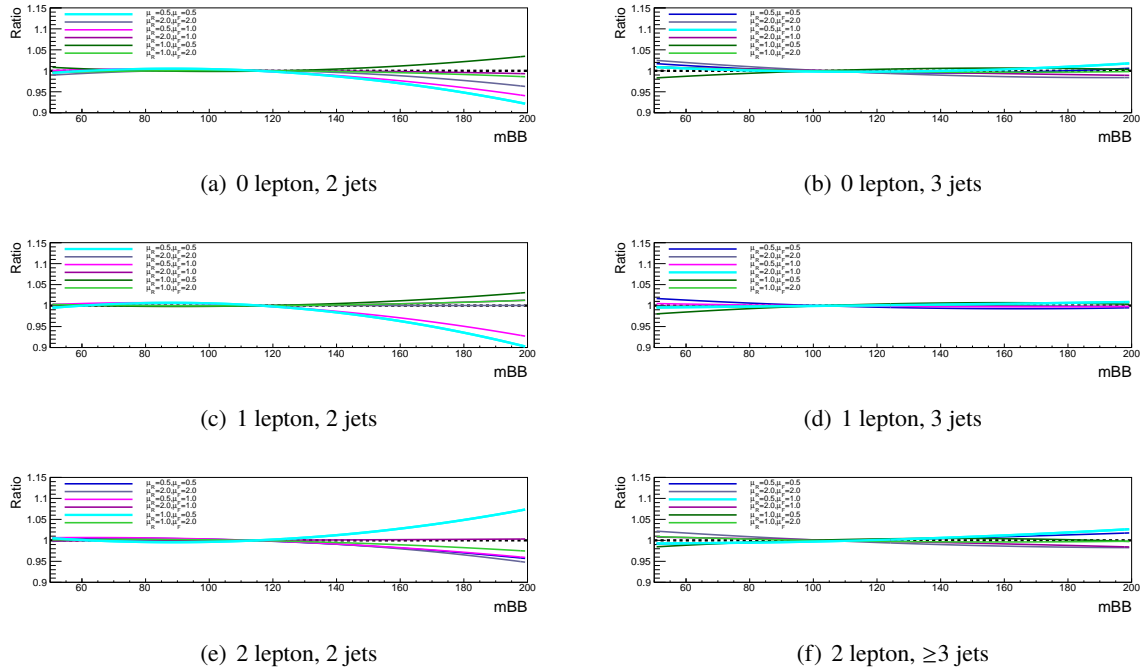


Figure 8: $m_{bb\bar{b}}$: Fits through the deviations originating from each scale variation for each VH process, i.e. lepton channel, split into the 2 jet and 3(3p) jet category. The cyan line shows the envelope of those variations and was chosen as a systematic uncertainty for the $m_{bb\bar{b}}$ shape.

326 **PDF + α_s uncertainties**

327 For the PDF and α_s variations acceptance and shape uncertainties were derived. To derive those the
 328 nominal Powheg +MiNLO+Pythia 8 samples were compared to those generated with the uncertainties
 329 from the PDF4LHC15_30 PDF set. As mentioned earlier, these uncertainties were generated using
 330 reco-level distributions. This is mainly due to technical limitations in the rivet framework as it is very
 331 cumbersome and inefficient to run over a large number of weight variations. The first set of systematics are
 332 overall acceptance uncertainties. No distinction was made between the 2 jet and 3(3p) jet categories since
 333 they both yield similar uncertainties. All acceptance uncertainties for the 2 lepton channel are calculated
 334 inclusive in p_T^V and additional p_T^V shape uncertainties were derived. To derive the PDF component of the
 335 uncertainty, the sum in quadrature of variations from altering the PDF uncertainty was taken. The α_s
 336 component of the uncertainty was derived by taking the average of the variations coming from altering α_s .
 337 The final uncertainty then came from adding these two components in quadrature. For the ZH channels
 338 these uncertainties are only used for the $qq \rightarrow ZH$ channel. For the $gg \rightarrow ZH$ production channel the
 339 Run 1 numbers were used since those are significantly larger than the ones derived in these studies. The
 340 values of these acceptance uncertainties are summarised in table 6.

341 To derive the shape uncertainties for $m_{b\bar{b}}$ and p_T^V the deviation between each variation and the nominal
 342 description was parametrised by a linear fit for p_T^V and a second order polynomial for $m_{b\bar{b}}$ which is
 343 shown in figure 9 and 10 respectively. It was found that the PDF and α_s variations only have a negligible
 344 effect on the $m_{b\bar{b}}$ shape and therefore no shape uncertainty was assigned to this distribution. For p_T^V
 345 the uncertainties were determined separately for the 2 jet and 3 jet category. These shapes deviations
 346 were also found to be very small and extremely consistent across all channels, therefore the largest shape
 347 variation of these was taken as the final shape uncertainty. For the ZH channels the same uncertainties
 348 are used for the $gg \rightarrow ZH$ production channel and are de-correlated to the uncertainties for the $qq \rightarrow ZH$
 349 production channel based on Run 1 experience.

NP name	0L: $ZH \rightarrow v\bar{v}b\bar{b}$		1L: $WH \rightarrow \ell v b\bar{b}$		2L: $ZH \rightarrow \ell^+ \ell^- b\bar{b}$	
	2j	3j	2j	3j	2j	$\geq 3j$
pdf_HIGGS_VH_ANA_hbb	1.1%	1.1%	1.3%	1.3%	0.5%	0.5%
pdf_VH_ANA_hbb_VPT	shape only				shape+norm	
pdf_VH_ANA_hbb_MBB	shape only					

Table 6: Summary of all systematic uncertainties on the VH acceptance and shapes originating from altering the PDF and α_s uncertainties, including their corresponding nuisance parameter name.

Not reviewed, for internal circulation only

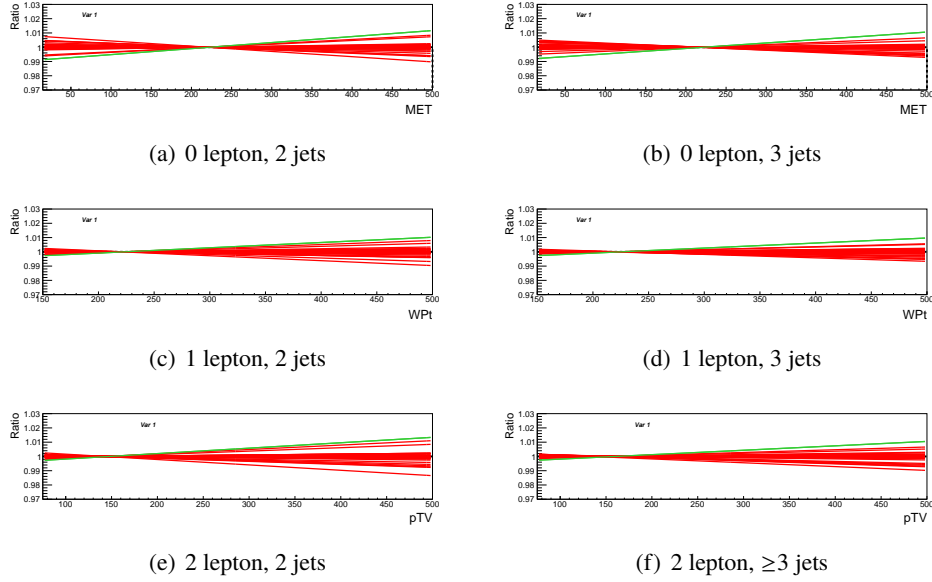


Figure 9: p_T^V : Fits through the deviations originating from each PDF and α_s variation for each VH process, i.e. lepton channel, split into the 2 jet and 3(3p) jet category. The green line shows the envelop of those variations and was chosen as a systematic uncertainty for the p_T^V shape.

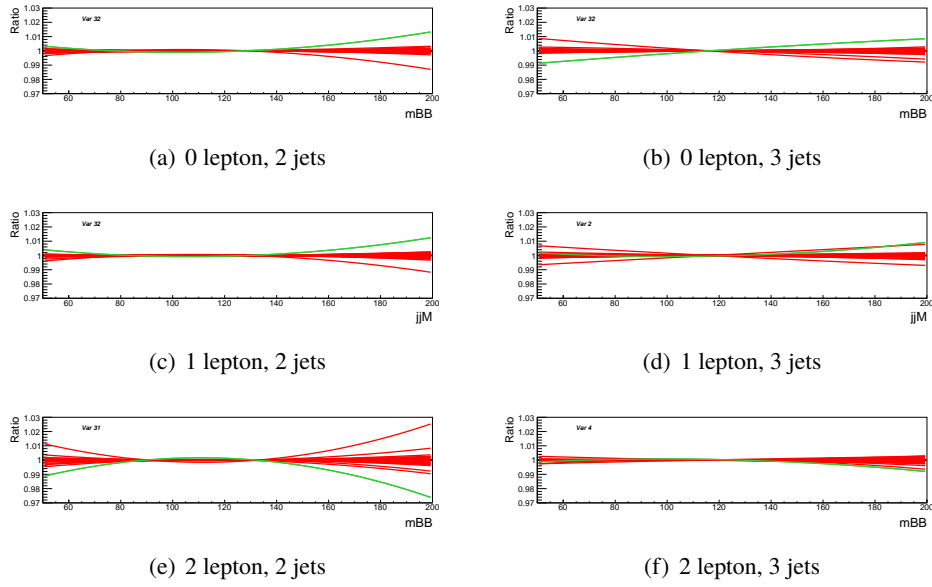


Figure 10: $m_{b\bar{b}}$: Fits through the deviations originating from each PDF and α_s variation for each VH process, i.e. lepton channel, split into the 2 jet and 3(3p) jet category. The variations were found to be negligible and no systematic uncertainty was assigned.

350 **3. Backgrounds**

351 The goal of this section is to give a full and comprehensive overview of the MC samples used in this
352 analysis, covering both the samples used for the nominal MC prediction, and alternative samples produced
353 in order to estimate modelling systematic uncertainties. To provide a clear description of these points the
354 section is divided in several sub-sections for the different background processes: for each background the
355 different MC samples produced and utilised are described in full detail, and the methods used to assess
356 systematic uncertainties are outlined. V+jets processes are described in Section 3.1, $t\bar{t}$ in Section 3.2 and
357 single-top in Section 3.3.

358 **3.1. Vector Boson+Jets Production**

359 **3.1.1. Nominal Monte Carlo Prediction**

360 The production of V ($V=W$ or Z) bosons in association with jets is one of the main backgrounds for all
 361 the lepton channels considered in these analyses. The production of high statistics, reliable V +jets MC
 362 samples is important for this and many other ATLAS analyses. Therefore, efforts have been made by
 363 ATLAS to update to the latest V +jets MC generators, including moving from LO to NLO generation,
 364 and updating parameter tunings for the Run 2 data taking period. Details on this effort for V +jets MC
 365 programs can be found in [22]. Furthermore, since ICHEP 2016, the default generator has been updated
 366 from SHERPA 2.2 to SHERPA 2.2.1, and a new phase-space slicing has been adopted.

367 The V +jet processes are simulated with SHERPA 2.2.1 [23] interfaced with the NNPDFs [5] for both the ME
 368 calculation and the parton shower tuning. In order to provide a good modelling of large jet multiplicities
 369 (events with many jets produced in association with the W or the Z boson, which largely contributes to
 370 the background in the phase space considered by these analyses) SHERPA 2.2.1 provides a combination
 371 of different matrix elements with different parton multiplicities: up to two extra partons are included
 372 in the next-to-leading order (NLO) ME, and 3 or 4 extra partons are included at leading order (LO) in
 373 QCD. The merging of different parton multiplicities is achieved through a matching scheme based on the
 374 CKKW-L [24] [25] merging technique using a merging scale of $Q_{cut} = 20$ GeV. The modeling of even
 375 higher jet multiplicities relies on the parton shower algorithm. The parton shower and underlying event
 376 models used are the ones provided internally by SHERPA.

377 The SHERPA 2.2.1 generator adopts a full 5-flavour scheme, with massless b-quarks and c-quarks in the
 378 matrix elements, while massive quarks can be produced in the parton shower (heavy flavours can be
 379 produced directly in the scattering processes of the underlying event as well).

380 The analyses treated here include phase spaces corresponding to high p_T of the vector boson (boosted
 381 phase space) or large values of the invariant mass: it is therefore important to ensure that statistical
 382 fluctuations of the background prediction are small compared to those in data, to be able fully to exploit
 383 the sensitivity of these regions. To achieve this aim the SHERPA 2.2.1 V +jets samples are split according
 384 to the p_T of the vector boson and the H_T of the event, introducing a cut at generation level, and producing
 385 samples for different slices in $\max(H_T, p_T^V)$ (where p_T^V is defined as the transverse momentum of the true
 386 lepton pair from the decay of the V boson). The split in $\max(H_T, p_T^V)$ uses the following intervals:

387 $[0\text{--}70, 70\text{--}140, 140\text{--}280, 280\text{--}500, 500\text{--}1000, >1000] \text{ GeV}$

388 This is a change from the ICHEP 2016 analyses, for which the samples were instead split in the variable
 389 p_T^V , and in a greater number of intervals.

390 In these analyses we consider final states with b-tagged jets (requiring 1, 2 or more b-tagged jets); it
 391 is therefore important to make sure that the MC statistics in this specific heavy-flavour enriched phase
 392 space is large enough to provide a robust MC prediction to be compared to data. The V +jets samples
 393 are therefore generated applying different filters to select the flavour composition of the jets produced in
 394 association with the V boson. The filters used for these samples are outlined in Table 7. The filters are
 395 not applied to the highest slices (which is a change from the ICHEP 16 analysis).

396 All V +jets samples with the corresponding $\max(H_T, p_T^V)$ slices and heavy-flavour filters are listed in
 397 Tables 8 9, and 10.

Filter	Description
BFILTER	at least 1 b-hadron with $p_T > 0$ GeV and $ \eta < 4$
CFilterBVeto	at least 1 c-hadron with $p_T > 4$ GeV and $ \eta < 3$ veto events which pass the BFILTER
CVetoBVeto	veto events which pass the BFILTER or the CFilterBVeto

Table 7: Heavy flavour filters used for $V+jets$.

DS ID	Process	Generator	$\sigma \times BR$ [pb]	k-factor	ϵ_{filter}	Events
364184	$W \rightarrow \tau\nu, 0 < \max(H_T, p_T^W) < 70$ GeV, C veto & B veto	SHERPA 2.2.1	19152.0	0.9702	0.82495	24964000
364185	$W \rightarrow \tau\nu, 0 < \max(H_T, p_T^W) < 70$ GeV, C filter & B Veto	SHERPA 2.2.1	19153.0	0.9702	0.12934	9994600
364186	$W \rightarrow \tau\nu, 0 < \max(H_T, p_T^W) < 70$ GeV, B filter	SHERPA 2.2.1	19163.0	0.9702	0.044594	17487200
364187	$W \rightarrow \tau\nu, 70 < \max(H_T, p_T^W) < 140$ GeV, C veto & B veto	SHERPA 2.2.1	947.65	0.9702	0.67382	14999500
364188	$W \rightarrow \tau\nu, 70 < \max(H_T, p_T^W) < 140$ GeV, C filter & B Veto	SHERPA 2.2.1	946.73	0.9702	0.22222	10000000
364189	$W \rightarrow \tau\nu, 70 < \max(H_T, p_T^W) < 140$ GeV, B filter	SHERPA 2.2.1	943.3	0.9702	0.10391	10000000
364190	$W \rightarrow \tau\nu, 140 < \max(H_T, p_T^W) < 280$ GeV, C veto & B veto	SHERPA 2.2.1	339.36	0.9702	0.59622	10000000
364191	$W \rightarrow \tau\nu, 140 < \max(H_T, p_T^W) < 280$ GeV, C filter & B Veto	SHERPA 2.2.1	339.63	0.9702	0.29025	7500000
364192	$W \rightarrow \tau\nu, 140 < \max(H_T, p_T^W) < 280$ GeV, B filter	SHERPA 2.2.1	339.55	0.9702	0.11229	24999900
364193	$W \rightarrow \tau\nu, 280 < \max(H_T, p_T^W) < 500$ GeV, C veto & B veto	SHERPA 2.2.1	72.065	0.9702	0.54569	4999200
364194	$W \rightarrow \tau\nu, 280 < \max(H_T, p_T^W) < 500$ GeV, C filter & B Veto	SHERPA 2.2.1	71.976	0.9702	0.31648	2998400
364195	$W \rightarrow \tau\nu, 280 < \max(H_T, p_T^W) < 500$ GeV, B filter	SHERPA 2.2.1	72.026	0.9702	0.13426	2999100
364196	$W \rightarrow \tau\nu, 500 < \max(H_T, p_T^W) < 1000$ GeV	SHERPA 2.2.1	15.046	0.9702	1.0	6000000
364197	$W \rightarrow \tau\nu, 1000 < \max(H_T, p_T^W) < 13000$ GeV	SHERPA 2.2.1	1.2339	0.9702	1.0	4000000
364196	$W \rightarrow \mu\nu, 0 < \max(H_T, p_T^W) < 70$ GeV, C veto & B veto	SHERPA 2.2.1	19143.0	0.9702	0.8238	24986000
364197	$W \rightarrow \mu\nu, 0 < \max(H_T, p_T^W) < 70$ GeV, C filter & B Veto	SHERPA 2.2.1	19146.0	0.9702	0.13035	19984000
364198	$W \rightarrow \mu\nu, 0 < \max(H_T, p_T^W) < 70$ GeV, B filter	SHERPA 2.2.1	19147.0	0.9702	0.044601	34971800
364199	$W \rightarrow \mu\nu, 70 < \max(H_T, p_T^W) < 140$ GeV, C veto & B veto	SHERPA 2.2.1	945.52	0.9702	0.67464	29933500
364200	$W \rightarrow \mu\nu, 70 < \max(H_T, p_T^W) < 140$ GeV, C filter & B Veto	SHERPA 2.2.1	945.53	0.9702	0.23255	19948600
364201	$W \rightarrow \mu\nu, 70 < \max(H_T, p_T^W) < 140$ GeV, B filter	SHERPA 2.2.1	945.11	0.9702	0.075648	19915000
364202	$W \rightarrow \mu\nu, 140 < \max(H_T, p_T^W) < 280$ GeV, C veto & B veto	SHERPA 2.2.1	339.93	0.9702	0.61058	20000000
364203	$W \rightarrow \mu\nu, 140 < \max(H_T, p_T^W) < 280$ GeV, C filter & B Veto	SHERPA 2.2.1	340.02	0.9702	0.2894	15000000
364204	$W \rightarrow \mu\nu, 140 < \max(H_T, p_T^W) < 280$ GeV, B filter	SHERPA 2.2.1	339.54	0.9702	0.10872	24585000
364205	$W \rightarrow \mu\nu, 280 < \max(H_T, p_T^W) < 500$ GeV, C veto & B veto	SHERPA 2.2.1	72.104	0.9702	0.54647	4999000
364206	$W \rightarrow \mu\nu, 280 < \max(H_T, p_T^W) < 500$ GeV, C filter & B Veto	SHERPA 2.2.1	72.14	0.9702	0.31743	2999000
364207	$W \rightarrow \mu\nu, 280 < \max(H_T, p_T^W) < 500$ GeV, B filter	SHERPA 2.2.1	72.051	0.9702	0.13337	2999500
364208	$W \rightarrow \mu\nu, 500 < \max(H_T, p_T^W) < 1000$ GeV	SHERPA 2.2.1	15.015	0.9702	1.0	5998500
364209	$W \rightarrow \mu\nu, 1000 < \max(H_T, p_T^W) < 13000$ GeV	SHERPA 2.2.1	1.2348	0.9702	1.0	4000000
364210	$W \rightarrow e\nu, 0 < \max(H_T, p_T^W) < 70$ GeV, C veto & B veto	SHERPA 2.2.1	19151.0	0.9702	0.82447	24998000
364211	$W \rightarrow e\nu, 0 < \max(H_T, p_T^W) < 70$ GeV, C filter & B Veto	SHERPA 2.2.1	19148.0	0.9702	0.13033	19991000
364212	$W \rightarrow e\nu, 0 < \max(H_T, p_T^W) < 70$ GeV, B filter	SHERPA 2.2.1	19145.0	0.9702	0.044141	17492400
364213	$W \rightarrow e\nu, 70 < \max(H_T, p_T^W) < 140$ GeV, C veto & B veto	SHERPA 2.2.1	945.33	0.9702	0.67111	29680000
364214	$W \rightarrow e\nu, 70 < \max(H_T, p_T^W) < 140$ GeV, C filter & B Veto	SHERPA 2.2.1	946.77	0.9702	0.22823	11580400
364215	$W \rightarrow e\nu, 70 < \max(H_T, p_T^W) < 140$ GeV, B filter	SHERPA 2.2.1	946.23	0.9702	0.10341	9905900
364216	$W \rightarrow e\nu, 140 < \max(H_T, p_T^W) < 280$ GeV, C veto & B veto	SHERPA 2.2.1	339.88	0.9702	0.59977	20000000
364217	$W \rightarrow e\nu, 140 < \max(H_T, p_T^W) < 280$ GeV, C filter & B Veto	SHERPA 2.2.1	340.12	0.9702	0.28965	7500000
364218	$W \rightarrow e\nu, 140 < \max(H_T, p_T^W) < 280$ GeV, B filter	SHERPA 2.2.1	339.79	0.9702	0.10898	24999800
364219	$W \rightarrow e\nu, 280 < \max(H_T, p_T^W) < 500$ GeV, C veto & B veto	SHERPA 2.2.1	72.093	0.9702	0.54441	4998800
364220	$W \rightarrow e\nu, 280 < \max(H_T, p_T^W) < 500$ GeV, C filter & B Veto	SHERPA 2.2.1	72.136	0.9702	0.31675	2999400
364221	$W \rightarrow e\nu, 280 < \max(H_T, p_T^W) < 500$ GeV, B filter	SHERPA 2.2.1	72.111	0.9702	0.13386	3019000
364222	$W \rightarrow e\nu, 500 < \max(H_T, p_T^W) < 1000$ GeV	SHERPA 2.2.1	15.04	0.9702	1.0	5999600
364223	$W \rightarrow e\nu, 1000 < \max(H_T, p_T^W) < 13000$ GeV	SHERPA 2.2.1	1.2336	0.9702	1.0	4000000

Table 8: W+jets samples used in the analysis. The dataset ID, MC generator, production cross-section, k-factor, filter efficiency and total number of generated events are shown.

Not reviewed, for internal circulation only

DS ID	Process	Generator	$\sigma \times BR [pb]$	k-factor	ϵ_{filter}	Events
364128	$Z\tau\tau, 0 < \max(H_T, p_T^Z) < 70 \text{ GeV}, C \text{ veto \& } B \text{ veto}$	SHERPA 2.2.1	1981.6	0.9751	0.82142	7996000
364129	$Z\tau\tau, 0 < \max(H_T, p_T^Z) < 70 \text{ GeV}, C \text{ filter \& } B \text{ Veto}$	SHERPA 2.2.1	1978.8	0.9751	0.11314	4999000
364130	$Z\tau\tau, 0 < \max(H_T, p_T^Z) < 70 \text{ GeV}, B \text{ filter}$	SHERPA 2.2.1	1981.8	0.9751	0.064453	7995800
364131	$Z\tau\tau, 70 < \max(H_T, p_T^Z) < 140 \text{ GeV}, C \text{ veto \& } B \text{ veto}$	SHERPA 2.2.1	110.37	0.9751	0.68883	5998500
364132	$Z\tau\tau, 70 < \max(H_T, p_T^Z) < 140 \text{ GeV}, C \text{ filter \& } B \text{ Veto}$	SHERPA 2.2.1	110.51	0.9751	0.1829	1999200
364133	$Z\tau\tau, 70 < \max(H_T, p_T^Z) < 140 \text{ GeV}, B \text{ filter}$	SHERPA 2.2.1	110.87	0.9751	0.110886	5999550
364134	$Z\tau\tau, 140 < \max(H_T, p_T^Z) < 280 \text{ GeV}, C \text{ veto \& } B \text{ veto}$	SHERPA 2.2.1	40.781	0.9751	0.60821	5000000
364135	$Z\tau\tau, 140 < \max(H_T, p_T^Z) < 280 \text{ GeV}, C \text{ filter \& } B \text{ Veto}$	SHERPA 2.2.1	40.74	0.9751	0.22897	3000000
364136	$Z\tau\tau, 140 < \max(H_T, p_T^Z) < 280 \text{ GeV}, B \text{ filter}$	SHERPA 2.2.1	40.761	0.9751	0.13442	4999950
364137	$Z\tau\tau, 280 < \max(H_T, p_T^Z) < 500 \text{ GeV}, C \text{ veto \& } B \text{ veto}$	SHERPA 2.2.1	8.5502	0.9751	0.56036	2000000
364138	$Z\tau\tau, 280 < \max(H_T, p_T^Z) < 500 \text{ GeV}, C \text{ filter \& } B \text{ Veto}$	SHERPA 2.2.1	8.6707	0.9751	0.26245	1000000
364139	$Z\tau\tau, 280 < \max(H_T, p_T^Z) < 500 \text{ GeV}, B \text{ filter}$	SHERPA 2.2.1	8.6804	0.9751	0.17313	1999950
364140	$Z\tau\tau, 500 < \max(H_T, p_T^Z) < 1000 \text{ GeV}$	SHERPA 2.2.1	1.8096	0.9751	1.0	2999800
364141	$Z\tau\tau, 1000 < \max(H_T, p_T^Z) < 13000 \text{ GeV}$	SHERPA 2.2.1	0.14834	0.9751	1.0	1000000
364100	$Z\mu\mu, 0 < \max(H_T, p_T^Z) < 70 \text{ GeV}, C \text{ veto \& } B \text{ veto}$	SHERPA 2.2.1	1983.0	0.9751	0.8221	7982000
364101	$Z\mu\mu, 0 < \max(H_T, p_T^Z) < 70 \text{ GeV}, C \text{ filter \& } B \text{ Veto}$	SHERPA 2.2.1	1978.4	0.9751	0.11308	4983000
364102	$Z\mu\mu, 0 < \max(H_T, p_T^Z) < 70 \text{ GeV}, B \text{ filter}$	SHERPA 2.2.1	1982.2	0.9751	0.064161	7984000
364103	$Z\mu\mu, 70 < \max(H_T, p_T^Z) < 140 \text{ GeV}, C \text{ veto \& } B \text{ veto}$	SHERPA 2.2.1	108.92	0.9751	0.68873	5983000
364104	$Z\mu\mu, 70 < \max(H_T, p_T^Z) < 140 \text{ GeV}, C \text{ filter \& } B \text{ Veto}$	SHERPA 2.2.1	109.42	0.9751	0.18596	1996800
364105	$Z\mu\mu, 70 < \max(H_T, p_T^Z) < 140 \text{ GeV}, B \text{ filter}$	SHERPA 2.2.1	108.91	0.9751	0.11375	5981600
364106	$Z\mu\mu, 140 < \max(H_T, p_T^Z) < 280 \text{ GeV}, C \text{ veto \& } B \text{ veto}$	SHERPA 2.2.1	39.878	0.9751	0.60899	5000000
364107	$Z\mu\mu, 140 < \max(H_T, p_T^Z) < 280 \text{ GeV}, C \text{ filter \& } B \text{ Veto}$	SHERPA 2.2.1	39.795	0.9751	0.23308	3000000
364108	$Z\mu\mu, 140 < \max(H_T, p_T^Z) < 280 \text{ GeV}, B \text{ filter}$	SHERPA 2.2.1	39.908	0.9751	0.14618	12499900
364109	$Z\mu\mu, 280 < \max(H_T, p_T^Z) < 500 \text{ GeV}, C \text{ veto \& } B \text{ veto}$	SHERPA 2.2.1	8.5375	0.9751	0.55906	2000000
364110	$Z\mu\mu, 280 < \max(H_T, p_T^Z) < 500 \text{ GeV}, C \text{ filter \& } B \text{ Veto}$	SHERPA 2.2.1	8.5403	0.9751	0.26528	999600
364111	$Z\mu\mu, 280 < \max(H_T, p_T^Z) < 500 \text{ GeV}, B \text{ filter}$	SHERPA 2.2.1	8.4932	0.9751	0.17559	1999400
364112	$Z\mu\mu, 500 < \max(H_T, p_T^Z) < 1000 \text{ GeV}$	SHERPA 2.2.1	1.7881	0.9751	1.0	2996500
364113	$Z\mu\mu, 1000 < \max(H_T, p_T^Z) < 13000 \text{ GeV}$	SHERPA 2.2.1	0.14769	0.9751	1.0	1000000
364114	$Zee, 0 < \max(H_T, p_T^Z) < 70 \text{ GeV}, C \text{ veto \& } B \text{ veto}$	SHERPA 2.2.1	1981.8	0.9751	0.82106	8000000
364115	$Zee, 0 < \max(H_T, p_T^Z) < 70 \text{ GeV}, C \text{ filter \& } B \text{ Veto}$	SHERPA 2.2.1	1980.8	0.9751	0.11295	4999000
364116	$Zee, 0 < \max(H_T, p_T^Z) < 70 \text{ GeV}, B \text{ filter}$	SHERPA 2.2.1	1981.7	0.9751	0.063809	7995600
364117	$Zee, 70 < \max(H_T, p_T^Z) < 140 \text{ GeV}, C \text{ veto \& } B \text{ veto}$	SHERPA 2.2.1	110.5	0.9751	0.69043	5997000
364118	$Zee, 70 < \max(H_T, p_T^Z) < 140 \text{ GeV}, C \text{ filter \& } B \text{ Veto}$	SHERPA 2.2.1	110.63	0.9751	0.18382	1999200
364119	$Zee, 70 < \max(H_T, p_T^Z) < 140 \text{ GeV}, B \text{ filter}$	SHERPA 2.2.1	110.31	0.9751	0.11443	5970000
364120	$Zee, 140 < \max(H_T, p_T^Z) < 280 \text{ GeV}, C \text{ veto \& } B \text{ veto}$	SHERPA 2.2.1	40.731	0.9751	0.61452	5000000
364121	$Zee, 140 < \max(H_T, p_T^Z) < 280 \text{ GeV}, C \text{ filter \& } B \text{ Veto}$	SHERPA 2.2.1	40.67	0.9751	0.23044	3000000
364122	$Zee, 140 < \max(H_T, p_T^Z) < 280 \text{ GeV}, B \text{ filter}$	SHERPA 2.2.1	40.694	0.9751	0.14927	12499600
364123	$Zee, 280 < \max(H_T, p_T^Z) < 500 \text{ GeV}, C \text{ veto \& } B \text{ veto}$	SHERPA 2.2.1	8.6743	0.9751	0.56134	1999800
364124	$Zee, 280 < \max(H_T, p_T^Z) < 500 \text{ GeV}, C \text{ filter \& } B \text{ Veto}$	SHERPA 2.2.1	8.6711	0.9751	0.26294	999900
364125	$Zee, 280 < \max(H_T, p_T^Z) < 500 \text{ GeV}, B \text{ filter}$	SHERPA 2.2.1	8.6766	0.9751	0.17223	1999850
364126	$Zee, 500 < \max(H_T, p_T^Z) < 1000 \text{ GeV}$	SHERPA 2.2.1	1.8081	0.9751	1.0	3000000
364127	$Zee, 1000 < \max(H_T, p_T^Z) < 13000 \text{ GeV}$	SHERPA 2.2.1	0.14857	0.9751	1.0	1000000

Table 9: $Z(\ell\ell)$ samples used in the analysis. The dataset ID, MC generator, production cross-section, k -factor, filter efficiency and total number of generated events are shown.

DS ID	Process	Generator	$\sigma \times BR [pb]$	k-factor	ϵ_{filter}	Events
364142	$Zvv, 0 < \max(H_T, p_T^Z) < 70 \text{ GeV}, C \text{ veto \& } B \text{ veto}$	SHERPA 2.2.1	10700.0	0.9728	0.8216	10000000
364143	$Zvv, 0 < \max(H_T, p_T^Z) < 70 \text{ GeV}, C \text{ filter \& } B \text{ Veto}$	SHERPA 2.2.1	10702.0	0.9728	0.11123	8000000
364144	$Zvv, 0 < \max(H_T, p_T^Z) < 70 \text{ GeV}, B \text{ filter}$	SHERPA 2.2.1	10709.0	0.9728	0.066175	8000000
364145	$Zvv, 70 < \max(H_T, p_T^Z) < 140 \text{ GeV}, C \text{ veto \& } B \text{ veto}$	SHERPA 2.2.1	603.23	0.9728	0.68924	14974000
364146	$Zvv, 70 < \max(H_T, p_T^Z) < 140 \text{ GeV}, C \text{ filter \& } B \text{ Veto}$	SHERPA 2.2.1	608.15	0.9728	0.18243	14980800
364147	$Zvv, 70 < \max(H_T, p_T^Z) < 140 \text{ GeV}, B \text{ filter}$	SHERPA 2.2.1	603.32	0.9728	0.11955	19984500
364148	$Zvv, 140 < \max(H_T, p_T^Z) < 280 \text{ GeV}, C \text{ veto \& } B \text{ veto}$	SHERPA 2.2.1	222.28	0.9728	0.60735	14998800
364149	$Zvv, 140 < \max(H_T, p_T^Z) < 280 \text{ GeV}, C \text{ filter \& } B \text{ Veto}$	SHERPA 2.2.1	221.88	0.9728	0.22527	12498500
364150	$Zvv, 140 < \max(H_T, p_T^Z) < 280 \text{ GeV}, B \text{ filter}$	SHERPA 2.2.1	222.4	0.9728	0.15103	19998300
364151	$Zvv, 280 < \max(H_T, p_T^Z) < 500 \text{ GeV}, C \text{ veto \& } B \text{ veto}$	SHERPA 2.2.1	47.375	0.9728	0.55887	4996400
364152	$Zvv, 280 < \max(H_T, p_T^Z) < 500 \text{ GeV}, C \text{ filter \& } B \text{ Veto}$	SHERPA 2.2.1	47.397	0.9728	0.26201	3497500
364153	$Zvv, 280 < \max(H_T, p_T^Z) < 500 \text{ GeV}, B \text{ filter}$	SHERPA 2.2.1	47.476	0.9728	0.17514	8996350
364154	$Zvv, 500 < \max(H_T, p_T^Z) < 1000 \text{ GeV}$	SHERPA 2.2.1	9.9099	0.9728	1.0	10000000
364155	$Zvv, 1000 < \max(H_T, p_T^Z) < 13000 \text{ GeV}$	SHERPA 2.2.1	0.81809	0.9728	1.0	5000000

Table 10: $Z(vv)$ samples used in the analysis. The dataset ID, MC generator, production cross-section, k -factor, filter efficiency and total number of generated events are shown.

398 3.1.2. Alternative Monte Carlo Samples

399 Alternative samples for the MC prediction and the modelling of V+jets processes are considered. The
 400 alternative samples provide a cross-check for the nominal prediction used in the analyses (understanding
 401 how much the nominal MC prediction is robust for certain variables and phase space regions can provide
 402 useful insights to check possible data/MC discrepancies or MC mismodellings) and are used to estimate
 403 modelling uncertainties on the nominal prediction.

404 The alternative samples considered for V+jets processes are generated using **MADGRAPH** 5 [26] interfaced
 405 to **PYTHIA** 8 for the modelling of the parton shower and the underlying event. The **MADGRAPH** 5
 406 v2 generator provides a LO (QCD) description of these processes, merging together matrix-element
 407 calculations with different parton multiplicities, up to 4 additional jets (higher jet multiplicities are
 408 modelled by the parton shower algorithm). The merging scheme applied to combine different parton
 409 multiplicities is the CKKW-L scheme with a merging scale of $Q_{cut} = 30$ GeV.

410 For the LO ME calculation the NNPDF2.3 LO PDFs are used (with $\alpha_S = 1.3$). The parton shower tune
 411 used is the ATLAS A14 tune, which also makes use of the NNPDF2.3 LO PDFs. Similarly to **SHERPA** 2.2,
 412 also **MADGRAPH** adopts a full 5-flavour scheme with massless quarks in the ME calculation, while massive
 413 quarks can be produced by the parton shower. All the alternative MC samples for V+jets processes are
 414 listed in Tables 11 and 12 for the Z+jets and W+jets respectively.

415 The **SHERPA** 2.2.1 V+jets now include systematic variations written as additional weights to the event gen-
 416 eration files. Every **SHERPA** 2.2.1 sample has an event weight corresponding to the following variations:

- 417 - factorisation scale $2\mu_F$
- 418 - factorisation scales $0.5\mu_F$
- 419 - renormalisation scale $2\mu_R$
- 420 - renormalisation scale $0.5\mu_R$
- 421 - PDF variation for MMHT2014nnlo68cl and CT14nnlo

422 The present version of **SHERPA** 2.2.1 is not technically able to produce all the required variations therefore
 423 use is made of the **SHERPA** 2.1 samples available at particle level. These samples are used to evaluate the
 424 following variations:

- 425 - resummation scale doubled
- 426 - resummation scale halved
- 427 - ckkw merging scale with cut at 15 GeV
- 428 - ckkw merging scale with cut at 30 GeV

Not reviewed, for internal circulation only

DS ID	Process	Generator	$\sigma \times BR$ [pb]	k-factor	ϵ_{filter}	Events
361500	$Z \rightarrow ee$ Np=0	MADGRAPH +PYTHIA 8	1401.6	1.232	1.0	6871800
361501	$Z \rightarrow ee$ Np=1	MADGRAPH +PYTHIA 8	211.99	1.232	1.0	3597000
361502	$Z \rightarrow ee$ Np=2	MADGRAPH +PYTHIA 8	67.305	1.232	1.0	2540800
361503	$Z \rightarrow ee$ Np=3	MADGRAPH +PYTHIA 8	18.679	1.232	0.99	634200
361504	$Z \rightarrow ee$ Np=4	MADGRAPH +PYTHIA 8	7.291	1.232	1.0	222500
361505	$Z \rightarrow \mu\mu$ Np=0	MADGRAPH +PYTHIA 8	1402	1.232	1.0	6878400
361506	$Z \rightarrow \mu\mu$ Np=1	MADGRAPH +PYTHIA 8	211.95	1.232	1.0	3599000
361507	$Z \rightarrow \mu\mu$ Np=2	MADGRAPH +PYTHIA 8	67.353	1.232	1.0	2542600
361508	$Z \rightarrow \mu\mu$ Np=3	MADGRAPH +PYTHIA 8	18.633	1.232	1.0	633200
361509	$Z \rightarrow \mu\mu$ Np=4	MADGRAPH +PYTHIA 8	7.3013	1.232	1.0	220500
361510	$Z \rightarrow \tau\tau$ Np=0	MADGRAPH +PYTHIA 8	1397.8	1.232	1.0	6840000
361511	$Z \rightarrow \tau\tau$ Np=1	MADGRAPH +PYTHIA 8	211.4	1.232	1.0	3391000
361512	$Z \rightarrow \tau\tau$ Np=2	MADGRAPH +PYTHIA 8	67.176	1.232	1.0	2542000
361513	$Z \rightarrow \tau\tau$ Np=3	MADGRAPH +PYTHIA 8	18.609	1.232	1.0	634200
361514	$Z \rightarrow \tau\tau$ Np=4	MADGRAPH +PYTHIA 8	7.2749	1.232	1.0	224500
361515	$Z \rightarrow vv$ Np=0	MADGRAPH +PYTHIA 8	7518.4	1.2283	1.0	1645600
361516	$Z \rightarrow vv$ Np=1	MADGRAPH +PYTHIA 8	1200.1	1.2283	1.0	10767600
361517	$Z \rightarrow vv$ Np=2	MADGRAPH +PYTHIA 8	387.16	1.2283	1.0	6096200
361518	$Z \rightarrow vv$ Np=3	MADGRAPH +PYTHIA 8	110.08	1.2283	1.0	3801800
361519	$Z \rightarrow vv$ Np=4	MADGRAPH +PYTHIA 8	43.389	1.2283	1.0	2835100

Table 11: Alternative Z +jets samples used in the analysis. The dataset ID, MC generator, production cross-section, k -factor, filter efficiency, and total number of generated events are shown.

DS ID	Process	Generator	$\sigma \times BR$ [pb]	k-factor	ϵ_{filter}	Events
361520	$W \rightarrow ev$ Np=0	MADGRAPH +PYTHIA 8	13939.0	1.2019	1.0	13936475
361521	$W \rightarrow ev$ Np=1	MADGRAPH +PYTHIA 8	1894.0	1.2019	1.0	9432600
361522	$W \rightarrow ev$ Np=2	MADGRAPH +PYTHIA 8	642.66	1.2019	1.0	6490000
361523	$W \rightarrow ev$ Np=3	MADGRAPH +PYTHIA 8	179.18	1.2019	1.0	3499000
361524	$W \rightarrow ev$ Np=4	MADGRAPH +PYTHIA 8	70.785	1.2019	1.0	4456600
361525	$W \rightarrow \mu\nu$ Np=0	MADGRAPH +PYTHIA 8	13935.0	1.2019	1.0	13922800
361526	$W \rightarrow \mu\nu$ Np=1	MADGRAPH +PYTHIA 8	1893.3	1.2019	1.0	9456750
361527	$W \rightarrow \mu\nu$ Np=2	MADGRAPH +PYTHIA 8	642.7	1.2019	1.0	6488600
361528	$W \rightarrow \mu\nu$ Np=3	MADGRAPH +PYTHIA 8	179.19	1.2019	1.0	3483000
361529	$W \rightarrow \mu\nu$ Np=4	MADGRAPH +PYTHIA 8	70.761	1.2019	1.0	4487400
361530	$W \rightarrow \tau\nu$ Np=0	MADGRAPH +PYTHIA 8	13920.0	1.2019	1.0	13982400
361531	$W \rightarrow \tau\nu$ Np=1	MADGRAPH +PYTHIA 8	1891.9	1.2019	1.0	9455400
361532	$W \rightarrow \tau\nu$ Np=2	MADGRAPH +PYTHIA 8	641.87	1.2019	1.0	6492400
361533	$W \rightarrow \tau\nu$ Np=3	MADGRAPH +PYTHIA 8	179.21	1.2019	1.0	3533000
361534	$W \rightarrow \tau\nu$ Np=4	MADGRAPH +PYTHIA 8	71.012	1.2019	1.0	4473600

Table 12: Alternative W +jets samples used in the analysis. The dataset ID, MC generator, production cross-section, k -factor, filter efficiency, and total number of generated events are shown.

429 **3.1.3. Cross-Section**

430 The single boson production cross sections are known at NNLO (QCD): the values used to normalise the
 431 V+jets samples in these analyses are taken from [27].

432 As outlined in Section 3.1.1 and 3.1.2, the MC generators used for these samples provide a NLO (QCD)
 433 prediction, merging different parton or jet multiplicities to achieve higher accuracy in the phase space
 434 studies in these analyses. We can therefore derive NNLO rescaling factors to normalise the MC predictions
 435 to the best theoretical knowledge of the cross section.

436

437 **SHERPA 2.2.1 and MADGRAPH Cross-Sections** For the $W^\pm(l\nu) + jets$ samples the total cross section from
 438 SHERPA or from MADGRAPH, averaged for all 3 lepton flavours taking into account the different hadron
 439 filter efficiencies, is scaled to the NNLO prediction obtaining a $k_{NNLO}^{QCD} = 0.9702$. For $Z(\ell\ell) + jets$
 440 we have to account for the cut at generator level applied in the MC production (for both SHERPA and
 441 MADGRAPH), which corresponds to $m_{\ell\ell} > 40 \text{ GeV}$. The MC cross section can be therefore obtained with
 442 the truth-level cut used for the NNLO calculation ($66 < m_{\ell\ell} < 116 \text{ GeV}$) or without additional cuts on
 443 top of the $m_{\ell\ell} > 40 \text{ GeV}$ from the MC generators. The k_{NNLO}^{QCD} correction factor can be calculated for
 444 different mass ranges as:

445

$$446 f = \frac{N_{\text{events}}(m_{\ell\ell} > 40 \text{ GeV})}{N_{\text{events}}(66 < m_{\ell\ell} < 116 \text{ GeV})} = 1.105$$

$$447 k_{NNLO}^{QCD} = \frac{\sigma_{NNLO}(66 < m_{\ell\ell} < 116 \text{ GeV})}{\sigma_{\text{SHERPA, MADGRAPH}}(66 < m_{\ell\ell} < 116 \text{ GeV})} = \frac{\sigma_{NNLO}(66 < m_{\ell\ell} < 116 \text{ GeV})}{\sigma_{\text{SHERPA, MADGRAPH}}(m_{\ell\ell} > 40 \text{ GeV})/f}$$

448 Hence the k -factor is found to be $k = 0.9751$. For $Z(vv) + jets$ the NNLO theoretical cross section is not
 449 calculated: we therefore correct for the difference between the $\text{BR}(Z \rightarrow vv)$ and the $\text{BR}(Z \rightarrow \ell\ell)$ from
 450 the PDG, and consider the dilepton NNLO cross section without any mass cuts applied and removing the
 451 Z/γ^* interference, to calculate the k_{NNLO}^{QCD} scale factors which is found to be $k = 0.9728$.

452 The differences between the scale factors for the $Z(\ell\ell) + jets$ and $Z(vv) + jets$ samples (for both SHERPA
 453 and MADGRAPH) can be explained by the differences in the BRs used in the MC generators with respect
 454 to the higher order theoretical calculations (related to the higher EW orders not included in the MC). It is
 455 interesting to note that while the scale factors for MADGRAPH are larger than 1 (meaning that the NNLO
 456 corrections are positive), the corresponding ones for SHERPA are smaller than 1: part of the reason is
 457 related to the different EW scheme used by SHERPA with respect to the PDG recommendation applied for
 458 the theoretical calculations.

459 3.1.4. V+jets Systematic Uncertainties

460 The estimate of systematic uncertainties on the theoretical prediction of the V+jets background relies on
 461 two main studies:

- 462 - Particle-level studies of the **SHERPA** 2.2.1 and **SHERPA** 2.1 samples produced with varied scales
 463 settings to assess acceptance uncertainties and comparisons of the nominal **SHERPA** 2.2.1 samples
 464 to **MADGRAPH**.
- 465 - Where possible, data-driven shape comparisons in high purity control regions.

466 The approach chosen to evaluate systematic uncertainties on our knowledge and prediction of the V+jets
 467 derives from the structure of the Profile Likelihood Fit (PLF) utilised in this search, in which the overall
 468 normalisation of the dominant heavy flavour component of the V+jet backgrounds is left floating in the
 469 PLF and can be adjusted by the fit of the MC prediction to data in the analysis phase space (see details in
 470 Ref [28]).

471 The V+jets background is divided in three main components, based on the flavour composition of the
 472 events. The split in flavour components and the event labelling for the detector-level simulated samples
 473 is defined in Ref [28], while for the particle-level simulated samples the details are given in A. The three
 474 main components are:

- 475 - V+heavy flavours (V+hf): which includes V+bb, V+bc, V+cc and V+bl events.
- 476 - V+c_l, including events labelled as V+c_l
- 477 - V+l, including events labelled as V+light

478 The first step of the approach to V+jets systematic uncertainties is to consider the relative variation in
 479 acceptance between different analysis regions, based upon comparing the nominal to the alternative MC
 480 samples. Acceptance uncertainties are evaluated for the following regions:

- 481 • 2-jet versus 3-jet events (for events passing the 2-lepton selection ‘3-jet’ corresponds to ‘> 2-jets’)
- 482 • 2-jet versus 3-jet events (for events passing the 0 and 1-lepton selection ‘3-jet’ corresponds to
 483 ‘3-jets’)
- 484 • 0-Lepton versus 2-lepton events (for Z+hf events)
- 485 • 0-Lepton versus 1-lepton events (for W+hf events)
- 486 • WCR versus SR in 1-lepton events (for W+hf events)

487 The purpose of this step is to understand the correlation between the different regions of phase space
 488 by implementing nuisance parameters in the Profile Likelihood Fit which control their relative accept-
 489 ance. These nuisance parameters are parametrised in the fit with a Gaussian PDF (however the inter-
 490 polation/extrapolation choices in HistFactory beyond 1σ create a log-normal behaviour) and with these
 491 MC-based studies we are able to provide a prior on this Gaussian constraint, which helps the fit to de-
 492 termine the best value of the parameter, and reflects our knowledge of the acceptance variation based on
 493 the MC prediction. The priors on the Gaussian constraints, which are applied to the nuisance parameters
 494 which control the relative acceptance variations across different analysis regions and flavour components,
 495 are estimated at particle level with a Rivet based analysis, as described in A. This significantly increases

496 the available number of events to reduce the statistical uncertainty in these studies. Cross-checks are
 497 also carried out to verify consistent results are achieved after full simulation and reconstruction. The
 498 acceptance uncertainties are calculated as double-ratios:

$$499 \frac{\text{Acceptance}[\text{Category}_A(\text{nominal MC})]}{\text{Acceptance}[\text{Category}_B(\text{nominal MC})]} \Big/ \frac{\text{Acceptance}[\text{Category}_A(\text{alternative MC})]}{\text{Acceptance}[\text{Category}_B(\text{alternative MC})]}$$

500 The final uncertainty is obtained by summing in quadrature the variations originating from four contribu-
 501 tions¹:

- 502 • envelope of the effect of varying factorisation and renormalisation scales in the SHERPA sample
- 503 • sum in quadrature of half of the variation obtained from the with different resumption and ckkw
 504 merging scales²
- 505 • maximal variation between the nominal SHERPA prediction and the prediction obtained by reweighing
 506 to alternative PDF
- 507 • difference between SHERPA and MADGRAPH predictions

508 The second step in estimating the V+jet systematic uncertainties is to derive shape uncertainties for the
 509 most important underlying physical variables that are used in the Boosted Decision Tree: $m_{b\bar{b}}$ and p_T^V .
 510 Two approaches are taken for the shape uncertainties, which incorporate both data-driven modelling
 511 comparisons and also MC based comparisons. For the shape uncertainties the distributions for the V+jet
 512 variations are normalised to the same area and compared. To define an uncertainty a functional form is
 513 fitted through the largest variation and symmetrised. If variations were found to be similar for certain
 514 analysis regions then a common uncertainty is derived and implemented for those regions

515 For the W+jets, where it is very hard to isolate an high purity sample that isn't biased to a particular region
 516 of phase space, the modelling uncertainties are completely derived from comparisons of the SHERPA
 517 samples with varied scales settings and also to the MADGRAPH sample. For Z+jets, where it is possible to
 518 isolate a high purity control region, the uncertainties are derived from comparisons between the nominal
 519 MC samples and the data, with the derived uncertainties compared to the uncertainties predicted from
 520 the MC comparisons. In both cases additional particle level comparisons are carried out to motivate the
 521 scheme used to correlate the uncertainties between the various analysis channels and regions in the PLF.

522 A summary of the Z+jet uncertainties is provided in Section 3.1.5 and for W+jet uncertainties in Sec-
 523 tion 3.1.5.

524 3.1.5. W+jets uncertainties

525 Both normalisation and shape uncertainties on the W+jets processes in the 0 and 1 lepton channels have
 526 been derived from considering truth-based comparisons of different MC generators and their parameter
 527 variations. More detailed results are from the studies used to estimate the uncertainties are documented
 528 in Appendix F.

¹ In the table presented in appendices, some contribution might not be visible due to pre-pruning

² Those samples are generated with SHERPA 2.1 therefore half of the 'up' and 'down' variation is considered as uncertainty instead of comparing then to the central value of SHERPA 2.2.1.

529 **Normalisation and acceptance uncertainties**

530 An overview of the $W+jets$ normalisation systematics and their effect in the various analysis regions
 531 are detailed in Table 13. The total uncertainties are derived as described in Section 3.1.4 and the full
 532 breakdown of the uncertainties is outlined in Appendix F.

Process	Name	Prior in Region					
		0-Lepton		1-Lepton			
		2-Jets	3-Jets	WCR 2-Jets	SR 2-Jets	WCR 3-Jets	SR 3-Jets
$W+l$	SysWlNorm					32%	
$W+cl$	SysWlNorm					37%	
$W+hf$	norm_Wbb					Floating Normalisation	
$W+hf$	SysWbbNorm_J3	—	18%	—	—	18%	18%
$W+hf$	SysWbbNorm_DWhfCR_L1	—	—	—	10%	—	10%
$W+hf$	SysWbbNorm_L0	5%	5%	—	—	—	—

Table 13: Summary of the normalisation uncertainties on the $W+jets$ predictions in the various categories of the 0 and 1-lepton channels. For systematic uncertainties implemented with a prior the effect of $1-\sigma$ variation is reported. The uncertainties labelled as Wbb act on the entire $W+hf$ background.

533 The $W+l$ and $W+cl$ background processes are strongly suppressed by the requirement of 2 b -tags and as
 534 such compose less than 1% of the background in any region. As such it is sufficient to apply a single
 535 normalisation uncertainty for each of these backgrounds, , referred to as SysWlNorm and SysWlNorm
 536 respectively, which are individually correlated across all regions. The uncertainties were computed for
 537 the ICHEP analysis considering the effect of all the systematic variations on the Sherpa predictions.

538 Given the large uncertainty on the normalisation of the $W+hf$ processes, a floating normalisation is
 539 adopted, norm_Wbb, which is heavily constrained by the large number of events and purity of the 1-lepton
 540 $W+hf$ control region. Additional nuisance parameters have been introduced to model the extrapolation
 541 uncertainties on the relative normalisation across regions³:

- 542 • **3-to-2 jets:** uncertainties have been computed on the relative yields between 3 and 2-jet regions. The
 543 effect is dominated by the variation of the re-normalisation scale in the Sherpa sample. There is no
 544 strong evidence for any category dependency for this uncertainty; therefore a correlated uncertainty
 545 (SysWbbNorm_J3) of value 18% is applied to all the 3-jets regions. A detailed breakdown is
 546 documented in Appendix F.1.1 (Table 64).
- 547 • **CR-SR extrapolation:** uncertainties have been computed on the relative yields between the SR
 548 and WCR in the 1-lepton channel. A common uncertainty (SysWbbNorm_DWhfCR_L1) of 10% is
 549 assigned to both the 2 and 3-jet signal regions. A detailed breakdown of the current uncertainty is
 550 documented in Appendix F.1.2 (Table 65).
- 551 • **0-to-1 lepton:** an additional uncertainty on the ratio of the yields between the 0 and 1-lepton regions.
 552 A common uncertainty (SysWbbNorm_L0) of 5% is applied to the 2-jet and 3-jet the 0-lepton regions,
 553 as the most precise constraint on the $W+hf$ prediction is obtained in the 1-lepton channel due to the

³ While the prior is obtained comparing double ratios, due to technical reason, the effect of the uncertainty is applied to only one of the two regions considered in the double ratio. This choice does not affect the result but only the interpretation of the normalisation factor.

dedicated $W+hf$ control region. The effect is dominated by the comparison between **MADGRAPH** and **SHERPA**. A detailed breakdown of the uncertainty is documented in Appendix F.1.3 (Table 66).

556 Flavour composition uncertainties

557 The $W+hf$ background is composed of the contributions from the bb , bc , bl and cc backgrounds; the
 558 relative composition of the various sub-components in the 1-lepton analysis regions after full reconstruction
 559 selection is summarised in Table 14. Uncertainties on the relative composition of these processes are
 560 estimated as summarised in Table 15. The uncertainties are implemented as normalisation uncertainties on
 561 each of the smaller components (bc [`SysWbcWbbRatio`], bl [`SysWblWbbRatio`], cc [`SysWccWbbRatio`])
 562 relative to the bb component.

Process	2 jet		3 jet	
	WCR	SR	WCR	SR
W_{cc}	0.04	0.09	0.05	0.07
W_{bl}	0.02	0.06	0.02	0.04
W_{bc}	0.05	0.12	0.05	0.13
W_{bb}	0.88	0.73	0.88	0.76

Table 14: The fractional contribution of each $W+hf$ subprocesses to the total $W+hf$ yields in all the 1-lepton analysis regions.

Category	Nuisance Parameter Name	Prior	Applied to
$W+bc/W+bb$	<code>SysWbcWbbRatio</code>	15%	$W+bc$ events (0-Lepton)
		30%	$W+bc$ events (1-Lepton)
$W+bl/W+bb$	<code>SysWblWbbRatio</code>	26%	$W+bl$ events (0-Lepton)
		23%	$W+bl$ events (1-Lepton)
$W+cc/W+bb$	<code>SysWccWbbRatio</code>	10%	$W+cc$ events (0-Lepton)
		30%	$W+cc$ events (1-Lepton)

Table 15: The priors on the relative acceptance variations for $Z+hf$. The first column details the flavour components across which the acceptance variation is being considered, the second column quotes the name of the corresponding nuisance parameter in the Profile Likelihood Fit, the third contains the value of the prior and the fourth column the processes and categories to which this nuisance parameter is applied.

563 Full information on the uncertainty evaluation can be found in Appendix F.1.4. The largest systematic
 564 variation between the regions has been used and is applied as a common variation in all the analysis
 565 regions (the same value is used for both the 2 and 3-jet bins as well as for the WCR and SR); this approach
 566 is justified by the relatively small contribution of the non- bb components after the 2 b-tag requirement
 567 which makes the impact of the choice of the correlation scheme negligible in the final fit.

568 Variations of the flavour composition are also partly accounted for in the WCR/SR extrapolation uncertainty
 569 since the $W+hf$ components have an intrinsically different m_{bb} distribution⁴.

570 p_T^V shape uncertainty

⁴ In particular differences are observed between processes containing gluon splitting diagrams ($W+bb$ and $W+cc$) and processes not containing it ($W+bc$ and $W+bl$).

571 The shape uncertainties are derived as described in Section 3.1.4 and the full breakdown of the comparisons
 572 are outlined in Appendix F. For the p_T^V distributions differences between generators and variations of
 573 internal generator parameters can be parametrised by a straight line. In all the channels, the largest
 574 variation is produced by the comparison between the SHERPA 2.2.1 and the MADGRAPH predictions. A
 575 summary of the linear fits used to parametrise the uncertainties in the 2 and 3-jet regions for the 0 and
 576 1-lepton channels is shown in Figure 11.

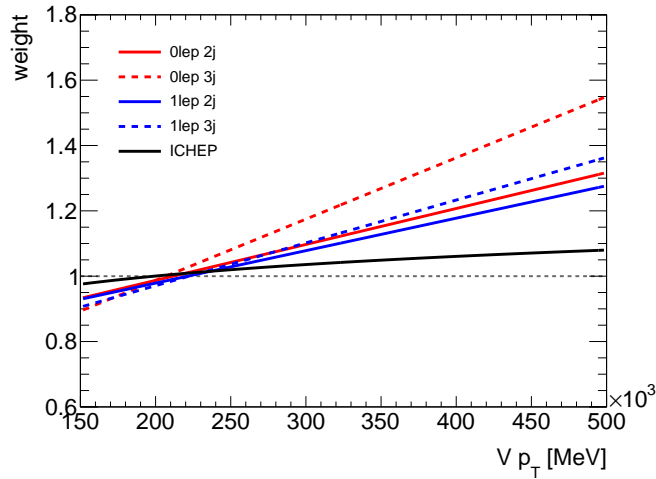


Figure 11: p_T^V shape uncertainties: comparison of the linear fit to the ratio of MADGRAPH and SHERPA 2.2.1 predictions in the 2 and 3-jet regions in the 0 and 1-lepton channels. The solid black line represent the shape uncertainty used in the ICHEP version of the analysis

577 It can be seen that the shape effects in all the channels are in a consistent direction and of a similar
 578 magnitude. The variation in the 1-lepton 3-jet region has been adopted as the shape uncertainty for
 579 all channels/regions. This uncertainty is treated in a correlated manner with the name SysWPtV⁵. The
 580 proposed uncertainty is significantly larger than the previous uncertainty used for ICHEP, which was
 581 estimated from data/MC comparisons in the $W+jet$ 1-tag regions as a direct MC-based comparison
 582 in the SR was not possible due to the low number of events in the MADGRAPH sample. The new
 583 approach represent a more conservative choice; nevertheless data/MC studies in the 1-tag region (with
 584 additional selection to increase the $W+hf$ purity) are being performed with the aim of possibly reducing
 585 this uncertainty. Finally, while the current baseline is to consider the variation fully correlated across all
 586 the analysis regions, residual uncertainties are being computed in order to perform decorrelation studies;
 587 preliminary plots are available in Appendix F.3 and show relatively small residual effects.

588 **m_{bb} shape uncertainty**

589 As for the p_T^V case, the largest effect on the m_{bb} shape is observed in the comparison between the
 590 MADGRAPH and SHERPA 2.2.1 predictions. A full breakdown of all the comparisons are outlined in
 591 Appendix F.2. In all cases, the variation can be parametrised with a straight line. The summary of the
 592 linear fits used to parameterise the uncertainties in the 2 and 3-jet regions for the 0 and 1-lepton channels
 593 are shown in Figure 12.

⁵ While being presented as a shape only uncertainty, the p_T^V systematic can also change the normalisation of the sample. This feature is important in the cut-based analysis where the high p_T^V region is split into 2 sub-regions.

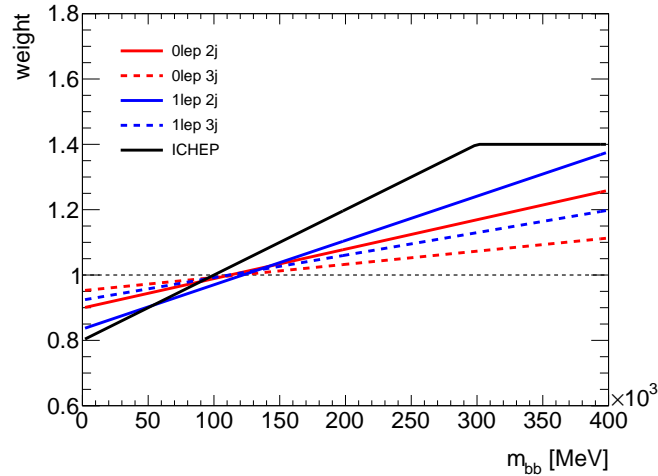


Figure 12: m_{bb} shape uncertainties: comparison of a linear fits to the MADGRAPH and SHERPA 2.2.1 ratios in the 2 and 3-jet regions in the 0 and 1-lepton channels. The solid black line represent the shape uncertainty used in the ICHEP analysis

594 The systematic uncertainty is in the same direction and of similar amplitude in all channels and categories.
 595 The variation in the 1-lepton 2-jet region has been adopted as the shape-only uncertainty for all channels
 596 and regions in a correlated manner, using the name SysWMbb. The proposed uncertainty is similar to that
 597 used for the ICHEP analysis. Data/MC studies in the 1-tag region (with additional selection to improve the
 598 $W+hf$ purity) are being performed with the aim of possibly reducing the shape uncertainty. Finally, while
 599 the current baseline is to consider the variation fully correlated across all the analysis regions, residual
 600 uncertainties are being computed in order to perform decorrelation studies; preliminary plots are available
 601 in Appendix F.3 and show relatively small residual effects.

602 **3.1.6. Z+jets uncertainties**

603 Only signal regions in the 0 and 2-lepton channels have been considered in the following since the
 604 contribution of Z+jets in the 2-lepton topEMCR region and in the 1-lepton channel are negligible.

605 **Normalisation and acceptance uncertainties**

606 An overview of the Z+jets normalisation systematics and their effects in the analysis regions is reported
 607 in Table 16. The total uncertainties are derived as described in Section 3.1.4 and the full breakdown of
 608 the uncertainties is outlined in Appendix G.

Process	Name	prior in region					
		2jet			2L: low Vpt 2L high Vpt 0L	(≥)3jets	
Z+l	SysZclNorm	18%					
Z+cl	SysZlNorm	23%					
Z+hf	norm_Zbb	Floating Normalisation					
Z+hf	SysZbbNorm_L2_J3	–	–	–	30%	30%	–
Z+hf	SysZbbNorm_J3	–	–	–	–	–	17%
Z+hf	SysZbbNorm_0L	–	–	7%	–	–	7%
Z+hf	SysZbbPTV	effect on each region obtained from shape rw					

Table 16: Effect of modelling systematics on Z+jets normalisation in the 2lepton regions. For systematic uncertainties implemented with a prior the effect of $1-\sigma$ variation is reported. The uncertainties labelled as Zbb act on the entire $Z+hf$ background.

609 The $Z+l$ and $Z+cl$ background processes are strongly suppressed by the requirement of 2 b -tags and as
 610 such compose less than 1% of the background in any region. As such it is sufficient to apply a single
 611 normalisation uncertainty for each of these backgrounds, referred to as $SysZlNorm$ and $SysZclNorm$
 612 respectively, which are individually correlated across all regions. The uncertainties were computed for
 613 the ICHEP analysis considering the effect of all the systematic variations on the Sherpa predictions.

614 Given the large uncertainty on the normalisation of the $Z+hf$ processes, a floating normalisation is
 615 adopted, $norm_Zbb$, which is heavily constrained by the large number of events and the high $Z+hf$ purity
 616 of the 2-lepton SR m_{bb} sidebands. Additional nuisance parameters have been introduced to model the
 617 extrapolation uncertainties on the relative normalisation across regions⁶:

- 618 • **3-to-2 jets:** uncertainties have been computed on the relative yields between 3 and 2-jet regions.
 619 The effect is dominated by the variation of the re-normalisation scale in the Sherpa sample. For
 620 the 2-lepton channel the variation ($SysZbbNorm_L2_J3$) is considered correlated between the low
 621 and high Vpt regions, but an additional uncorrelated nuisance parameter ($SysZbbNorm_J3$) has
 622 been implemented for the 0-lepton channel. This is justified by the different selection in the two
 623 channels, which have different Vpt (the 2-lepton channel includes the lower Vpt region between 75
 624 and 150 GeV) and number of jet requirements (the 0-lepton channel has a 3-jet exclusive selection
 625 while the 2-lepton channel has a 3-jet inclusive selection). A detailed breakdown of the uncertainties
 626 can be found in Appendix G.1.1.

⁶ While the prior is obtained comparing double ratios as explained, due to technical reason, the effect of the uncertainty is applied to only one of the two regions considered in the double ratio. This choice does not affect the result but only the interpretation of the normalisation factor.

- **0-to-2 lepton:** an additional uncertainty (`SysZbbNorm_0L`) on the ratio of the yields between the 0 and 2-lepton regions. This uncertainty is applied to the 0-lepton region, as a better constraint on the $Z+hf$ prediction is obtained in the 2-lepton channel due to the larger purity. The uncertainty has been computed by only comparing the high V_{PT} regions of the two channels, which reduces the size of the extrapolation uncertainty compared to ICHEP, due to the smaller extrapolation between these two regions of phase space⁷. There are similar contributions to the total uncertainty from the comparison between `MADGRAPH` and `SHERPA` and the evaluation of the `SHERPA` internal parameter variations. A detail breakdown of the uncertainty is documented in Appendix G.1.2.
- **low-high $Z\ p_T$:** an additional uncertainty (`SysZbbPTV`) is also derived on the shape of the Z_{PT} distribution. The determination of this shape uncertainty is discussed in the following sections. As well as affecting the distribution of the final discriminants in each analysis regions, a variation in the shape of the $Z\ p_T$ distribution will also alter the relative normalisation between the low and high $Z\ p_T$ regions. This normalisation effect is also propagated to the 0-lepton channel.

Flavour composition uncertainties The $Z+hf$ background is composed of the contributions from the bb , bc , bl and cc backgrounds. Uncertainties on the relative composition of these processes are estimated as summarised in Table 17. The uncertainties are implemented as normalisation uncertainties on each of the smaller components (bc [`SysZbcZbbRatio`], bl [`SysZblZbbRatio`], cc [`SysZccZbbRatio`]) relative to the bb component.

Category	Nuisance Parameter Name	Prior	Applied to
$Z+bc/Z+bb$	<code>SysZbcZbbRatio</code>	40%	$Z+bc$ events (0-Lepton)
		40%	$Z+bc$ events (2-Lepton 2jet)
		30%	$Z+bc$ events (2-Lepton ≥ 3 jet)
$Z+bl/Z+bb$	<code>SysZblZbbRatio</code>	25%	$Z+bl$ events (0-Lepton)
		28%	$Z+bl$ events (2-Lepton 2jet)
		20%	$Z+bl$ events (2-Lepton ≥ 3 jet)
$Z+cc/Z+bb$	<code>SysZccZbbRatio</code>	15%	$Z+cc$ events (0-Lepton)
		16%	$Z+cc$ events (2-Lepton 2jet)
		13%	$Z+cc$ events (2-Lepton ≥ 3 jet)

Table 17: The priors on the relative acceptance variations for $Z+hf$. The first column details the flavour components across which the acceptance variation is being considered, the second column lists the names of the corresponding nuisance parameter in the Profile Likelihood Fit, the third contains the value of the prior and the fourth column the processes and categories to which this nuisance parameter is applied.

Different prior uncertainties have been adopted for the 0-lepton and 2-lepton channels; for the latter, separate uncertainties are also adopted for the 2-jet and ≥ 3 -jet regions, but for each $Z+hf$ sub-process the variations are considered as correlated across regions. There is no evidence of a strong dependence as a function of $Z\ p_T$ and so the same prior is applied in the low and high Z_{PT} bins. The relatively small contribution of the non- bb components after the 2 b-tag requirement which makes the impact of the choice of the correlation scheme negligible in the final fit. The value of the uncertainty is completely dominated by the difference between `SHERPA` 2.2.1 and `MADGRAPH`; additional details can be found in Appendix G.1.3.

⁷ The $Z+hf$ normalisation factor is mainly determined in the low V_{PT} 2-lepton region, but the same low-high V_{PT} uncertainty will be considered for both the high V_{PT} 2-lepton region and the 0-lepton SR.

653 **p_T^V and $m_{b\bar{b}}$ shape uncertainties**

654 Control regions are chosen in data which are dominated by the Z+jet background. In this region the
 655 total Monte Carlo background is compared to data for the distributions for which the shape uncertainties
 656 are being derived. The control regions are chosen such that the dominant background is Z+jets and the
 657 assumption can be made that all observed data MC differences originate from modelling uncertainties in
 658 the Z+jets samples.

659 The Z+jets shape uncertainties are studied in the 2 lepton channel, which has the highest purity. To reduce
 660 the contribution of $t\bar{t}$ a MET significance cut < 3.5 is made (which is the same as the cut-based analysis).
 661 The Z+jet background is then scaled to the data after subtracting off the non-Z+jet backgrounds. The
 662 distributions are studied in the 0, 1 and 2 tag categories, which correspond to different flavour compositions.
 663 In addition, the tag categories are studied for different jet multiplicities: 2jet and 3jet. For the 0 and 1
 664 tag category the full m_{jj} range was used to study systematic effects, whereas for the 2 tag category events
 665 in the signal region with $110 \text{ GeV} < m_{b\bar{b}} < 140 \text{ GeV}$ were cut out when studying the m_{jj} distribution.

666 The data Monte Carlo comparisons for p_T^Z , and $m_{b\bar{b}}$ in the medium (70-150 GeV) and high ($> 150 \text{ GeV}$)
 667 p_T^Z regions are shown in Figs. 13, 14 and 15 respectively. For the p_T^Z and $m_{b\bar{b}}$ distributions the shape
 668 uncertainty was derived by assigning functions to encompass the observed data Monte Carlo differences.
 669 The shape uncertainties are indicated by the blue dotted lines in the figures. The function for the uncertainty
 670 vs p_T^Z is $\pm 0.2 \log 10(p_T^V/50\text{GeV})$. The function representing the systematic uncertainty on the m_{jj} shape
 671 is the same as using Run 1 as $\pm 0.0005 \times (m_{jj} - 100 \text{ GeV})$ which continues to provide a reasonable
 672 estimate.

673 The Z+jets shape uncertainties are listed in Table 18, the uncertainties are also applied to the 0 lepton
 674 channel in a fully correlated manner. Finally, while the current baseline is to consider the variation fully
 675 correlated across all the analysis regions, residual uncertainties are being computed in order to perform
 676 decorrelation studies.

Process	Uncertainty	Value	Source	Nuisance Parameter
Z+jets	p_T^V shape	shape +norm	fit to data in 2 lepton control region	ZPtV
Z+jets	$m_{b\bar{b}}$ shape	shape only	fit to data in 2 lepton control region	ZMbb

Table 18: Summary of overall shape uncertainties for the Z+jets processes with short descriptions and the name of the corresponding nuisance parameters.

Not reviewed, for internal circulation only

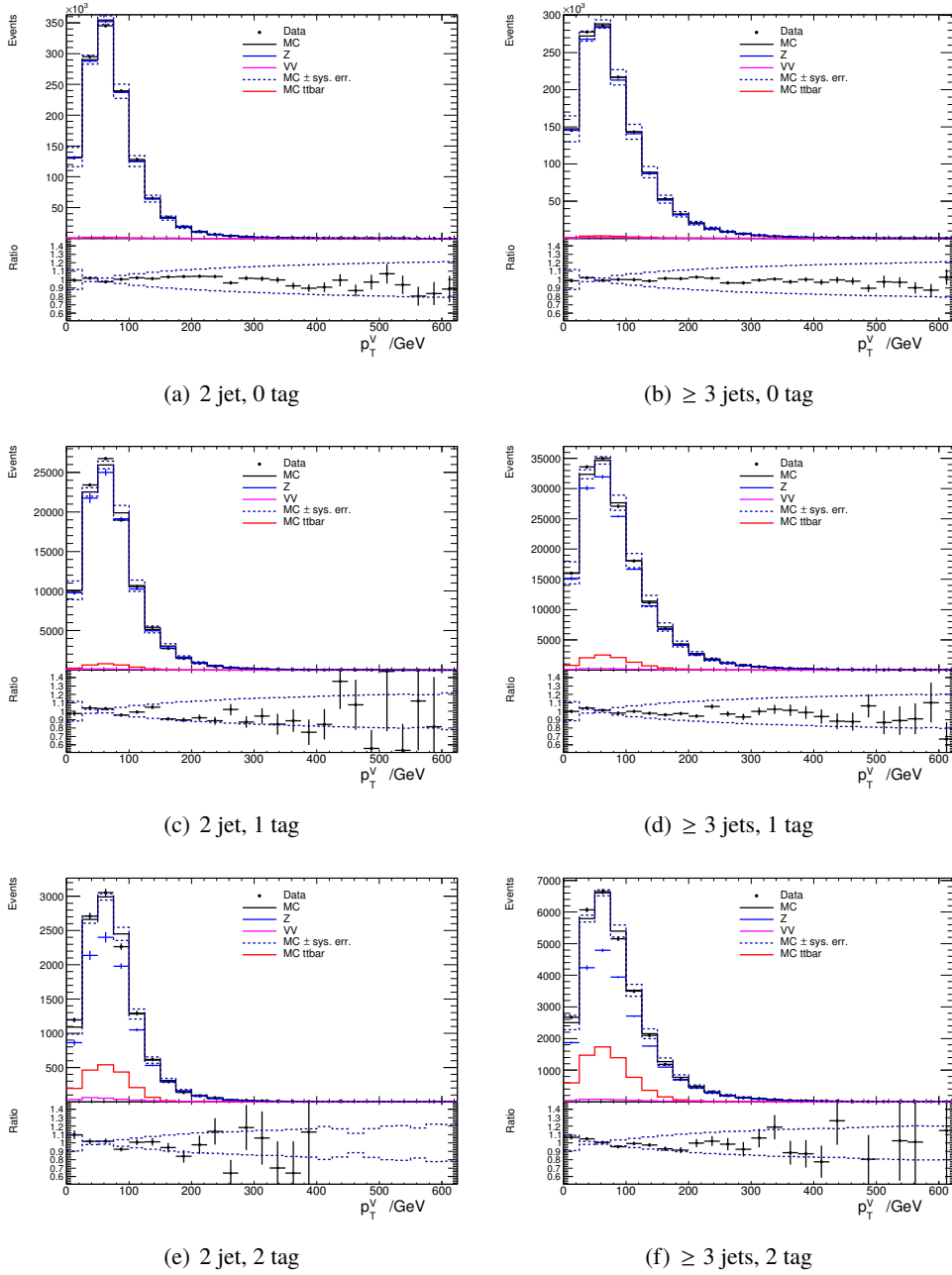


Figure 13: The transverse momentum of the Z p_T^Z for the 2 lepton control region for 2 jets and (a) 0, (c) 1 and (e) 2 tags and for ≥ 3 jets with (b) 0, (d) 1 and (f) 2 tags.

Not reviewed, for internal circulation only

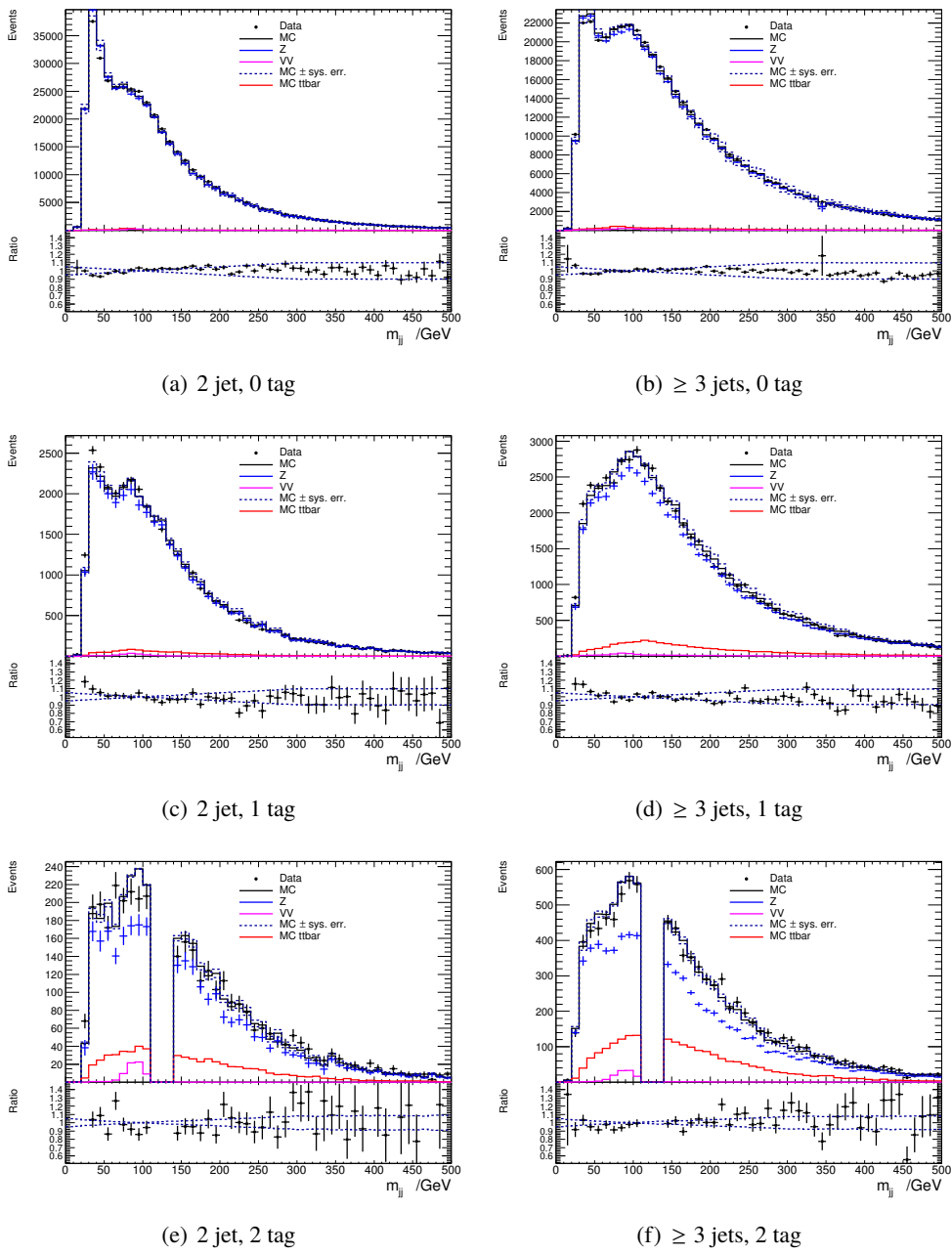


Figure 14: The m_{jj} distribution for the medium p_T^Z region ($75 < p_T^Z < 150$ GeV) 2 lepton control region for 2 jets and (a) 0, (c) 1 and (e) 2 tags and for ≥ 3 jets with (b) 0, (d) 1 and (f) 2 tags.

Not reviewed, for internal circulation only

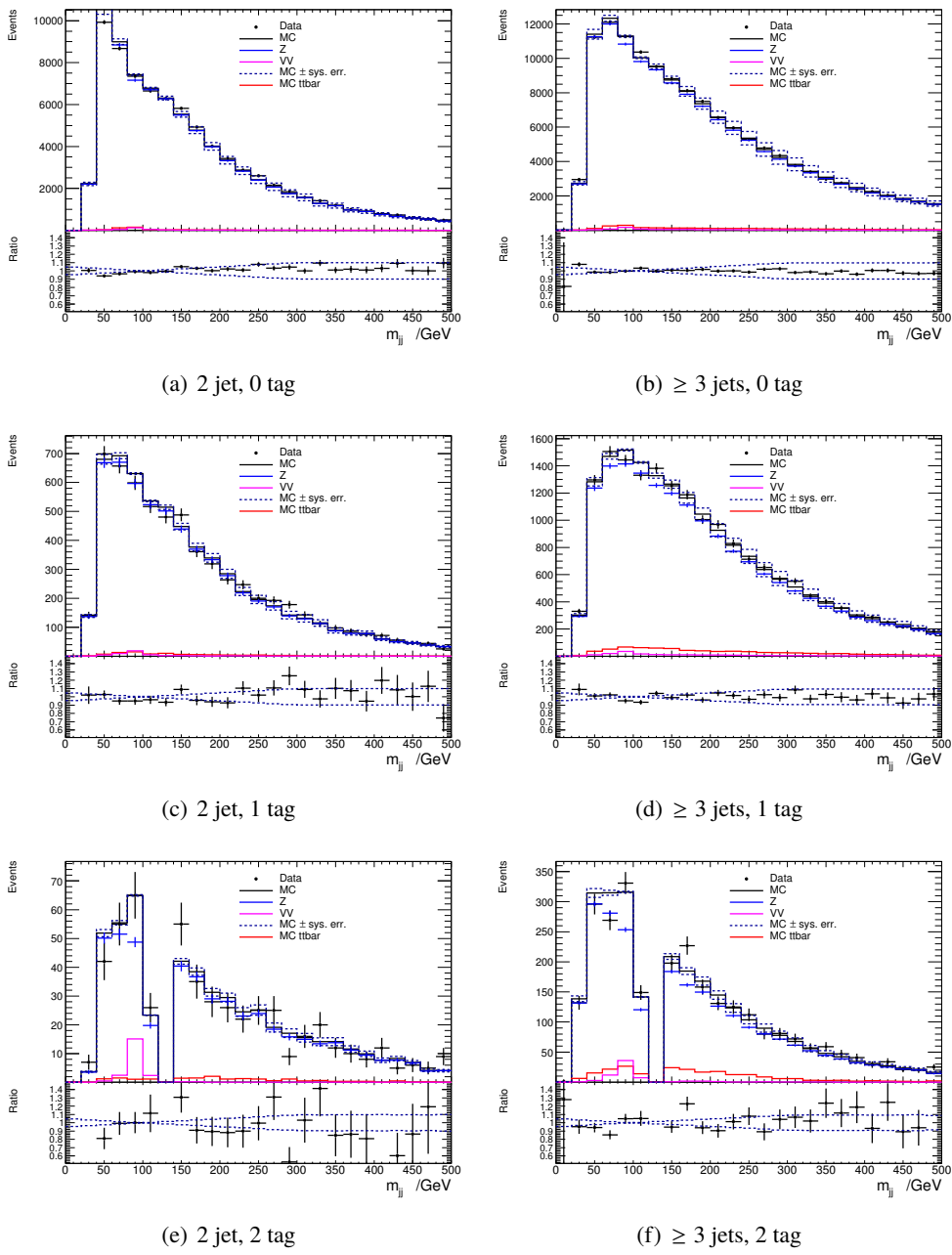


Figure 15: The m_{ll} distribution for the high p_T^Z region ($p_T^Z > 150$ GeV) 2 lepton control region for 2 jets and (a) 0, (b) 1 and (c) 2 tags and for ≥ 3 jets with (d) 0, (e) 1 and (f) 2 tags.

677 3.2. Top-Pair Production

678 The default MC sample for the $t\bar{t}$ process is Powheg + Pythia 8, which is generated with the Powheg
 679 generator using an NLO calculation for the matrix element (ME) [29, 30] and interfaced to Pythia
 680 8.210[31] using the A14 set[6] of parameters for the parton shower, hadronization, underlying event and
 681 multiple parton interactions description. In this sample, the PDF used in the ME calculation is NNPDF3.0
 682 (NLO), and NNPDF2.3 (LO) in the parton shower. This new sample has been chosen after examining
 683 various combinations of generator and parton shower models by comparing Run-1 and Run-2 data[32].
 684 The systematic variations are also chosen from these studies. There are several important parameters
 685 in Powheg + Pythia 8 that are optimized. The first parameter is Powheg h_{damp} , which is used as a
 686 resummation damping factor controlling the ME/PS matching in Powheg and effectively regulates the
 687 high p_T radiation. In the comparison with 8 TeV data in various variables ($t\bar{t}$ system p_T , mass, top p_T , jet
 688 multiplicity, jet pTs and so on), $h_{damp} < m_{top}$ is strongly disfavoured. The best description is given with
 689 $h_{damp} = 1.5 \cdot m_{top}$ for both 8 TeV data and 13 TeV data (there are slightly different trends between the
 690 two datasets). Therefore, this value has been chosen for the main sample generation. Other parameters
 691 that are optimized are Pythia 8 pTdef and pTHard which control the merging between Powheg and
 692 Pythia 8 through the use of vetoed showering. These parameters are strongly related to the choice of
 693 the p_T definition for ISR and FSR, and the procedure to calculate the matching scale. These parameters
 694 are varied with $h_{damp} = 1.5 \cdot m_{top}$, and the chosen settings are pTdef= 2 and pTHard= 0 (See Section
 695 2.2.2 of Ref[32]). Based on the new setup with Powheg +Pythia 8 with well-tuned parameters, the
 696 description of the data by the $t\bar{t}$ background is much improved. In Run-1 analysis, there was relatively
 697 large mismodeling of the p_T of the $t\bar{t}$ system and the top p_T with Powheg +Pythia 6. Those are now
 698 described by the new sample within uncertainties described later. Therefore we do not assign additional
 699 systematics based on measurement of data, nor NNLO expectation.

700 Samples are listed in Tab. 19, including the alternative $t\bar{t}$ samples whose setup is described in Section 3.2.2.
 701 Those are generated with filtering at generator level using truth information. Samples with "non-all-had"
 702 are required to have at least one W boson decaying leptonically, and "dilepton" samples are required to
 703 have both W bosons decaying leptonically. Those filtering efficiencies are also listed in the table.

DS ID	Process	Generator	$\sigma \times BR$ [nb]	k -factor	ϵ_{filter}	Events
410501	non-all-had $t\bar{t}$	Powheg +Pythia 8	0.83176	1	0.54386	60,000,000
410503	dilepton $t\bar{t}$	Powheg +Pythia 8	0.83176	1	0.10537	20,000,000
410511	non-all-had $t\bar{t}$ radUp	Powheg +Pythia 8	0.83176	1	0.54383	60,000,000
410512	non-all-had $t\bar{t}$ radDo	Powheg +Pythia 8	0.83176	1	0.54391	60,000,000
410525	non-all-had $t\bar{t}$	Powheg +Herwig 7	0.83176	1	0.54377	60,000,000
410527	dilepton $t\bar{t}$	Powheg +Herwig 7	0.83176	1	0.10537	20,000,000
410225	non-all-had $t\bar{t}$	aMC@NLO+Pythia 8.2	0.83176	1	0.54715	60,000,000
410226	dilepton $t\bar{t}$	aMC@NLO+Pythia 8.2	0.83176	1	0.10537	20,000,000

Table 19: $t\bar{t}$ samples used in the analysis, both for the nominal prediction and the systematic variations. The dataset ID, MC generator, production cross-section, k -factor, filter efficiency and total number of generated events are shown. Note that all samples are normalised to the same NNLO cross-section value. The sample with DS ID of 410501 is the default sample.

704 3.2.1. Cross-Section

705 The $t\bar{t}$ cross section for pp collisions at a centre-of-mass energy of $\sqrt{s} = 13\text{TeV}$ is $\sigma_{t\bar{t}} = 831.76^{+40}_{-46}\text{pb}$ for
 706 a top quark mass of 172.5 GeV. It has been calculated at next-to-next-to leading order (NNLO) in QCD
 707 including resummation of next-to-next-to-leading logarithmic (NNLL) soft gluon terms with top++2.0
 708 [33–39]. The PDF and α_S uncertainties were calculated using the PDF4LHC prescription [8] with the
 709 MSTW2008 68% CL NNLO [40, 41], CT10 NNLO [42, 43] and NNPDF2.3 5f FFN [5] PDF sets, added
 710 in quadrature to the scale uncertainty. PDFs uncertainties by themselves correspond to a $\pm 35.06\text{ pb}$ error
 711 on the total cross section, while QCD scale variations correspond to an error of $^{+19.77}_{-29.20}\text{ pb}$ on the total
 712 cross section. It is important to remember that the $t\bar{t}$ cross section at $\sqrt{s} = 13\text{TeV}$ is predicted to be 3.3
 713 times larger than the cross-section at $\sqrt{s} = 8\text{TeV}$: while this background was already crucial for the Run1
 714 analyses, we expect it to play an even more important role for the Run2 analyses of 13TeV data.
 715 As can be seen from Table 19 all the $t\bar{t}$ MC samples used for these analyses (both for the nominal MC
 716 prediction and the systematic variations) are normalised to the best NNLO+NNLL prediction of the cross
 717 section, therefore the total normalisation doesn't vary across the different samples.

718 3.2.2. Alternative Samples

719 Several alternative $t\bar{t}$ samples have been produced with the goal of assessing modelling systematic uncer-
 720 tainties for this process, by comparing different MC predictions at truth level. In Table 20 the different MC
 721 samples generated for this purpose have been listed, along with a short description of the main differences
 722 with respect to the nominal Powheg +Pythia 8 prediction. All the alternative samples are generated
 723 applying the same lepton filter as the nominal one. The samples considered are the following:

- 724 • Powheg +Herwig 7: this sample is generated using the same setup for Powheg as for the nominal
 725 Powheg +Pythia 8 sample, while parton shower (PS), hadronisation, underlying event (UE) and
 726 multiple parton interactions (MPI) are simulated with Herwig 7.0 [44, 45] with the H7UE tune [45]
 727 tune. The main purpose of this sample is to provide a comparison with a different parton shower
 728 model (Herwig 7 vs Pythia 8) with respect to the nominal prediction, while maintaining the same
 729 hard scattering simulation with Powheg.
- 730 • MadGraph 5_aMC@NLO+Pythia 8.2: these samples are produced using MadGraph 5_aMC@NLO [7]
 731 for the hard scattering generation at NLO precision and Pythia 8.2 for the PS, hadronisation, UE
 732 and MPI simulation. These samples can be compared to the nominal sample to assess the systematic
 733 uncertainties related to the use of different models for the hard scattering generation (MadGraph
 734 5_aMC@NLO vs Powheg) while maintaining the same parton shower model with Pythia 8.2.
- 735 • Powheg +Pythia 8 with low or high radiation: these two samples are produced with exactly the
 736 same setup as the nominal Powheg +Pythia 8 samples, with the following exception:
 - 737 - low radiation sample: both renormalisation scale μ_R and factorisation scale μ_F are doubled,
 738 the Powheg +Pythia 8 parameters are kept at their nominal values, $hdamp = 1.5 \cdot m_{top}$,
 739 $pTdef = 2$ and $pThard = 0$, while the A14 tune (Var3c) Down variation is used ($radLo$).
 - 740 - high radiation sample: both renormalisation scale μ_R and factorization scale μ_F are halved,
 741 the Powheg +Pythia 8 parameters are kept at their nominal values, $pTdef = 2$ and $pThard = 0$
 742 except $hdamp$ set to $3.0 \cdot m_{top}$, and the A14 tune (Var3c) Up variation is used ($radHi$).

743 Some points can be made about the high and low radiation Powheg +Pythia 8 samples. The `hdamp`
 744 parameter used to assess the low/high radiation systematics in Powheg corresponds to the transverse
 745 momentum scale around which the Sudakov resummation becomes unimportant and can therefore be
 746 damped (the pure NLO matrix element provides a good description in these regions), meaning that
 747 smaller values of `hdamp` correspond to a larger suppression of the hardest emission cross section. This
 748 parameter is set to a finite value for the $t\bar{t}$ Powheg samples to avoid an underestimate of the scale
 749 dependence in the high- p_T region.

750 The μ_R and μ_F scales variations and the `hdamp` variations are kept correlated since the two proposed
 751 variations envelope the full set of uncertainties obtained by changing the scales and the resummation
 752 damping parameter independently. The correlation with the PS scale (from the A14 tune) does not have a
 753 big impact.

Generator	Setup Details	Systematic Effect
POWHEG +PYTHIA 8	A14 tune NNPDF30NLO & NNPDF23LO <code>hdamp</code> = $1.5 \cdot m_{top}$ nonallhad filter	nominal sample
POWHEG +PYTHIA 8	nominal setup scale variations low ($\mu_R = \mu_F = 2$) <code>hdamp</code> = $1.5 \cdot m_{top}$ Up variation of A14 tune (Var3c) nonallhad filter	<i>low variation</i> for additional radiation
POWHEG +PYTHIA 8	nominal setup scale variations high ($\mu_R = \mu_F = 0.5$) <code>hdamp</code> = $3.0 \cdot m_{top}$ Down variation of A14 tune (Var3c) nonallhad filter	<i>high variation</i> for additional radiation
POWHEG +HERWIG 7	H7UE tune CT10 & MMHT2014lo68cl <code>hdamp</code> =175.2GeV nonallhad filter	fragmentation/hadronisation model
MADGRAPH 5_aMC@NLO+PYTHIA 8	A14 tune NNPDF30NLO & NNPDF23LO nonallhad filter	hard scatter generation and matching

Table 20: $t\bar{t}$ MC samples generated for the estimate of systematic uncertainties.

754 3.2.3. $t\bar{t}$ Systematic Uncertainties

755 In order to profit from increased statistics, a particle level study has been performed to assign modelling
 756 uncertainties for the $t\bar{t}$ process in the Standard Model $V(H \rightarrow b\bar{b})$ analysis, although a cross check was
 757 conducted with fully reconstructed events to investigate the influence of NNLO effects on the $p_T^{t\bar{t}}$ and p_T^t
 758 distributions on the p_T^V , p_T^{b1} and $m_{b\bar{b}}$ shapes. These studies are described in Section 3.2.5 of the modeling
 759 support note of the previous analysis [46].

760 The particle level studies were performed using Rivet; the object definitions and selection as well as
 761 the event selection are described in Appendix A and mirror the analysis as closely as possible. The
 762 samples that are available are the same as for the detector-level analysis and are listed in Table 20. All
 763 modelling uncertainty studies are based on the comparisons of these samples with each other. To decouple

764 effects originating from production of radiation, the fragmentation model and the matrix element POWHEG
 765 +PYTHIA 8 with increased and decreased radiation, as well as Powheg +HERWIG 7 and MADGRAPH
 766 5_aMC@NLO+PYTHIA 8, were compared with the nominal POWHEG +PYTHIA 8 description. This is the
 767 default for all studies.

768 The approach chosen to evaluate systematic uncertainties on our knowledge and prediction of the $t\bar{t}$
 769 contribution stems from the structure of the Profile Likelihood Fit used in this search, in which the overall
 770 normalisation of this background is left freely floating, without any priors or parameterisations, and can
 771 be adjusted by the fit of the MC prediction to data in the analysis phase space (see details in Ref [47]).

772 This approach consists of two main steps: first we consider the variation in acceptance for different analysis
 773 categories when using the alternative MC samples. The purpose of this first step is to obtain control of
 774 the correlations between the different analysis categories and regions of the phase space by implementing
 775 nuisance parameters in the Profile Likelihood Fit which control their relative acceptances. These nuisance
 776 parameters are parametrised in the fit with a Gaussian PDF, however the interpolation/extrapolation choices
 777 in HistFactory beyond 1σ create a log-normal behaviour. With this MC-based study we are able to provide
 778 a prior on this Gaussian constraint, which helps the fit to determine the best value of the parameter, and
 779 reflects our knowledge of the acceptance variation based on the MC prediction. The priors on the Gaussian
 780 constraints applied on the nuisance parameters which control the correlation between these categories are
 781 calculated as double ratios:

$$\frac{\text{Acceptance}[\text{Category}_A(\text{nominal MC})]}{\text{Acceptance}[\text{Category}_B(\text{nominal MC})]} \left| \frac{\text{Acceptance}[\text{Category}_A(\text{alternative MC})]}{\text{Acceptance}[\text{Category}_B(\text{alternative MC})]} \right. \quad (2)$$

782 This double ratio is calculated for all alternative MC samples normalised to the same NNLO cross-
 783 section, therefore no effect of changes in the total cross-section from the different MC schemes enters
 784 this calculation. The final uncertainties are given by the sum in quadrature of the three main variations:
 785 parton shower uncertainty (Powheg +HERWIG 7 versus Powheg +PYTHIA 8), matrix element uncertainty
 786 (MADGRAPH 5_aMC@NLO+PYTHIA 8 versus Powheg +PYTHIA 8) and radiation uncertainties. For the
 787 latter case, half the difference between the Powheg +PYTHIA 8 with different radiation samples was taken
 788 into account in the sum in quadrature.

789 The second step of determining the systematic uncertainties consists of evaluating possible effects on the
 790 shape of important variables of the analysis from the comparison of the alternative MC samples. Since the
 791 impact of these variation of the analysis acceptance are already taken into account as described before, this
 792 comparison is performed between variable templates normalised to the same area to obtain a systematic
 793 affecting only the shape of the variable.

794 For the shape uncertainties the distributions for all $t\bar{t}$ variations were normalised to the same area and
 795 compared. The definition of the 2 b -tag category follows the same prescriptions as for the acceptance
 796 uncertainties. To define an uncertainty a functional form was fitted through the variation that was found
 797 to be the largest, and symmetrised. If variations were found to be similar for certain analysis regions then
 798 a common uncertainty was derived for these regions.

799 3.2.4. Assignment of systematic variations on the $t\bar{t}$ background

800 It is important to note that the analysis in the 0 and 1 lepton channel is only performed for $p_T^V > 150$
 801 while the 2 lepton phase space is split into a $75 \text{ GeV} < p_T^V < 150 \text{ GeV}$ and $p_T^V > 150 \text{ GeV}$ categories.
 802 Furthermore the 2 lepton channel is split into 2 jet events and event with 3 or more jets contrary to

Not reviewed, for internal circulation only

803 the 0 and 1 lepton analysis which restrict themselves to a 2 jet and exactly 3 jet category. Studies on
 804 fully reconstructed events show that the $t\bar{t}$ events with 2 b -tags consist mainly of bb events and also a
 805 significant amount of bc events in the 0 and 1 lepton channel. Therefore to mimic the 2 b -tag region
 806 bb and bc events were used and each scaled by their corresponding b -tagging efficiencies. The 0 and 1
 807 lepton channel both contain $t\bar{t}$ events with at least one object that was not reconstructed while the $t\bar{t}$ events
 808 in the 2 lepton channel are mostly fully reconstructed⁸. This feature can be observed in the p_T^{top} and
 809 the $p_T^{t\bar{t}}$ shown in Fig. 16. This is reflected in the different flavour compositions in the 0+1 lepton and 2
 810 lepton channel. Owing to this and the fact that the order of magnitude and which variation is dominant is
 811 significantly different for the 0+1 lepton and 2 lepton channel, their systematic uncertainties are considered
 812 uncorrelated.

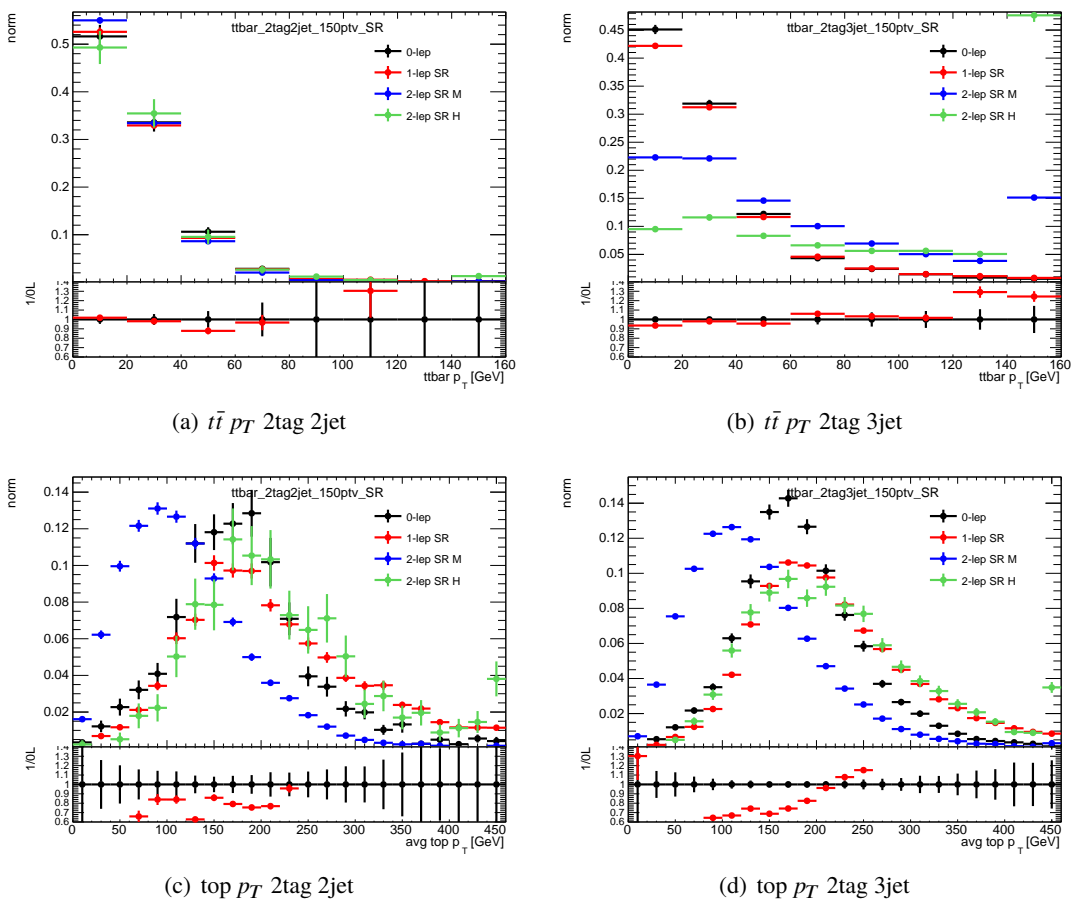


Figure 16: Comparison on transverse momentum on top and $t\bar{t}$ system for each signal category on the 0-,1- and 2-lepton. The top p_t is average of t and \bar{t} . Parton level distributions are shown here for events fulfilling the reconstructed-level selection of the analysis.

813 Acceptance uncertainties

814

⁸ In addition the physical meaning of the "V" system is completely different between 0/1lepton and 2lepton; in the former case, objects originating from a single top decay are considered while in the dilepton case the ll system is combining particles originating from the two tops.

815 To control the correlations between different analysis regions relative to the overall $t\bar{t}$ floating normalisation
 816 (`norm_ttbar`) the following acceptance uncertainties are assessed by calculating double ratios between
 817 the following regions:

- 818 - 3-to-2 jet uncertainty (0+1 lepton): 3 jet region of the 0+1 lepton channel and the 2 jet region of
 819 the 0+1 lepton channel (`SysttbarNorm_J2`)
- 820 - SR-to-WCR uncertainty (1 lepton): SR in the 1-lepton channel and the WCR in the 1-lepton channel
 821 (`SysttbarNorm_DWhfCR_L1`); in the context of the $t\bar{t}$ process the SR acts as the purer region.
- 822 - 1-to-0-lepton uncertainty (0+1 lepton): 2+3 jet regions in 1-lepton channel and the 2+3 jet regions
 823 in the 0-lepton channel (`SysttbarNorm_L0`).

824 The comparisons of the 3-to-2 jet variations show similar behaviour and order of magnitude for the 0
 825 and 1 lepton channel which is why a common uncertainty is assigned for both channels. For the 2-
 826 lepton channel, given the presence of a dedicated topCR with high purity and sufficient statistics, separate
 827 floating normalisation factors have been implemented in the 2j (`norm_ttbar_J2_L2`) and the 3+-jet
 828 regions (`norm_ttbar_J3_L2`) regions.

829 An overview of the $t\bar{t}$ normalisation systematics and their effect in the various analysis regions are detailed
 830 in Tables 21 and 22. The total uncertainties are derived as described in Section 3.2.3 and the full breakdown
 831 of the uncertainties is outlined in Appendix C.

	0-lepton		1-lepton			
	2j	3j	WCR 2j	SR 2j	WCR 3j	SR 3j
floating normalisation						
<code>SysttbarNorm_L0</code>	8%	8%	–	–	–	–
<code>SysttbarNorm_J2</code>	9%	–	9%	9%	–	–
<code>SysttbarNorm_DWhfCR_L1</code>	–	–	25%	–	25%	–

Table 21: Effect of modelling systematics on $t\bar{t}$ normalisation in the 0 and 1-lepton analysis region.

	2jet		≥ 3 jets	
	low Vpt [SR/CR]	high Vpt [SR/CR]	low Vpt [SR/CR]	high Vpt [SR/CR]
<code>norm_ttbar_J2_L2</code>	floating normalisation		–	
<code>norm_ttbar_J3_L2</code>	–		floating normalisation	
<code>SysTTbarPTV_L2_L2</code>	effect on each region obtained from shape rw			

Table 22: Effect of modelling systematics on $t\bar{t}$ normalisation in the 2lepton regions. The `SysTTbarPTV_L2_L2` systematic is implemented as a shape systematic over the full $VpT > 75$ GeV range, and as a result has different acceptance effects in the low and high VpT regions.

832 Shape uncertainties

833

834 Since the $V(H \rightarrow b\bar{b})$ analysis uses Boosted Decision Trees as a discriminating variable it is important
 835 to consider modelling uncertainties for the most important underlying physical quantities input to the
 836 BDT. Therefore shape uncertainties were derived for the p_T^V and $m_{b\bar{b}}$. Shape uncertainties are derived as
 837 described in Section 3.2.3 and a full breakdown of the studies is detailed in Appendix C. A summary of

838 the nuisance parameter used to model the shape uncertainties can be found in Table 23. A summary of
 839 the derivation of the shape uncertainties for p_T^V and $m_{b\bar{b}}$ can be found below.

840 The default for the p_T^V and $m_{b\bar{b}}$ shape systematics is to decorrelate them but also the approach of correlating
 841 these two uncertainties in the fit was tested. These studies showed no influence on the expected significance
 842 of the analysis and therefore the default of decorrelating these two shape uncertainties was chosen.

Analysis region	Uncertainty	Value	Source	Nuisance Parameter
0,1 lepton	p_T^V shape	shape	fit through largest deviation (aMC@NLO+PYTHIA 8)	TTbarPTV
2 lepton	p_T^V shape	norm + shape	fit through largest deviation (aMC@NLO+PYTHIA 8)	TTbarPTV_L2
0,1 lepton	$m_{b\bar{b}}$ shape	shape only	fit through largest deviation (aMC@NLO+PYTHIA 8)	TTbarMBB
2 lepton	$m_{b\bar{b}}$ shape	shape only	fit through largest deviation (aMC@NLO+PYTHIA 8)	TTbarMBB_L2

Table 23: Summary of all shape uncertainties for the $t\bar{t}$ process with short descriptions and the name of the corresponding nuisance parameters.

843 $m_{b\bar{b}}$ dependence

844

845 Figure 17 shows the systematic variations of $m_{b\bar{b}}$ dependences for each signal category for the 2-lepton
 846 signal regions. The comparisons include the distributions for the nominal as well as the alternative samples
 847 listed in Table 20. The ratio of each variation compared to the nominal sample is shown on the bottom
 848 of each figure. The ratios are fitted with a suitable functional form which will allow to the effect of the
 849 systematic variation to be propagated to the analysis through a reweighting procedure. A linear slope was
 850 found to be sufficient to describe the observed variations in the 2-lepton case. The fits to each variation in
 851 each regions are included in Appendix C.2.3.

852 Equivalent plots for the 0-lepton and 1-lepton regions are in Appendices C.2.1 and C.2.2 (Figures 46
 853 and 48), with just the final parametrisations of the uncertainties summarised here. The variations are
 854 described by an exponential function. Even in the case of particle level studies (and after including all
 855 sample extensions) the 0-lepton channel has limited statistics; for this reason, while the shape uncertainties
 856 will be studied in this channel, the result should be taken with some caution especially in case of outliers.
 857 It has then been decided to mainly use the 1-lepton uncertainties for the 0-lepton channel as well. This
 858 choice is further justified by the similar region of phase space being probed in the two channels and the
 859 fact that the trends observed in 0-lepton are similar to 1-lepton.

860 Figure 18 shows a summary of the fits to the variations in each region. Here the ISR variation is the
 861 scale variation, ME variation is comparison to aMC@NLO, and PS variation is comparison to POWHEG
 862 +HERWIG 7. In addition, all figures show the corresponding symmetrised shape uncertainties that were
 863 used for the ICHEP 2016 analysis as a black line. *The strategy is to use the single largest variation as the
 864 uncertainty and where there are any inconsistencies, different options as described below will be tested in
 865 the fit.*

- 866
- 867 • 0-lepton and 1-lepton: The largest differences originate from the Matrix element variation (POWHEG
 to aMC@NLO) in the 2-jet bins. The magnitude and direction of the shape variations are very

consistent between the 2 and 3-jet regions, therefore in the baseline approach the systematic will be fully correlate across all the regions. It should be noted that the new variation (solid red line on the figure) is very similar to what has been adopted in the ICHEP analysis for the 1-lepton while it represents a large reduction with respect to the uncertainty in the 0-lepton channel.

- 2-lepton: Observed variations show complicated patterns. However, the largest variation comes from the Matrix element variation. We decided to assign the largest single variation (Matrix element in 2jet medium Vpt region) and fully correlate it across all the regions. Alternative approaches where different shape 'priors' are used in the 2jets and ≥ 3 jets as well as the implementation of uncorrelated residual uncertainties (see Appendix C.3) will be tested in the fit.

One new feature of this round of analysis is the use of an $e\mu$ control region for the 2-lepton channel. By requiring a combination of an electron and a muon in an event, $t\bar{t}$ events can be extracted from data with high purity. By including this region in a final statistical analysis, we can constrain the systematic uncertainties on the $t\bar{t}$ background in the 2-lepton channel⁹. A comparison between the $e\mu$ control region

⁹ there is a study to replace the MC-based estimation with a full data-driven estimation. It might be possible to use the full data-driven approach, but for now this note describes the MC-based approach as the default analysis.

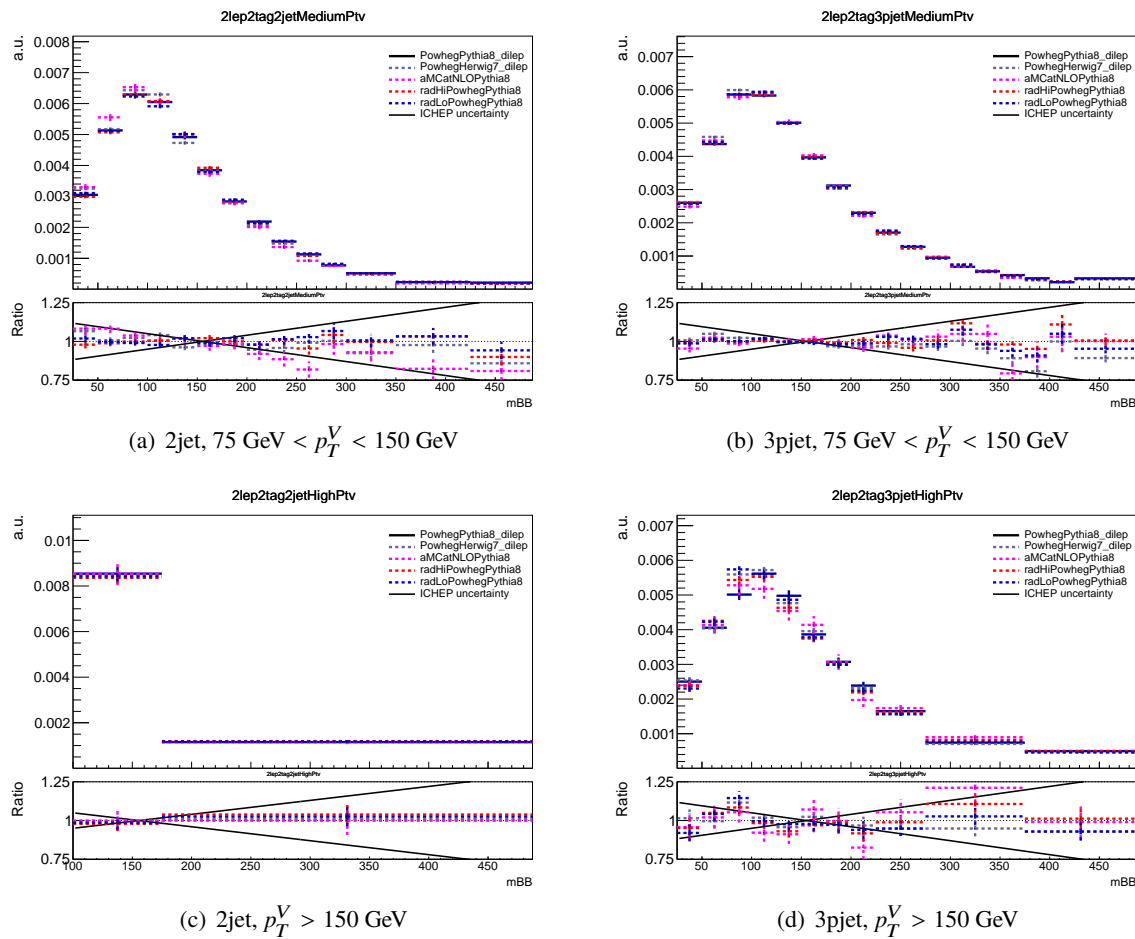
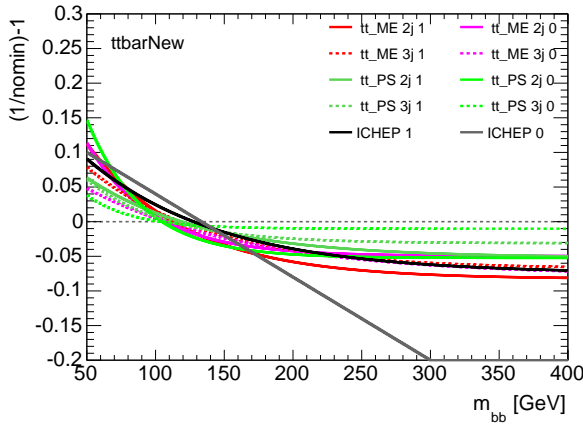


Figure 17: $m_{b\bar{b}}$ shape variation in 2-lepton.

Not reviewed, for internal circulation only

and the signal region are shown in Fig. 19 for the $m_{b\bar{b}}$ dependence. Note that this comparison is done with $p_T^V > 75$ GeV inclusively. There is little evidence for any difference between the two cases, therefore we do not assign an additional uncertainty to the $e\mu$ control region. For the same reason and since the $e\mu$ control region shares the same kinematics as the $ee/\mu\mu$ signal region both regions were added together for the derivation of systematic uncertainties.



(a) 0+1 lepton mbb dependence. The new assigned systematic corresponds to the solid red line.

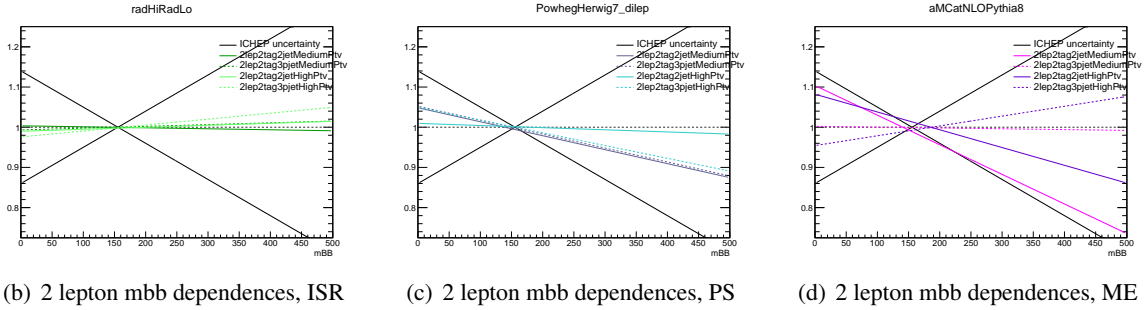


Figure 18: Relative shape variations for $m_{b\bar{b}}$ for the 0+1 lepton and the 2 lepton channel.

Not reviewed, for internal circulation only

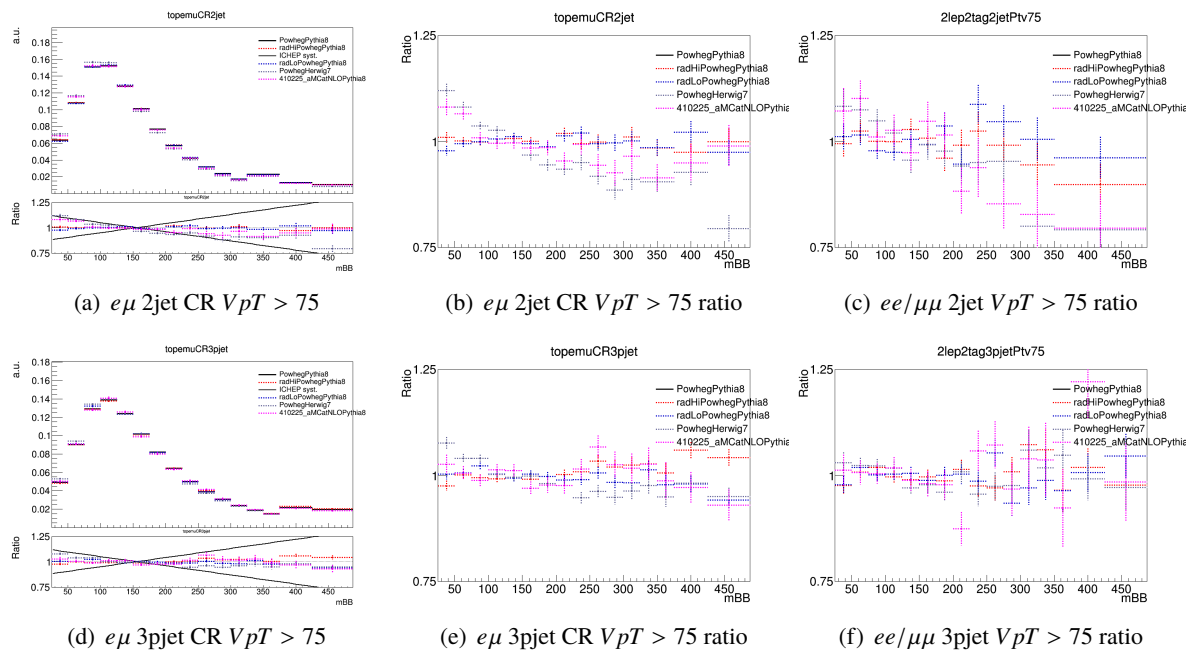


Figure 19: Comparisons of systematic variations for the 2-lepton signal region and $e\mu$ control region for both 2jet and 3jet regions.

886 **p_T^V dependence**

887

888 Figure 20 show the same systematic variations as for $m_{b\bar{b}}$ but as a function of p_T^V for each of the 2-lepton
 889 signal categories. Due to the steeply falling V_{PT} distribution the statistical uncertainty rapidly increases,
 890 making some of the fits unreliable. The full comparison of the p_T^V variations in each region are shown in
 891 Appendix C.

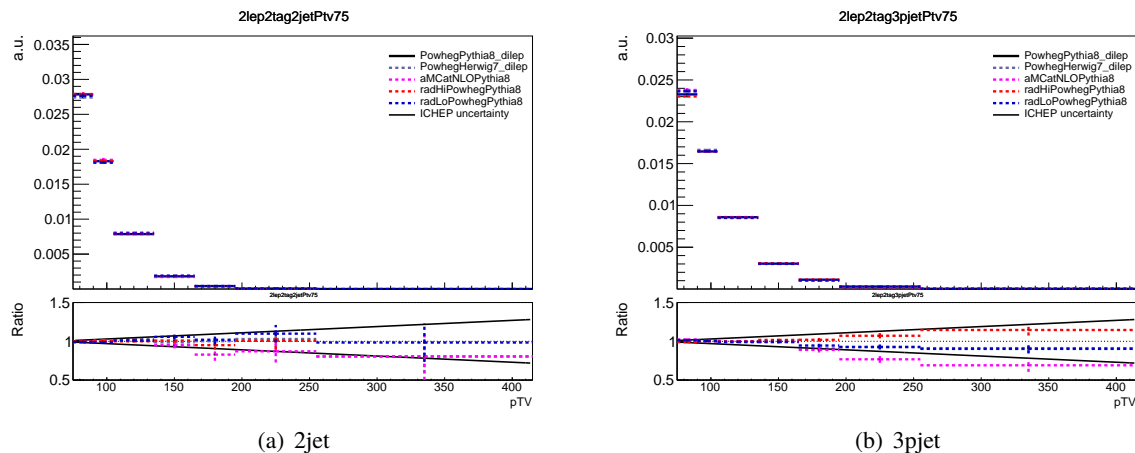


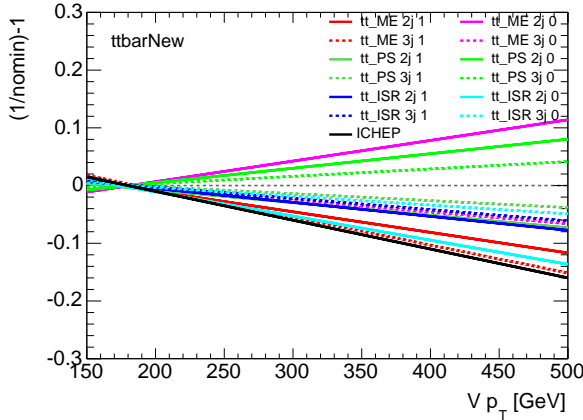
Figure 20: p_T^V shape variation in 2-lepton.

892 Full comparisons of the p_T^V variations in the 1 and 0-lepton channels, including the parametrised fit func-
 893 tions, are detailed in Appendices C.2.1 and C.2.2 (Figures 47 and 49) with just the final parametrisations
 894 summarised here. The strategy for the evaluation of systematic uncertainties is the same as for $m_{b\bar{b}}$ and
 895 the 1-lepton uncertainties will be used for 0-lepton. In the case of p_T^V a linear slope was found to be
 896 sufficient to describe the observed variations.

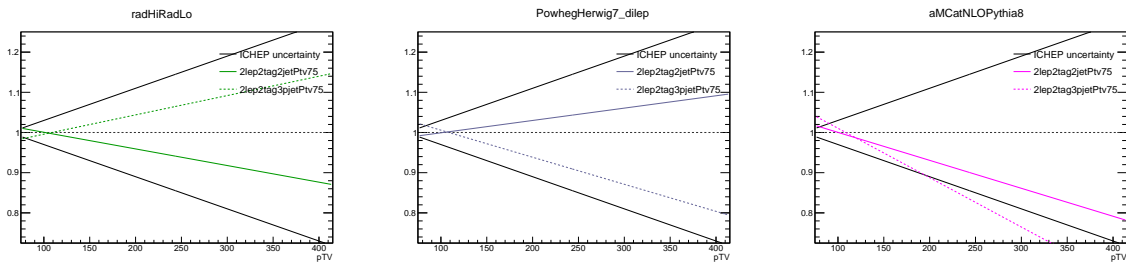
897 Figure 21 shows a summary of the fits to the variations in each region. In addition, all figures show the
 898 corresponding shape uncertainties that were used for the ICHEP 2016 analysis as a black line. *The ICHEP*
 899 *uncertainty will continue to be used for the 0- and 1-lepton channels. For 2-lepton different trends and*
 900 *magnitudes of the uncertainties are observed compared to ICHEP. In general the strategy will be to use*
 901 *the single largest variation as the uncertainty and different options as described below will be tested in*
 902 *the fit.*

- 903 • 0-lepton and 1-lepton: The largest shape variation comes from the Matrix element variation
 904 (POWHEG to aMC@NLO) in the 3 jet region. A relative good consistency is observed among
 905 all the variations in the 1-lepton channel while a larger spread is observed for the 0-lepton channel
 906 variations (as a result of a larger MC statistical uncertainty). The maximum observed variation is
 907 in good agreement with the value used in the previous analysis, as such the ICHEP uncertainty has
 908 been kept. In the baseline model the uncertainty will be used in a correlated way across all the
 909 regions.
- 910 • 2-lepton: The largest shape variation comes from the Matrix element variation (POWHEG to
 911 aMC@NLO) in the ≥ 3 jet region. This is assigned as a shape variation for 2-lepton in the baseline
 912 model and it will be implemented in a correlated way in the 2jet and ≥ 3 jet regions. However, a non

913 trivial pattern is observed for the ISR and parton shower variations which vary in different directions
 914 between the two jet regions. Decorrelation studies will be performed to test the imparatnce of this
 915 issue.



(a) 0+1 lepton VpT dependence



(b) 2 lepton VpT dependences, ISR

(c) 2 lepton VpT dependences, PS

(d) 2 lepton VpT dependences, ME

Figure 21: Relative shape variations for p_T^V for the 0+1 lepton and the 2 lepton channels.

Not reviewed, for internal circulation only

916 3.3. Single-Top Production

917 Single-top processes are generated separately for the different channels (s-channel, t-channel, Wt-channel)
 918 using the POWHEG MC generator for the hard scattering prediction with CT10 NLO PDFs, interfaced
 919 with the PYTHIA 6 algorithm for the simulation of parton shower, underlying event and multiple parton
 920 interactions. The PERUGIA2012 parton shower tune is applied with the corresponding CTEQ6L1 LO
 921 PDFs. The PYTHIA 6 algorithm is furthermore interfaced to PHOTOS for the modelling of QED final-state
 922 radiation, and to TAUOLA for the simulation of τ decays. Single top samples in the t- and s-channels are
 923 generated applying a lepton filter to require the leptonic decay of the W boson, while Wt-channel samples
 924 are generated both applying a dilepton filter (both W bosons decay leptonically) and inclusively: in these
 925 analyses the inclusive samples are used. All single-top samples, including the alternative ones described
 926 in Section 3.3.2, are listed in Table 24.

DS ID	Process	Generator	$\sigma \times BR$ [nb]	k-factor	ϵ_{filter}	Events
410013	Single top Wt incl t	POWHEG +PYTHIA 6	0.034009	1.054	1	4985800
410014	Single top Wt incl \bar{t}	POWHEG +PYTHIA 6	0.033989	1.054	1	4985600
410062	Single top DS Wt incl t	POWHEG +PYTHIA 6	0.032384	1.054	1	4948600
410063	Single top DS Wt incl \bar{t}	POWHEG +PYTHIA 6	0.03235	1.054	1	4983000
410099	Single top Wt incl t radHigh	POWHEG +PYTHIA 6	0.034917	1.027	1	4977000
410100	Single top Wt incl t radLow	POWHEG +PYTHIA 6	0.033407	1.073	1	4966000
410101	Single top Wt incl \bar{t} radHigh	POWHEG +PYTHIA 6	0.034893	1.027	1	4960000
410102	Single top Wt incl \bar{t} radLow	POWHEG +PYTHIA 6	0.033388	1.073	1	4959000
410147	Single top Wt incl t	POWHEG +HERWIG ++	0.0340	1.054	1	4827000
410148	Single top Wt incl \bar{t}	POWHEG +HERWIG ++	0.0340	1.054	1	4842000
410165	Single top Wt incl $t + \bar{t}$	MADGRAPH 5_aMC@NLO+HERWIG ++	0.073588	0.9743	1	9765000
410011	Single top t -chan t	POWHEG +PYTHIA 6	0.04373	1.0094	1	4986200
410012	Single top t -chan \bar{t}	POWHEG +PYTHIA 6	0.025778	1.0193	1	4989800
410017	Single top t -chan t radLow	POWHEG +PYTHIA 6	0.040343	1.0944	1	2968000
410018	Single top t -chan t radHigh	POWHEG +PYTHIA 6	0.04438	0.9949	1	2986000
410019	Single top t -chan \bar{t} radLow	POWHEG +PYTHIA 6	0.023751	1.1063	1	1990000
410020	Single top t -chan \bar{t} radHigh	POWHEG +PYTHIA 6	0.026387	0.9958	1	1985000
410047	Single top t -chan t	POWHEG +HERWIG ++	0.043614	1	1	4879000
410048	Single top t -chan \bar{t}	POWHEG +HERWIG ++	0.025744	1	1	4880000
410141	Single top t -chan $t + l\bar{l}$	MADGRAPH 5_aMC@NLO+HERWIG ++	0.068768	1	1	4872000
410025	Single top s -chan t	POWHEG +PYTHIA 6	0.002052	1.0046	1	997800
410026	Single top s -chan \bar{t}	POWHEG +PYTHIA 6	0.001262	1.0215	1	995400
410107	Single top s -chan t radHigh	POWHEG +PYTHIA 6	0.002076	1	1	990000
410108	Single top s -chan t radLow	POWHEG +PYTHIA 6	0.002033	1	1	996000
410109	Single top s -chan \bar{t} radHigh	POWHEG +PYTHIA 6	0.001275	1	1	994000
410110	Single top s -chan \bar{t} radLow	POWHEG +PYTHIA 6	0.001251	1	1	997000

Table 24: Single-top samples used in the winter analysis. The dataset ID, MC generator, production cross-section, k-factor, filter efficiency and total number of generated events are shown.

927 3.3.1. Cross-Section

928 The predicted t-channel single-top cross section for pp collisions at a centre-of-mass energy of $\sqrt{s} = 13$ TeV
 929 is $\sigma_t = 136.02^{+5.4}_{-4.6}\text{pb}$ for the top quark and $\sigma_{\bar{t}} = 80.95^{+4.1}_{-3.6}\text{pb}$ the anti-top quark, respectively. For the same
 930 scenario the s-channel single-top cross section is $\sigma_t = 6.35^{+0.2}_{-0.2}\text{pb}$ for the top quark and $\sigma_{\bar{t}} = 3.97^{+0.19}_{-0.17}\text{pb}$
 931 for the anti-top quark. These cross sections are calculated for a top quark mass of 172.5 GeV at next-to-
 932 leading order (NLO) in QCD with HATHOR v2.1 [48, 49]. The PDF and alphaS uncertainties are calculated
 933 using the PDF4LHC prescription with the MSTW2008 68% CL NLO, CT10 NLO and NNPDF2.3 PDF
 934 sets, added in quadrature to the scale uncertainty.

935 The Wt-channel single-top cross section is $\sigma_t = 71.7^{+3.8}_{-3.8}$ pb for the top quark plus the anti-top quark
 936 processes. This cross section is the result of an approximate NNLO calculation, with $m_{top}=172.5$ GeV,
 937 using the MSTW2008 NNLO PDFs. The PDF uncertainties are evaluated using the 90% CL PDFs set for
 938 MSTW2008 NNLO. Scale uncertainties are obtained as for the t- and s-channels, using the MSTW2008
 939 NNLO PDFs.

940 All the single-top samples used in these analyses are normalised to the cross sections from these higher
 941 order calculations, which represent the best theoretical prediction of the inclusive production cross section
 942 for single-top production processes. However, for the samples which are generated applying a lepton
 943 filter, the normalisation is corrected for the leptonic branching ratio by multiplying the cross sections by
 944 3×0.1082 . Similarly, the Wt-channel samples are generated separately for the top and anti-top processes,
 945 therefore they are normalised assuming that the Wt-channel top and anti-top cross section are both half
 946 the total Wt-channel cross section quoted above.

947 3.3.2. Alternative Samples

948 Alternative MC samples describing the single-top production have been generated for the estimation of
 949 systematic uncertainties and the comparison with the nominal Powheg +Pythia 6 prediction, using fully
 950 reconstructed detector objects or alternatively a particle-level analysis similar to the $t\bar{t}$ studies. Table 25
 951 summarizes the different samples with a short description of the setup. For all the alternative samples the
 952 same lepton filters used for the corresponding nominal ones (if applied) is used. The single-top alternative
 953 samples are the following:

- 954 • Powheg +Pythia 6 with low or high radiation: these samples correspond to the low and high
 955 radiation samples generated for top-pair production described in 3.2.2, in which μ_R and μ_F and
 956 the PERUGIA2012 tune variations are considered as correlated. However, single-top samples
 957 don't make use of the Powheg resummation damping parameter `hdamp`, therefore its variations are
 958 not considered for these samples. Low and high radiation samples are generated for all available
 959 single-top production mechanisms (t-, s- and Wt-channel)
- 960 • Powheg +Pythia6 Wt-channel DS: these Wt-channel single-top samples are generated with
 961 the same setup and generator as the nominal samples, however the scheme for the matrix element
 962 calculation applied is the ‘diagram subtraction’ (DS) one, instead of the ‘diagram removal’ (DR) used
 963 for the nominal prediction. The comparison of the nominal samples with this different calculation
 964 can give an estimate of single-top interference effects, to be used as systematic uncertainty.
- 965 • Powheg +Herwig ++: these single-top samples are generated with the same setup and generator
 966 as the nominal samples for the matrix element. For the parton shower Powheg was interfaced to
 967 Herwig ++ which uses the CTEQ6L1-UE-EE-5 tune. The comparison of the nominal samples with
 968 this samples allows to assess effects of the parton shower model.
- 969 • MadGraph 5_aMC@NLO+Herwig ++: these single-top samples are generated with an alternative
 970 generator for the matrix element and parton shower. The matrix element uses the CT10f4 PDF set
 971 and the CTEQ6L1-UE-EE-5 tune. The comparison of this sample with the Powheg +Herwig ++
 972 samples allows to eliminate parton shower effects originating from the difference between Pythia
 973 6 and Herwig ++ and only assess the matrix element differences between Powheg and MadGraph
 974 5_aMC@NLO+Herwig ++.

975 These alternative samples have been used to assess the systematic uncertainties of the single-top prediction.
 976 A detailed comparison of the nominal prediction and the alternative MC generator is given in Ref [50].

Generator	Setup Details	Systematic Effect
POWHEG +PYTHIA 6	nominal setup scale variations low ($\mu_R = \mu_F = 2$) low radiation PERUGIA2012 tune variation	<i>low variation</i> for additional radiation
POWHEG +PYTHIA 6	nominal setup scale variations high ($\mu_R = \mu_F = 0.5$) high radiation PERUGIA2012 tune variation	<i>high variation</i> for additional radiation
POWHEG +PYTHIA 6	Wt -channel nominal setup 'diagram subtraction' scheme setup in the Powheg ME calculation	alternative ME calculation scheme
POWHEG +HERWIG ++	nominal setup parton showering with HERWIG ++ CTEQ6L1-UE-EE-5 tune for PS	alternative PS
MADGRAPH 5_aMC@NLO+HERWIG ++	alternative setup ME with MADGRAPH 5_aMC@NLO CT10f4 PDF in ME	alternative ME

Table 25: Single-top MC samples generated for the estimate of systematic uncertainties.

977 3.3.3. Single-top Systematic Uncertainties

978 Overall normalisation uncertainties following the recommendations given by the LHC top working group
 979 are derived for each of the single-top processes. These uncertainties account for renormalisation and
 980 factorisation scale variations, the α_S uncertainty and the errors on the parton density functions. The sum
 981 in quadrature of these uncertainties give the total overall normalisation uncertainties of 4.4%, 4.6% and
 982 6.2% for the t- (`stopNorm`), s- (`stopsNorm`) and Wt-channel (`stopWtNorm`) respectively.

983 Analysis specific single-top modelling uncertainties were estimated by comparisons of the alternative
 984 samples described in Table 25 and the approach is very similar to the extraction of systematic uncertainties
 985 for the $t\bar{t}$ modelling. The studies also use a particle-level analysis implemented in Rivet as described in
 986 Appendix A. The single top process has a vanishing contribution to the overall background in most analysis
 987 regions therefore the studies were focussed on the 1-lepton channel where a sizeable single top contribution
 988 from the Wt and t -channel production channel is expected. For these two processes, normalisation
 989 uncertainties in the 2 jet and 3 jet regions and shape uncertainties for the $m_{b\bar{b}}$ and p_T^V distributions are
 990 derived. Those uncertainties were derived by comparing the acceptances and shapes respectively with the
 991 nominal sample to the acceptances and shapes in the alternative samples. For the acceptance uncertainties
 992 we have separate normalisation uncertainties for the 2 jet and 3 jet region in the Wt (`stopWtAcc`) and
 993 t -channel (`stopTAcc`) which are detailed in the summary Table 28. The numbers were obtained by taking
 994 the sum in quadrature of all variations. For the POWHEG +PYTHIA 6 with increased and decreased radiation
 995 half the difference between them was taken into account in the sum in quadrature. The normalisation
 996 uncertainties for the 2 jet and 3 jet region vary in the same direction for each of the different alternative
 997 samples therefore these two uncertainties are correlated in the fit.

998 Since normalisation and acceptance effects are already accounted for in the overall normalisation and
 999 analysis region acceptance uncertainties the $m_{b\bar{b}}$ and p_T^V distribution were normalised to the same area
 1000 before the comparisons. Figure 22 shows the comparisons of the p_T^V distributions of the available samples

for the Wt channel in the 1 lepton analysis regions. A shape uncertainty (StopWtPTV) was derived by fitting a linear slope through the largest variation which is given by POWHEG +PYTHIA 6 with the diagram subtraction scheme for the matrix element calculation and symmetrising the result. The fit was performed in the region with the largest Monte Carlo statistics which is the 3 jet region. The same uncertainty will be used for the 2 jet region as the variations show the same order of magnitude there and will be correlated between the two regions. The variations with the symmetrised fitted function overlaid is also shown in figure 22. The same strategy was used to extract the shape uncertainty for the $m_{b\bar{b}}$ distribution (StopWtMBB): a linear slope was fit to the largest variation which is given by POWHEG +PYTHIA 6 with the diagram subtraction scheme. The fit was performed in the 2 jet region where the variation was observed to be largest, and the extracted shape was symmetrised and also used as a systematic uncertainty in the 3 jet channel since the variations observed there are very consistent with the 2 jet channel; the 2 jet and 3 jet channel uncertainties are therefore treated as completely correlated. Figure 23 shows the comparisons of the $m_{b\bar{b}}$ distributions as well as the variations with the shape uncertainty overlaid.

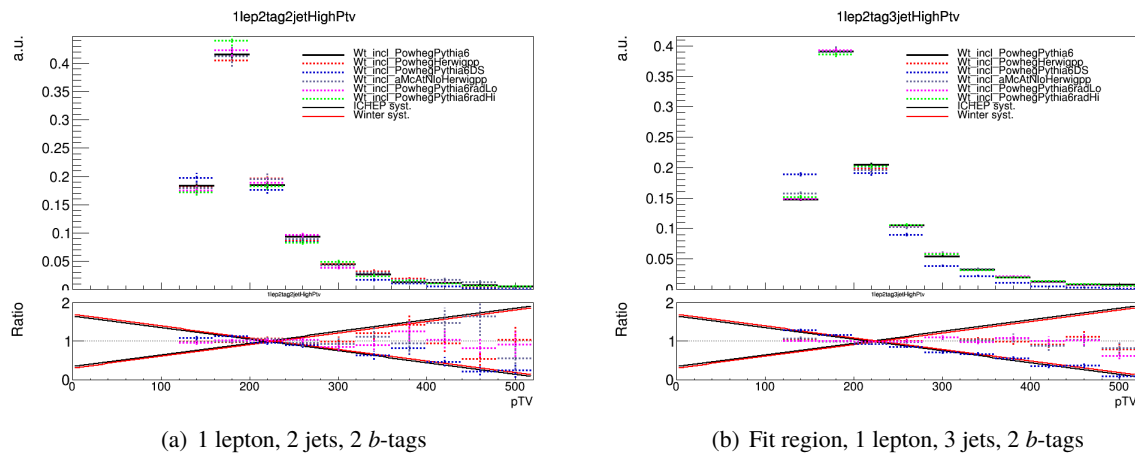


Figure 22: Shape comparison of the p_T^V distributions in the 1 lepton regions, comparing the nominal Wt POWHEG +PYTHIA 6 samples and POWHEG +PYTHIA 6 with increased and decreased radiation as well as with diagram subtraction (DS) in the matrix element calculation and _aMC@NLO+HERWIG ++. The shape uncertainty is derived from a fit to the POWHEG +PYTHIA 6 DS variation in the 3 jet region.

The whole procedure was repeated to extract the systematic uncertainties on the p_T^V and $m_{b\bar{b}}$ shape for the single top t -channel production. The nominal POWHEG +PYTHIA 6 sample was compared to the POWHEG +PYTHIA 6 with increased and decreased radiation as well as to the alternative POWHEG +HERWIG ++ sample, and the POWHEG +HERWIG ++ sample was compared with the MADGRAPH 5_aMC@NLO+HERWIG ++ sample. All of these samples are described in Section 3.3.2. For the p_T^V shape uncertainty the POWHEG +HERWIG ++ radiation variation was found to cause the largest deviations. The comparisons and the variations overlaid with the determined shape uncertainties (StopptPTV) for p_T^V are shown in Fig. 24. For the $m_{b\bar{b}}$ uncertainty (StopWtMBB) the increased and decreased radiation samples gave a slightly larger variation than the MADGRAPH 5_aMC@NLO+HERWIG ++ sample (which was used for the ICHEP systematics) and the increased/decreased radiation samples were therefore fitted with a linear slope in the 2 jet region; the same variation will be used to describe the $m_{b\bar{b}}$ shape uncertainty in the 2 jet region. All comparisons and variations with the shape uncertainty overlaid are shown in figure 25.

Since single top production has a negligible contribution to the backgrounds in the 0 and 2 lepton channel systematic uncertainties for single top will have no large impact on the final result in those channels and no

Not reviewed, for internal circulation only

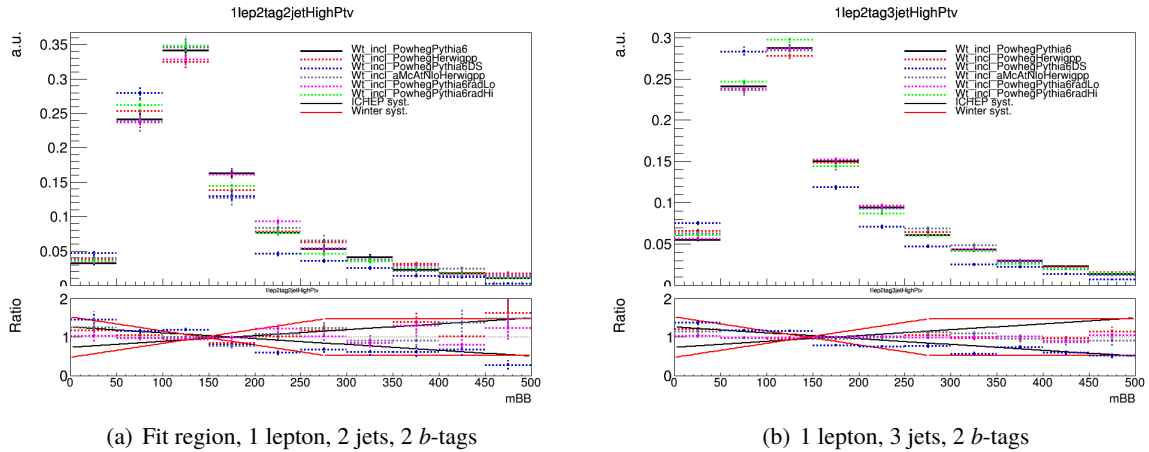


Figure 23: Shape comparison of the $m_{b\bar{b}}$ distributions in the 1 lepton regions, comparing the nominal Wt POWHEG +PYTHIA 6 samples and POWHEG +PYTHIA 6 with increased and decreased radiation as well as with diagram subtraction in the matrix element calculation and _aMC@NLO+HERWIG ++. The shape uncertainty is derived from the POWHEG +PYTHIA 6 DS variation in the 2 jet region.

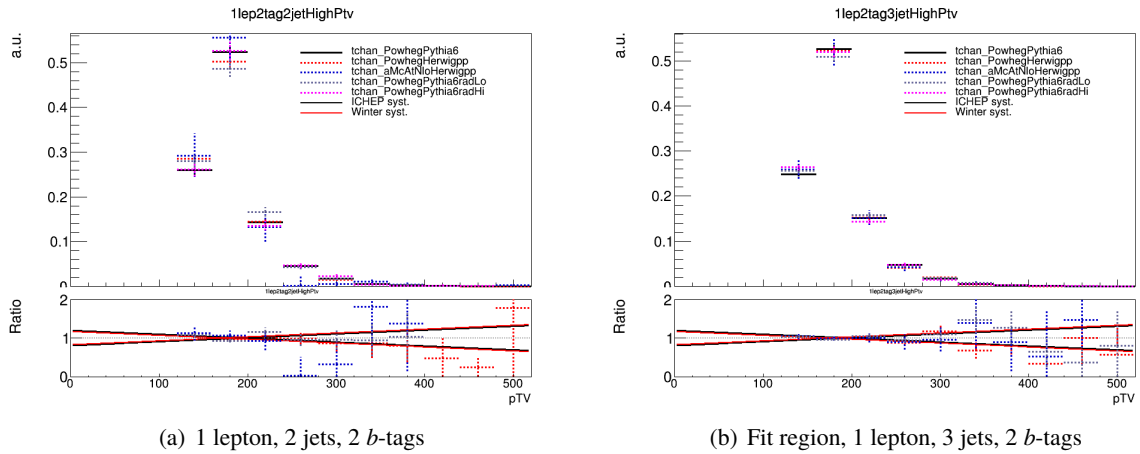


Figure 24: Shape comparison of the p_T^V distributions in the 1 lepton regions, comparing the nominal t -channel POWHEG +PYTHIA 6 samples and POWHEG +PYTHIA 6 with increased and decreased radiation as well as POWHEG +HERWIG ++ and MADGRAPH 5_aMC@NLO+HERWIG ++. The shape uncertainty is derived from the MADGRAPH 5_aMC@NLO+HERWIG ++ variation in the 3 jet region.

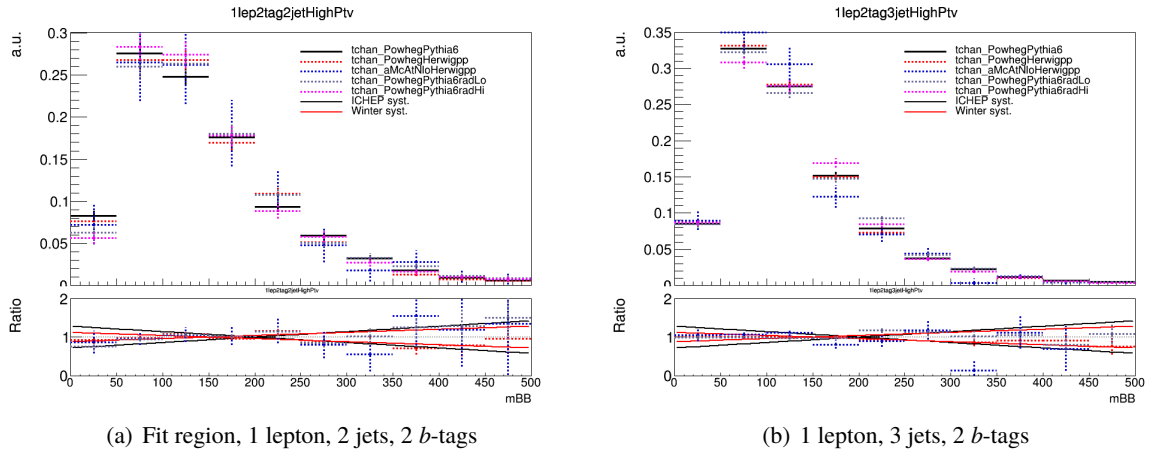


Figure 25: Shape comparison of the $m_{b\bar{b}}$ distributions in the 1 lepton regions, comparing the nominal t -channel POWHEG +PYTHIA 6 samples and POWHEG +PYTHIA 6 with increased and decreased radiation as well as POWHEG +HERWIG ++ and MADGRAPH 5_aMC@NLO+HERWIG ++. The shape uncertainty is derived from the POWHEG +PYTHIA 6 with increased and decreased radiation samples ("radHi/Lo").

1028 dedicated studies have been conducted. The single top uncertainties that derived in the 1 lepton channel
 1029 are also applied in the 0 and 2 lepton channels and are fully correlated.
 1030 The acceptance systematics are given in Tables 26 and 27, along with comparisons to the ICHEP values.
 1031 The values are very similar to those obtained for the ICHEP analysis, except that in the Wt channel, the
 1032 newly-available POWHEG +HERWIG ++ sample adds a significant contribution to the total. It can be seen
 1033 that the significant contributions are correlated between the 2-jet and 3-jet channels.
 1034 A summary of all systematic uncertainties for the single top process are listed in Table 28 including a
 1035 short description and the name of the corresponding nuisance parameter in the fit.

Systematic (ICHEP Total, no PH7)	SR 2j ($\pm 25\%$)	SR 3j ($\pm 32\%$)
Wt (RadHi)	+3.2 %	-1.0 %
Wt (RadLo)	-0.4 %	-2.1 %
Wt (DS)	-28.2 %	-35.4 %
Wt (PH7)	-14.8 %	-15.0 %
Wt (aMC)	-13.4 %	-12.6 %
TOTAL	$\pm 34.7\%$	$\pm 40.6\%$

Table 26: Acceptance uncertainties for the single-top Wt channel (top+antitop). Uncertainties are very similar to ICHEP values except that the newly-available POWHEG +HERWIG ++ sample adds a significant contribution to the total. Significant contributions are correlated in the 2-jet and 3-jet channels.

Systematic (ICHEP Total)	SR 2j	SR 3j
	($\pm 16\%$)	($\pm 19\%$)
t-chan (RadLo)	+0.7 %	+2.1 %
t-chan (RadHi)	+0.5 %	-3.8 %
t-chan (PH7)	-10.6 %	-19.2 %
t-chan (aMC)	+13.1 %	+3.2 %
TOTAL	$\pm 16.8\%$	$\pm 19.9\%$

Table 27: Acceptance uncertainties for the single-top t-channel (top+antitop). Uncertainties are very similar to ICHEP values.

Production	Uncertainty	Value	Source	Nuisance Parameter
s -channel	overall normalisation	4.6%	sum in quadrature of μ_R , μ_F , α_S and PDF uncertainties	<code>stopsNorm</code>
t -channel	overall normalisation	4.4%	sum in quadrature of μ_R , μ_F , α_S and PDF uncertainties	<code>stoptNorm</code>
t -channel	2 jet region acceptance	17%	sum in quadrature of deviations in alternative generators	correlated with 2 jet and 3 jet case <code>stoptAcc</code>
t -channel	3 jet region acceptance	20%	sum in quadrature of deviations in alternative generators	correlated with overall and 3 jet case <code>stoptAcc</code>
Wt channel	overall normalisation	6.2%	sum in quadrature of μ_R , μ_F , α_S and PDF uncertainties	<code>stopWtNorm</code>
Wt channel	2 jet region normalisation	35%	sum in quadrature of deviations in alternative generators	correlated with 2 jet and 3 jet case <code>stopWtAcc</code>
Wt channel	3 jet region normalisation	41%	sum in quadrature of deviations in alternative generators	correlated with overall and 3 jet case <code>stopWtAcc</code>
t -channel	p_T^V shape	shape	fit through largest deviation (POWHEG +HERWIG++) $\pm 0.001 \times p_T^V \mp 0.17 + 1$	<code>StoptPTV</code>
t -channel	$m_{b\bar{b}}$ shape	shape	fit through largest deviation (POWHEG +PYTHIA 6 [radHi-radLo]) $\pm 0.0008 \times m_{b\bar{b}} \mp 0.12 + 1$	<code>StoptMBB</code>
Wt channel	p_T^V shape	shape	fit through largest deviation (POWHEG +PYTHIA 6 with diagram subtraction) $\pm 0.003 \times p_T^V \mp 0.69 + 1$	<code>StopWtPTV</code>
Wt channel	$m_{b\bar{b}}$ shape	shape	fit through largest deviation (POWHEG +PYTHIA 6 with diagram subtraction) $\pm 0.0036 \times m_{b\bar{b}} \mp 0.52 + 1$ ($m_{b\bar{b}} < 275$ GeV) $\mp 0.47 + 1$ ($m_{b\bar{b}} \geq 275$ GeV)	<code>StopWtMBB</code>

Table 28: Summary of all uncertainties for the single top process with short descriptions and the name of the corresponding nuisance parameters, updated for the winter baseline analysis.

1036 **3.4. Diboson Production**1037 **3.4.1. Nominal Monte Carlo Simulation**

1038 The diboson background consists of final states arising from WW, WZ, and ZZ events. Several diboson
 1039 processes can give a significant contribution in the analysis phase space: $Z \rightarrow b\bar{b}$ and $Z \rightarrow \nu\bar{\nu}$ for the
 1040 0-lepton channel; $Z \rightarrow b\bar{b}$ and $Z \rightarrow ll$ for the 2-lepton channel; and $Z \rightarrow b\bar{b}$ and $W \rightarrow l\nu$ for the 1-lepton
 1041 channel. Additional processes can give smaller contributions arising from the mistagging of a jet from
 1042 the W decay or the failed reconstruction of one of the leptons, for example in $Z \rightarrow \nu\bar{\nu}$ and $W \rightarrow q\bar{q}$,
 1043 $Z \rightarrow ll$ and $W \rightarrow q\bar{q}$, and $W \rightarrow l\nu$ and $W \rightarrow q\bar{q}$ production. As with the modelling of $V+jets$ processes,
 1044 ATLAS has upgraded to improved MC programs for diboson event generation for the Run 2 data-taking
 1045 period. Details on the baseline diboson MC programs and the evaluation of systematic uncertainties are
 1046 documented in [51].

1047 The nominal description for modelling these diboson processes is currently the SHERPA 2.2.1 MC generator,
 1048 interfaced with the NNPDF 3.0 PDF sets for both the ME calculation and the parton shower. SHERPA
 1049 2.2.1 provides a combination of different matrix elements with different parton multiplicities: processes
 1050 with zero or 1 additional partons are calculated at NLO in the ME for WW, WZ, and ZZ, while 2 or 3
 1051 additional partons are included at LO in QCD. The merging of different parton multiplicities is achieved
 1052 through the CKKW-L merging technique using a merging scale of $Q_{cut} = 20$ GeV. The modelling of even
 1053 higher jet multiplicities relies on the parton shower algorithm. [Note, owing to a problem with the SHERPA
 1054 2.2.1 WW samples the SHERPA 2.1 WW samples are still being used. However, the contribution of these
 1055 samples to the analysis selection is found to be negligible.]

1056 The nominal samples are listed in Table 29.

DS ID	Process	Generator	$\sigma \times BR$ [pb]	k -factor	ϵ_{filter}	Events
361091	WplvWmqq	SHERPA 2.1	24.893	0.91	1.0	3993900
361092	WpqqWmlv	SHERPA 2.1	25.898	0.91	1.0	3993700
363489	WlvZqq	SHERPA 2.2.1	11.413	1.0	1.0	7100000
363358	WqqZll	SHERPA 2.2.1	3.437	1.0	1.0	5324000
363357	WqqZvv	SHERPA 2.2.1	6.797	1.0	1.0	5939000
363356	ZqqZll	SHERPA 2.2.1	15.563	1.0	0.13961	5317000
363355	ZqqZvv	SHERPA 2.2.1	15.564	1.0	0.27976	5324000

Table 29: Nominal diboson samples used in the winter analysis. The dataset ID, MC generator, production cross section, k -factor, filter efficiency, and total number of generated events are shown.

1057 **3.4.2. Update of Nominal Predictions**

1058 In the ICHEP version of the analysis, all the nominal predictions were produced using SHERPA 2.1
 1059 interfaced with the CT10 NLO PDFs. SHERPA 2.1 gave predictions for VV plus one extra parton at NLO
 1060 in QCD only for ZZ, while WZ and WW plus one extra parton were given at LO in QCD; 2 or 3 additional
 1061 partons were included at LO in QCD for all samples, with higher multiplicities given by the PS. The
 1062 new nominal SHERPA 2.2.1 samples give predictions at NLO in QCD for all the VV plus one extra parton

1063 samples, then 2 or 3 additional partons are included at LO in QCD and higher multiplicities given by the
 1064 PS. The new samples also have significantly higher statistics than the ICHEP samples.

1065 A further point to note is that the **SHERPA** 2.1 calculations for the diboson cross-sections used a set of the
 1066 electroweak (EW) parameters that did not correspond to the most up-to-date prescription from the PDG
 1067 group, as used by **POWHEG**. To take into account the effect of the correct choice of EW parameters the
 1068 **SHERPA** 2.1 diboson cross sections were scaled by a factor 0.91, however this is not done for the **SHERPA**
 1069 2.2.1 cross-sections.

1070 The **SHERPA** 2.1 WW samples are still being used owing to a problem with the **SHERPA** 2.2.1 WW samples.
 1071 However, the contribution of the WW processes to the analysis selection is negligible.

1072 3.4.3. Cross-Sections

1073 The generator used for the nominal samples already provides the NLO calculation for the diboson cross-
 1074 sections, therefore the samples are not normalised to a higher order prediction.

1075 3.4.4. Alternative Monte Carlo Samples

1076 **SHERPA** 2.2.1 samples are produced with internal weights stored; using them to reweight the samples
 1077 allows the effect of varying the renormalisation and factorisation scales to be assessed. The weights
 1078 correspond to doubling and halving the renormalisation scale ($2\mu_R$ and $0.5\mu_R$) and doubling and halving
 1079 the factorisation scale ($2\mu_F$ and $0.5\mu_F$).

1080 Several sets of additional samples are available to assess other systematic uncertainties:

- 1081 • **POWHEG +PYTHIA** 8: this sample uses the **POWHEG** v2 generator, interfaced to the **PYTHIA** 8 parton
 1082 shower model. The CT10 NLO set is used for PDF of the hard-scattering process while the
 1083 CTEQ6L1 PDF set is used for the parton shower. Non-perturbative effects are modelled using the
 1084 AZNLO tune. The EvtGen v1.2.0 program is used for properties of the bottom and charm hadron
 1085 decays. The generator cross sections are used in this case (already at NLO). Note, duplicate events
 1086 in the reconstructed **POWHEG +PYTHIA** 8 samples were found not to have been handled properly,
 1087 however systematic uncertainties were assessed on the particle level and were not affected by the
 1088 problem.
- 1089 • **POWHEG +HERWIG ++**: this sample is generated using the same setup for **POWHEG** as for the **POWHEG**
 1090 +**PYTHIA** 8 sample, while parton shower (PS), hadronisation, underlying event (UE) and multiple
 1091 parton interactions (MPI) are simulated with **HERWIG ++** (version 2.7.1) [44] with the UE-EE-5 [52]
 1092 tune and the corresponding CTEQ6L1 PDF set. The main purpose of this sample is to provide a
 1093 comparison with a different parton shower model (**HERWIG ++** vs **PYTHIA** 6).

1094 The alternative diboson samples are listed in Table 30.

DS ID	Process	Generator	$\sigma \times BR$ [pb]	k -factor	ϵ_{filter}	Events
361606	WlvWqq	POWHEG +PYTHIA	44.18	1.0	1.0	4343000
361607	WqqZll	POWHEG +PYTHIA	3.2777	1.0	1.0	1469000
361608	WqqZvv	POWHEG +PYTHIA	5.7576	1.0	1.0	2921000
361609	WlvZqq	POWHEG +PYTHIA	10.086	1.0	1.0	9693000
361610	ZqqZll	POWHEG +PYTHIA	2.2699	1.0	1.0	3933000
361611	ZqqZvv	POWHEG +PYTHIA	3.9422	1.0	1.0	9591000
361592	WlvWqq	POWHEG +HERWIG ++	44.166	1.0	1.0	4271000
361593	WqqZll	POWHEG +HERWIG ++	3.2774	1.0	1.0	1446000
361594	WqqZvv	POWHEG +HERWIG ++	5.7571	1.0	1.0	2888000
361595	WlvZqq	POWHEG +HERWIG ++	10.085	1.0	1.0	9580000
361596	ZqqZll	POWHEG +HERWIG ++	2.2699	1.0	1.0	3051000
361597	ZqqZvv	POWHEG +HERWIG ++	3.9421	1.0	1.0	9556000

Table 30: Alternative diboson samples used in this analysis to study systematic uncertainties. The dataset ID, MC generator, production cross section, k -factor, filter efficiency, and total number of generated events are shown.

1095 **3.4.5. Diboson Systematic Uncertainties**

1096 **Inclusive cross-section uncertainties**

1097 The diboson samples are normalised to their generator cross-sections. The same normalisation uncer-
 1098 tainties used in the ICHEP analysis have been adopted. The numbers are obtained considering the effect
 1099 of scale variations in the Sherpa samples as well as the difference in the prediction between Sherpa and
 1100 Powheg.

Sys Name	source	Norm. effect	applied to
SysWWNorm	overall cross section uncertainty	25%	WW in all regions
SysWZNorm	overall cross section uncertainty	26%	WZ in all regions
SysZZNorm	overall cross section uncertainty	20%	ZZ in all regions

Table 31: Summary of all systematic uncertainties on the diboson cross section including their value, source and the corresponding nuisance parameter name.

1101 **Analysis specific uncertainties**

1102 Analysis-specific diboson modelling uncertainties are estimated using the sample reweighting and al-
 1103 ternative samples described in Section 3.4.4. A particle-level analysis implemented in Rivet is used, as
 1104 described in Appendix A.

1105 In each analysis channel, a primary process is considered and the full assessment of systematic uncertainty
 1106 on the shape and acceptance effect has been considered. Secondary diboson processes are either reducible
 1107 background (events with hadronically decaying W and Z bosons not producing a pair of b-jets¹⁰), or they
 1108 represent a subleading contribution (i.e. ZZ events in 1 lepton channel). For these processes, only simple
 1109 normalisation systematics have been considered.

1110 The main processes are:

- 1111 • 0-lepton channel: $ZZ \rightarrow q\bar{q}vv$
- 1112 • 1-lepton channel: $WZ \rightarrow l\nu qq$
- 1113 • 2-lepton channel: $ZZ \rightarrow q\bar{q}ll$

1114 In the Profile Likelihood Fit the diboson normalisation is fixed by a set of nuisance parameters that control
 1115 the normalisation and the shape of the background distribution. The nuisance parameters controlling the
 1116 shape and the relative acceptance across regions are treated as uncorrelated in order to have a clearer
 1117 definition of the effect of the various parameters on the ingredient of the fit. Furthermore separated
 1118 uncertainties are considered following parton shower and scale variation systematics. Given that for the
 1119 diboson processes, a coherent set of samples and systematic prescriptions has been adopted, the bulk
 1120 effect of the various uncertainties will be considered as correlated across samples in the various regions;
 1121 additional residual uncertainties will also be considered.

1122 The nuisance parameters are included in the Profile Likelihood Fit parametrised with a Gaussian con-
 1123 straint.

¹⁰ For WZ and ZZ the focus of these studies is on processes with one hadronically decaying Z boson, which give the dominant contribution in the $VH(b\bar{b})$ phase space, as diboson processes with hadronically decaying W bosons are strongly suppressed by the requirement of 2 b-tagged jets.

1124 For all diboson processes, we consider uncertainties in the shapes of the variables m_{bb} and p_T^V . Since
 1125 the normalisation across the different categories is controlled by overall nuisance parameters, for all
 1126 shape comparisons the template histograms are normalised to unit area. To consider different sources
 1127 of uncertainty we compare shape effects from the parton shower variation, scale variations (considering
 1128 the single scale variation that shows the largest impact), and from comparing POWHEG +PYTHIA 8 with
 1129 SHERPA 2.2.1, and we take the largest variation as the shape systematic. Scale variations are found to
 1130 have a smaller impact for the variables considered, and are in general well-covered by the parton-shower
 1131 variation, therefore the shape systematics are extracted from the parton-shower variations and the POWHEG
 1132 +PYTHIA 8 versus SHERPA 2.2.1 comparison. The shapes are approximated by a suitable functional form,
 1133 which is then propagated to the analysis. Note that given the extremely small contribution of the WW
 1134 background (<1% across all categories) to the analysis, no shape variations are considered for it.
 1135 The following sections address PS and UE variations, scale variations, and PDF and α_s variations as well
 1136 as residual uncertainties between sample prediction in different regions.

1137

1138 PS and UE variations

1139 There are two approaches to assessing the parton shower uncertainties: the first is to use the four parton
 1140 shower tuning variations (Var1, Var2, Ren, and MPI); and the second is to compare different parton
 1141 shower models, such as PYTHIA versus HERWIG. The prescription used is as recommended by the Physics
 1142 Modelling Group (PMG), which is to sum in quadrature the maximum of each of the parton shower tune
 1143 variations, and then to take the envelope of the combined parton shower tuning variations and the parton
 1144 shower model variations.

1145 The parton shower uncertainties on the acceptance are summarized for the 0-, 1-, and 2-lepton selections
 1146 in Table 32 and their detailed breakdown is given in Appendix E. Two separated (uncorrelated) nuisance
 1147 parameters are used to describe the overall acceptance uncertainty in 2-jet events and the relative acceptance
 1148 between 2 and 3jet events. Such allow to separate the common acceptance effects from the modelling of
 1149 the jet multiplicity ¹¹

1150 No shape uncertainty is found in the p_T^V distribution from the PS and UE variations, within the MC
 1151 statistical uncertainty. For ICHEP a straight-line fit was used to cover the MC statistical uncertainty on the
 1152 shape, and those ICHEP uncertainties are kept for the current analysis. An example is shown in Figure 26
 1153 and plots for all regions and variations are included in Appendix E.

1154 The shape uncertainty on the m_{bb} distribution from PS and UE variations is found to be complicated
 1155 and no valid simple functional form has been found to approximate it. The uncertainty is taken from the
 1156 comparison between PYTHIA 8 and HERWIG ++, parameterised using a binned histogram after smoothing
 1157 has been applied.

1158 Scale variations

1159 The uncertainty arising from the choice of renormalisation and factorisation scales is assessed by re-
 1160 weighting the SHERPA 2.2.1 nominal samples by their internal weights, which correspond to doubling and
 1161 halving the renormalisation scale ($2\mu_R$ and $0.5\mu_R$) and doubling and halving the factorisation scale ($2\mu_F$
 1162 and $0.5\mu_F$).

1163 The scale variation uncertainties on the acceptance, in inclusive jet multiplicity bins for use as input to the
 1164 Stewart-Tackman method, are given in Table 33. Their detailed breakdown is given in Appendix E. The

¹¹ In addition it allows to easily remove the common acceptance component when performing the diboson cross check measurement.

NP name	0L: $ZZ \rightarrow v\bar{v}bb$		1L: $WZ \rightarrow \ell vbb$		2L: $ZZ \rightarrow \ell^+\ell^-bb$	
	2j	3j	2j	3j	2j	$\geq 3j$
SysVZ_UEPS_Acc	5.6%	5.6%	3.9%	3.9%	5.8%	5.8%
SysVZ_UEPS_32JR	–	7.3%	–	10.8%	–	3.1%
SysVZ_UEPS_VPT	shape+norm		shape only		shape+norm	
SysVZ_UEPS_MBB			shape only			

Table 32: Summary of the effects of parton shower and underlying event variations on the VH acceptance in each analysis region and on the p_T^V and m_{bb} shapes, including their nuisance parameter name.

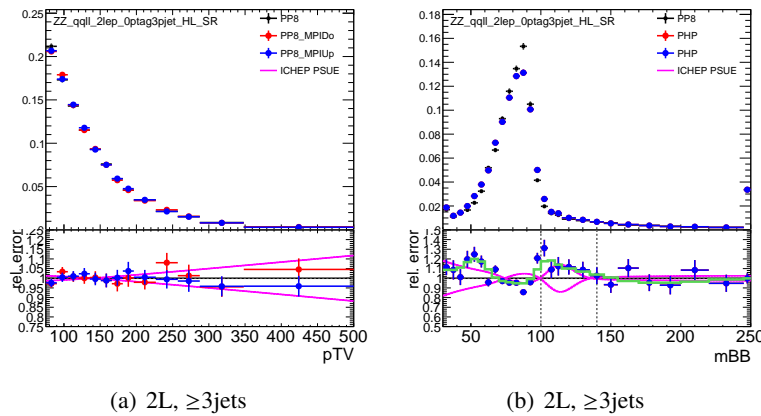


Figure 26: Example shape variations from PS and UE uncertainties in the p_T^V (left) and m_{bb} (right) variables, shown for the 2-lepton ≥ 3 -jet selection. Plots for all regions and variations are given in Appendix E.

procedure produce 3 independent nuisance parameters; one governing the overall acceptance, another one controlling the relative migration between 2 and 3 jets and a last one assessing additional uncertainty due to the veto of events with 4 jets. The latter uncertainty is not present in the 2-lepton channel due to the more inclusive jet selection.

For the shape uncertainty in both the p_T^V and m_{bb} distributions arising from the scale variations, the effect of changing the factorisation scale is found to be subleading compared with the change from the renormalisation scale, and therefore only the effects of coherent variations are considered.

For the p_T^V distribution these coherent variations are compatible with the MC statistical uncertainties of the nominal samples. The shapes derived for ICHEP are found to remain appropriate, except for the case of the 0-lepton, 3-jet channel where the ICHEP uncertainty was overestimated and is replaced by the 2-jet uncertainty.

For the m_{bb} distribution no strong effects are visible in the 2-jet channel, while a common effect is observed in the high m_{bb} tail in the ≥ 3 -jet regions. The effect is not completely captured in all regions by the ICHEP shape uncertainties, however the effect is significantly smaller than the difference between POWHEG and SHERPA.

1180 SHERPA versus POWHEG

1181 The difference between POWHEG and SHERPA is considered only as a shape uncertainty, and not in the list of
1182 acceptance uncertainties, given the very different strategy in the modelling of extra jet radiation between

NP name	0L: $ZZ \rightarrow v\bar{v} b\bar{b}$		1L: $WZ \rightarrow \ell v b\bar{b}$		2L: $ZZ \rightarrow \ell^+ \ell^- b\bar{b}$	
	2j	3j	2j	3j	2j	$\geq 3j$
SysVZ_QCDscale_J2	10.3%	–	12.7%	–	11.9%	–
SysVZ_QCDscale_J3	-15.2%	+17.4%	-17.7%	+21.2%	-16.4%	+10.1%
SysVZ_QCDscale_JVeto	–	+18.2%	–	+19.0%	–	–
SysVZ_QCDscale_VPT	shape+norm		shape only		shape+norm	
SysVZ_QCDscale_MBB				shape only		

Table 33: Summary of the systematic uncertainties on the VH acceptance in each analysis region and on the p_T^V and $m_{b\bar{b}}$ shapes originating from altering the QCD scale, including their nuisance parameter name.

1183 the two samples. For the p_T^V shape no major differences are found compared with the MC statistical
 1184 uncertainties. However, for the m_{bb} distribution, the shape variation is described by a tanh function in the
 1185 2-jet region, and by a 3rd-degree polynomial with range capped at 250 GeV for the 3-jet region; examples
 1186 are given in Figure 27 and the full set of plots is in Appendix E.

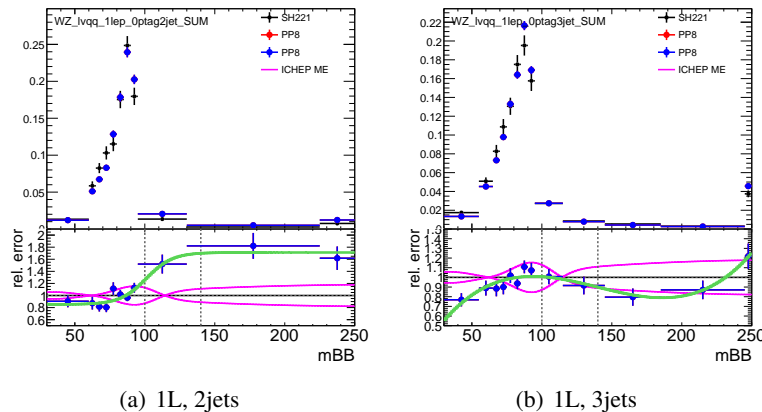


Figure 27: Example shape variations from SHERPA versus Powheg in the m_{bb} variable, shown for the 1-lepton 2-jet (left) and (\geq)3-jet (right) selections, approximated by tanh and capped 3rd-degree polynomial functions respectively. Plots for all regions are given in Appendix E.

PDF and α_s uncertainties Studies using the signal samples have shown the effect of PDF and α_s choice to be small, and so these uncertainties are not considered for now for the diboson backgrounds.

Region extrapolation Finally residual effect of the systematics have been considered for the normalisation of the same process across analysis regions. The effect mainly refer to:

- 0-lepton versus 1-lepton events (for $q\bar{q}l\nu$ events). SysWZNorm_L0 prior unc. = 11%
 - 0-lepton versus 2-lepton events (for $q\bar{q}ll$ and $q\bar{q}\nu\bar{\nu}$ events). SysZZNorm_L0 prior unc. = 6%

1193 The uncertainties have been computed taking into account the difference in relative acceptance between
 1194 the pair of analysis regions for all the systematic effects described previously. A detailed breakdown
 1195 of the numbers can be found in Appendix ?? In case of the ZZ sample the residual effect of the scale
 1196 uncertainties has not been considered since the 0-lepton channel already includes the additional Stewart-
 1197 Tackman uncertainty due to the jet veto. The current uncertainty mainly covers the effect of different Vpt
 1198 range among the 2 channels.

1199 From the technical point of view, the nuisance parameters have been implemented as additional normal-
1200 isation uncertainties on the 0L channel which represent the channel where the process is subdominant.

1201 (It is therefore expected that the uncertainties will appear in the highest position of the ranking when
1202 performing the fit in the 0-lepton channel alone.

1203 3.5. Multi Jet Production

1204 Multijet backgrounds arise purely from QCD production of jets, subsequently faking leptons or E_T^{miss} , or
 1205 decaying to non-prompt leptons. Due to the difficulty to model this background using MC simulation,
 1206 data driven approaches are used to estimate this background in the 1-lepton channel. In the 0- and 2-lepton
 1207 channels, where the analysis selection rejects most of the multijet contamination, MC and data-driven
 1208 approaches are used to verify that the residual level of contamination is negligible, as outlined in the
 1209 main analysis note. This section describes the estimation of the multijet in the 1-lepton channel and its
 1210 associated uncertainties.

1211 For the 1-lepton channel two methods have been proposed, the *fake factor* method and the *template*
 1212 method. Presently the *template* method is employed as default.

1213 3.5.1. 1-lepton channel

1214 In the 1-lepton channel, the contribution of the multijet background is greatly reduced by only considering
 1215 the high p_T^V region. However, the multijet background still contributes a significant fraction of the
 1216 background events in this region, and a robust procedure is necessary to estimate the contributions of
 1217 this background both in the electron and muon W decay modes. In both modes, the template method is
 1218 employed.

1219 Template Method

1220

1221 In order to reduce the multi-jet contribution of fake leptons from photons and light jets and from non-
 1222 prompt heavy flavour decays to a minimum, an AND of two isolation criteria is adopted in the 1-lepton
 1223 channel. The loose isolation (`IsLooseTrackIso`) is used for the loose lepton definition that separates
 1224 events between the 0-, 1- and 2-lepton channels, and thus also for the object overlap removal. It has a
 1225 flat signal efficiency versus lepton p_T of around 99%. An additional tighter isolation is then applied in
 1226 addition for the tight lepton definition (exclusively for the signal lepton in the 1-lepton channel), applying
 1227 a tight absolute cut on either calorimeter isolation (for the electro channel) or on the track isolation (for
 1228 the muon channel). This additional cut corresponds to a signal efficiency, w.r.t. the already applied loose
 1229 isolation, of around 95%, as evaluated on signal Monte Carlo after applying all analysis specific selection
 1230 criteria. According to the Sherpa multi b -jet ($bb + X$) Monte Carlo sample, the additional rejection of
 1231 this tighter isolation is 10 (3) for the electron (muon) channel, where this additional rejection has been
 1232 evaluated for $p_T(V) > 150$ GeV, but removing several of the final analysis selection cuts in order to gain
 1233 statistics. The real multi-jet contamination in the signal region cannot be extracted using simulations, both
 1234 because the simulation is very statistically limited and because the simulation is not expected to reproduce
 1235 fakes correctly.

1236 A template method is therefore employed to estimate the multi-jet contribution in the signal region, using
 1237 data in a multijet enriched control region. The MJ enriched control region is defined using inverted lepton
 1238 isolation cuts. Table 34 summarises both the isolation cuts applied in the signal region and the inverted
 1239 selection used for the multi-jet enhanced control region. The transverse W-candidate mass (m_T^W) is chosen
 1240 as the variable offering the best discrimination between pure strong multi-jet production and electroweak
 1241 induced processes, while not being excessively sensitive to systematics. A multi-jet template for this
 1242 variable is obtained in the inverted isolation region. The contribution from electroweak background

processes in the inverted isolation region is subtracted based on Monte Carlo predictions. Systematic variations of the MC predictions are later applied as a source of systematic uncertainty. A fit to the transverse W -candidate mass distribution is then applied in the signal region to extract simultaneously the normalization factors for both the multi-jet and the electroweak components. Separate templates for the multi-jet contributions are obtained depending on lepton flavor (e/μ) and jet multiplicity (2/3-jet regions); for each of these four signal regions a corresponding multi-jet control region is thus defined. While this procedure is used to determine the normalization of the multi-jet background in the signal regions, the distribution of the discriminating variable used in the signal extraction fit (BDT) or of any other control variable is obtained in the same way as the m_T^W distribution used in the template fit.

The statistics in the multijet enhanced control region is limited: it is expected to be around 9 (2) times the signal region statistics for the electron (muon) channel. To reduce the impact of statistical fluctuations when deriving the template, instead of requiring 2 b -tags as in the signal region, only 1 b -tag is required in the control region. The plots in Figure 28 show the m_T^W distributions for the data and electroweak processes in the inverted isolation e/μ , 2/3-jet regions with requiring exactly 1 b -tag.

	Isolated Region	Inverted Isolation Region
Electron	<code>IsLooseTrackOnlyIso</code> <code>TopoEtCone20<3.5 GeV</code>	<code>IsLooseTrackOnlyIso</code> <code>TopoEtCone20>3.5 GeV</code>
Muon	<code>IsLooseTrackOnlyIso</code> <code>PtCone20<1.25 GeV</code>	<code>IsLooseTrackOnlyIso</code> <code>PtCone20>1.25 GeV</code>

Table 34: Summary of differences in lepton isolation between the isolated and inverted isolation regions used for the template method. In each region the AND of the two isolation criteria listed in the table is used.

The main assumption of the template method is that the template distribution used in the signal region and extracted in the multi-jet enhanced control region are the same. Since this assumption is not expected to be perfectly valid, this can introduce a bias in the template, and ultimately in the estimated multi-jet contribution in the signal region. The templates derived in the control regions are therefore corrected for such a bias before being used in the signal regions, by applying event-by-event extrapolation factors that depend on lepton pT and η , and, in the electron channel, also on the value of E_T^{miss} . These extrapolation factors are derived in additional control regions where the 2- and 3-jet requirement of the nominal selection is replaced by a 1-jet requirement, and any b -tagging requirement is removed. The extrapolation factors are computed as the ratio between events with an isolated and an isolation-reverted lepton, after removing the EW background contribution based on MC predictions (see details in Appendix H). For cross check, this bias is also evaluated using the high statistic multi b -jet MC samples, listed in Table 35, and is estimated as the ratio of the yield in the isolated region, divided by the yield in the inverted isolation region, as a function of the variable of interest. Only $p_T^W > 150$ GeV and trigger selection cuts are used for this evaluation due to the limited statistic. Example plots for m_T^W are presented in Figure 29, with these scale factors ("bias corrections") then used to correct the template derived in the inverted isolation region to the isolated region. In the muon channel a clear trend is seen, with the tight isolation requirement being more efficient in rejecting the background at high m_T^W , while in the electron case the behaviour is much flatter. The two approaches actually show similar trends for the multijet template correction.

The $t\bar{t}$ and $W+\text{jets}$ processes are dominant in the signal region, and their normalization can have a significant impact on the multijet estimate. Their normalization is therefore extracted simultaneously to the multi-jet estimate itself. While the m_T^W variable provides discrimination mainly between processes

Not reviewed, for internal circulation only

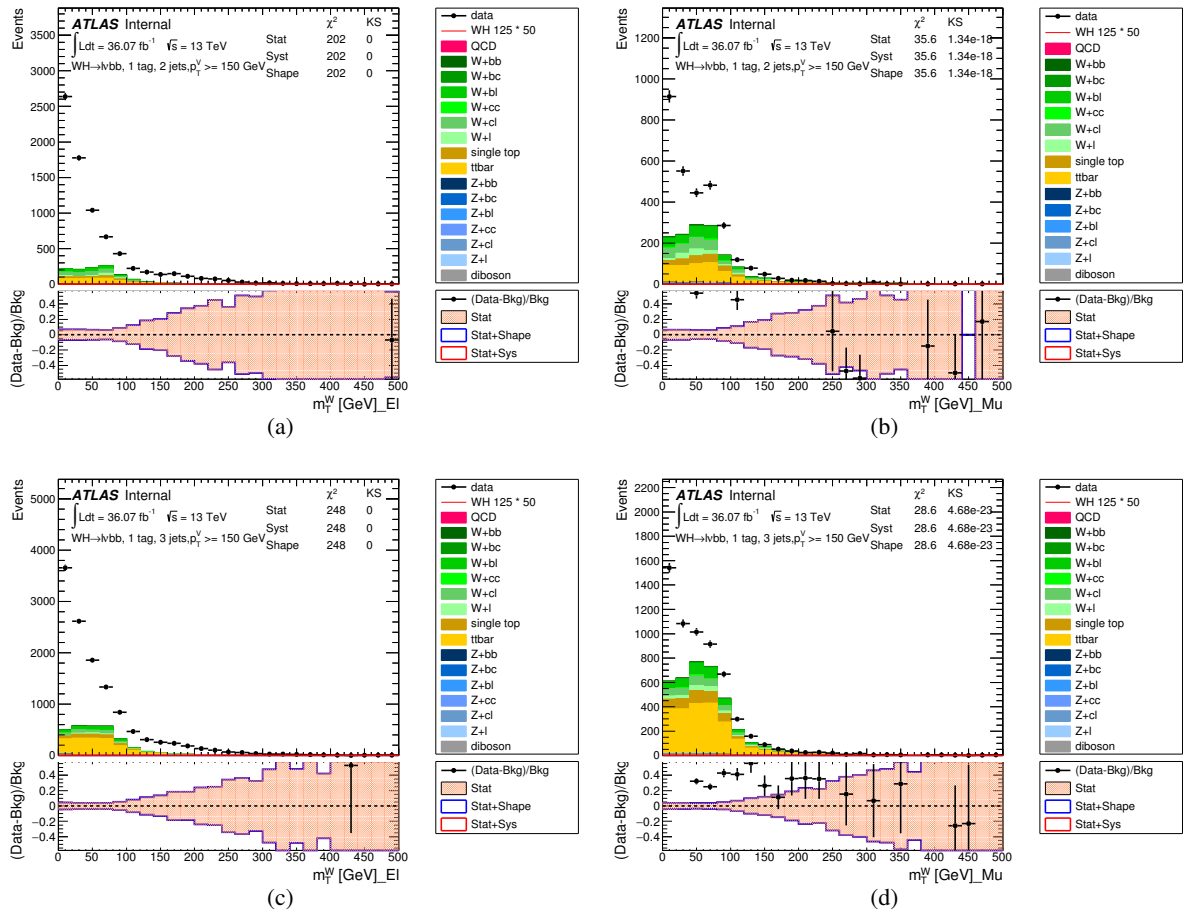
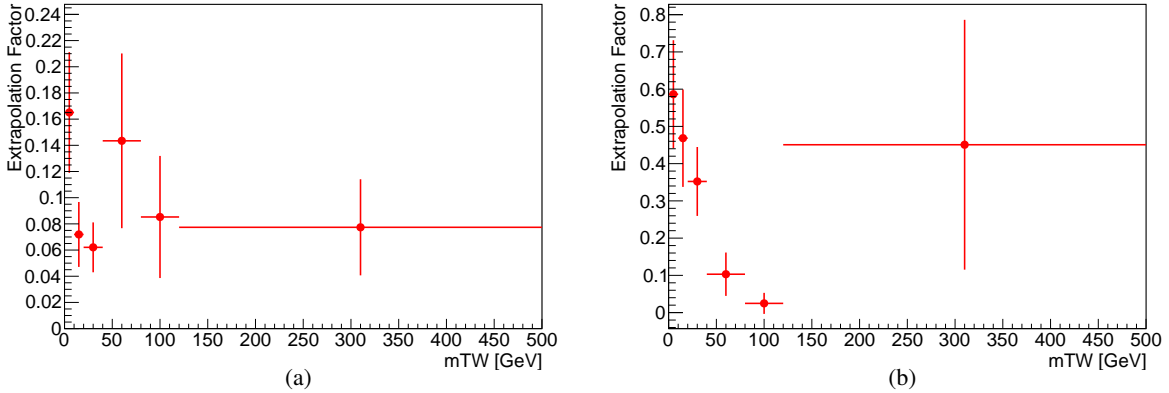


Figure 28: The m_T^W distribution in the inverted isolation 1-lepton $p_T^W > 150$ GeV region, requiring exactly 1 b -tag with 2 signal jets in e channel(a), 2 signal jets in μ channel(b), 3 signal jets in e channel(c), 3 signal jets μ channel(d)

1278 without and with a W boson, the distributions of m_T^W for the $t\bar{t}$ and $W+\text{jets}$ processes are not identical,
1279 since di-leptonic $t\bar{t}$ events induce a tail at high values of m_T^W . In order to avoid a bias onto the multi-jet
1280 estimate, separate normalization factors are extracted for the Top ($t\bar{t} + \text{single top}$) and $W+\text{jet}$ contributions.
1281 However, the m_T^W distribution alone only provides marginal separation between these two background
1282 components, so to determine their respective contribution a simultaneous fit is applied to the signal region
1283 and the $W+\text{HF}$ enhanced region (the same used also in the main Higgs boson signal extraction fit). Since
1284 the relative $W+\text{jet}$ / Top purity is very different in these two regions and is known from simulation, a
1285 simultaneous fit to the two regions allows the extraction of the two separate normalizations with decent
1286 precision. The m_T^W distribution is then used in the fit basically only to disentangle the multi-jet contribution
1287 from both the Top and $W+\text{jets}$ backgrounds. Due to the limited statistics, the m_T^W distribution is exploited
1288 in the signal region, while only the overall yield is used in the $W+\text{HF}$ control region. To increase the
1289 statistical precision in the determination of the Top and $W+\text{jet}$ normalization factors further, the fit is also
1290 applied simultaneously in the electron and muon channel, extracting simultaneously the normalizations
1291 for the electron multi-jet, muon multi-jet, Top and $W+\text{jets}$ components.

1292 Technically, the multi-jet fit is implemented as a template fit to a single region, with distributions/yields
1293 from different regions merged to adjacent intervals/bins of a single final distribution. The overall yield

Generator	DSID	Leading jet p_T range [GeV]	σ [pb]
Sherpa 2.2.1	344715	30-50	283697.214
Sherpa 2.2.1	344716	50-80	67501.441
Sherpa 2.2.1	344717	80-130	13612.655
Sherpa 2.2.1	344718	130-200	1819.401
Sherpa 2.2.1	344719	200- \sqrt{s}	296.265

Table 35: MC Multi b -jet samples used to evaluate extrapolation factors of the MJ template.Figure 29: Inverted isolation to isolated region extrapolation factors as a function of m_T^W for the e channel (a) and μ channel (b).

of the $W+HF$ enhanced region is being represented by an additional bin at the extreme right of the m_T^W distribution. The electron channel is then put on the left in the final fit distribution, while the muon channel is put on the right. The binning of the m_T^W distribution is optimised in such a way to yield a roughly constant MC statistical uncertainty. Separate templates are used for the electron multi-jet, muon multi-jet, Top and $W+jets$ components, and the normalization factor extracted for each contribution is presented in Table 36. Post-fit plots for the distribution exploited in the fit are shown in Figure 30. Apart from the m_T^W distribution which is directly used in the multi-jet fit, Figure 31 to Figure 34 also show some other post-fit distributions for other variables in both electron and muon channels. In these distributions, the normalization is fixed to the result of the multi-jet fit. The multi-jet shapes are derived, analogously to the m_T^W distribution used as template in the fit, from the inverted isolation regions, after subtracting the electroweak backgrounds. The normalization factors extracted in the multi-jet fit for the Top and $W+jets$ processes can be significantly different from unity: the difference from unity is later considered as a source of systematic uncertainty for the electroweak background subtraction procedure in the inverted isolation region.

Region	Top ($t\bar{t}$ + single top)	$W+\text{jets}$
2-tag, 2-jet	1.01	1.39
2-tag, 3-jet	0.98	1.35

Table 36: Summary of normalisation scale factors for Top ($t\bar{t}$ + single top) and $W+\text{jets}$ derived in the isolated lepton region.

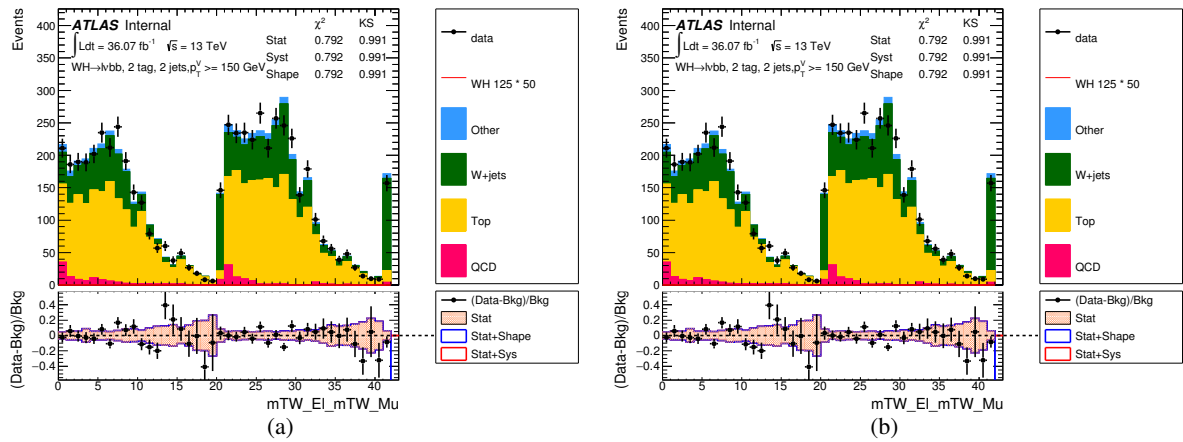


Figure 30: The m_T^W distribution in the isolated 1-lepton $p_T^W > 150$ GeV requiring exactly 2 b -tags with 2 signal jets (a), 3 signal jets (b), after applying Top ($t\bar{t}$ + single top) and $W+\text{jets}$ normalisation factors. Bins 1-21 correspond to the e only channel, bins 22 to 42 correspond to the μ only channel, and bins 21 and 42 represent the $W + hf$ control region.

Not reviewed, for internal circulation only

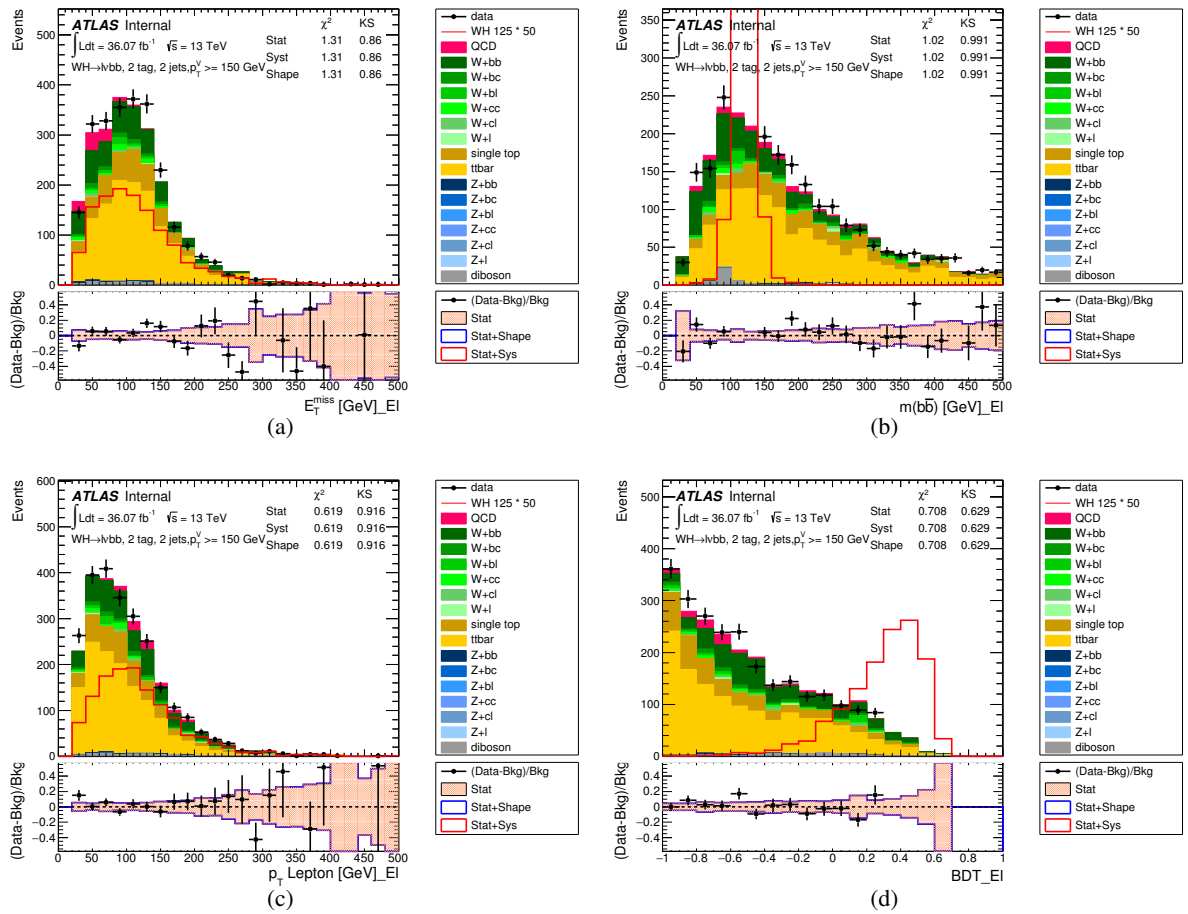


Figure 31: The distributions, for the 2-tag 2-jet category in electron channel $W + hf$ signal region, of (a) E_T^{miss} (b) $m_{b\bar{b}}$ (c) lepton p_T and (d) BDT are shown

Not reviewed, for internal circulation only

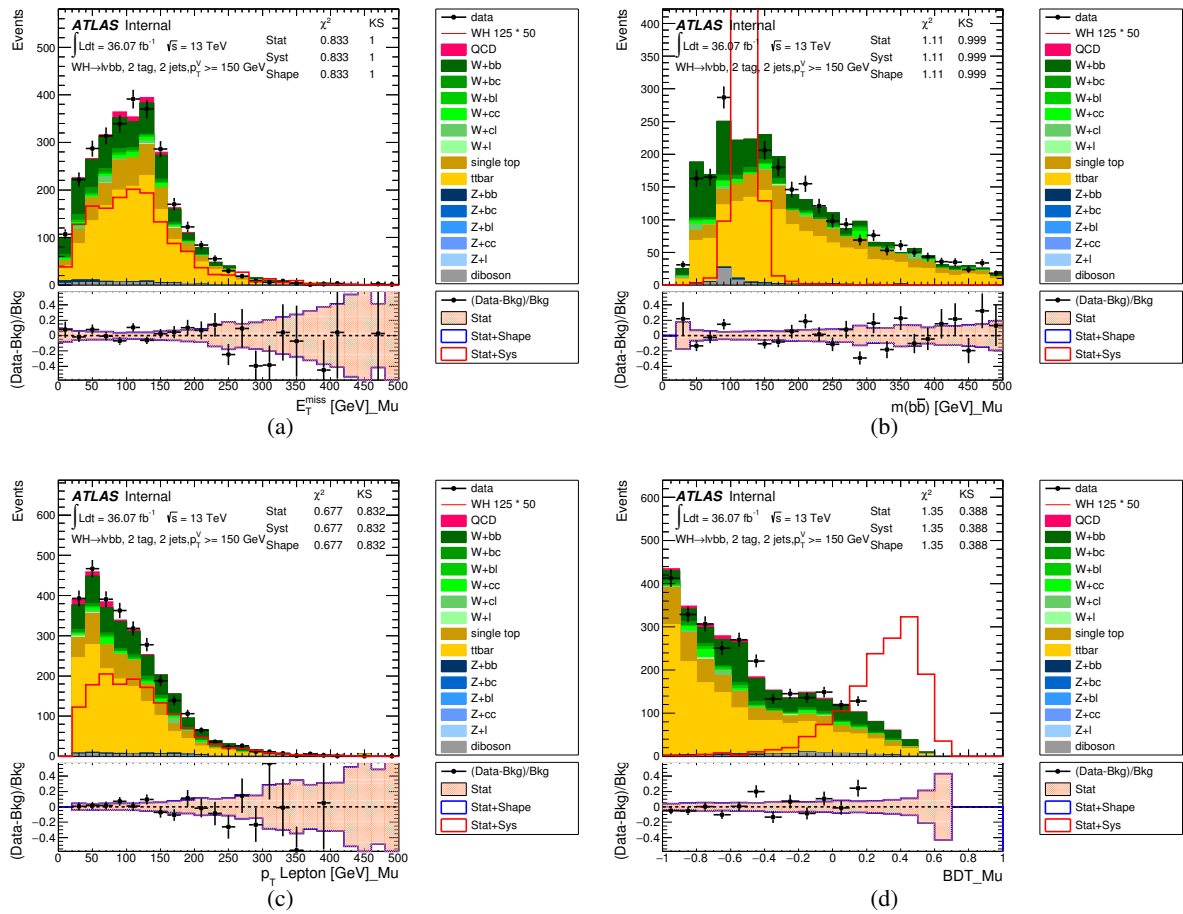


Figure 32: The distributions, for the 2-tag 2-jet category in muon channel $W + hf$ signal region, of (a) E_T^{miss} (b) $m_{b\bar{b}}$ (c) lepton p_T and (d) BDT are shown

Not reviewed, for internal circulation only

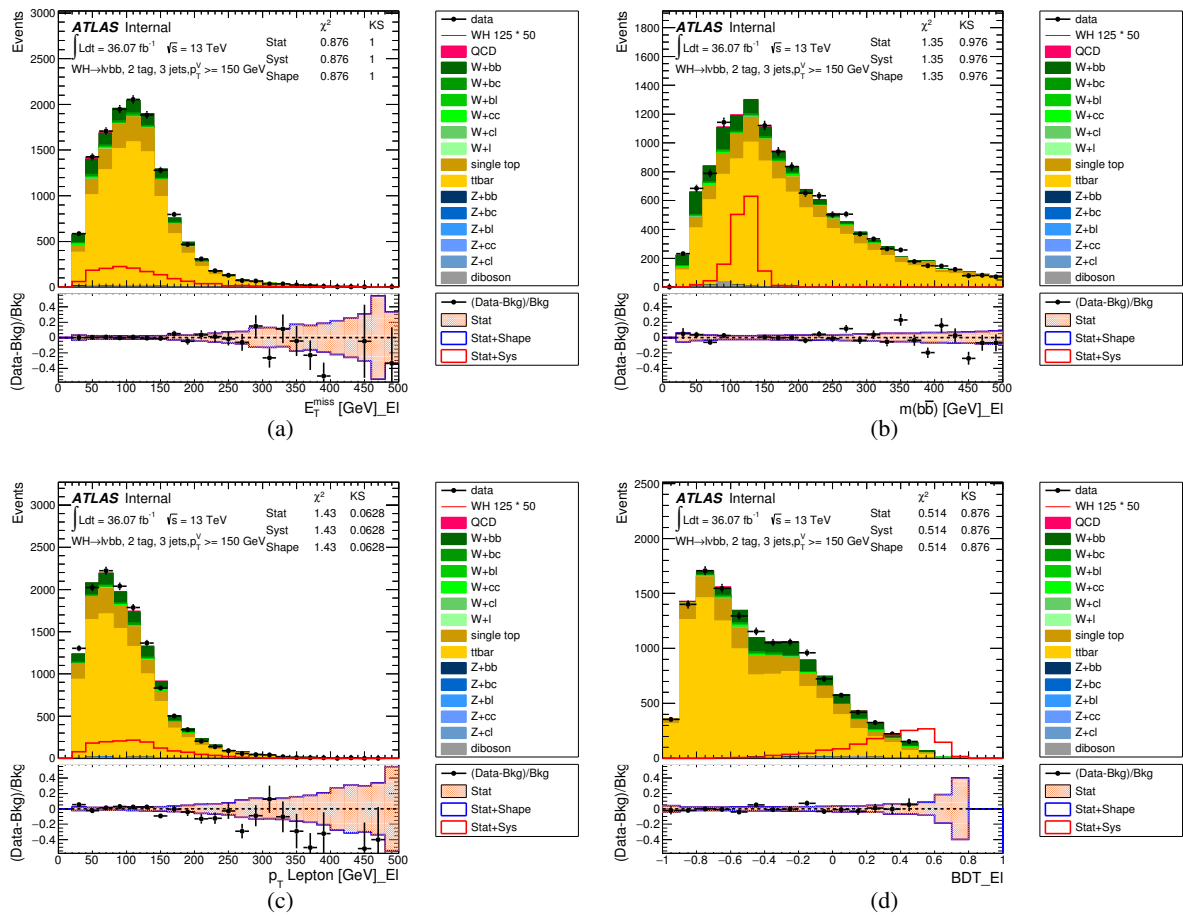


Figure 33: The distributions, for the 2-tag 3-jet category in electron channel $W + hf$ signal region, of (a) E_T^{miss} (b) $m_{b\bar{b}}$ (c) lepton p_T and (d) BDT are shown

Not reviewed, for internal circulation only

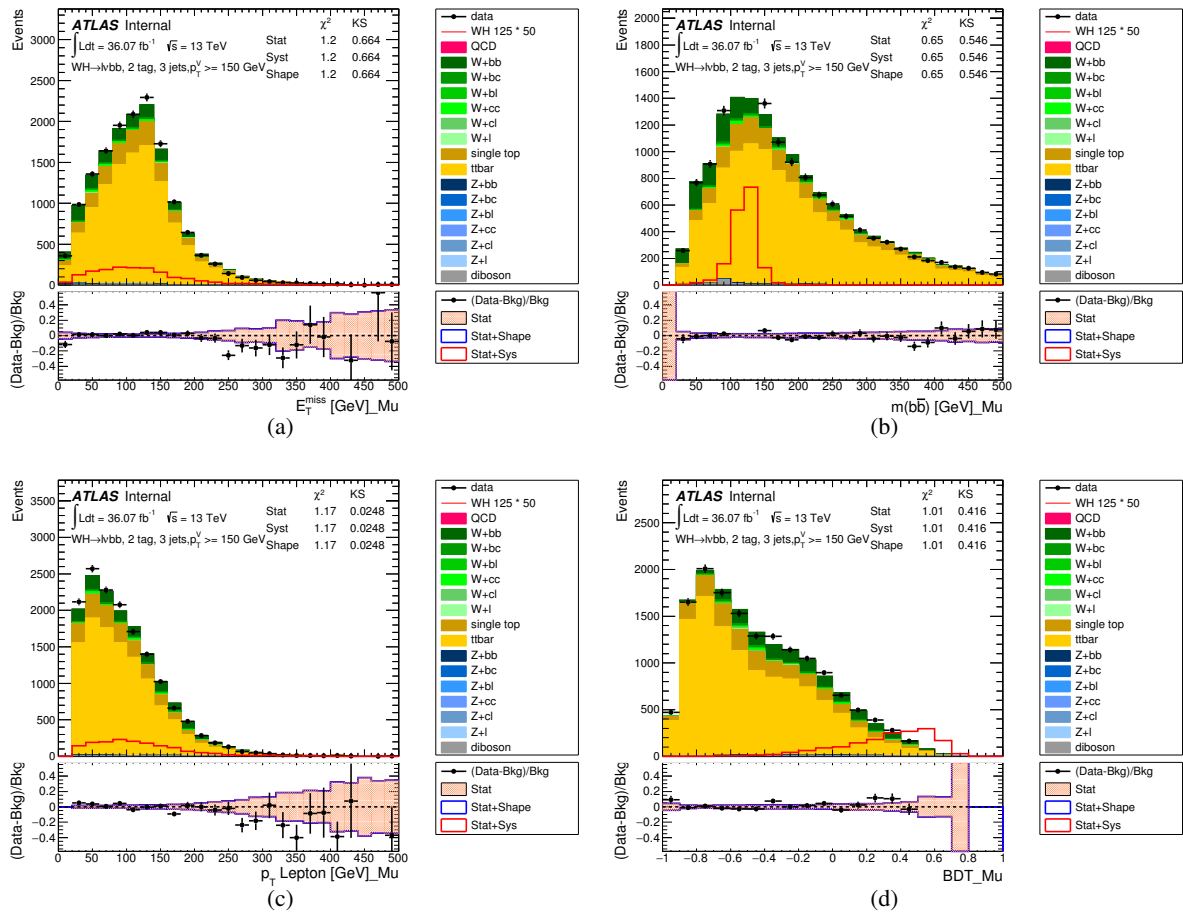


Figure 34: The distributions, for the 2-tag 3-jet category in muon channel $W + hf$ signal region, of (a) E_T^{miss} (b) $m_{b\bar{b}}$ (c) lepton p_T and (d) BDT are shown

1308 In both the electron and muon modes, a number of sources of systematic uncertainty are considered that
 1309 have an impact on the normalization and shape of the BDT distribution used for the multi-jet background
 1310 component in the final signal extraction fit. The systematic uncertainties that impact the shape will be
 1311 described first, since most of these are also considered for the normalization.

1312 **Shape Uncertainties**

1313
 1314 In order to evaluate the shape uncertainty of the MJ background estimate, a number of shape systematic
 1315 uncertainties are considered:

- 1316 • **In the e and μ modes**, the impact of using the 1-tag region to extract the MJ shape is evaluated.
 1317 The shape of the 1-tag MJ template is compared with the 2-tag MJ template, and the difference is
 1318 taken as a systematic uncertainty. This uncertainty is correlated between the 2 and 3 jet regions,
 1319 and decorrelated between e/μ channels.
- 1320 • **In the e and μ modes**, the impact of applying the bias correction is evaluated. The MJ template
 1321 shape is evaluated without applying the bias corrections, and the difference in shape taken as
 1322 a systematic uncertainty. This uncertainty is correlated between the 2 and 3 jet regions, and
 1323 decorrelated between e/μ channels.
- 1324 • **In the e mode**, the impact of the choice of electron trigger on the MJ estimate is evaluated, as this
 1325 may introduce a bias in the inverted isolation region. Instead of using the combination of triggers,
 1326 listed in Section 5.2.1 of Ref [VHobjectsupportnote], simply the lowest p_T trigger is used. This
 1327 corresponds to the trigger selections for each data period listed in Table 37. This uncertainty is
 1328 correlated between the 2 and 3 jet regions. Plots in Figure 35 show the MJ template comparison for
 1329 using the combination of triggers and simply lowest p_T triggers in the inverted isolation region.
- 1330 • **In the e and μ modes**, an evaluation of the uncertainty introduced by the extrapolation from the
 1331 full inverted isolation region to the signal region is considered. Instead, a reduced inverted-isolation
 1332 region is defined, with additional isolation cuts applied to the inverted isolation region defined in
 1333 Table 34. In the e mode, this is defined with additionally requiring $\text{topoetcone20} < 11 \text{ GeV}$, and
 1334 in the μ mode, $\text{ptcone20} < 2.25 \text{ GeV}$. The additional cuts are optimized for keeping about half of
 1335 data events in the full inverted regions for both e and μ modes, keeping the fraction that is closer
 1336 to the signal region and thus is subject to a smaller extrapolation uncertainty. This uncertainty is
 1337 correlated between the 2 and 3 jet regions, and decorrelated between e/μ channels.
- 1338 • **In the e and μ modes**, the impact of using the normalization factors extracted in the multi-jet fit for
 1339 the Top and W+jets processes in the electroweak background subtraction procedure in the inverted
 1340 isolation region. The MJ template shape is evaluated without applying the normalization factors,
 1341 and the difference in shape taken as a systematic uncertainty. This uncertainty is correlated between
 1342 the 2 and 3 jet regions, and decorrelated between e/μ channels.

Dataset	Single e Trigger
2015	e24_1hmedium
2016	e26_1htight_nod0_ivarloose

Table 37: Reduced triggers used to evaluate possible trigger bias in inverted electron isolation region.

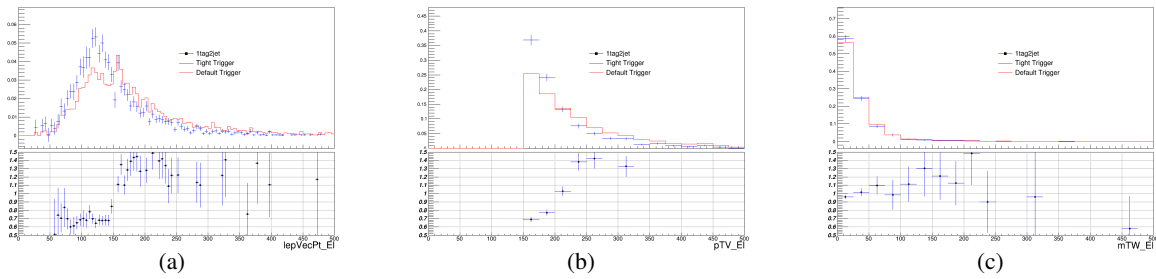


Figure 35: Inverted isolation 2 jet region MJ template comparison for using the combination of triggers (in red) and simply lowest p_{T} triggers (in blue) in the lepton p_{T} (a) p_{T}^{W} (b) and m_{T}^{W} (c) distributions with requiring exactly 1 b-tag.

1343 These systematic uncertainties are implemented as shape only systematic uncertainties by normalising
 1344 the variation to the nominal MJ yield. Plots in Figure 36 to Figure 37 show the shape comparison for
 1345 the nominal BDT and the main shape systematics variations in the 2jet 2tag region for both electron and
 1346 muon channels.

1347 Normalisation Uncertainty

1348

1349 The sources of systematic uncertainty that have an impact on the BDT shape are also considered to derive
 1350 an uncertainty on the estimated multi-jet normalization. The impact on the multi-jet normalization is
 1351 indirectly driven by changes to the m_{T}^{W} template distributions, and to the relative yield in the signal
 1352 and $W+\text{HF}$ control regions. The individual contributions to the normalization uncertainty are added in
 1353 quadrature to give the overall normalization uncertainty, separately in the 2 and 3 jet regions, and for the
 1354 electron and muon modes. In addition to the sources considered for the shape uncertainties, a few more
 1355 are considered exclusively for the normalization uncertainty:

- 1356 • The impact of applying $t\bar{t} m_{bb}$ and p_{T}^{V} shape systematics in the isolation region. The m_{bb} uncertainty
 1357 for example changes the relative contribution of $t\bar{t}$ background in the $W+\text{HF}$ and signal region, and
 1358 can thus vary the fitted normalizations factor for the Top and $W+\text{jets}$, having an indirect impact on
 1359 the multijet estimate as well.
- 1360 • Including the $E_{\text{T}}^{\text{miss}} < 30 \text{ GeV}$ region in the template fit (e mode only), which induces a significant
 1361 change to the m_{T}^{W} distribution both for the multi-jet component derived from the inverted isolation
 1362 region in data and for the electroweak background components estimated using simulations.
- 1363 • Using the $E_{\text{T}}^{\text{miss}}$ distribution instead of m_{T}^{W} in the template fit

1364 The combination of these uncertainties gives rise to the normalization scale factor uncertainties presented
 1365 in Table 38. The corresponding fractions of the multi-jet contribution compared to the total background
 1366 and their uncertainties are presented in Table 39. Systematic uncertainties are completely dominant with
 1367 respect to the statistic only component.

Not reviewed, for internal circulation only

Region	MJ Scaling Factor
2-tag, 2-jet, e	$1.91^{+1.18}_{-1.13} \times 10^{-2}$
2-tag, 2-jet, μ	$5.62^{+4.35}_{-5.62} \times 10^{-2}$
2-tag, 3-jet, e	$0.87^{+1.70}_{-0.87} \times 10^{-2}$
2-tag, 3-jet, μ	$2.60^{+13.61}_{-2.60} \times 10^{-2}$

Table 38: Summary of multi-jet normalisation scale factors, along with their associated uncertainty.

Region	MJ Fractions (%)	MJ norm. uncertainty
2-tag, 2-jet, e	$4.53^{+2.68}_{-2.79}$	-62% / +60%
2-tag, 2-jet, μ	$3.16^{+2.45}_{-3.16}$	-100% / +76%
2-tag, 3-jet, e	$0.56^{+1.09}_{-0.56}$	-100% / +194%
2-tag, 3-jet, μ	$0.38^{+1.99}_{-0.38}$	-100% / +520%

Table 39: Summary of MJ fractions, along with their associated uncertainty in the 2-jet and 3-jet 1-lepton regions (WCR and SR are combined) separate

Not reviewed, for internal circulation only

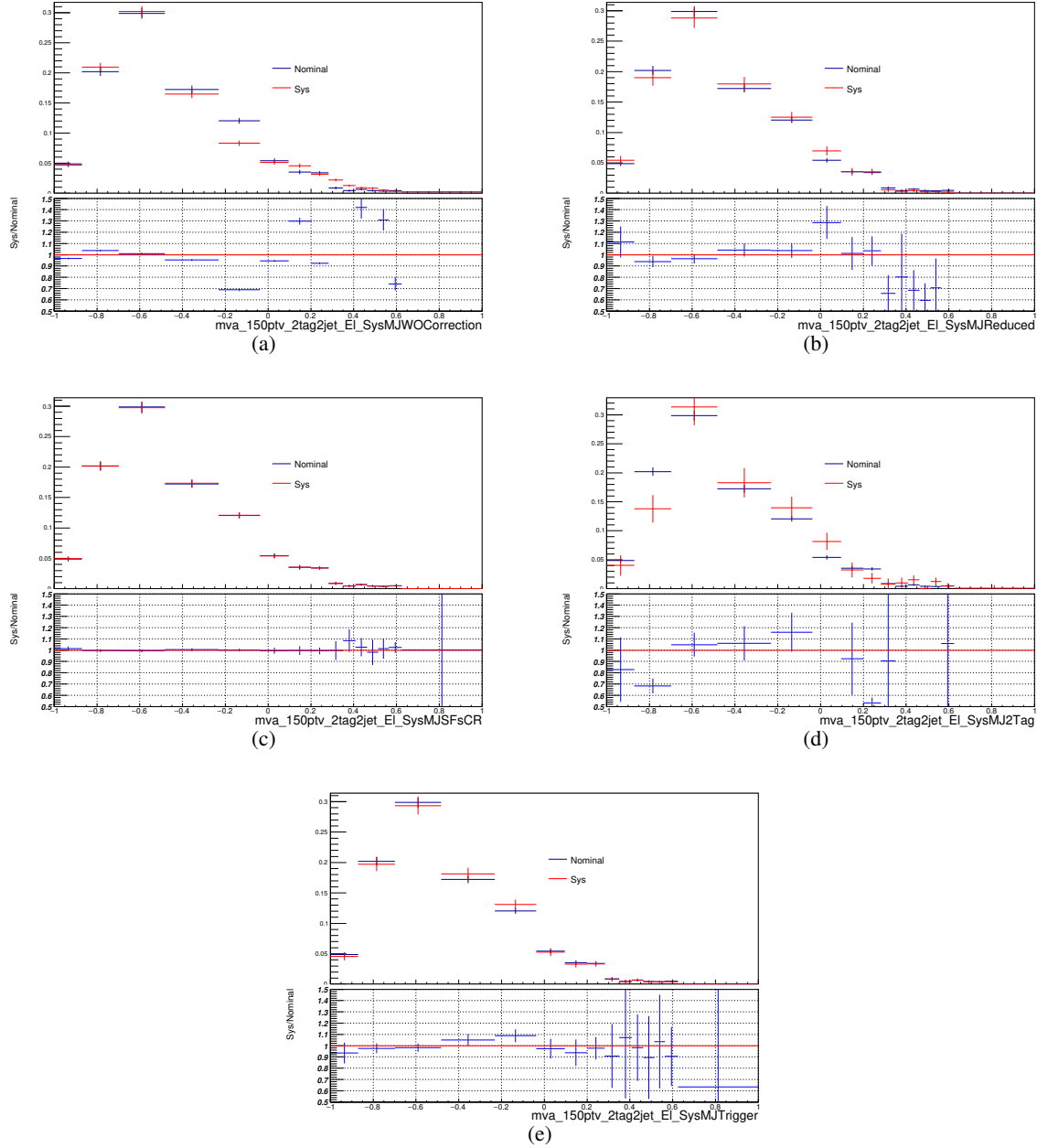


Figure 36: The MJ BDT shape comparison for the nominal (in blue) and some main shape variations (in red) in the electron channel, for the impact of without applying the bias corrections (a), the impact of using the reduced inverted isolation region (b), the impact of using the Top and W+jets normalization factors in the inverted isolation region (c), the impact of using 2-tag MJ template (d), and the impact of using the lowest p_T trigger (e).

Not reviewed, for internal circulation only

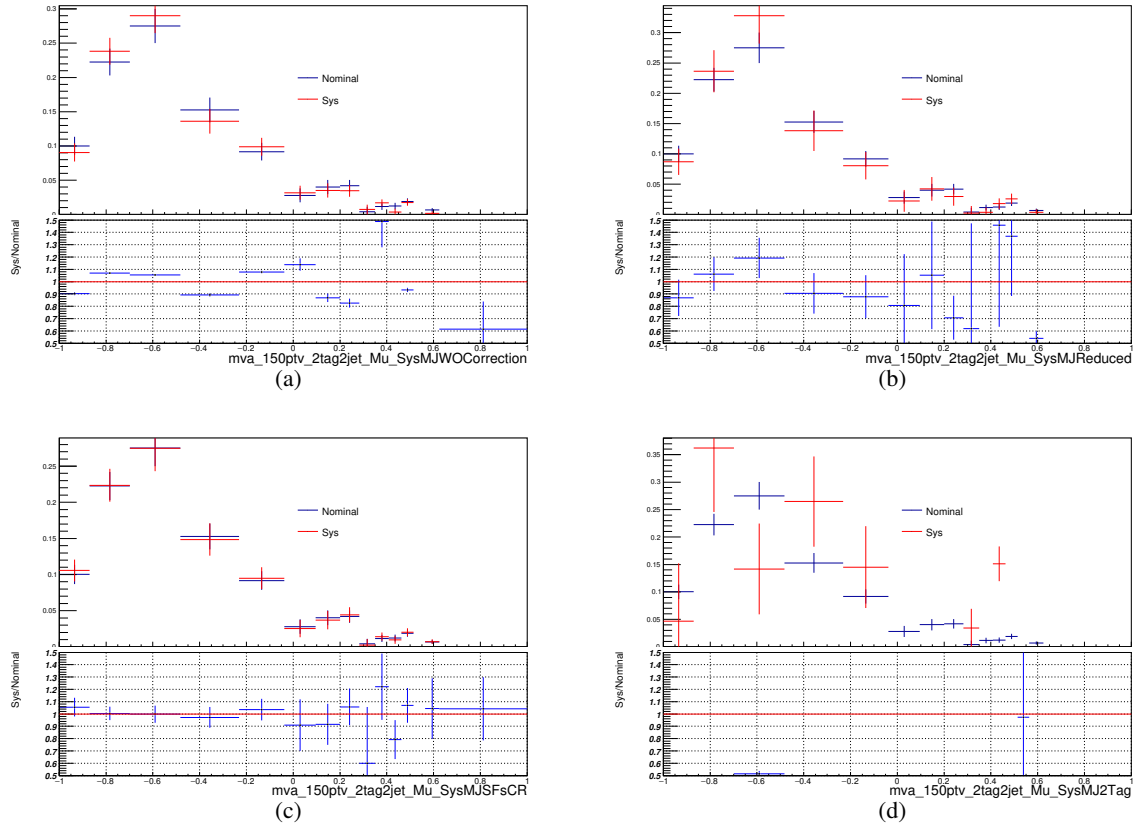


Figure 37: The MJ BDT shape comparison for the nominal (in blue) and some main shape variations (in red) in the muon channel, for the impact of without applying the bias corrections (a), the impact of using the reduced inverted isolation region (b), the impact of using the Top and W+jets normalization factors in the inverted isolation region (c), and the impact of using 2-tag MJ template (d).

1368 Appendix

1369 A. Particle-Level Analysis Definition

1370 In order to study certain variations of Monte Carlo samples that have been produced only on truth level
 1371 or to increase statistics by eliminating reconstruction efficiencies and similar effects certain studies on
 1372 modelling uncertainties have been carried out with a particle-level analysis selection implemented in
 1373 Rivet. These particle level analyses are reproducing the analysis cuts as closely as possible. The truth
 1374 level studies were performed for assessing the $V+\text{jets}$, single top and $t\bar{t}$ modelling uncertainties in the
 1375 $V(H \rightarrow b\bar{b})$ analysis.

1376 Electrons and muons with $p_T > 7$ GeV and within $|\eta| < 2.47$ (for electrons) or $|\eta| < 2.7$ (for muons) are
 1377 considered in this study if the p_T sum of all charged particles (excluding the lepton candidate) within a
 1378 cone of $\Delta R = 0.2$ around the lepton is less than 10 % of the lepton p_T . These are referred to as ‘loose’
 1379 selection criteria. Leptons passing ‘medium’ selection criteria are required to have $p_T > 25$ GeV in
 1380 addition to passing the loose selection. For leptons passing ‘tight’ selection criteria the isolation cut is
 1381 reduced to 4 % in addition to passing the medium selection.

1382 Where jets are used, they are reconstructed using the anti- k_T clustering algorithm with a jet-radius
 1383 parameter of $R = 0.4$. The jet transverse momentum is required to be greater than 20 GeV for central jets
 1384 ($|\eta| < 2.5$) and greater than 30 GeV for forward jets ($2.5 < |\eta| < 5$). Jets with $|\eta| > 5$ are ignored. An
 1385 overlap removal procedure is applied between selected jets and leptons. A jet is rejected if an electron
 1386 passing the loose identification criteria can be matched to it in η - ϕ space ($\Delta R = 0.4$). Similarly a muon-jet
 1387 overlap removal procedure is applied, provided that at most three charged particle tracks are pointing
 1388 to the primary vertex associated with an overlapping muon candidate. Selected central jets are labelled
 1389 according to their flavour with the following procedure:

- 1390 1. if a B -hadron is found within a cone of $\Delta R = 0.3$ centered along the jet axis (considering all particles
 1391 that belong to the jet constituents and their ancestors in the MC truth record) the jet is b -labelled
- 1392 2. if a jet is not b -labelled, and a C -hadron is found within a cone of $\Delta R = 0.3$ centered along the jet
 1393 axis the jet is c -labelled
- 1394 3. if a jet is not b -labelled neither c -labelled, it is l -labelled

1395 The missing transverse energy is reconstructed by taking the transverse momentum of the negative sum of
 1396 the quadrimomenta of all the visible particles, and the missing transverse momentum is defined consistently
 1397 summing over all the charged particles.

1398 A.1. Standard Model VH Analysis

1399 For the $V(H \rightarrow b\bar{b})$ analysis the available $V+\text{jets}$ samples and variations as well as the $t\bar{t}$ samples have been
 1400 investigated with a Rivet based truth level analysis. The studies use the object definitions and selections as
 1401 described above. In addition, it implements three event selections: the 0, 1 and 2-lepton channel selections.
 1402 All selections require at least 2 central jets. To reconstruct the Higgs candidate a pair of signal jets (j_1, j_2)
 1403 is selected by first ordering all central jets according to their flavor — with a priority on b - than c - and last l -
 1404 jets — and then reordering the first two jets according to their transverse momentum. This ordering scheme

1405 also determines the flavour-label of the event: bb , bc , bl , cc , cl or l (if no b or c -jets are found in the event).

1406

1407 The 0-lepton particle-level selection is defined as follow:

- 1408 • exactly 0 leptons passing the ‘loose’ selection
- 1409 • $E_T^{miss} > 150$ GeV
- 1410 • $\Delta\Phi(E_T^{miss}, p_T^{miss}) < \pi/2$
- 1411 • $\min[\Delta\Phi(E_T^{miss}, jets)] < 20^\circ$ (using the first 3 leading jets)
- 1412 • $\sum p_T(jets) > 120(150)$ GeV for 2(> 2)-jet events (the sum is over the first 2 leading central jets
1413 and the first additional jet in p_T)
- 1414 • $p_T(j_1) > 45$ GeV
- 1415 • $\Delta\Phi(j_1, j_2) < 140^\circ$
- 1416 • $\Delta\Phi((E_T^{miss}, j_1 + j_2) < 120^\circ$

1417 The 1-lepton particle-level selection is defined as follow:

- 1418 • exactly 1 lepton passing the ‘tight’ selection
- 1419 • $p_T^W > 150$ GeV
- 1420 • $p_T(j_1) > 45$ GeV

1421 The 2-lepton particle-level selection is defined as follow:

- 1422 • exactly 2 same-flavour (in case of muons also opposite charge) leptons passing the ‘loose’ selection,
1423 of which at least 1 passing the ‘medium’ selection;
- 1424 • $71 \text{ GeV} < m_{ll} < 121 \text{ GeV}$
- 1425 • $p_T(j_1) > 45$ GeV

1426 The 2-lepton channel also features a control region to constrain the top-quark background which is also
1427 implemented in the particle-level analysis. The selection is similar to the 2-lepton selection but requires
1428 the leptons to be a muon and an electron and has a relaxed m_{ll} cut of $m_{ll} > 40$ GeV.

1429 With these selections in place the events in the particle level analysis are categorised according to the
1430 lepton channels, the flavour-label of the event, the number of jets in the event and the transverse momentum
1431 of the vector boson ($p_T^V < 150$ GeV or $p_T^V > 150$ GeV). The described selections and categorisations are
1432 very close to the analysis phase phase and allow to study modelling uncertainties.

Not reviewed, for internal circulation only

1433 B. Additional material for SM VH modelling systematics

1434 This appendix describes detailed information on the modelling uncertainties for the SM VH signal
 1435 described in Section 2.

1436

B.1. PS/UE

1437 Detailed breakdown of the acceptance uncertainties due to PS/UE effects is reported in 40. These are
 1438 percentage uncertainties for each variation with respect to the nominal sample. Also shown are the
 1439 percentage uncertainties from the comparison of the Powheg+Herwig 7 sample to the nominal.

Tune variation	0L: $ZH \rightarrow v\bar{v}bb$			1L: $WH \rightarrow \ell vbb$			2L: $ZH \rightarrow \ell^+ \ell^- bb$		
	2j	3j	3/2j	2j	3j	3/2j	2j	$\geq 3j$	$\geq 3/2j$
Var 1	$\pm 1.97\%$	$\pm 2.43\%$	$\pm 4.48\%$	$\pm 2.04\%$	$\pm 2.73\%$	$\pm 1.72\%$	$\pm 1.38\%$	$\pm 2.26\%$	$\pm 3.31\%$
Var 2	$\pm 0.84\%$	$\pm 1.42\%$	$\pm 2.04\%$	$\pm 0.42\%$	$\pm 3.82\%$	$\pm 3.50\%$	$\pm 2.10\%$	$\pm 2.11\%$	$\pm 0.18\%$
Var 3a	$\pm 0.47\%$	$\pm 0.98\%$	$\pm 0.94\%$	$\pm 1.1\%$	$\pm 0.43\%$	$\pm 1.52\%$	$\pm 0.55\%$	$\pm 2.24\%$	$\pm 1.70\%$
Var 3b	$\pm 1.16\%$	$\pm 2.84\%$	$\pm 4.04\%$	$\pm 0.9\%$	$\pm 2.70\%$	$\pm 3.31\%$	$\pm 0.39\%$	$\pm 2.90\%$	$\pm 2.85\%$
Var 3c	$\pm 6.94\%$	$\pm 3.65\%$	$\pm 11.40\%$	$\pm 7.02\%$	$\pm 3.91\%$	$\pm 11.76\%$	$\pm 5.80\%$	$\pm 5.99\%$	$\pm 12.51\%$
TotPStune	7.37%	5.50%	13.09%	7.46%	6.69%	12.92%	6.36%	7.67%	13.36%
Herwig 7	$\pm 10.01\%$	$\pm 10.42\%$	$\pm 0.37\%$	$\pm 12.05\%$	$\pm 16.47\%$	$\pm 3.95\%$	$\pm 13.87\%$	$\pm 14.38\%$	$\pm 0.45\%$
TOT PS/UE	$\pm 10.01\%$	$\pm 10.42\%$	$\pm 13.09\%$	$\pm 12.05\%$	$\pm 16.47\%$	$\pm 6.36\%$	$\pm 13.87\%$	$\pm 14.38\%$	$\pm 13.16\%$

Table 40: The maximum acceptance uncertainty of the up/down variation for the A14 tune variations, in each analysis region. The total is the sum in quadrature of each row. Shown in the bottom row is the acceptance uncertainty from comparing the Powheg+Herwig7 samples to the nominal.

1440 Full plots showing the ratios and their fits for m_{bb} and p_T^V are shown in Figures 38 and 39, respectively
 1441 for the PS/UE tunes. The full set of plots showing the p_T^V shapes for the parton shower model comparison
 1442 are shown in Figure 40. It can be seen these shapes are consistent with those seen for the A14 tune
 1443 comparisons.

Not reviewed, for internal circulation only

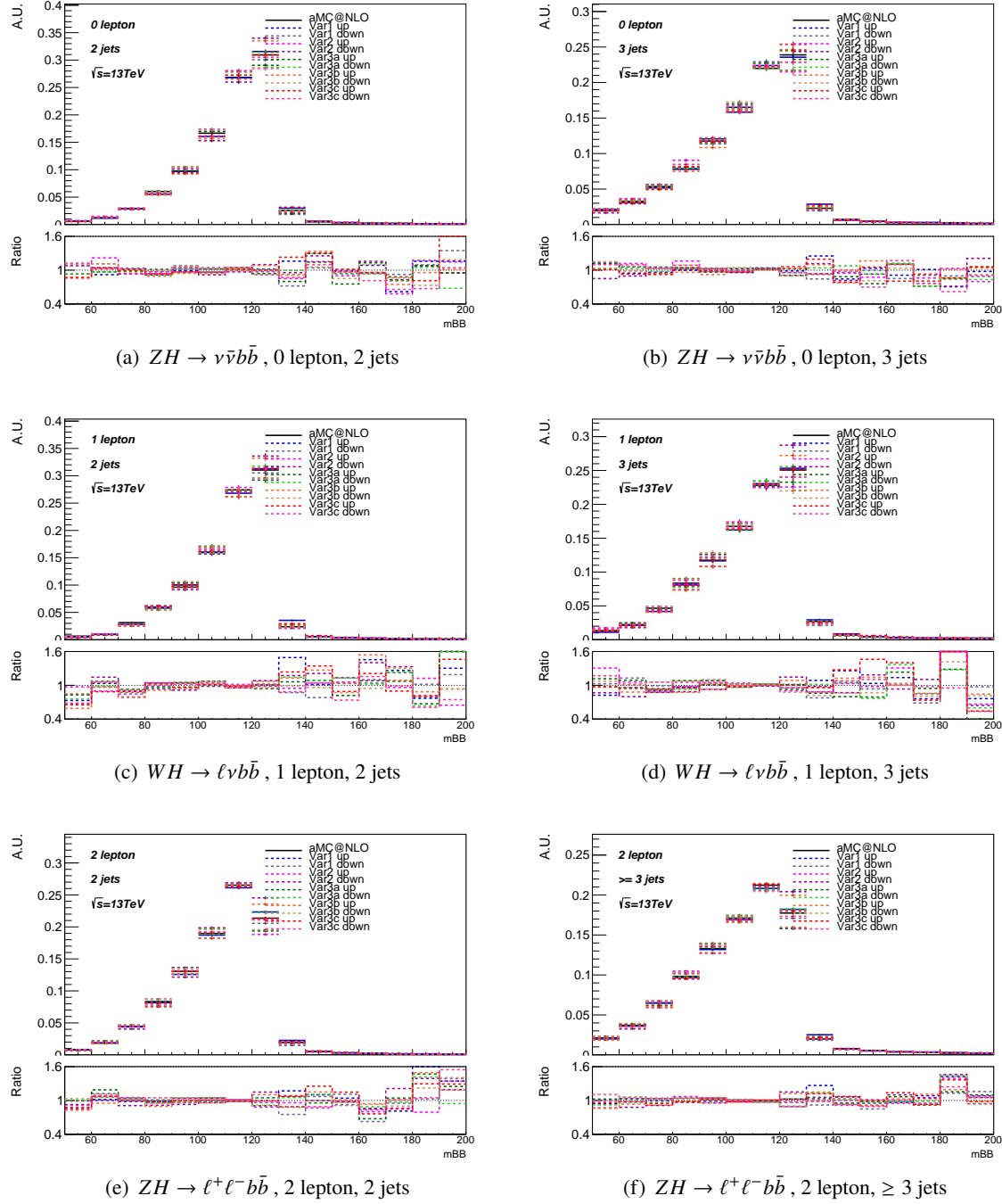


Figure 38: Shape comparison of the $m_{b\bar{b}}$ distributions for each VH process, i.e. lepton channel, and each number of jets category. The ratio between each variation and the nominal is shown in the bottom panel.

Not reviewed, for internal circulation only

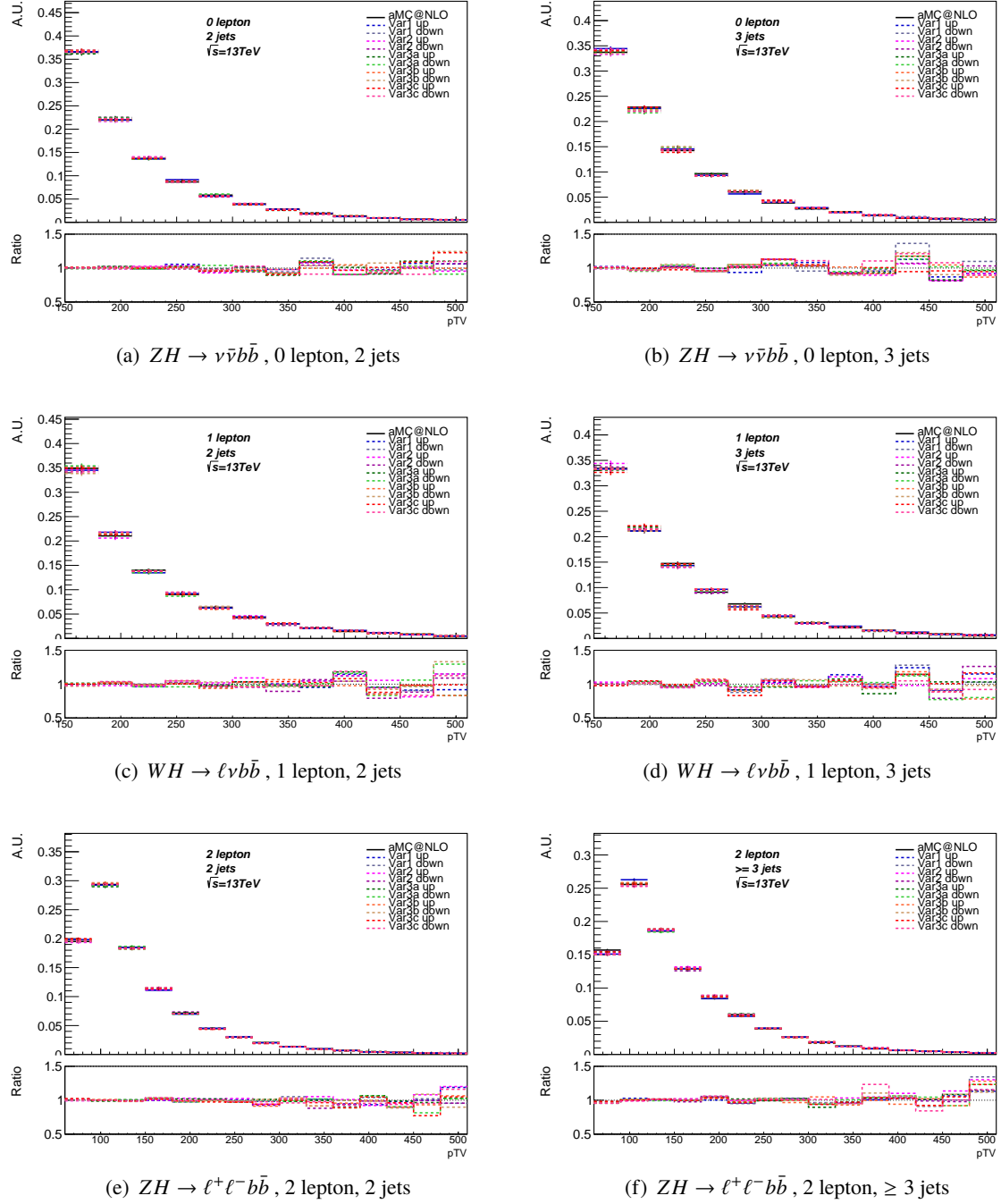


Figure 39: Shape comparison of the p_T^V distributions for each VH process, i.e. lepton channel, and each number of jets category. The ratio between each variation and the nominal is shown in the bottom panel.

Not reviewed, for internal circulation only

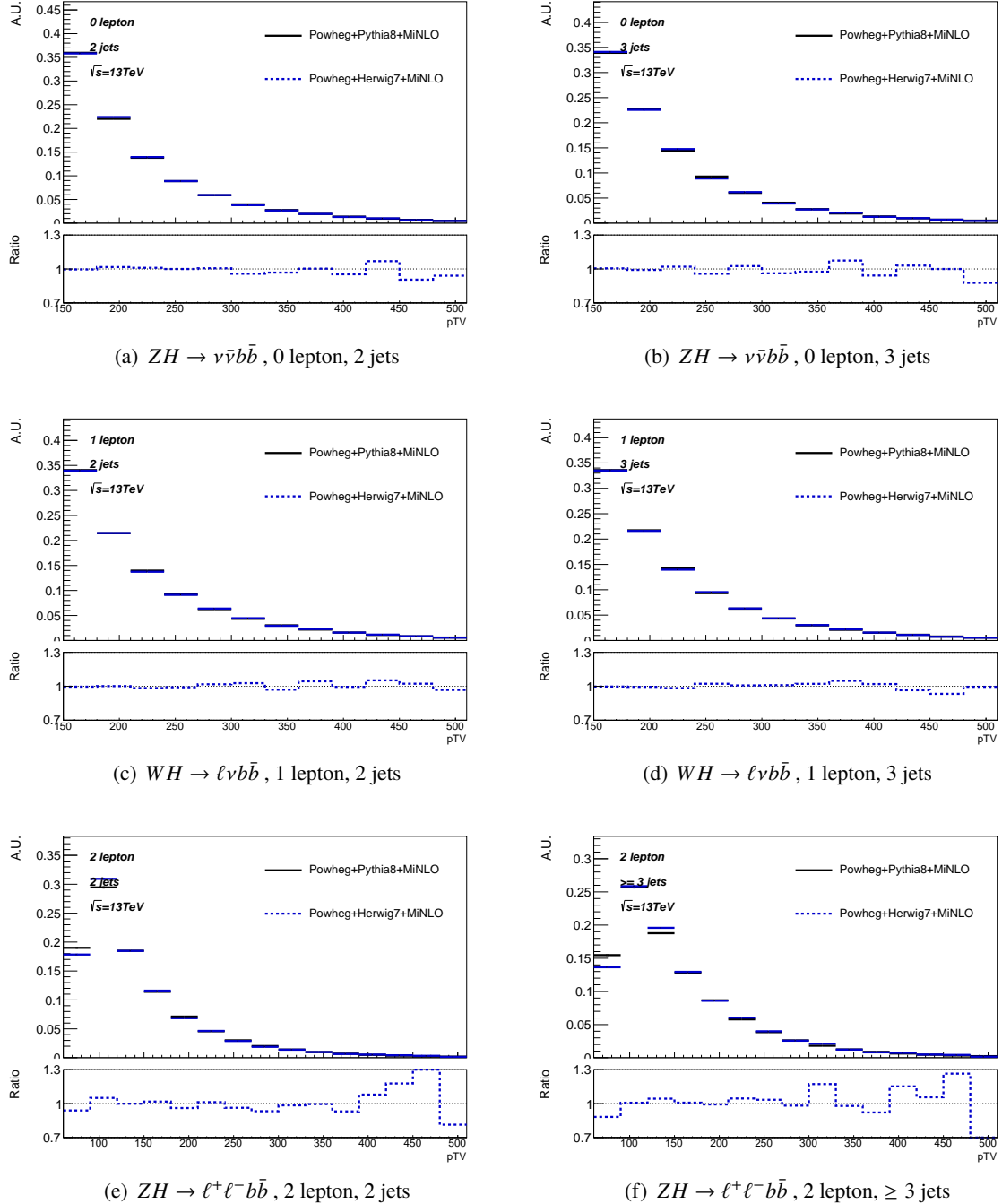


Figure 40: Shape comparison of the p_T^V distributions for each VH process, i.e. lepton channel, and each number of jets category for the parton shower model comparison. The ratio between each variation and the nominal is shown in the bottom panel.

¹⁴⁴⁴ **B.2. Scale uncertainties**

¹⁴⁴⁵ Detailed breakdown of the acceptance uncertainties due to altering the renormalisation and factorisation
¹⁴⁴⁶ scales is reported in [41](#). These are used as ingredients for the Stewart Tackmann procedure.

Scale variation	0L: $ZH \rightarrow v\bar{v}b\bar{b}$			1L: $WH \rightarrow \ell v b\bar{b}$			2L: $ZH \rightarrow \ell^+ \ell^- b\bar{b}$		
	$\geq 2j$	$\geq 3j$	$\geq 4j$	$\geq 2j$	$\geq 3j$	$\geq 4j$	$\geq 2j$	$\geq 3j$	$\geq 4j$
$\mu_R 0.5, \mu_F 0.5$	-1.7 %	-1.3 %	0.8 %	-1.4 %	-0.7 %	1.4 %	-0.7 %	0.3 %	2.9 %
$\mu_R 2.0, \mu_F 2.0$	-1.1 %	-3.0 %	-4.7 %	0.0 %	0.0 %	0.0 %	-0.6 %	-3.2 %	-5.2 %
$\mu_R 0.5, \mu_F 1.0$	-2.5 %	-1.7 %	0.4 %	-2.3 %	-1.2 %	0.8 %	-1.3 %	-0.1 %	2.5 %
$\mu_R 2.0, \mu_F 1.0$	1.5 %	0.5 %	-0.6 %	-0.3 %	0.1 %	0.6 %	0.6 %	-0.4 %	-1.6 %
$\mu_R 1.0, \mu_F 0.5$	3.0%	4.0%	4.7 %	3.5%	4.5%	5.2 %	1.5 %	3.2 %	4.1 %
$\mu_R 1.0, \mu_F 2.0$	-1.6 %	-2.1 %	-2.7 %	-0.3 %	0.1 %	0.6 %	-0.8 %	-1.7 %	-2.4 %
MAX	3.0 %	4.0 %	4.7 %	3.5 %	4.5 %	5.2 %	1.5 %	3.2 %	5.2 %
yield _{region} /yield _{$\geq 2j$}	1	0.56	0.24	1	0.60	0.29	1	0.55	0.24

Table 41: The acceptance uncertainty of each scale variation , in each of the analysis regions shown. The maximum of these is shown at the bottom. Also shown in the bottom row, is the fraction of the yield in each inclusive jet region compared to the 2-jet inclusive region.

¹⁴⁴⁷ Full plots showing the ratios and their fits for m_{bb} and p_T^V are shown in Figures [43](#) and [41](#), respectively.
¹⁴⁴⁸ The plots for m_{bb} shape comparisons split into number-of-jet channels is shown in Figure [42](#).

Not reviewed, for internal circulation only

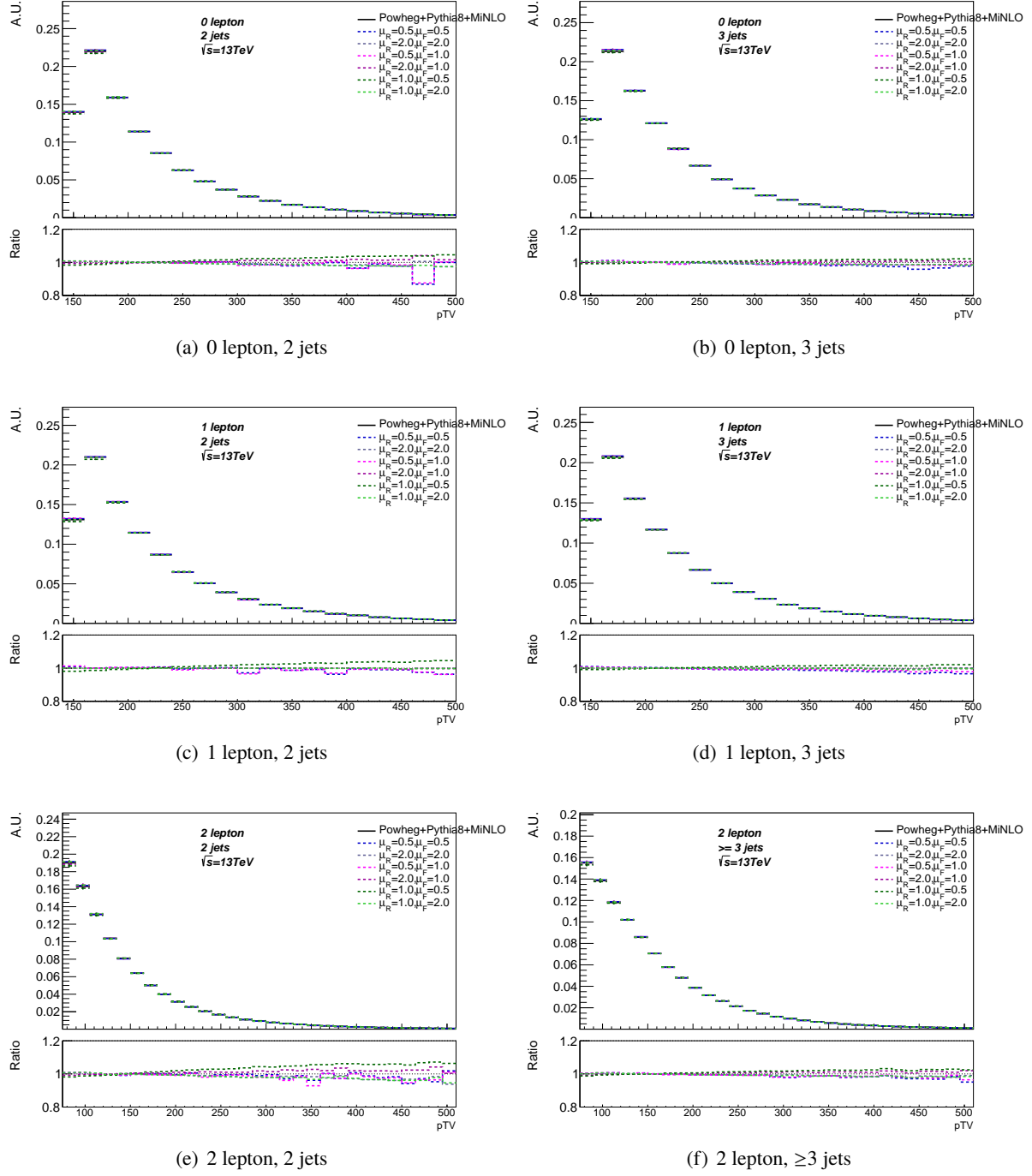


Figure 41: p_T^V : Shape comparisons for each scale variation to the nominal for each VH process, i.e. lepton channel, split into the 2 jet and 3(3p) jet category. The ratios of these are shown in the bottom panel.

Not reviewed, for internal circulation only

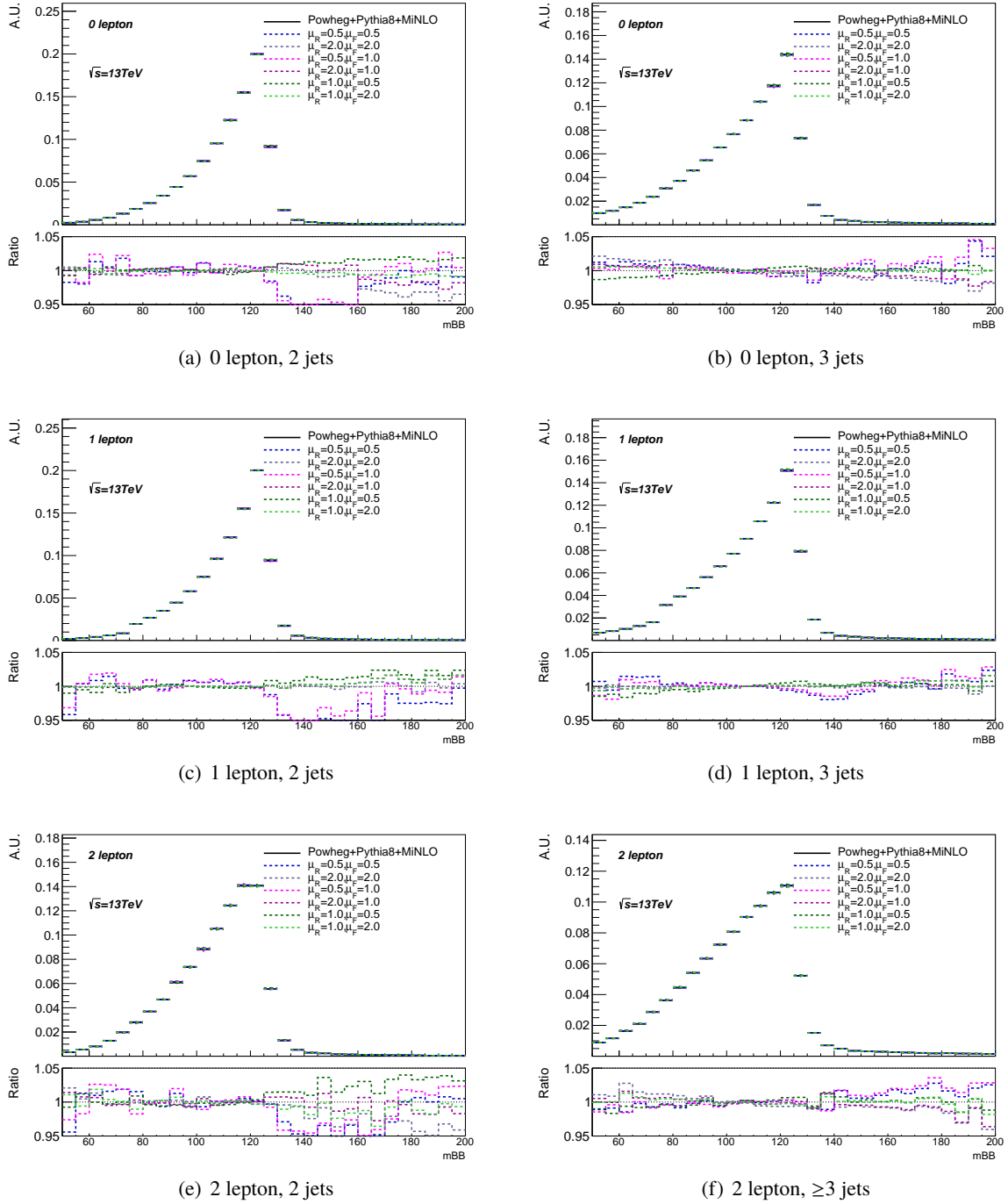


Figure 42: $m_{b\bar{b}}$: Shape comparisons for each scale variation to the nominal for each VH process, i.e. lepton channel, split into the 2 jet and 3(3p) jet category. The ratios of these are shown in the bottom panel.

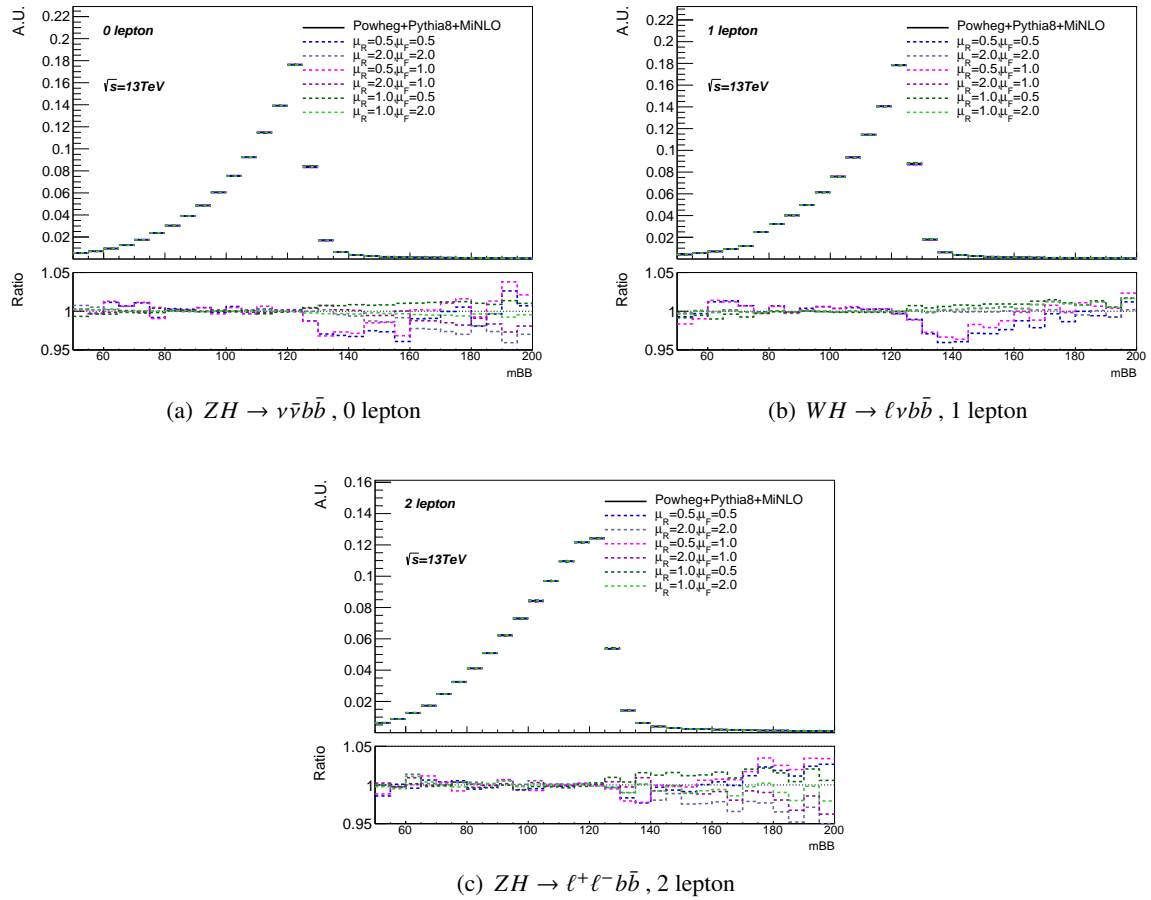


Figure 43: $m_{b\bar{b}}$: Shape comparisons for each scale variation to the nominal for each VH process, i.e. lepton channel, split into the 2 jet and 3(3p) jet category. The ratios of these are shown in the bottom panel.

1449 **B.3. PDF+ α_s**

1450 Detailed breakdown of the acceptance uncertainties due to altering the PDF and α_s uncertainties is
 1451 reported in 41. In each lepton channel, all of the uncertainties listed for each channel (both α_s and PDF)
 1452 were added in quadrature to get the total uncertainty, which is the uncertainty given in the table in the
 1453 main body of the note.

process	PDF uncertainties							α_s uncertainty
0L : $ZH \rightarrow v\bar{v}b\bar{b}$	$\pm 0.46\%$	$\pm 0.32\%$	$\pm 0.01\%$	$\pm 0.18\%$	$\pm 0.37\%$	$\pm 0.34\%$	$\pm 0.00\%$	$\pm 0.60\%$
	$\pm 0.05\%$	$\pm 0.04\%$	$\pm 0.02\%$	$\pm 0.01\%$	$\pm 0.04\%$	$\pm 0.04\%$	$\pm 0.03\%$	
	$\pm 0.18\%$	$\pm 0.02\%$	$\pm 0.07\%$	$\pm 0.07\%$	$\pm 0.03\%$	$\pm 0.39\%$	$\pm 0.01\%$	
	$\pm 0.04\%$	$\pm 0.02\%$	$\pm 0.18\%$	$\pm 0.06\%$	$\pm 0.08\%$	$\pm 0.28\%$	$\pm 0.02\%$	
	$\pm 0.00\%$							
1L : $WH \rightarrow \ell v b\bar{b}$	$\pm 0.50\%$	$\pm 0.23\%$	$\pm 0.01\%$	$\pm 0.25\%$	$\pm 0.32\%$	$\pm 0.34\%$	$\pm 0.00\%$	$\pm 0.64\%$
	$\pm 0.11\%$	$\pm 0.02\%$	$\pm 0.02\%$	$\pm 0.00\%$	$\pm 0.20\%$	$\pm 0.06\%$	$\pm 0.18\%$	
	$\pm 0.21\%$	$\pm 0.00\%$	$\pm 0.05\%$	$\pm 0.09\%$	$\pm 0.01\%$	$\pm 0.46\%$	$\pm 0.02\%$	
	$\pm 0.04\%$	$\pm 0.02\%$	$\pm 0.19\%$	$\pm 0.07\%$	$\pm 0.03\%$	$\pm 0.30\%$	$\pm 0.02\%$	
	$\pm 0.10\%$							
2L : $ZH \rightarrow \ell^+\ell^-b\bar{b}$	$\pm 0.23\%$	$\pm 0.00\%$	$\pm 0.01\%$	$\pm 0.12\%$	$\pm 0.19\%$	$\pm 0.10\%$	$\pm 0.01\%$	$\pm 0.11\%$
	$\pm 0.04\%$	$\pm 0.01\%$	$\pm 0.00\%$	$\pm 0.07\%$	$\pm 0.07\%$	$\pm 0.02\%$	$\pm 0.02\%$	
	$\pm 0.04\%$	$\pm 0.01\%$	$\pm 0.10\%$	$\pm 0.00\%$	$\pm 0.05\%$	$\pm 0.22\%$	$\pm 0.01\%$	
	$\pm 0.01\%$	$\pm 0.01\%$	$\pm 0.15\%$	$\pm 0.05\%$	$\pm 0.09\%$	$\pm 0.15\%$	$\pm 0.08\%$	
	$\pm 0.01\%$							

Table 42: The acceptance uncertainty for each PDF and α_s uncertainty variation , in each of the analysis regions shown. The uncertainties here were added in quadrature to get the total acceptance uncertainty for each region (i.e lepton channel)

1454 Full plots showing the ratios and their fits for m_{bb} and p_T^V are shown in Figures 45 and 44, respectively.

Not reviewed, for internal circulation only

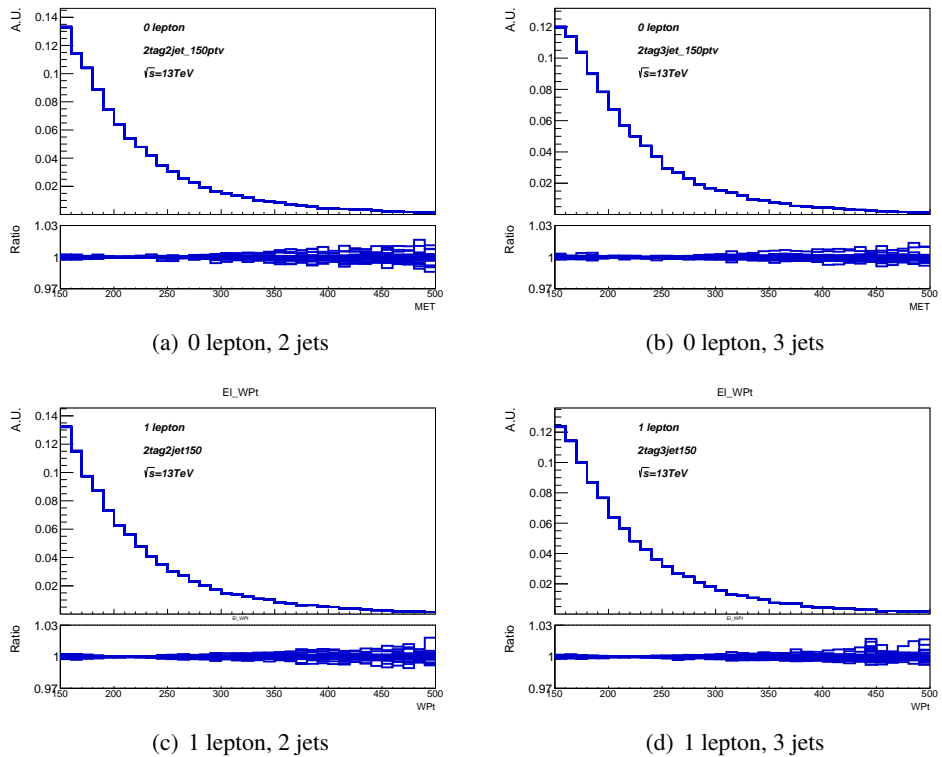


Figure 44: p_T^V : Shape comparison between each PDF and α_s variation for each VH process, i.e. lepton channel, split into the 2 jet and 3(3p) jet category.

Not reviewed, for internal circulation only

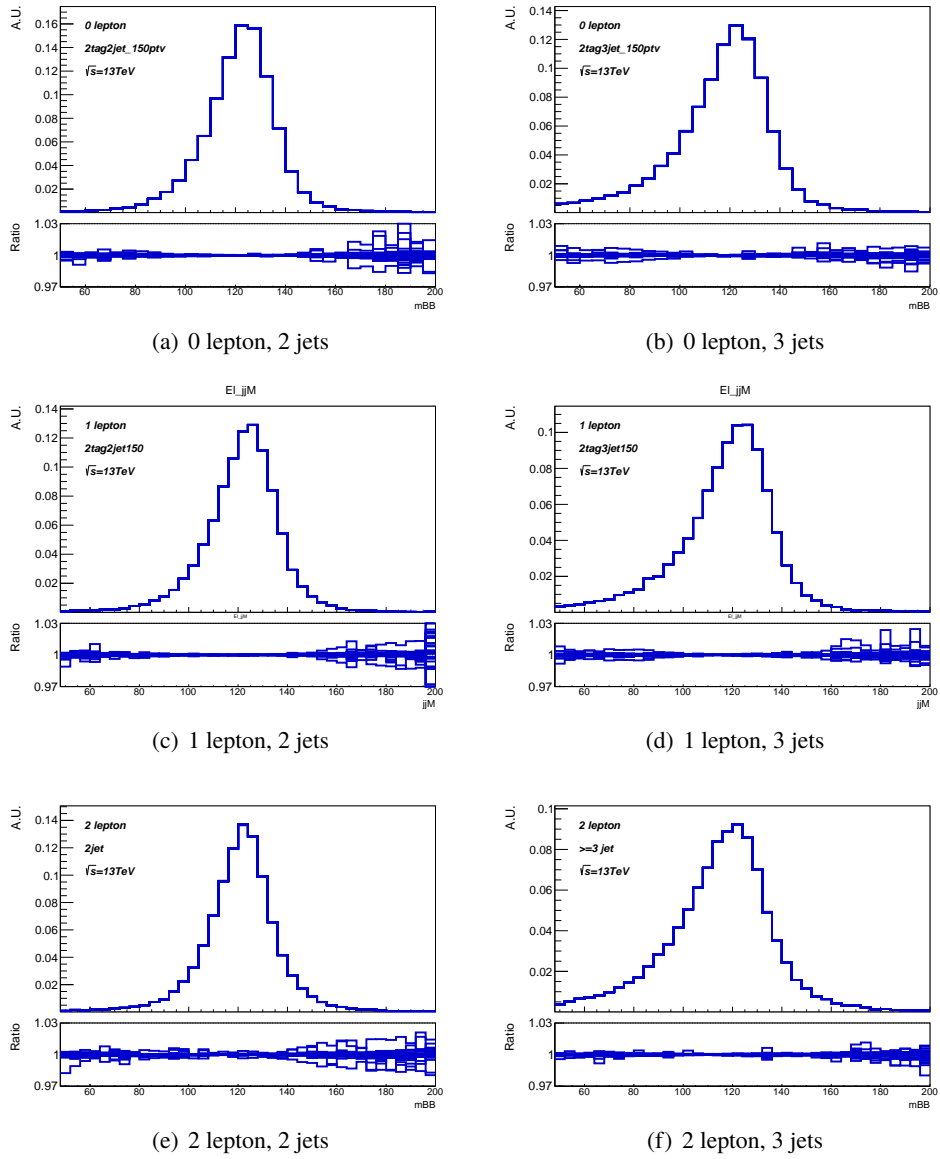


Figure 45: $m_{b\bar{b}}$: Shape comparison between each PDF and α_s variation for each VH process, i.e. lepton channel, split into the 2 jet and 3(3p) jet category

1455 C. Additional material for $t\bar{t}$ modeling systematics

1456 This appendix describes detailed information on the normalisation and shape uncertainties of the $t\bar{t}$
 1457 background described in Section 3.2.4.

1458 C.1. Normalisation uncertainties

1459 C.1.1. 0-lepton

1460 Table 43 contains the information on the 2j/3j extrapolation uncertainty (`ttbarNorm_J2`) in the 0-lepton
 1461 channel. The total uncertainty results from the sum in quadrature of the three variations recommended by
 1462 the topWG. The total uncertainty is dominated by the matrix element uncertainty. A value of 9% will be
 1463 assigned as extrapolation uncertainty.

Systematic	0Lep: 2j/3j
MCstat. (PP8)	$\pm 1.6 \%$
MCstat. (RadHi)	$\pm 1.3 \%$
MCstat. (RadLo)	$\pm 1.4 \%$
MCstat. (PH7)	$\pm 1.7 \%$
MCstat. (aMCP8)	$\pm 2.6 \%$
ISR (PP8)	$\pm 0.2 \%$
(PP8 VS H7)	-1.8 %
(aMCP8 VS PP8)	-8.2 %
TOTAL	$\pm 8.4 \%$

Table 43: Systematic uncertainties on the 2j/3j ratio on the 0 lepton channel. The MCstat. terms for the various generators are only shown for completeness and not included in the TOTAL.

1464 C.1.2. 1-lepton

1465 njet extrapolation

1466 Table 44 contains the information on the 2j/3j extrapolation uncertainty (`ttbarNorm_J2`) in the 1-lepton
 1467 channel. In this table, numbers are reported for the WCR and SR as well as the sum. It can be observed
 1468 that in the SR the pattern of uncertainties is very similar to the 0lepton SR. Therefore a value of 9% will be
 1469 assigned to both SR and CR and the uncertainty will be fully correlated with the 0lepton channel. A larger
 1470 effect is seen in the WCR as a result of the parton shower component; this could be adopted as a residual
 1471 10% uncertainty on the ratio to be applied only in the WCR. At the same time, the top contribution is
 1472 quite subleading in the WCR (and the WCR represent a small fraction of the total $t\bar{t}$ contribution) so an
 1473 increased uncertainty will not have an impact on the result. **this is still under consideration as the effect
 1474 only appeared in the latest round of H7.**

1475 WCR/SR extrapolation

1476 Table 45 contains the information on the WCR/SR extrapolation uncertainty (`ttbarNorm_1LWCR`) in the
 1477 1-lepton channel; numbers are reported for the 2jet and 3jet regions separately and their combination.

Systematic	1Lep: WCR 2j/3j	1Lep: SR 2j/3j	1Lep: SR+WCR 2j/3j
MCstat. (PP8)	$\pm 4.4\%$	$\pm 0.6\%$	$\pm 0.6\%$
MCstat. (RadHi)	$\pm 3.6\%$	$\pm 0.5\%$	$\pm 0.5\%$
MCstat. (RadLo)	$\pm 3.9\%$	$\pm 0.5\%$	$\pm 0.5\%$
MCstat. (PH7)	$\pm 4.2\%$	$\pm 0.6\%$	$\pm 0.6\%$
MCstat. (aMCP8)	$\pm 7.0\%$	$\pm 1.0\%$	$\pm 1.0\%$
ISR (PP8)	$\pm 3.2\%$	$\mp 0.5\%$	$\mp 0.5\%$
(PP8 VS H7)	$+11.1\%$	$\pm 0.0\%$	$+0.3\%$
(aMCP8 VS PP8)	-6.3%	-8.2%	-8.1%
TOTAL	$\pm 13.1\%$	$\pm 8.2\%$	$\pm 8.1\%$

Table 44: Systematic uncertainties on the 2j/3j ratio on the 1 lepton channel. The MCstat. terms for the various generators are only shown for completeness and not included in the TOTAL.

Given the relatively low importance of the WCR for $t\bar{t}$ the proposal is to use a conservative 25% as extrapolation uncertainty applied to the prediction in the WCR.

Systematic	1Lep 2j: WCR/SR	1Lep 3j: WCR/SR	1Lep 2+3j: WCR/SR
MCstat. (PP8)	$\pm 4.1\%$	$\pm 1.8\%$	$\pm 1.7\%$
MCstat. (RadHi)	$\pm 3.3\%$	$\pm 1.4\%$	$\pm 1.3\%$
MCstat. (RadLo)	$\pm 3.7\%$	$\pm 1.5\%$	$\pm 1.4\%$
MCstat. (PH7)	$\pm 3.8\%$	$\pm 1.8\%$	$\pm 1.6\%$
MCstat. (aMCP8)	$\pm 6.5\%$	$\pm 2.7\%$	$\pm 2.5\%$
ISR (PP8)	$\pm 3.0\%$	$\mp 0.7\%$	$\mp 0.1\%$
(PP8 VS H7)	$+20.7\%$	$+8.6\%$	$+10.5\%$
(aMCP8 VS PP8)	$+14.7\%$	$+12.3\%$	$+12.2\%$
TOTAL	$\pm 25.5\%$	$\pm 15.0\%$	$\pm 16.1\%$

Table 45: Systematic uncertainties on the WCR/SR ratio on the 1 lepton channel. The MCstat. terms for the various generators are only shown for completeness and not included in the TOTAL.

C.1.3. ttbar: 1lepton+0lepton

Table 46 show the uncertainty on the extrapolation factor between 0lepton and 1lepton $t\bar{t}$ predictions; in the case of 1lepton, the sum of WCR and SR has been considered. Very consistent value are observed in the 2j and 3j region and the conservative value of 8% is adopted.

C.1.4. bc/bb ratio

This study is not directly used to assign systematic uncertainty and has been carried out on a slightly outdated setup with respect to the rest of the results in this appendix. In the 0 and 1lepton channel the bc component, while being very subdominant in an inclusive sample with respect to the bb one, is the one with a shape most similar to the signal. The value of the bc/bb ratio as obtained by the river analysis are found in Table 47; the value is computed prior to application of the re-weighting emulating

Systematic	0/1Lep 2j	0/1Lep 3j	0/1Lep 2+3j
MCstat. (PP8)	$\pm 1.6\%$	$\pm 0.6\%$	$\pm 0.6\%$
MCstat. (RadHi)	$\pm 1.3\%$	$\pm 0.5\%$	$\pm 0.5\%$
MCstat. (RadLo)	$\pm 1.4\%$	$\pm 0.5\%$	$\pm 0.5\%$
MCstat. (PH7)	$\pm 1.7\%$	$\pm 0.7\%$	$\pm 0.6\%$
MCstat. (aMCP8)	$\pm 2.6\%$	$\pm 1.0\%$	$\pm 0.9\%$
ISR (PP8)	$\mp 0.4\%$	$\mp 1.1\%$	$\mp 1.0\%$
(PP8 VS H7)	-7.7 %	-5.8 %	-6.1 %
(aMCP8 VS PP8)	+2.5 %	+2.5 %	+2.4 %
TOTAL	$\pm 8.1\%$	$\pm 6.4\%$	$\pm 6.6\%$

Table 46: Systematic uncertainties on the Olepton/1lepton extrapolation. In case of 1lepton the sum of WCR and SR has been considered. The MCstat. terms for the various generators are only shown for completeness and not included in the TOTAL.

1490 the performance of the tagging algorithm, therefore, only relative variation across regions should be
 1491 considered.

region	bc/bb ratio
1lepton: WCR 2j	1.020 ± 0.07
1lepton: WCR 3j	0.628 ± 0.02
1lepton: SR 2j	0.7800 ± 0.007
1lepton: SR 3j	0.2897 ± 0.001
1lepton: WCR+SR 2j	1.01 ± 0.01
1lepton: WCR+SR 3j	0.4122 ± 0.002
Olepton: 2j	0.95 ± 0.02
Olepton: 3j	0.435 ± 0.005

Table 47: Value of the $t\bar{t}$ bc/bb yields ratio from Powheg+Pythia8 in each analysis region of the Olepton and 1lepton channel. Numbers have been computed before applying the scaling to mimic the effect of b -tagging efficiency therefore only the relative variation across regions should be considered and not the absolute scale of the ratio. The uncertainty only cover the MonteCarlo statistics.

1492 The ratio bc/bb has been monitored in the nominal sample as well as in the systematics ones for both 0
 1493 and 1 lepton channel. Results are shown in Table 48. After ignoring the WCR plagued by lack of stat. and
 1494 whose dedicated extrapolation uncertainty has already been assessed, the total uncertainty on the ratio is
 1495 around 10-15% and rather consistent in variation between 1lepton and Olepton analysis. No uncertainty
 1496 are implemented from this study since it has been shown that varying the bc/bb ratio by 10% has very
 1497 little impact on the shape of the BDT discriminat in the SR.

1498 C.1.5. ttbar: 2lepton

1499 NOTE: for the 2lepton results, only dilepton (when available) have been used. These samples have a
 1500 larger statistics but it was tested that, within statistics, the result of the non all had sample is consistent.
 1501 with the only exception of the aMC NLO case where the dilepton sample has been found to produce large
 1502 variation.

MC statistics	1l:WCR 2j	1l:WCR 3j	1l:SR 2j	1l:SR 3j	1l:SUM 2j	1l:SUM 3j	0l:SR 2j	0l:SR 3j
MCstat. (PP8)	$\pm 6.6\%$	$\pm 3.2\%$	$\pm 1.0\%$	$\pm 0.5\%$	$\pm 1.1\%$	$\pm 0.5\%$	$\pm 2.5\%$	$\pm 1.2\%$
MCstat. (RadHi)	$\pm 9.1\%$	$\pm 4.2\%$	$\pm 1.3\%$	$\pm 0.6\%$	$\pm 1.4\%$	$\pm 0.7\%$	$\pm 3.4\%$	$\pm 1.6\%$
MCstat. (RadLo)	$\pm 9.7\%$	$\pm 4.6\%$	$\pm 1.4\%$	$\pm 0.7\%$	$\pm 1.6\%$	$\pm 0.8\%$	$\pm 3.6\%$	$\pm 1.7\%$
MCstat. (PH7)	$\pm 9.3\%$	$\pm 4.4\%$	$\pm 1.3\%$	$\pm 0.7\%$	$\pm 1.5\%$	$\pm 0.8\%$	$\pm 3.6\%$	$\pm 1.8\%$
MCstat. (aMCP8)	$\pm 19.1\%$	$\pm 8.5\%$	$\pm 2.7\%$	$\pm 1.2\%$	$\pm 3.1\%$	$\pm 1.4\%$	$\pm 6.9\%$	$\pm 3.2\%$
Systematic	1l:WCR 2j	1l:WCR 3j	1l:SR 2j	1l:SR 3j	1l:SUM 2j	1l:SUM 3j	0l:SR 2j	0l:SR 3j
ISR (PP8)	$\mp 2.9\%$	$\pm 1.9\%$	$\pm 1.7\%$	$\mp 0.3\%$	$\pm 2.7\%$	$\pm 0.5\%$	$\pm 2.2\%$	$\mp 0.0\%$
(PP8 VS H7)	-13.3 %	-15.4 %	-7.7 %	-9.3 %	-9.8 %	-10.4 %	-6.4 %	-11.1 %
(aMCP8 VS PP8)	-9.7 %	-22.4 %	-6.1 %	+3.2 %	-8.1 %	-1.0 %	-14.7 %	-3.8 %
TOTAL	$\pm 16.8\%$	$\pm 27.3\%$	$\pm 10.0\%$	$\pm 9.9\%$	$\pm 13.0\%$	$\pm 10.5\%$	$\pm 16.2\%$	$\pm 11.8\%$

Table 48: Systematic uncertainties on the bc/bb ratio. The MCstat. terms for the various generators are only shown for completeness and not included in the TOTAL.

1503 NOTE2: for historical reasons the low and high Vpt regions are still referred to as ‘M’ and ‘H’; this will
 1504 be changed consistently in the next iteration

1505 topEM/SR extrapolation

1506 The 2lepton channel is significantly more convoluted and contains 4 SRs all accompanied by a related CR.
 1507 The first approach consisted in testing the assumption that the SR and the CR are statistically compatible.
 1508 Table 49 shows the uncertainty on the SR/CR extrapolation. It could be shown that, with the only exception
 1509 of the high Vpt 2jet region, the ration of yield between different generators is completely compatible with
 1510 the MC statistical uncertainty. For this reason, no extrapolation uncertainty is considered between CRs
 1511 and SRs the results in the following will be obtained by combining the results from the 2 regions. The
 1512 high since the $t\bar{t}$ contribution falls very quickly with Vpt, at high Vpt the $t\bar{t}$ contribution is subdominant.

Systematic	SR/CR 2jM	SR/CR 2jH	SR/CR $\geq 3jM$	SR/CR $\geq 3jH$
MCstat. (PP8)	$\pm 1.1\%$	$\pm 5.6\%$	$\pm 0.7\%$	$\pm 2.2\%$
MCstat. (PP8dl)	$\pm 0.8\%$	$\pm 4.2\%$	$\pm 0.5\%$	$\pm 1.8\%$
MCstat. (RadHi)	$\pm 0.8\%$	$\pm 4.4\%$	$\pm 0.6\%$	$\pm 1.9\%$
MCstat. (RadLo)	$\pm 0.9\%$	$\pm 4.7\%$	$\pm 0.6\%$	$\pm 1.8\%$
MCstat. (PH7dl)	$\pm 0.8\%$	$\pm 4.5\%$	$\pm 0.5\%$	$\pm 1.8\%$
MCstat. (aMCP8)	$\pm 1.7\%$	$\pm 9.7\%$	$\pm 1.1\%$	$\pm 4.1\%$
ISR (PP8)	$\pm 0.0\%$	$\pm 0.7\%$	$\pm 0.1\%$	$\mp 1.1\%$
(PP8 VS H7) DL	+0.7 %	+4.4 %	+0.4 %	-2.4 %
(aMCP8 VS PP8)	+0.8 %	-17.1 %	-0.4 %	-3.8 %
TOTAL	$\pm 1.0\%$	$\pm 17.7\%$	$\pm 0.6\%$	$\pm 4.6\%$

Table 49: Systematic uncertainties on SR/CR extrapolation in 2lepton. The MCstat. terms for the various generators are only shown for completeness and not included in the TOTAL.

1513 2j/3j extrapolation

1514 Table 50 shows the uncertainty on the extrapolation between 2jet and ≥ 3 jet yields. Extremely consistent
 1515 values are found in the medium and high V_{pT} regions where the differences are compatible with the large
 1516 statistical uncertainties of the high V_{pT} regions. The ball park numbers of the order of 30% are driven by
 1517 the matrix element uncertainty, and including this prior in the fit will result in a strong constraint. Such
 1518 value is substantially larger than the actual constraining power of the topem CR; therefore it has been
 1519 decided to use separate normalisation uncertainties for $t\bar{t}$ in the 2jet and 3jets inclusive analysis regions.

Systematic	SR: M 2/ \geq 3j	CR: M 2/ \geq 3j	SRCR: M 2/ \geq 3j	SR: H 2/ \geq 3j	CR: H 2/ \geq 3j	SRCR: H 2/ \geq 3j
MCstat. (PP8)	$\pm 0.9\%$	$\pm 0.9\%$	$\pm 0.6\%$	$\pm 4.3\%$	$\pm 4.2\%$	$\pm 3.0\%$
MCstat. (PP8dl)	$\pm 0.7\%$	$\pm 0.7\%$	$\pm 0.5\%$	$\pm 3.3\%$	$\pm 3.1\%$	$\pm 2.3\%$
MCstat. (RadHi)	$\pm 0.7\%$	$\pm 0.7\%$	$\pm 0.5\%$	$\pm 3.4\%$	$\pm 3.4\%$	$\pm 2.4\%$
MCstat. (RadLo)	$\pm 0.7\%$	$\pm 0.7\%$	$\pm 0.5\%$	$\pm 3.6\%$	$\pm 3.6\%$	$\pm 2.5\%$
MCstat. (PH7dl)	$\pm 0.7\%$	$\pm 0.7\%$	$\pm 0.5\%$	$\pm 3.4\%$	$\pm 3.4\%$	$\pm 2.4\%$
MCstat. (aMCP8)	$\pm 1.4\%$	$\pm 1.4\%$	$\pm 1.0\%$	$\pm 8.0\%$	$\pm 6.9\%$	$\pm 5.2\%$
ISR (PP8)	$\pm 6.7\%$	$\pm 6.8\%$	$\pm 6.8\%$	$\pm 16.5\%$	$\pm 14.0\%$	$\pm 15.3\%$
(PP8 VS H7) DL	-9.3 %	-9.5 %	-9.4 %	-12.0 %	-17.8 %	-15.0 %
(aMCP8 VS PP8)	-25.4 %	-26.3 %	-25.8 %	-32.8 %	-22.0 %	-27.2 %
TOTAL	$\pm 27.9\%$	$\pm 28.8\%$	$\pm 28.3\%$	$\pm 38.6\%$	$\pm 31.6\%$	$\pm 34.6\%$

Table 50: Systematic uncertainties on $2j/\geq 3j$ extrapolation in 2lepton; the sum of SR and CR has been considered. The MCstat. terms for the various generators are only shown for completeness and not included in the TOTAL.

1520 V_{pT} extrapolation

1521 Finally, the extrapolation uncertainty across different V_{pT} regions has been considered in Table 51;
 1522 The extrapolation between medium V_{pT} and high V_{pT} regions have been considered. An uncertainty
 1523 of 11-14% could be extracted, again dominated by matrix element effects. No uncertainty numbers
 1524 will be directly extracted from this as the relative normalisation uncertainty across V_{pT} regions will be
 1525 obtained as a result of the implementation of the V_{pT} shape uncertainty since this choice will allow to link
 1526 normalisation effects to shape effects within each region.

Systematic	SR+CR: H/M 2j	SR+CR: H/M \geq 3j
MCstat. (PP8)	$\pm 2.8\%$	$\pm 1.2\%$
MCstat. (PP8dl)	$\pm 2.1\%$	$\pm 0.9\%$
MCstat. (RadHi)	$\pm 2.2\%$	$\pm 1.0\%$
MCstat. (RadLo)	$\pm 2.4\%$	$\pm 0.9\%$
MCstat. (PH7dl)	$\pm 2.3\%$	$\pm 0.9\%$
MCstat. (aMCP8)	$\pm 4.9\%$	$\pm 2.1\%$
ISR (PP8)	$\pm 2.7\%$	$\mp 4.2\%$
(PP8 VS H7) DL	-7.5 %	-1.4 %
(aMCP8 VS PP8)	-11.4 %	-9.7 %
TOTAL	$\pm 13.9\%$	$\pm 10.7\%$

Table 51: Systematic uncertainties on extrapolation among various V_{pT} regions in 2lepton; the sum of SR and CR has been considered. The MCstat. terms for the various generators are only shown for completeness and not included in the TOTAL.

1527 **C.2. Fits for shape uncertainties**

1528 **C.2.1. 0-lepton fits**

- 1529 • $m_{b\bar{b}}$ shape variation in 0-lepton 2jet and 3jet regions in Fig. 46. For the case of ISR variations, no
1530 significant shapes are observed.
- 1531 • p_T^V shape variation in 0-lepton 2jet and 3jet regions in Fig. 46

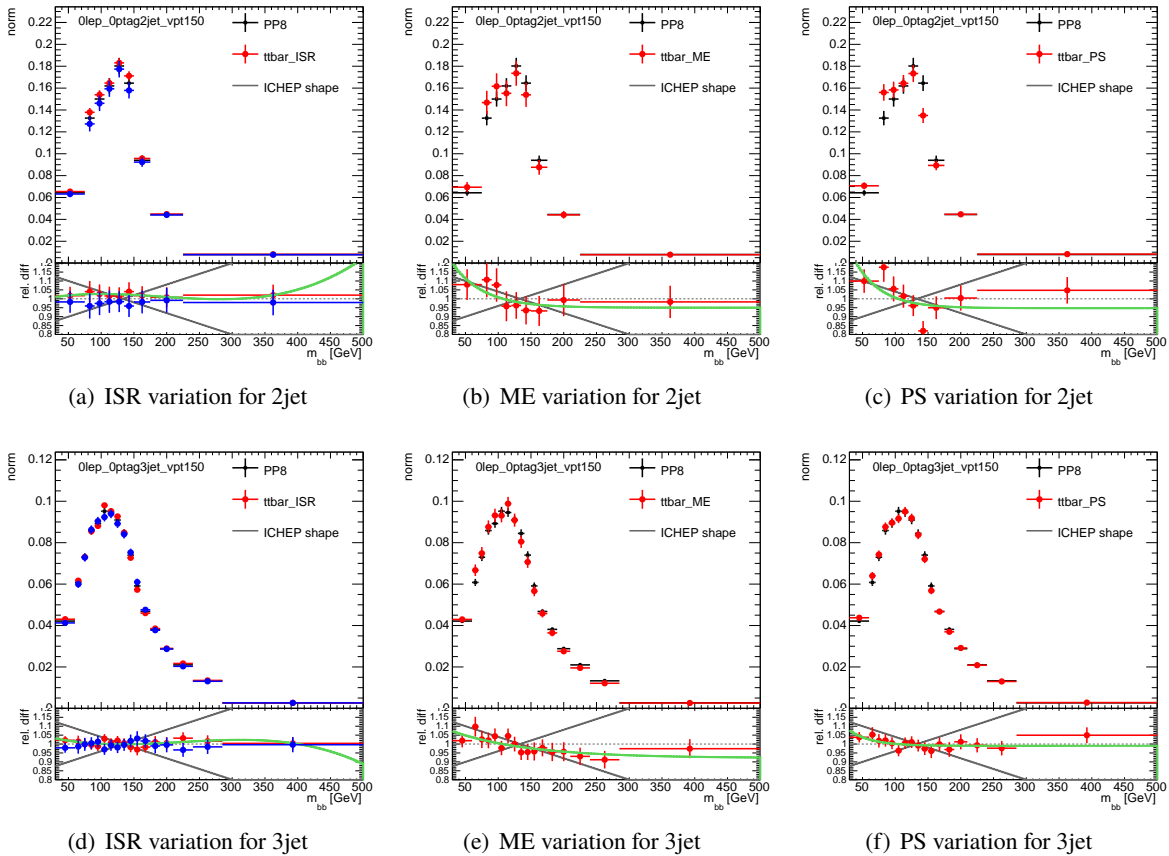


Figure 46: $m_{b\bar{b}}$ shape variation in 0-lepton. ISR variation is the scale variation, ME variation is comparison to aMC@NLO, and PS variation is comparison to Powheg +HERWIG 7.

Not reviewed, for internal circulation only

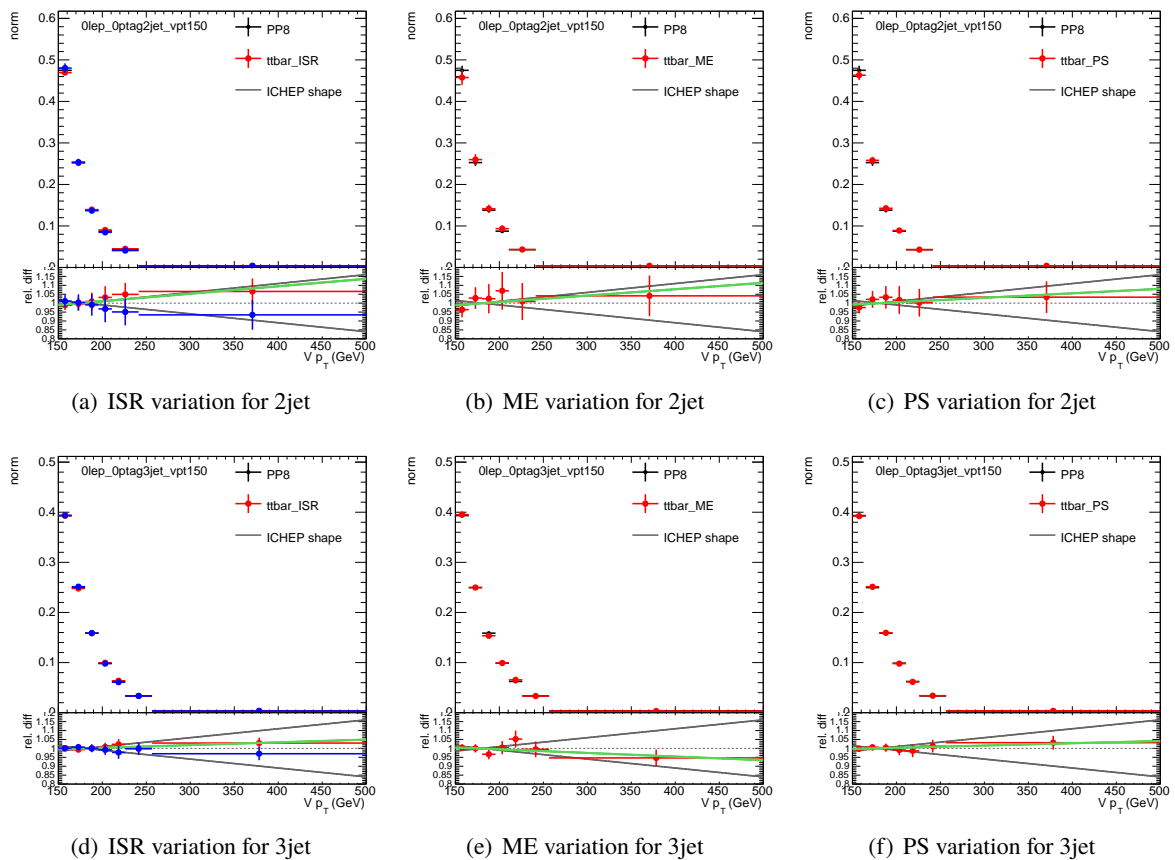


Figure 47: p_V^V shape variation in 0-lepton. ISR variation is the scale variation, ME variation is comparison to aMC@NLO, and PS variation is comparison to Powheg +Herwig 7.

1532 **C.2.2. 1-lepton fits**

- 1533 • $m_{b\bar{b}}$ shape variation in 1-lepton 2jet and 3jet regions in Fig. 48. For the case of ISR variations, no
1534 significant shapes are observed.
- 1535 • p_T^V shape variation in 1-lepton 2jet and 3jet regions in Fig. 48

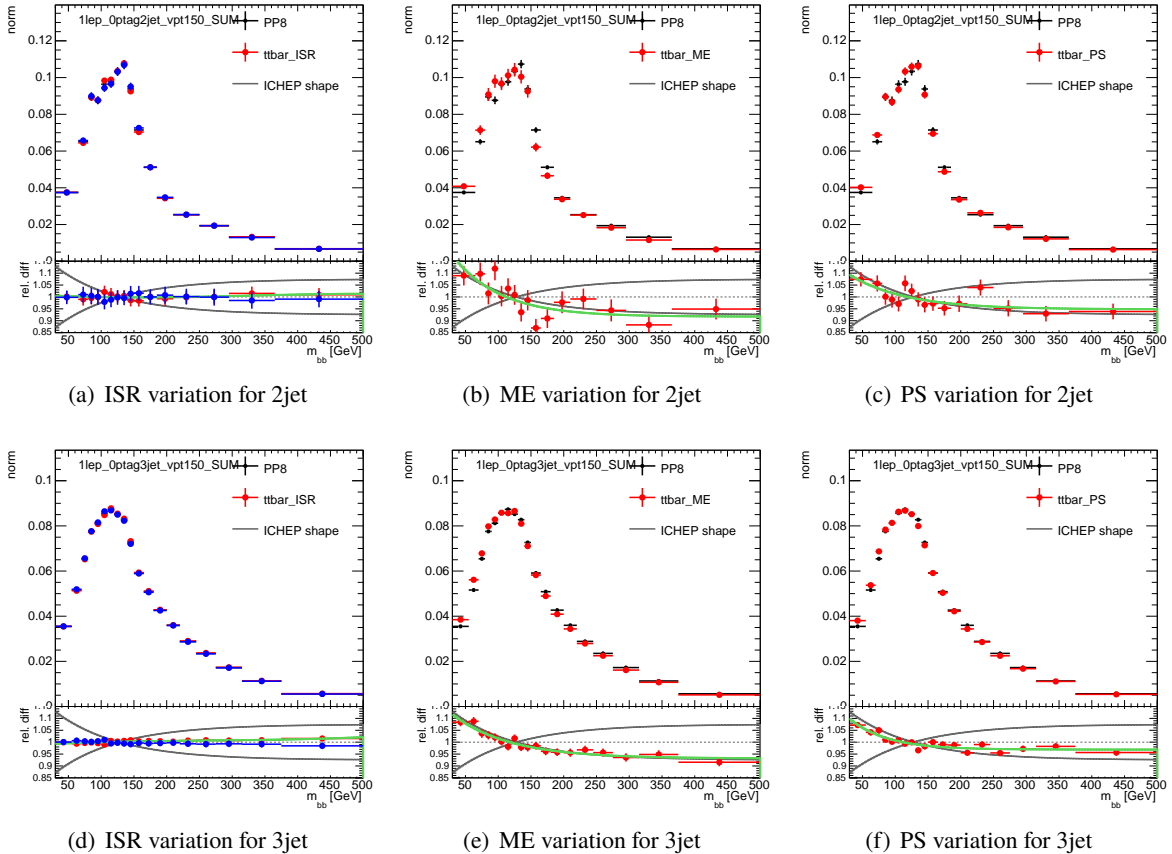


Figure 48: $m_{b\bar{b}}$ shape variation in 1-lepton. ISR variation is the scale variation, ME variation is comparison to aMC@NLO, and PS variation is comparison to Powheg +HERWIG 7.

Not reviewed, for internal circulation only

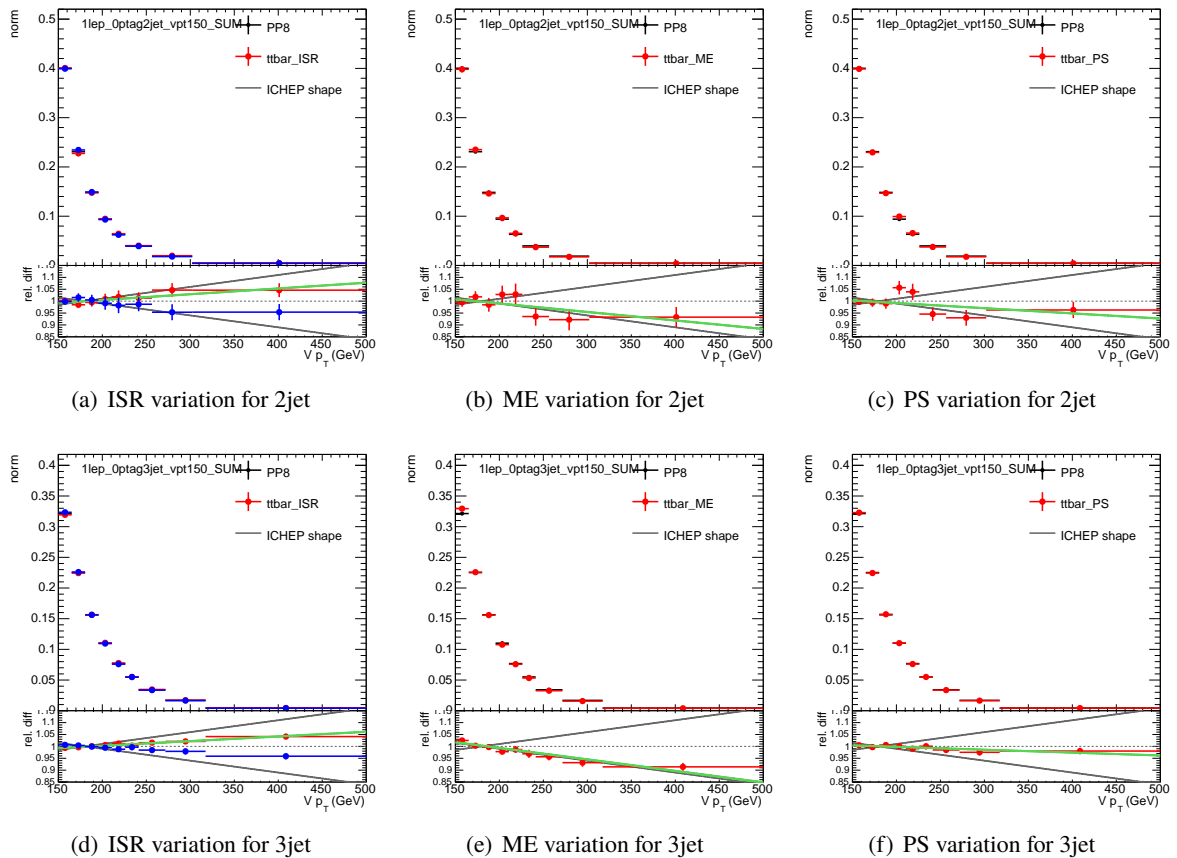


Figure 49: p_T^V shape variation in 1-lepton. ISR variation is the scale variation, ME variation is comparison to aMC@NLO, and PS variation is comparison to POWHEG + HERWIG 7.

1536 **C.2.3. 2-lepton fits**

1537 In this section, individual fits to the 2-lepton variations are shown.

- 1538 • $m_{b\bar{b}}$ shape variation in 2-lepton 2jet in Fig. 50
 1539 • $m_{b\bar{b}}$ shape variation in 2-lepton 3pjet in Fig. 51
 1540 • p_T^V shape variation in 2-lepton in Fig. 52

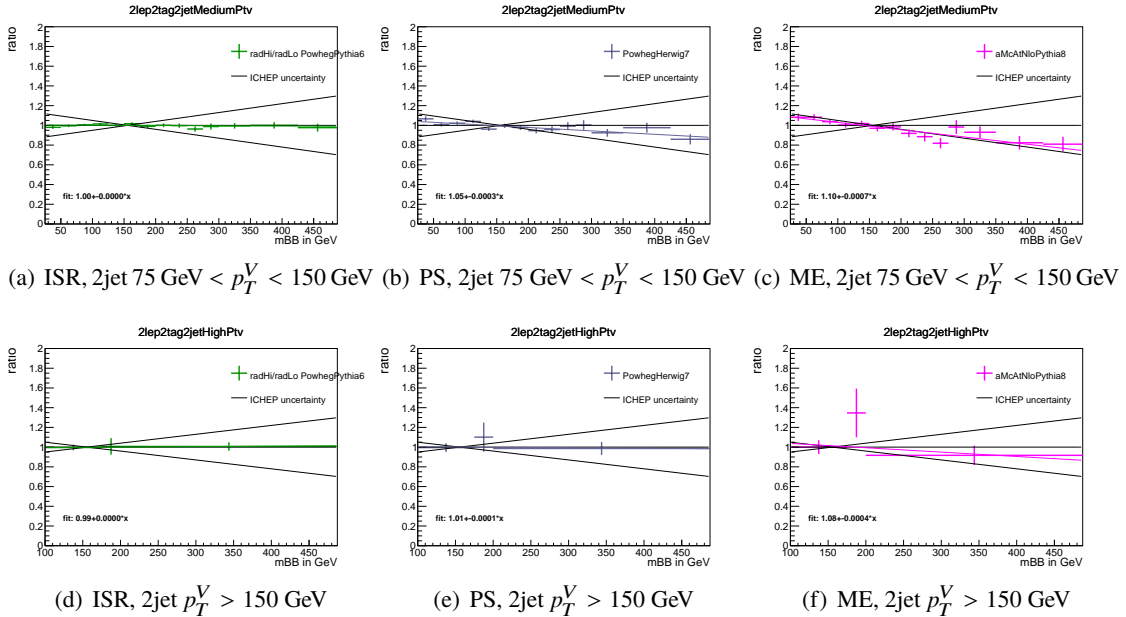


Figure 50: $m_{b\bar{b}}$ shape variation in 2-lepton 2jet. ISR variation is the scale variation, ME variation is comparison to aMC@NLO, and PS variation is comparison to POWHEG +HERWIG 7.

Not reviewed, for internal circulation only

Not reviewed, for internal circulation only

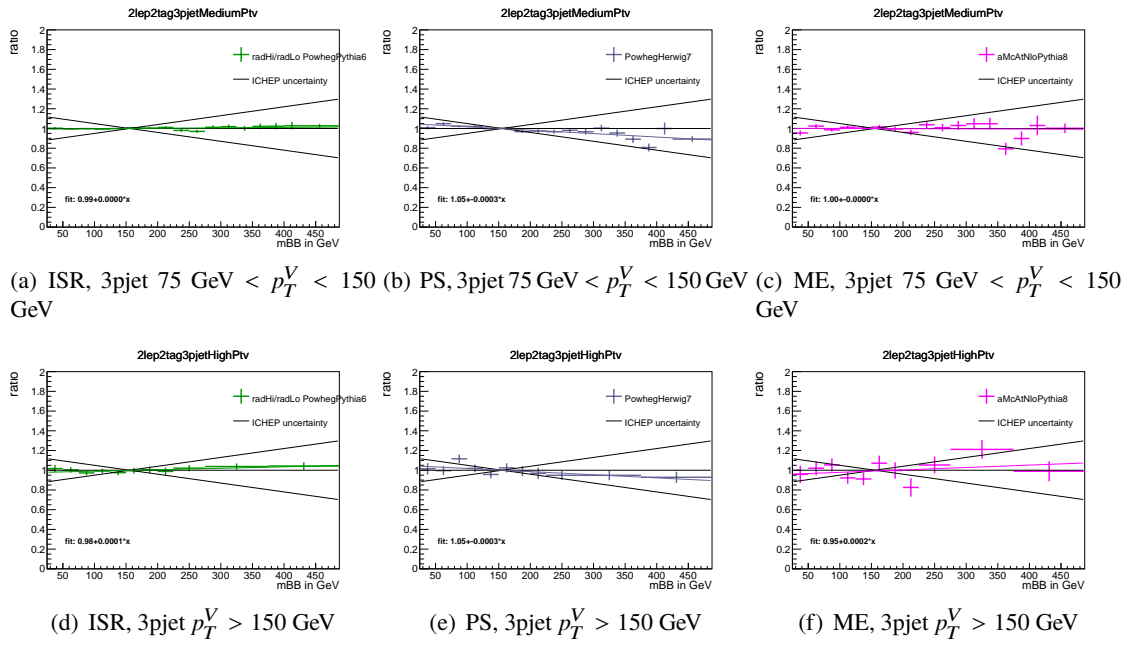


Figure 51: m_{bb} shape variation in 2-lepton 3jet. ISR variation is the scale variation, ME variation is comparison to aMC@NLO, and PS variation is comparison to Powheg +HERWIG 7.

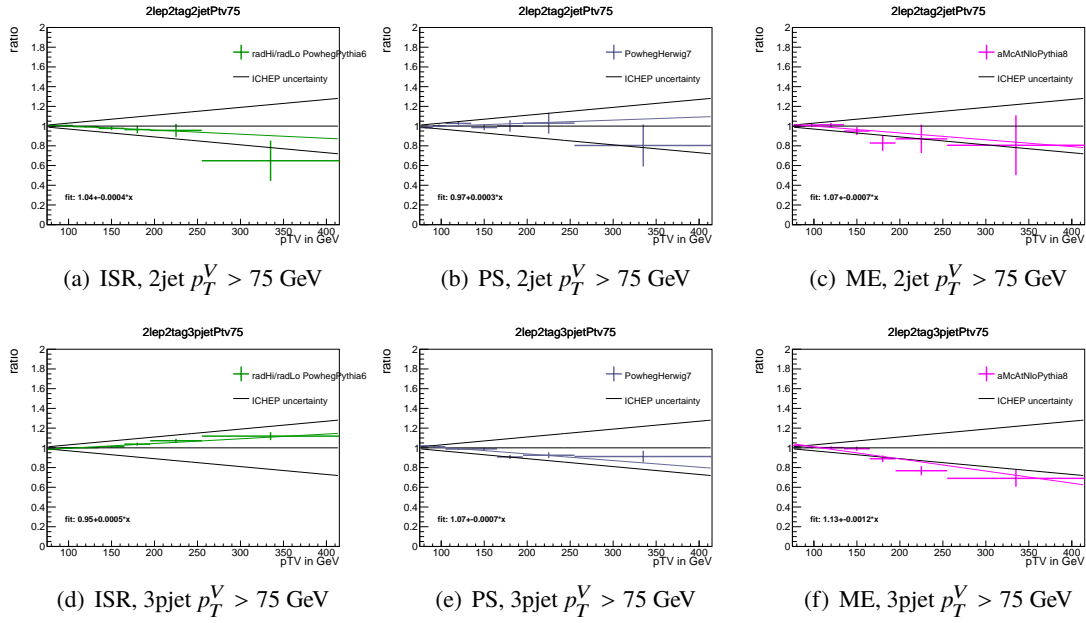


Figure 52: p_T^V shape variation in 2-lepton. ISR variation is the scale variation, ME variation is comparison to aMC@NLO, and PS variation is comparison to Powheg +HERWIG 7.

1541 C.3. Residual shape effects across regions

1542 A single shape variation for $m_{b\bar{b}}$ and p_T^V is currently implemented for the 0/1-lepton and 2-lepton analysis.
 1543 Additional uncertainties could be computed by comparing residual effects across analysis regions; this is
 1544 obtained by computing the ratio of the shape variation between different analysis regions.

1545 Figure 53 shows the shape of residual p_T^V uncertainties for different channel and jet multiplicity. Residual
 1546 effects between 2 jet and 3 jet regions are much smaller than the assigned uncertainty in 1-lepton. In
 1547 0-lepton the statistical uncertainties are a dominant effect, especially in the 2-jet region, and no clear
 1548 conclusion may be drawn from the residual plots. In 2-lepton the residual effects between the 2 and 3 jet
 1549 region are of the same size as the assigned uncertainty. Again one has to keep in mind that the high p_T^V
 1550 bins are dominated by statistical uncertainties nevertheless an additional uncertainty may be assigned in
 1551 the future *those plots are very fresh and were not discussed yet*. Residual effects between 0- and 1-lepton
 1552 in the 3-jet regions are smaller than the assigned uncertainty. The 2-jet regions are heavily affected by the
 1553 limited statistics available in 0-lepton.

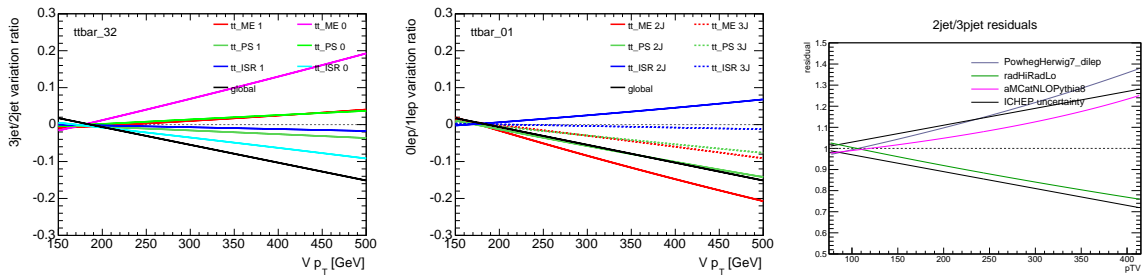


Figure 53: Residual shape uncertainties in p_T^V between different jet multiplicities in 0- and 1-lepton (left), between 0- and 1-lepton channel (middle) and differet jet multiplicities in 2-lepton lepton channel (right). The effect of the total common shape uncertainty is also reported for completeness.

1554 Figure 54 shows the shape of residual $m_{b\bar{b}}$ uncertainties for different channel and jet multiplicity. Similar
 1555 conclusion to the p_T^V residuals can be drawn for the residual effects in $m_{b\bar{b}}$ between 2 and 3jet regions.
 1556 Although the effects in 2-lepton are not as large as in p_T^V they are still sizeable compared to the assigned
 1557 uncertainty and also consistent between regions with sufficient statistics (medium p_T^V region) and low
 1558 statistics (high p_T^V region). The residual effects between 0- and 1-lepton and medium and high p_T^V in
 1559 2-lepton are more than 2 times smaller than the assigned uncertainty and no additional uncertainties have
 1560 to be assigned.

Not reviewed, for internal circulation only

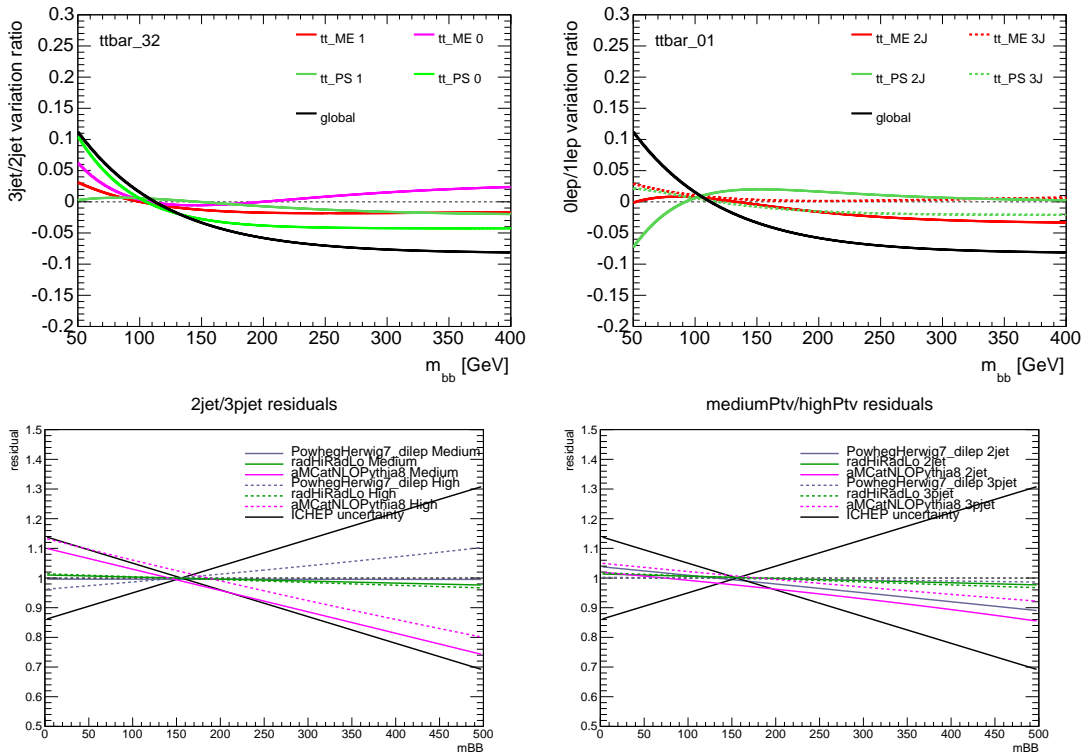


Figure 54: Residual shape uncertainties in m_{bb} between different jet multiplicities in 0- and 1-lepton (top left), between 0- and 1-lepton channel (top right), different jet multiplicities in 2-lepton lepton (bottom left) and different p_T^V categories in 2-lepton (bottom right). The effect of the total common shape uncertainty is also reported for completeness.

1561 D. Additional material for single top modeling systematics

1562 This appendix describes checks made on the modeling uncertainties for the single top backgrounds
 1563 described in Section 3.3.

1564 **D.1. 2-lepton modeling check**

1565 Of the single top processes only the Wt channel contributes to the 2-lepton analysis; the t-channel process
 1566 has very low statistics after the 2-lepton selection. Figures 55 and 56 demonstrate that the shape systematics
 1567 derived in the 1-lepton analysis are appropriate for use also in the 2-lepton analysis.

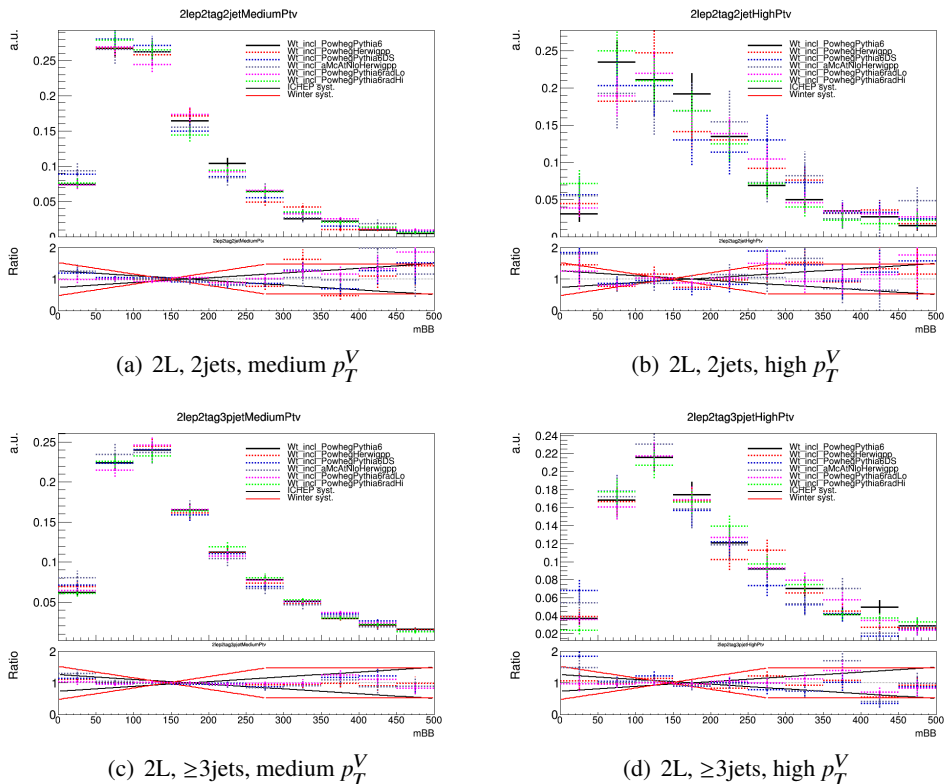


Figure 55: Shape variation in m_{bb} from the single-top Wt contribution with the 2-lepton selection for 2jet (top) and (≥ 3)jet (bottom) regions.

Not reviewed, for internal circulation only

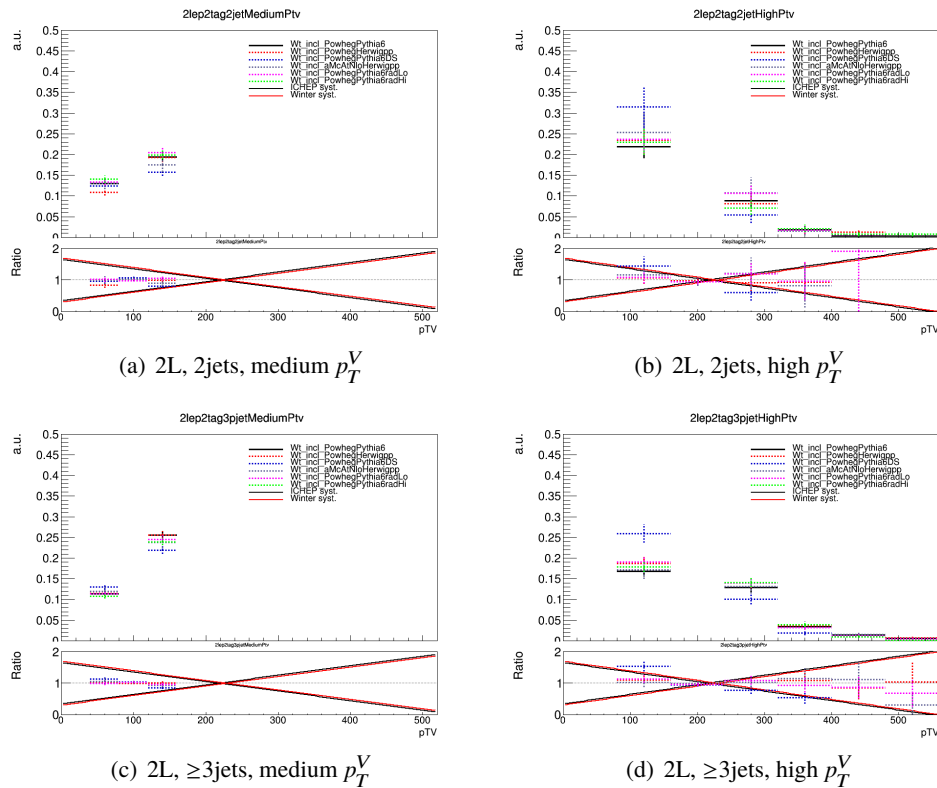


Figure 56: Shape variation in p_t^V from the single-top Wt contribution with the 2-lepton selection for 2jet (top) and (\geq)3jet (bottom) regions.

1568 E. Additional material for diboson modeling systematics

1569 This appendix describes detailed information on the modelling uncertainties for the diboson backgrounds
 1570 described in Section 3.4.

1571 **E.1. Breakdown of PS/UE uncertainties**

1572 The breakdown of contributions to the acceptance uncertainties from the different PS tunes, and the
 1573 POWHEG versus HERWIG comparisons, are given in Table 52.

1574 **E.1.1. 0L**

	$ZZ \rightarrow qqvv$		$WZ \rightarrow qqvv$		$WZ \rightarrow lvqq$	
	2j	3j	2j	3j	2j	3j
MCstat. PHP	$\pm 0.7\%$	$\pm 0.8\%$	$\pm 9.1\%$	$\pm 6.1\%$	$\pm 2.7\%$	$\pm 2.1\%$
MCstat. PP8	$\pm 0.7\%$	$\pm 0.8\%$	$\pm 7.9\%$	$\pm 5.6\%$	$\pm 2.5\%$	$\pm 2.0\%$
PStune: Var1	$+0.3 / -0.7\%$	$+1.4 / +1.6\%$	$-17.0 / -16.8\%$	$+11.3 / +9.3\%$	$-1.0 / -0.6\%$	$+4.5 / +5.2\%$
PStune: Var2	$-1.1 / -1.7\%$	$+1.2 / +2.4\%$	$+9.2 / -23.5\%$	$+15.9 / -9.9\%$	$+1.4 / -3.0\%$	$+4.4 / +4.6\%$
PStune: Ren	$+1.1 / -2.1\%$	$+0.9 / +1.3\%$	$+3.6 / +3.6\%$	$+17.8 / +17.8\%$	$+17.6 / -0.5\%$	$+19.4 / -0.6\%$
PStune: MPI	$-2.1 / -0.7\%$	$+2.5 / +1.1\%$	$+9.7 / +14.0\%$	$+8.7 / -4.7\%$	$-0.0 / -3.5\%$	$-2.6 / +2.5\%$
PS: Pythia VS Herwig	-5.6%	-6.8%	9.1%	24.1%	-10.8%	-4.2%
PStune: TOT	$\pm 3.5\%$	$\pm 4.0\%$	$\pm 32.4\%$	$\pm 27.8\%$	$\pm 18.2\%$	$\pm 20.7\%$
TOT PS	$\pm 5.6\%$	$\pm 6.8\%$	$\pm 32.4\%$	$\pm 27.8\%$	$\pm 18.2\%$	$\pm 20.7\%$

Table 52: Parton Shower uncertainties on the 2-jet and 3-jet acceptances for diboson processes in the 0L channel.

Systematic	$ZZ \rightarrow qqvv$	$WZ \rightarrow qqvv$	$WZ \rightarrow lvqq$
MCstat. PHP	$\pm 1.1\%$	$\pm 11.0\%$	$\pm 3.4\%$
MCstat. PP8	$\pm 1.0\%$	$\pm 9.7\%$	$\pm 3.2\%$
PStune: Var1	$-1.1 / -2.3\%$	$-25.5 / -23.9\%$	$-5.3 / -5.5\%$
PStune: Var2	$-2.3 / -4.0\%$	$-5.7 / -15.2\%$	$-2.9 / -7.2\%$
PStune: Ren	$+0.2 / -3.4\%$	$-12.1 / -12.1\%$	$-1.5 / +0.1\%$
PStune: MPI	$-4.4 / -1.8\%$	$+1.0 / +19.6\%$	$+2.7 / -5.8\%$
PStune: TOT	$\pm 7.3\%$	$\pm 37.5\%$	$\pm 10.9\%$
PS: Pythia VS Herwig	1.3%	-12.1%	-7.0%
TOT PS	$\pm 7.3\%$	$\pm 37.5\%$	$\pm 10.9\%$

Table 53: PS/UE uncertainties on the 3jet/2jet acceptance for the 0L channel for WZ and ZZ processes.

1575 **E.1.2. 1L**

1576 **E.1.3. 2L**

	$WZ \rightarrow l\nu qq$		$ZZ \rightarrow llqq$	
	2j	3j	2j	3j
MCstat. PHP	$\pm 1.3\%$	$\pm 1.0\%$	$\pm 4.7\%$	$\pm 3.8\%$
MCstat. PP8	$\pm 1.2\%$	$\pm 0.9\%$	$\pm 4.6\%$	$\pm 3.7\%$
PStune: Var1	$+0.3 / -1.3\%$	$+1.7 / +1.1\%$	$-3.3 / -4.7\%$	$-9.3 / -4.9\%$
PStune: Var2	$+2.0 / +1.2\%$	$+2.8 / +0.9\%$	$-0.9 / -1.5\%$	$-3.9 / -4.0\%$
PStune: Ren	$+22.2 / -1.6\%$	$+24.4 / +1.2\%$	$+8.6 / -0.2\%$	$-4.5 / -8.9\%$
PStune: MPI	$-1.6 / +0.3\%$	$-0.8 / +1.1\%$	$-2.8 / -2.0\%$	$-2.9 / -1.0\%$
PStune: TOT	$\pm 3.3\%$	$\pm 3.7\%$	$\pm 5.7\%$	$\pm 13.8\%$
PS: Pythia VS Herwig	-3.9%	-13.2%	-2.8%	-7.1%
TOT PS	$\pm 3.9\%$	$\pm 13.2\%$	$\pm 5.7\%$	$\pm 13.8\%$

Table 54: Parton Shower uncertainties on the 2J acceptance for $WZ(l\nu qq)$ and ZZ in the 1Lepton channel. Some problems have been found for the absolute normalisation of the "Ren" variation and therefore it has been excluded from the sum.

Systematic	$WZ \rightarrow l\nu qq$	$ZZ \rightarrow llqq$
MCstat. PHP	$\pm 1.6\%$	$\pm 6.1\%$
MCstat. PP8	$\pm 1.5\%$	$\pm 5.9\%$
PStune: Var1	$-1.4 / -2.4\%$	$+6.7 / +0.2\%$
PStune: Var2	$-0.8 / +0.3\%$	$+3.1 / +2.7\%$
PStune: Ren	$-1.7 / -2.7\%$	$+13.6 / +9.6\%$
PStune: MPI	$-0.9 / -0.7\%$	$+0.1 / -1.0\%$
PStune: TOT	$\pm 3.8\%$	$\pm 15.5\%$
PS: Pythia VS Herwig	10.8%	4.6%
TOT PS	$\pm 10.8\%$	$\pm 15.5\%$

Table 55: PS/UE uncertainties on the 3jet/2jet acceptance for the 1L channel for WZ and ZZ processes.

Systematic	low+high	low	high
MCstat. PHP	$\pm 0.8\%$	$\pm 0.9\%$	$\pm 1.7\%$
MCstat. PP8	$\pm 0.8\%$	$\pm 0.9\%$	$\pm 1.6\%$
PStune: Var1	$+0.6 / -0.3\%$	$+1.0 / +0.1\%$	$-0.6 / -1.5\%$
PStune: Var2	$-0.2 / -0.3\%$	$-0.1 / +0.0\%$	$-0.6 / -1.5\%$
PStune: Ren	$-0.3 / -0.4\%$	$-0.5 / -0.1\%$	$+0.5 / -1.3\%$
PStune: MPI	$-0.2 / +0.0\%$	$-0.0 / +0.5\%$	$-0.9 / -1.6\%$
PStune: TOT	$\pm 0.9\%$	$\pm 1.3\%$	$\pm 3.0\%$
PS: Pythia VS Herwig	-5.8%	-6.1%	-4.8%
TOT PS/UE	$\pm 5.8\%$	$\pm 6.1\%$	$\pm 4.8\%$

Table 56: $ZZ(qql)$ PS/UE uncertainties on the 2jet Acceptance for the 2L channel.

Systematic	low+high	low	high
MCstat. PHP	$\pm 1.8 \%$	$\pm 1.9 \%$	$\pm 2.0 \%$
MCstat. PP8	$\pm 1.7 \%$	$\pm 1.8 \%$	$\pm 2.0 \%$
PStune: Var1	$+0.6 / -0.3 \%$	$+0.2 / +0.3 \%$	$+1.2 / -1.5 \%$
PStune: Var2	$-0.2 / -0.7 \%$	$-1.2 / -1.7 \%$	$+1.9 / +1.5 \%$
PStune: Ren	$+2.9 / -1.8 \%$	$+2.8 / -2.7 \%$	$+3.1 / +0.1 \%$
PStune: MPI	$+0.1 / -0.2 \%$	$+0.0 / -0.3 \%$	$+0.2 / +0.1 \%$
PStune: TOT	$\pm 3.1 \%$	$\pm 3.3 \%$	$\pm 4.0 \%$
PS: Pythia VS Herwig	-1.7%	-1.0%	-3.0%
TOT PS	$\pm 3.1 \%$	$\pm 3.3 \%$	$\pm 4.0 \%$

Table 57: $ZZ(qqll)$ PS/UE uncertainties on the ≥ 3 jet/2jet acceptance for the 2L channel

1577 E.1.4. V p_T shape

1578 Figure 57 shows the comparison between Pohweg+Pythia8 and Powheg+Herwig++ for the p_T^V variable
 1579 in the three channels. No visible differences are found within the MC statistical uncertainty. The shape
 uncertainties derived for the ICHEP analysis are maintained in this analysis.

Not reviewed, for internal circulation only

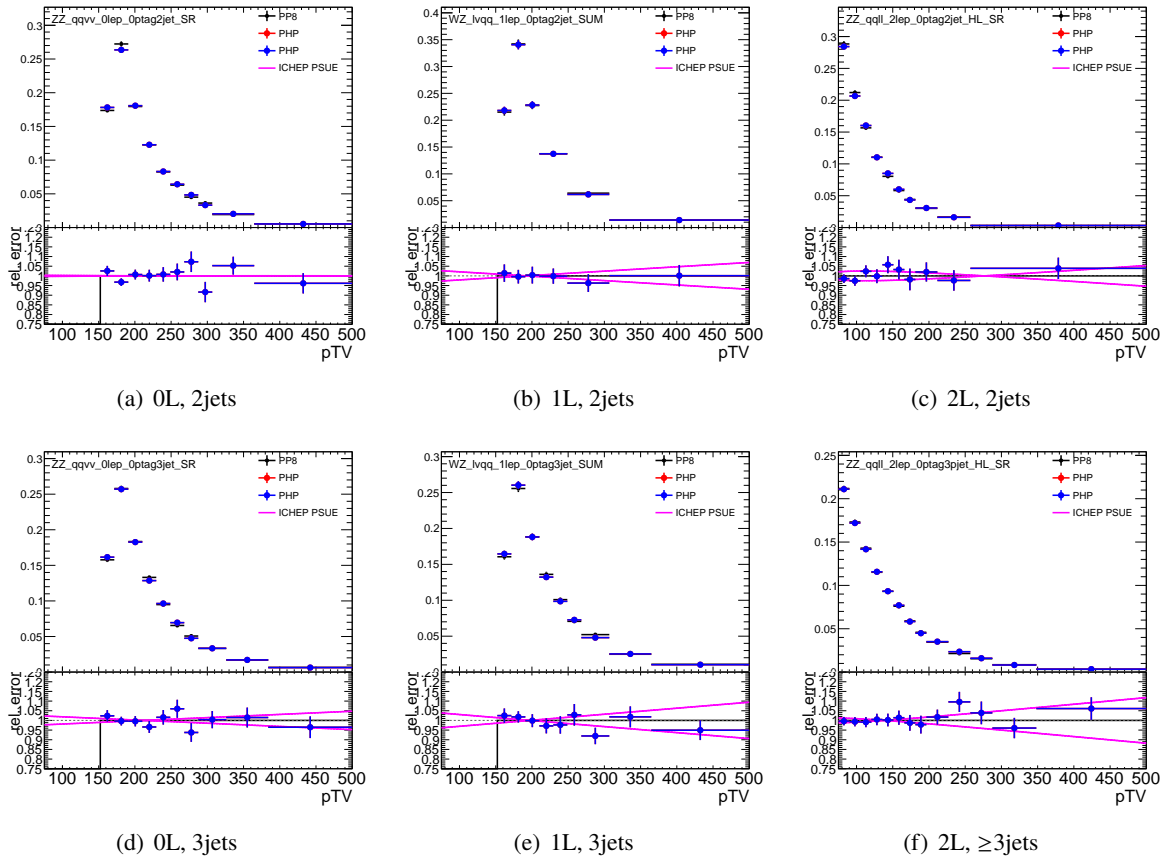


Figure 57: Shape variation of the Vp_T variable for 2 jet (top), (\geq)3 jet (bottom) in the 0L (left), 1L (middle) and 2L (right) regions comparing Powheg+Pythia8 and Powheg+Herwig++.

1580

1581 Figures 58, 59, 60, 61 show the comparison of the 4 shower tune variations for the p_T^V variable in the three
 1582 channels. The same conclusion as for the case of the comparison of different parton shower code could
 1583 be drawn and the uncertainties computed at ICHEP are maintained.

Not reviewed, for internal circulation only

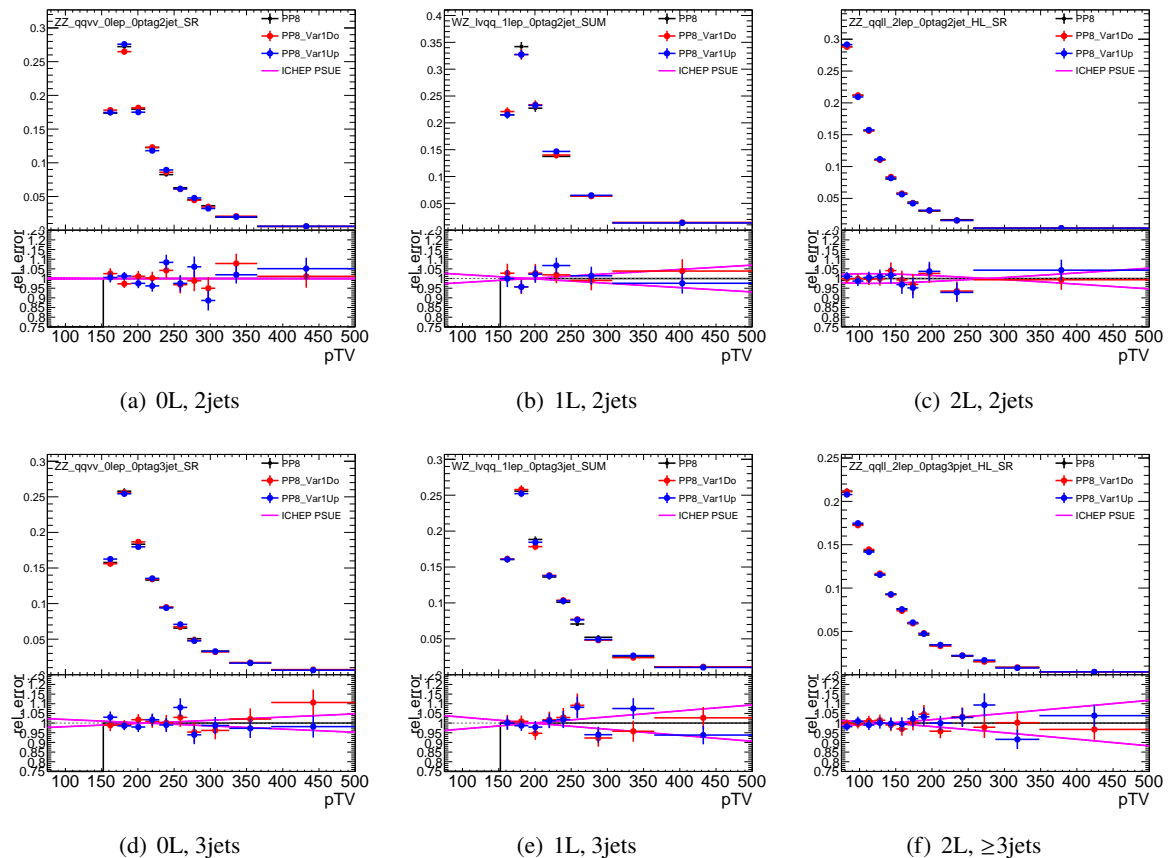


Figure 58: Shape variation of the p_T^V variable for 2 jet (top), (\geq)3 jet (bottom) in the 0L (left), 1L (middle) and 2L (right) regions for the Var1 shower tune component.

Not reviewed, for internal circulation only

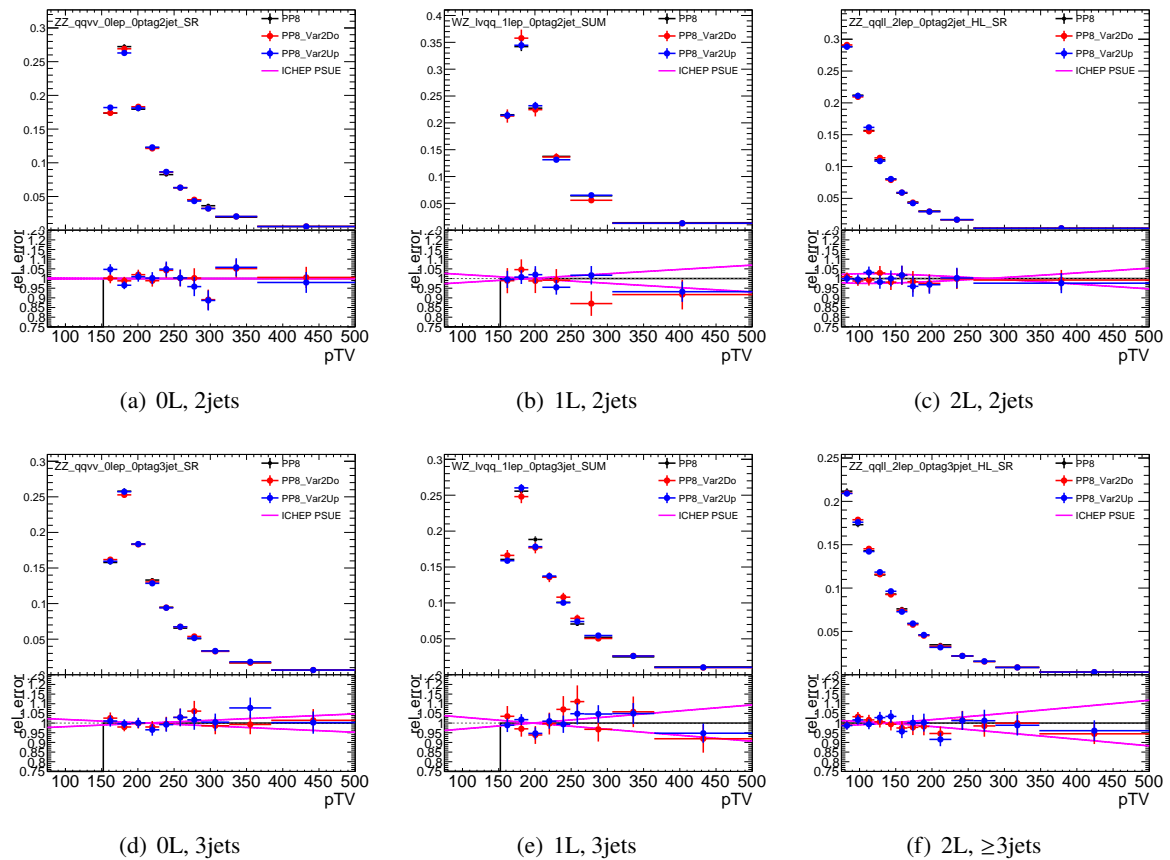


Figure 59: Shape variation of the p_T^V variable for 2 jet (top), (\geq)3 jet (bottom) in the 0L (left), 1L (middle) and 2L (right) regions for the Var2 shower tune component.

Not reviewed, for internal circulation only

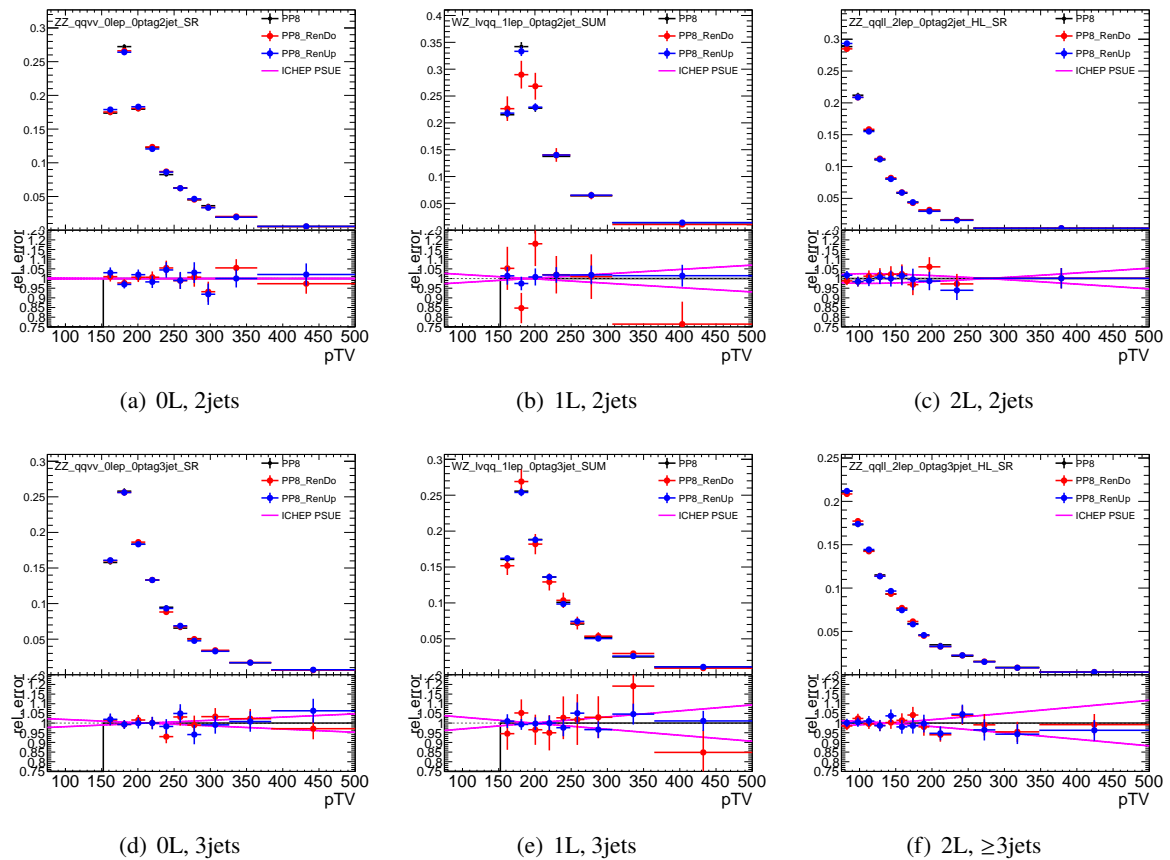


Figure 60: Shape variation of the p_T^V variable for 2 jet (top), (\geq)3 jet (bottom) in the 0L (left), 1L (middle) and 2L (right) regions for the Ren shower tune component.

Not reviewed, for internal circulation only

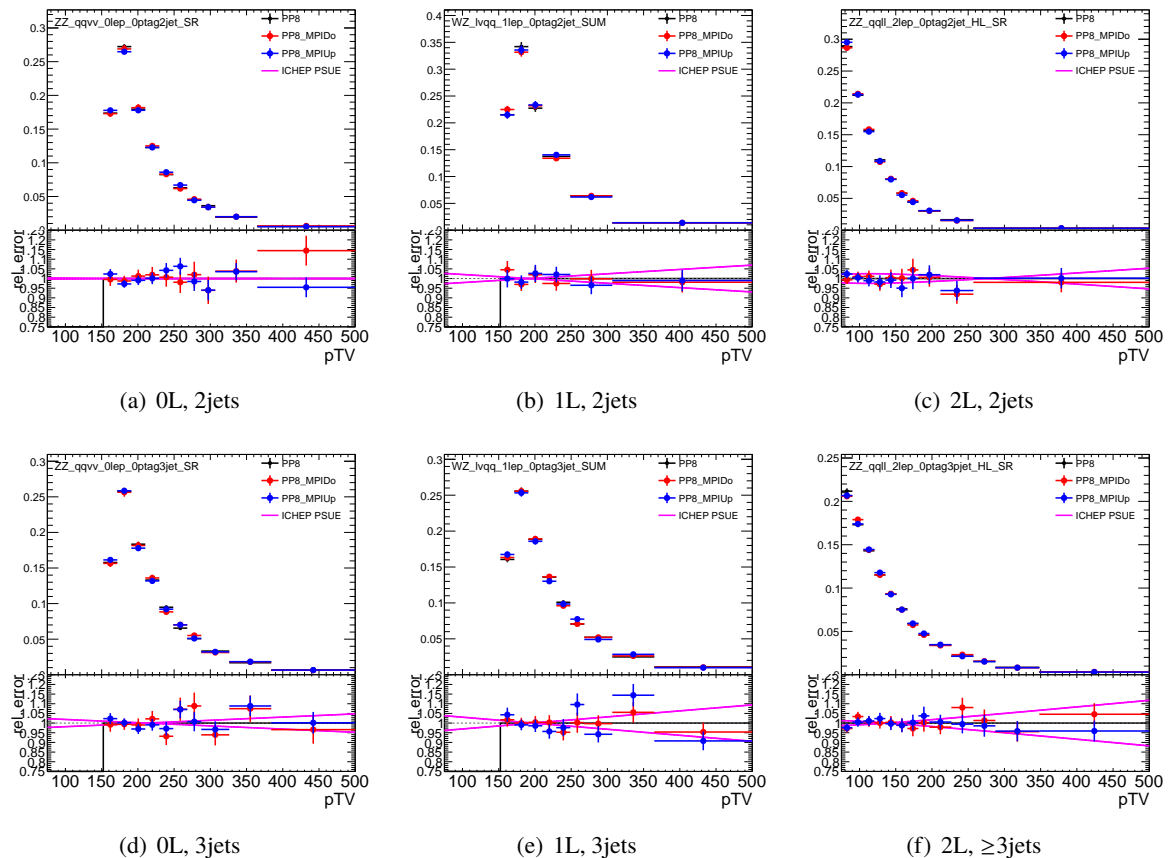


Figure 61: Shape variation of the p_T^V variable for 2 jet (top), (\geq)3 jet (bottom) in the 0L (left), 1L (middle) and 2L (right) regions for the MPI shower tune component.

1584 **E.1.5. m_{bb} shape**

1585 Figure 62 shows the comparison between Powheg+Pythia8 and Powheg+Herwig++ for the m_{bb} variable in
 1586 the three channels. No valid simple functional form has been found to approximate the observed variation.
 1587 For this reason the uncertainty will be parameterised with a binned histogram after the (TH1) smoothing
 1588 has been applied.

Not reviewed, for internal circulation only

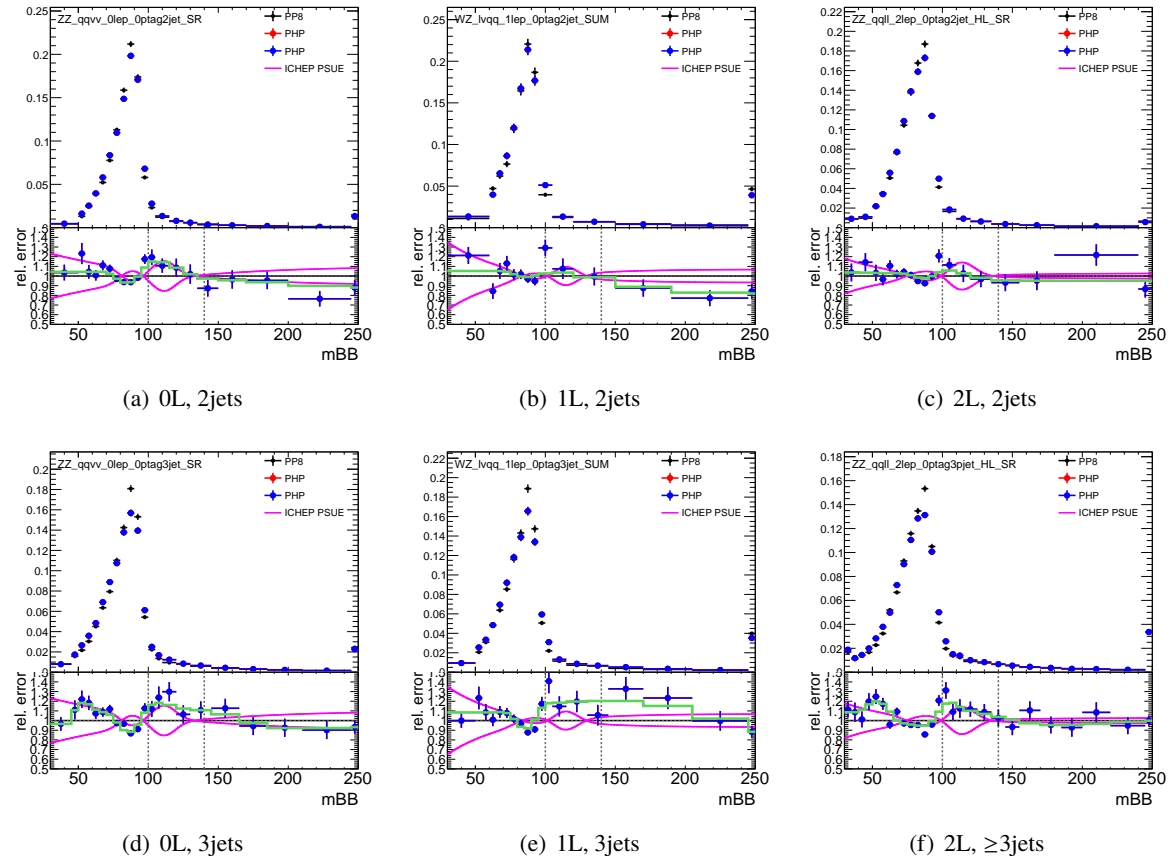


Figure 62: Shape variation of the m_{bb} variable for 2 jet (top), (\geq 3 jet (bottom) in the 0L (left), 1L (middle) and 2L (right) regions comparing Powheg+Pythia8 and Powheg+Herwig++.

1589 Figures 63, 64, 65, 66 show the comparison of the four shower tune variations for the m_{bb} variable in
 1590 the three channels. No appreciable effects can be seen within the available statistics. The parton shower
 1591 shape uncertainty will be extracted from the comparison between Pythia8 and Herwig++.

Not reviewed, for internal circulation only

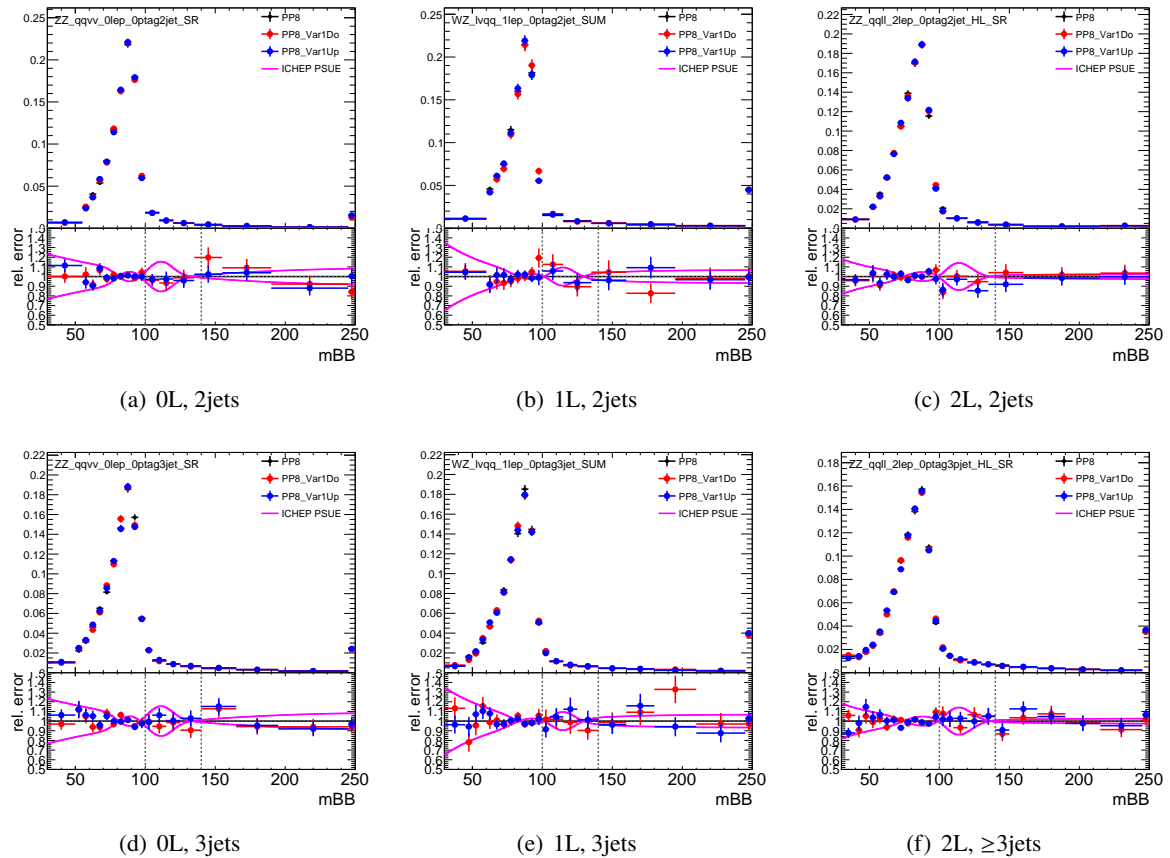


Figure 63: Shape variation of the m_{bb} variable for 2 jet (top), (\geq)3 jet (bottom) in the 0L (left), 1L (middle) and 2L (right) regions for the Var1 shower tune component.

Not reviewed, for internal circulation only

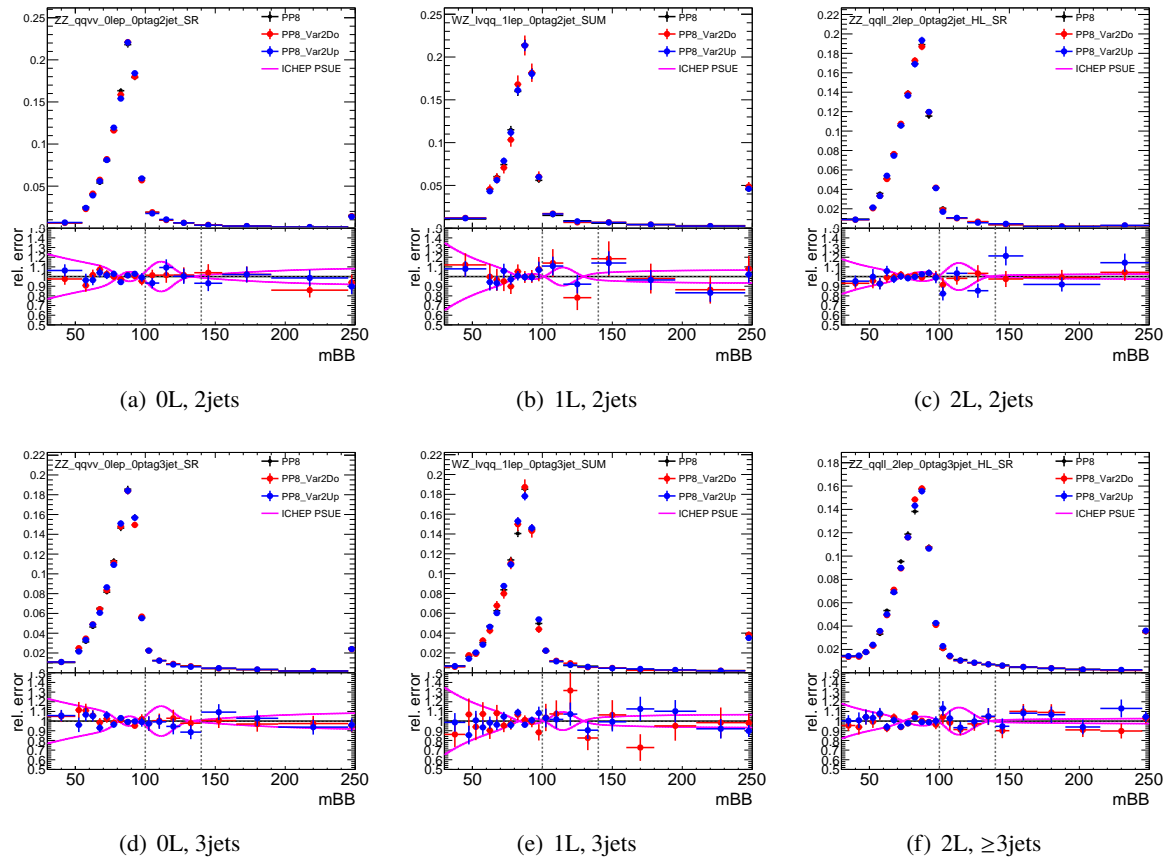


Figure 64: Shape variation of the m_{bb} variable for 2 jet (top), (\geq)3 jet (bottom) in the 0L (left), 1L (middle) and 2L (right) regions for the Var2 shower tune component.

Not reviewed, for internal circulation only

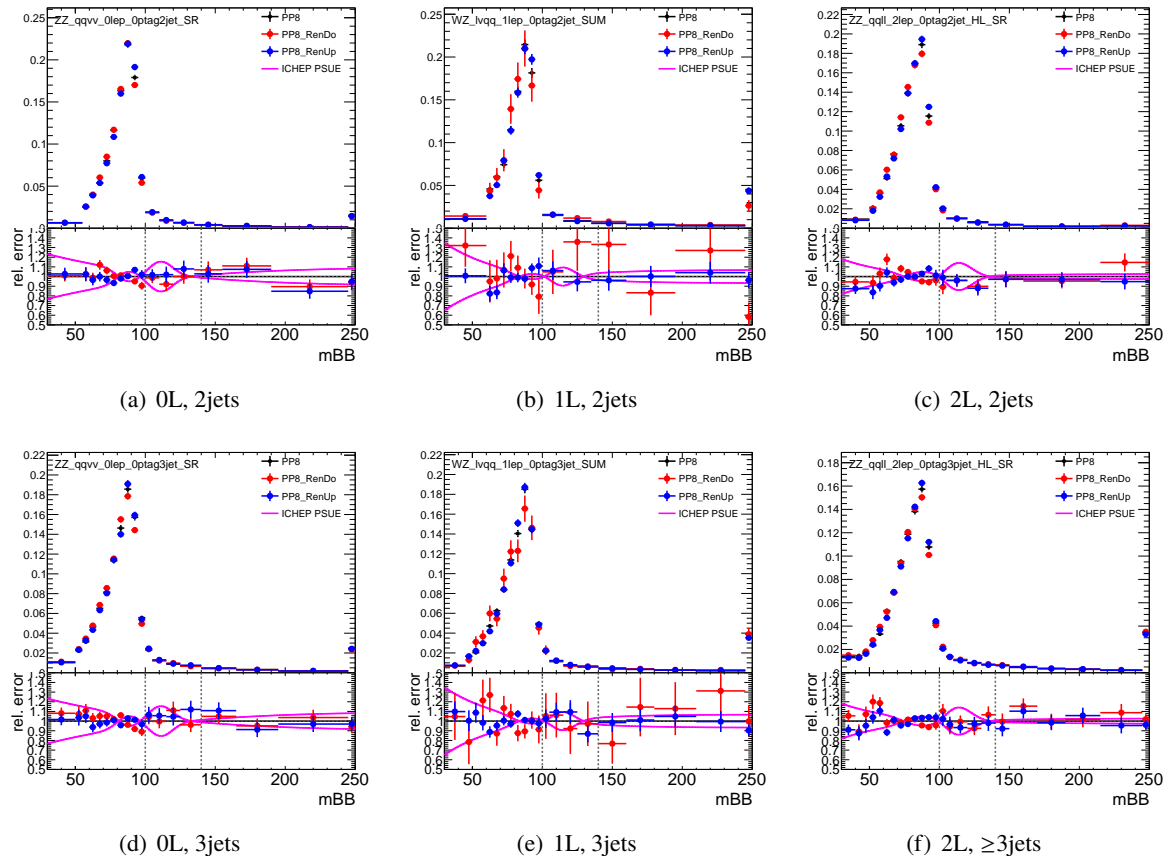


Figure 65: Shape variation of the m_{bb} variable for 2 jet (top), (\geq)3 jet (bottom) in the 0L (left), 1L (middle) and 2L (right) regions for the Ren shower tune component.

Not reviewed, for internal circulation only

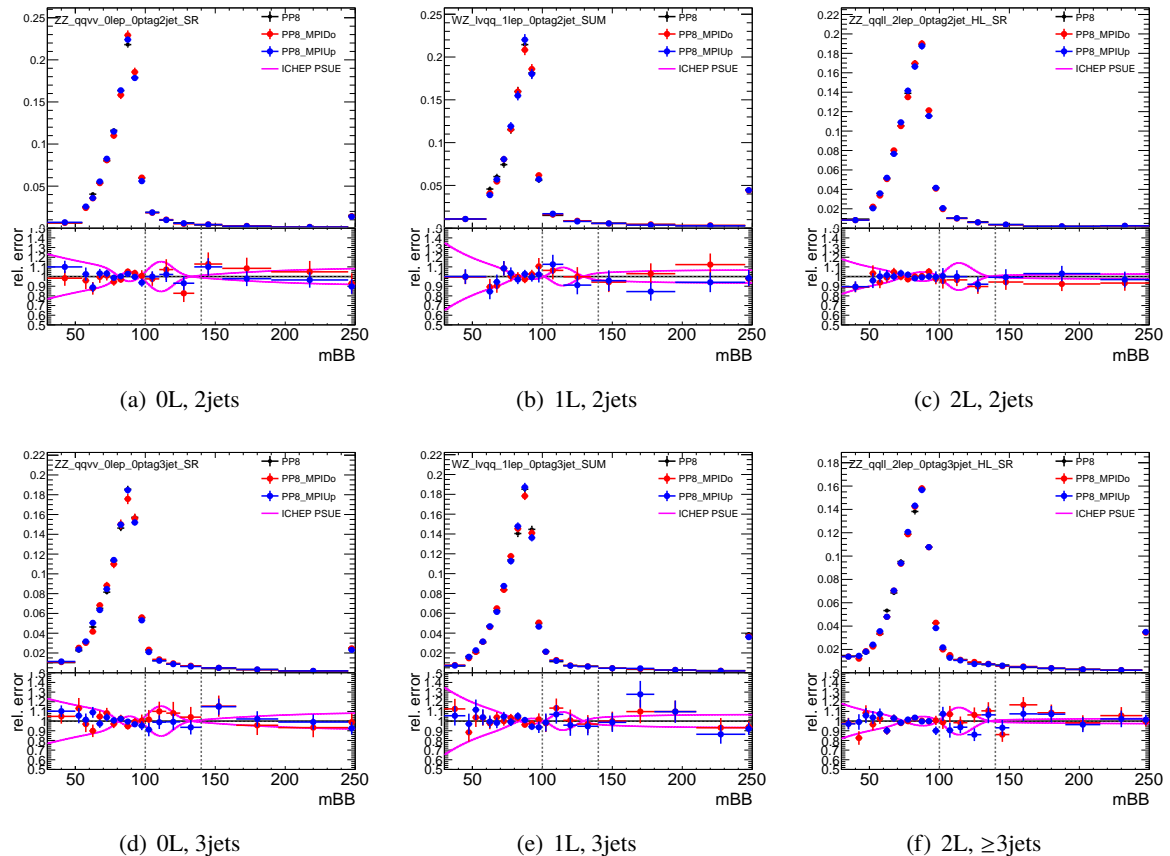


Figure 66: Shape variation of the m_{bb} variable for 2 jet (top), $(\geq)3$ jet (bottom) in the 0L (left), 1L (middle) and 2L (right) regions for the MPI shower tune component.

1592 **E.2. Breakdown of scale variations**

1593 The breakdown of contributions to the acceptance uncertainties from renormalisation and factorisation
 1594 scale variations, for inclusive jet bins as used as input to the Stewart-Tackman method are given here
 1595 for each channel. Both the primary signal process and the secondary (subdominant) process in a given
 1596 channel have been investigated.

1597 **E.2.1. 0L**

1598 For the 0-lepton channel the breakdown is given in Table 58 and Table 59. The very late uncertainties
 1599 for the $WZ \rightarrow qqvv$ are related to the fact that, when requesting 2 b-tagged jets, the process become
 1600 irreducible and the selected jets for the Higgs candidate often includes an ISR jet.

	$ZZ \rightarrow qqvv$		
	$\geq 2j$	$\geq 3j$	$\geq 4j$
MCstat. SH221	$\pm 1.1\%$	$\pm 1.3\%$	$\pm 1.6\%$
SH221: Ren	-3.1 / +3.2 %	-7.0 / +7.8 %	-13.5 / +16.9 %
SH221: Fac	+0.2 / +0.4 %	-0.0 / +0.7 %	-0.7 / +0.9 %
SH221: FR	-3.5 / +2.9 %	-7.4 / +8.0 %	-14.5 / +17.5 %
max scale	$\pm 3.5\%$	$\pm 8.0\%$	$\pm 17.5\%$
yield frac.	1.000	0.663	0.366

Table 58: Systematic uncertainties on inclusive jet bins acceptances for ZZ diboson process in the 0L channel.

	$WZ \rightarrow qqvv$			$WZ \rightarrow lvqq$		
	$\geq 2j$	$\geq 3j$	$\geq 4j$	$\geq 2j$	$\geq 3j$	$\geq 4j$
MCstat. SH221	$\pm 2.3\%$	$\pm 2.4\%$	$\pm 2.6\%$	$\pm 2.1\%$	$\pm 2.3\%$	$\pm 2.7\%$
SH221: Ren	-11.2 / +13.1 %	-12.2 / +14.5 %	-14.0 / +16.8 %	-3.8 / +4.0 %	-6.0 / +6.7 %	-10.2 / +12.0 %
SH221: Fac	+0.4 / -0.4 %	+0.4 / -0.3 %	+0.3 / -0.4 %	-0.0 / -0.1 %	+0.5 / -0.1 %	+0.3 / +0.0 %
SH221: FR	-11.1 / +12.8 %	-12.1 / +14.2 %	-13.8 / +16.6 %	-4.3 / +3.1 %	-6.0 / +5.9 %	-10.2 / +11.7 %
max scale	$\pm 12.8\%$	$\pm 14.2\%$	$\pm 16.6\%$	$\pm 4.3\%$	$\pm 6.0\%$	$\pm 11.7\%$
yield frac.	1.000	0.939	0.782	1.000	0.827	0.547

Table 59: Systematic uncertainties on inclusive jet bins acceptances for WZ diboson processes in the 0L channel.

1601 **E.2.2. 1L**

1602 For the 1-lepton channel the breakdown is given in Table 61.

1603 **E.2.3. 2L**

1604 For the 2-lepton channel the breakdown is given in Table ?? for the sum of the low and high Vp_T regions
 1605 and for the two regions independently.

	$WZ \rightarrow l\nu qq$			$ZZ \rightarrow ll qq$		
	$\geq 2j$	$\geq 3j$	$\geq 4j$	$\geq 2j$	$\geq 3j$	$\geq 4j$
MCstat. SH221	$\pm 0.9\%$	$\pm 1.0\%$	$\pm 1.1\%$	$\pm 2.9\%$	$\pm 3.2\%$	$\pm 3.8\%$
SH221: Ren	-5.5 / +6.4 %	-8.2 / +9.8 %	-12.2 / +15.1 %	-8.9 / +9.6 %	-13.4 / +17.1 %	-17.1 / +22.5 %
SH221: Fac	+0.9 / -0.3 %	+1.0 / -0.5 %	+1.1 / -0.5 %	+1.9 / -1.8 %	+0.9 / -0.8 %	+0.2 / -0.2 %
SH221: FR	-5.2 / +5.1 %	-7.8 / +8.2 %	-11.7 / +13.6 %	-7.6 / +7.4 %	-12.9 / +16.4 %	-17.0 / +22.9 %
max scale	$\pm 5.2\%$	$\pm 8.2\%$	$\pm 13.6\%$	$\pm 7.6\%$	$\pm 16.4\%$	$\pm 22.9\%$
yield frac.	1.000	0.835	0.597	1.000	0.845	0.568

Table 60: Systematic uncertainties on inclusive jet bins acceptances for diboson processes in the 1L channel.

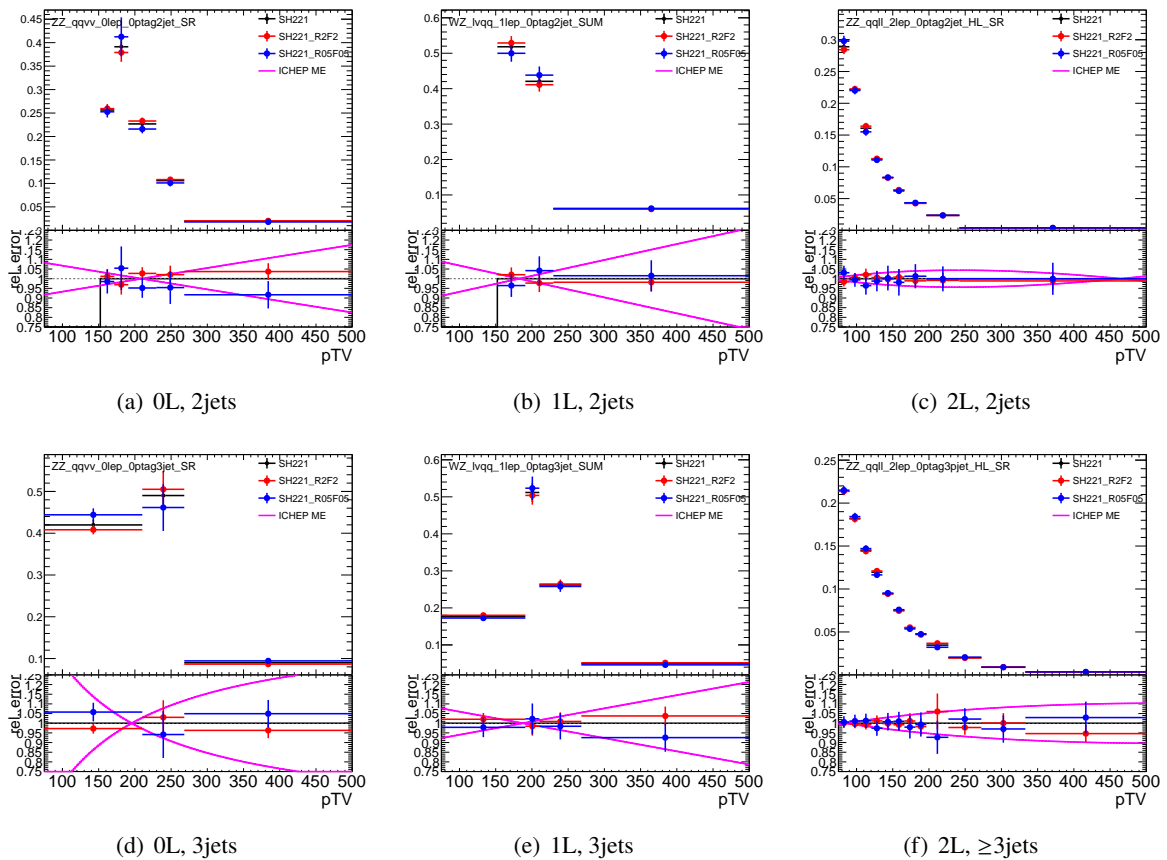
	low+high		low		high	
	$\geq 2j$	$\geq 3j$	$\geq 2j$	$\geq 3j$	$\geq 2j$	$\geq 3j$
MCstat. SH221	$\pm 0.7\%$	$\pm 0.9\%$	$\pm 0.8\%$	$\pm 1.1\%$	$\pm 1.3\%$	$\pm 1.5\%$
SH221: Ren	-3.4 / +4.6 %	-7.8 / +10.3 %	-3.1 / +4.3 %	-8.0 / +10.7 %	-4.0 / +5.1 %	-7.5 / +9.5 %
SH221: Fac	+0.9 / -0.1 %	+0.6 / +0.2 %	+0.9 / -0.2 %	+0.6 / +0.1 %	+0.9 / +0.1 %	+0.7 / +0.3 %
SH221: FR	-2.9 / +3.9 %	-7.6 / +9.9 %	-2.5 / +3.8 %	-7.6 / +10.5 %	-3.9 / +4.2 %	-7.5 / +8.7 %
max scale	$\pm 3.9\%$	$\pm 9.9\%$	$\pm 3.8\%$	$\pm 10.5\%$	$\pm 4.2\%$	$\pm 8.7\%$
yield frac.	1.000	0.620	1.000	0.591	1.000	0.688

Table 61: Systematic uncertainties on inclusive jet bins acceptances for ZZ diboson processes in the 2L channel.

1606 E.2.4. V p_T shape1607 Some common considerations on shape effects in the p_T^V distribution arising from scale uncertainties:

- 1608 • the effect of change in factorisation scale is subleading with respect to the change in renormalisation
1609 scale therefore only the effect of coherent variations will be shown
- 1610 • for the coherent RF variations the shape effect are always compatible with the MC statistical
1611 uncertainty of the nominal sample which is already included in the sys computation
- 1612 • the shape derived for ICHEP can continue to be used with the exception of the 0L 3j channel where
1613 the ICHEP uncertainty is certainly overestimated and the corresponding 2J variation will be used

Not reviewed, for internal circulation only

Figure 67: Shape variation of the p_T^V variable for 2 jet (top), (\geq 3 jet (bottom) in the 0L (left), 1L (middle) and 2L (right) regions comparing different renormalization and factorization scales from the diboson processes.

1614 **E.2.5. m_{bb} shape**1615 Some common considerations on shape effects in the m_{bb} distribution arising from scale uncertainties:

- 1616 • the effect of change in factorisation scale is subleading with respect to the change in renormalisation
1617 scale therefore only the effect of coherent variations will be shown
- 1618 • no strong effects are visible in the 2-jet channel while a common effect is observed in the high m_{bb}
1619 tail in the (\geq 3) regions
- 1620 • the effect is not completely captured by the shape uncertainties used at ICHEP in all regions. At the
1621 same time, the effect is significantly smaller than the difference between Powheg and Sherpa.

Not reviewed, for internal circulation only

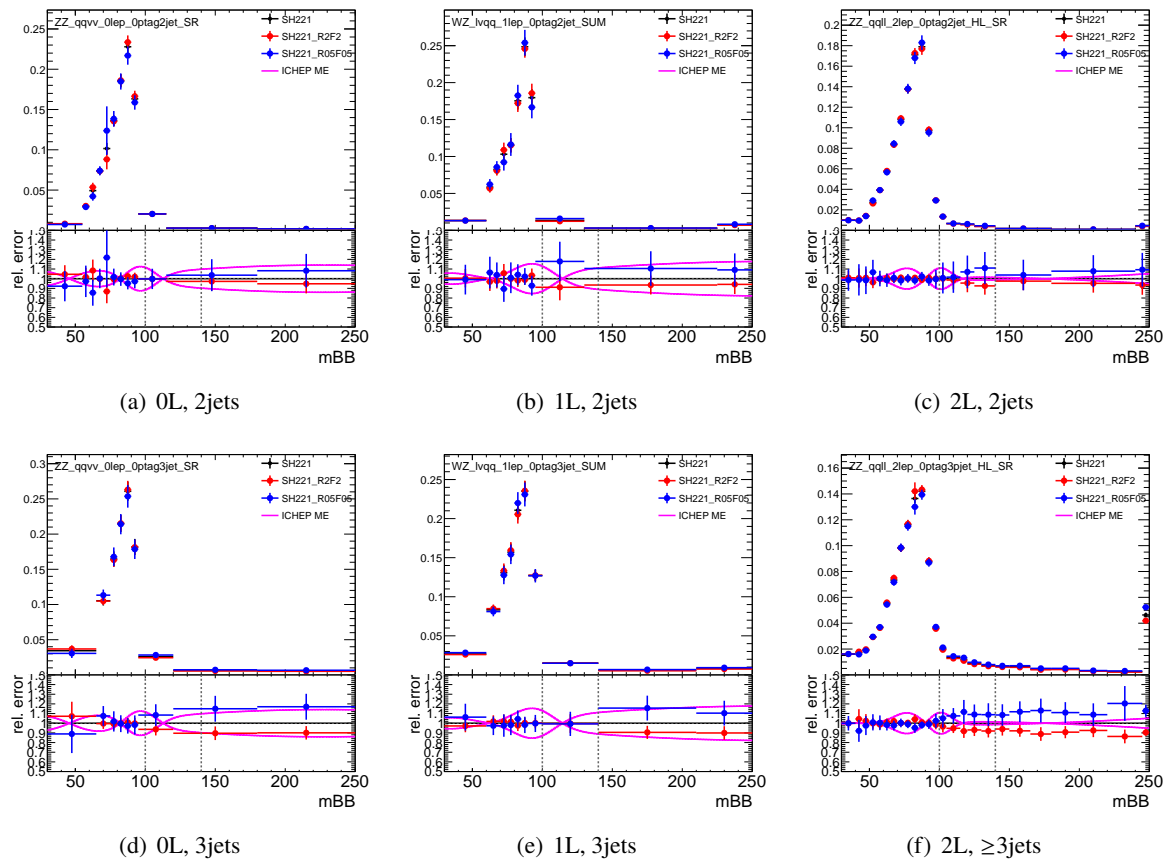


Figure 68: Shape variation of the m_{bb} variable for 2 jet (top), (\geq 3) jet (bottom) in the 0L (left), 1L (middle) and 2L (right) regions comparing different renormalization and factorization scales from the diboson processes.

1622 E.3. Sherpa vs Powheg

1623 As a special case the comparison between Powheg+Pythia8 and Sherpa2.2.1 is considered. Given the
 1624 very different strategy in the modelling of extra jet radiation between the 2 samples, the difference is not
 1625 considered in the list of acceptance uncertainties, nevertheless, the comparison of the shapes is performed.
 1626 In particular for the m_{bb} case the two generators have a different treatment of the γ^* contribution.
 1627 Figure 69 shows the comparison for the V_{PT} shape; no major differences are found within the MC
 1628 statistical uncertainty. Aside from the 0L 3-jets regions previously commented upon, the differences
 1629 between the two generators are encompassed by the shape uncertainties used at ICHEP.

Not reviewed, for internal circulation only

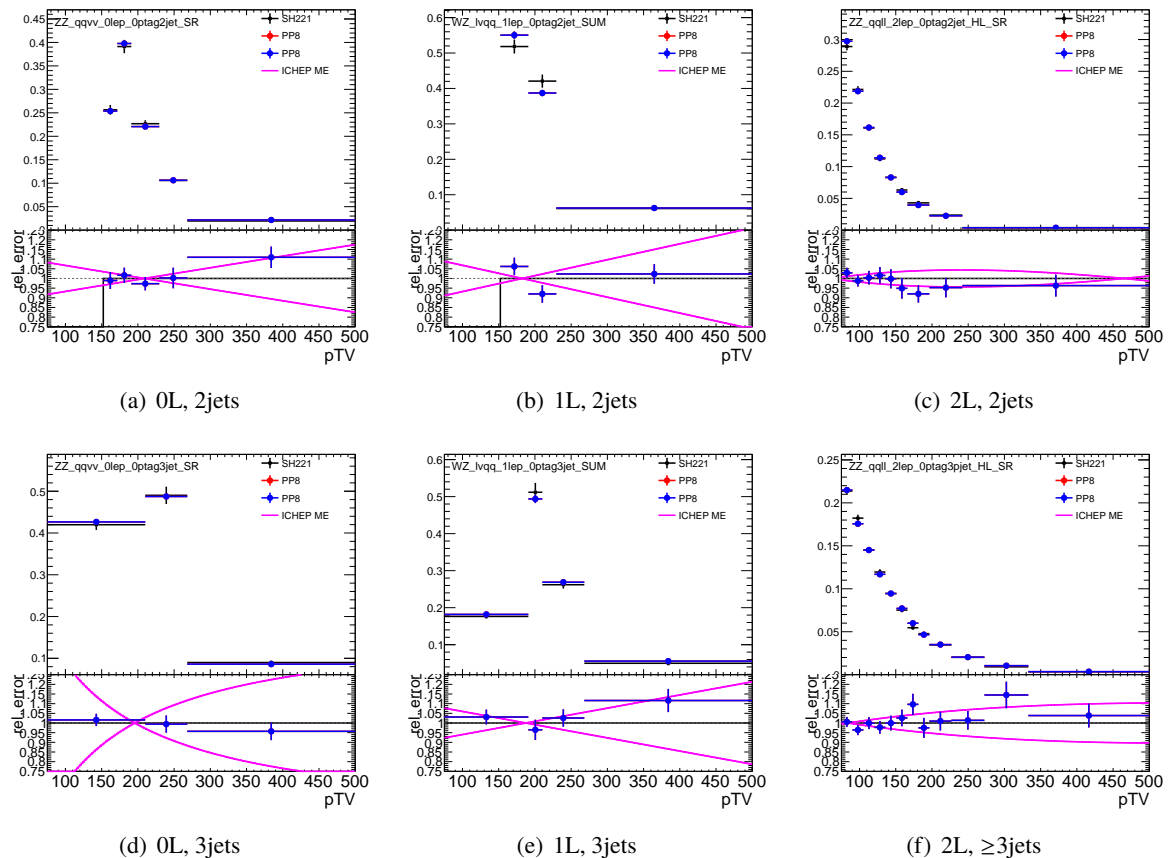


Figure 69: Shape variation of the p_T^V variable for 2 jet (top), (\geq)3 jet (bottom) in the 0L (left), 1L (middle) and 2L (right) regions comparing Sherpa 2.2.1 and Powheg+Pythia8 the diboson processes.

1630 Figure 70 shows the comparison for the m_{bb} shape. The variation in the 2-jet region could be well
 1631 described by a tanh function. The variations in the 3-jet regions will be approximated by a 3rd degree
 1632 polinomina whose range is capped at 250 GeV.

Not reviewed, for internal circulation only

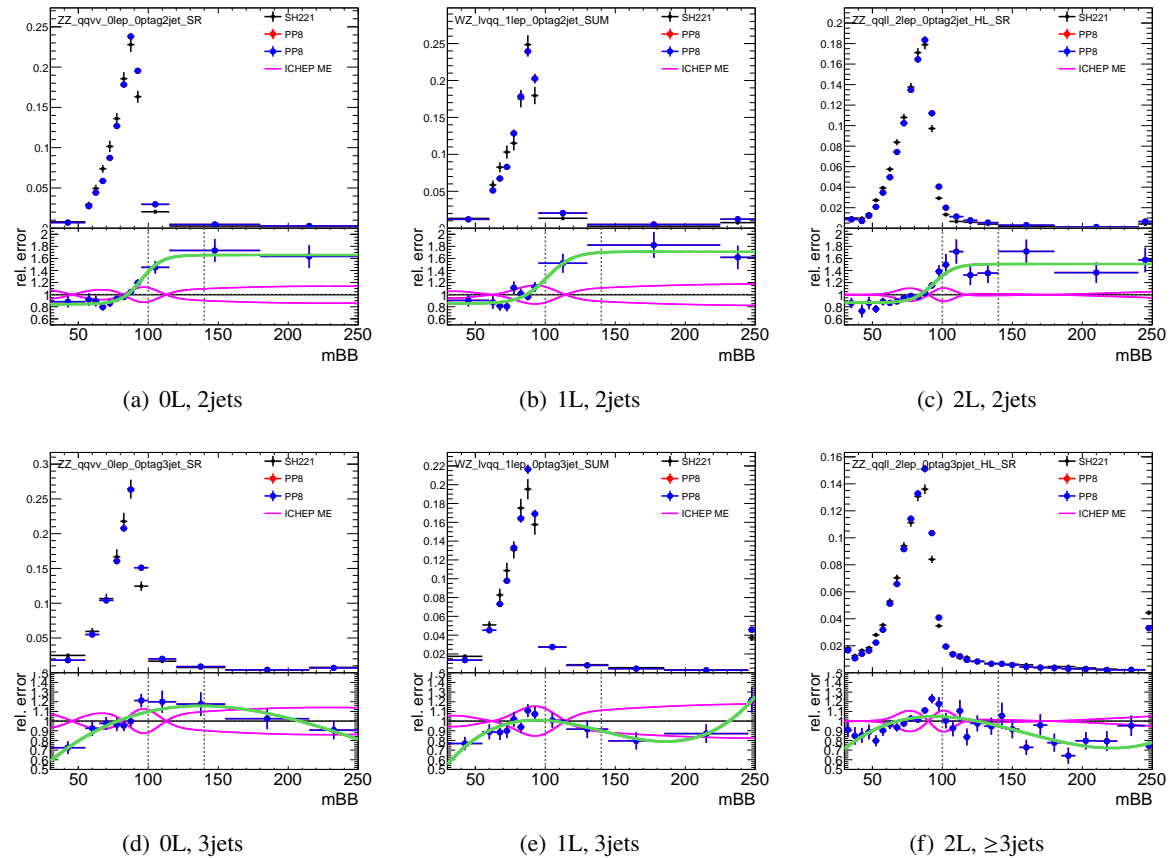


Figure 70: Shape variation of the m_{bb} variable for 2 jet (top), (\geq)3 jet (bottom) in the 0L (left), 1L (middle) and 2L (right) regions comparing Sherpa 2.2.1 and Powheg+Pythia8 the diboson processes.

1633 **E.4. Miscellanea**

1634 This section computes residual extrapolation uncertainties:

- 1635 • 1-to-0 lepton extrapolation uncertainties for the WZ process, Table 62. A maximum extrapolation
1636 uncertainty of 11% has been obtained.
- 1637 • 2-to-0 lepton extrapolation uncertainties for the ZZ process, Table 63. A maximum extrapolation
1638 uncertainty of 6% has been obtained. It should be noted that the effect of the factorisation and
1639 renormalisation scale has not been considered in this case given the different jet multiplicity selection
1640 of the two channel. At the same time, it should be noted that the full Stewart-Tackmann treatment
1641 has been applied hence the 0L selection already contain an additional uncertainty covering the 4-th
1642 jet veto.

Systematic	WZ: 2j	WZ: 3j	WZ: 2+3
MCstat. SH221	$\pm 6.0\%$	$\pm 4.7\%$	$\pm 3.7\%$
MCstat. PHP	$\pm 3.0\%$	$\pm 2.4\%$	$\pm 1.8\%$
MCstat. PP8	$\pm 2.8\%$	$\pm 2.2\%$	$\pm 1.7\%$
PStune: Var1	-1.3 / +0.7 %	+2.7 / +4.1 %	+1.1 / +2.6 %
PStune: Var2	-0.6 / -4.1 %	+1.5 / +3.6 %	+0.6 / +0.5 %
PStune: Ren	+1.1 / +1.1 %	-1.8 / -1.8 %	-0.8 / -0.8 %
PStune: MPI	+1.6 / -3.8 %	-1.9 / +1.4 %	-0.5 / -0.7 %
PStune: TOT	$\pm 5.8\%$	$\pm 6.0\%$	$\pm 2.9\%$
PS: Pythia VS Herwig	-7.2 %	10.5 %	3.4 %
TOT PS	$\pm 7.2\%$	$\pm 10.5\%$	$\pm 3.4\%$
SH221: Ren	-0.9 / +2.1 %	+0.3 / -0.1 %	-0.3 / +0.9 %
SH221: Fac	-2.9 / -0.6 %	-0.1 / +0.0 %	-1.1 / -0.2 %
SH221: FR	-3.3 / +0.6 %	+0.3 / -0.4 %	-1.3 / +0.1 %
max scale	$\pm 3.3\%$	$\pm 0.4\%$	$\pm 1.3\%$
TOTAL	$\pm 7.9\%$	$\pm 10.5\%$	$\pm 3.6\%$

Table 62: Systematic uncertainties on 1-to-0 lepton extrapolation for the $WZ \rightarrow l\nu qq$ process.

Systematic	ZZ: 2j	ZZ ($\geq 3j$)	ZZ all
MCstat. SH221	$\pm 2.1\%$	$\pm 2.3\%$	$\pm 1.5\%$
MCstat. PHP	$\pm 1.1\%$	$\pm 1.0\%$	$\pm 0.8\%$
MCstat. PP8	$\pm 1.1\%$	$\pm 1.0\%$	$\pm 0.7\%$
PStune: Var1	-0.3 / -0.4 %	+2.7 / +2.9 %	+1.3 / +1.2 %
PStune: Var2	-0.9 / -1.4 %	+1.7 / +3.3 %	+0.3 / +0.9 %
PStune: Ren	-1.7 / -1.7 %	+0.9 / +0.9 %	-0.6 / -0.6 %
PStune: MPI	-1.9 / -0.7 %	+3.4 / +2.6 %	+0.7 / +1.0 %
PStune: TOT	$\pm 2.9\%$	$\pm 5.7\%$	$\pm 2.0\%$
PS: Pythia VS Herwig	0.3 %	-3.7 %	-2.0 %
TOT PS	$\pm 2.9\%$	$\pm 5.7\%$	$\pm 2.0\%$

Table 63: Systematic uncertainties on 2-to-0 lepton extrapolation for the ZZ process.

1643 F. Additional material for $W+jets$ modeling systematics

1644 This appendix describes detailed information on the modelling uncertainties for the $W+jets$ background
 1645 described in Section 3.1.5.

1646 F.1. Breakdown of normalisation/extrapolation uncertainties

1647 F.1.1. njet extrapolation

1648 Table 64 contains the full breakdown of the uncertainty on the 3j/2j ratio in all the analysis regions for the
 1649 Olepton and 1lepton channel. The total uncertainties are reasonably consistent between 1lepton WCR, SR
 1650 and Olepton region. The uncertainty is mainly driven by the SHERPA 2.2.1 scale variations. A common
 1651 uncertainty of 18% is applied to all the 3jet regions. (residual effects could be consider for decor relation
 1652 purposes but they will only amount to a few % effects.

Systematic	1l: SR 2j/3j	1l: WCR 2j/3j	1l: SR+WCR 2j/3j	0l: 2j/3j
MCstat. 21: ckkw15	$\pm 1.4 \%$	$\pm 3.1 \%$	$\pm 1.3 \%$	$\pm 4.1 \%$
MCstat. 21: ckkw30	$\pm 1.8 \%$	$\pm 4.5 \%$	$\pm 1.6 \%$	$\pm 5.5 \%$
MCstat. 21: qsf025	$\pm 2.1 \%$	$\pm 7.1 \%$	$\pm 2.0 \%$	$\pm 4.4 \%$
MCstat. 21: qsf4	$\pm 1.8 \%$	$\pm 4.3 \%$	$\pm 1.7 \%$	$\pm 5.0 \%$
MCstat. 221: nomin	$\pm 1.1 \%$	$\pm 1.8 \%$	$\pm 1.0 \%$	$\pm 1.3 \%$
MCstat. MG Ht	$\pm 1.2 \%$	$\pm 2.6 \%$	$\pm 1.1 \%$	$\pm 2.3 \%$
2.1: ckkw	$\pm 3.3 \%$	$\pm 4.8 \%$	$\pm 3.6 \%$	$\pm 4.2 \%$
2.1: qsf	$\mp 2.8 \%$	$\mp 8.3 \%$	$\mp 3.6 \%$	$\mp 1.0 \%$
221: Ren	$-12.3 / +12.1 \%$	$-11.2 / +11.8 \%$	$-12.1 / +12.1 \%$	$-10.4 / +8.7 \%$
221: Fact	$+0.2 / +0.1 \%$	$+0.2 / +1.2 \%$	$+0.2 / +0.2 \%$	$-0.5 / -0.1 \%$
221: RenFact	$-12.8 / +11.7 \%$	$-11.6 / +12.4 \%$	$-12.6 / +11.8 \%$	$-10.3 / +9.0 \%$
PDF13000	$\mp 0.6 \%$	$\pm 0.9 \%$	$\mp 0.3 \%$	$\mp 0.7 \%$
PDF25300	$\mp 0.5 \%$	$\pm 0.7 \%$	$\mp 0.3 \%$	$\mp 0.4 \%$
PDFmax	$\mp 0.5 \%$	$\pm 0.9 \%$	$\mp 0.3 \%$	$\mp 0.4 \%$
Sherpa VS MG	$\mp 8.9 \%$	$\mp 13.2 \%$	$\mp 9.6 \%$	$\mp 10.4 \%$
TOTAL	$\pm 15.7 \%$	$\pm 20.0 \%$	$\pm 16.2 \%$	$\pm 14.7 \%$

Table 64: Systematic uncertainties on 2j/3j extrapolation for $W+hf$ in various analysis regions. The MCstat. terms for the various generators are only shown for completeness and not included in the TOTAL.

1653 F.1.2. CR-SR extrapolation

1654 Table 65 contains the full breakdown of the uncertainty on the SR/WCR yields ratio in all the 1lepton
 1655 analysis regions. The extrapolation uncertainty is particularly small with no single variation exceeding
 1656 3.5%. Such value could be considered surprising given that the extrapolation is performed over the
 1657 m_{bb} distribution which definitely shows large differences between SHERPA 221 and MADGRAPH. At the
 1658 same time, it has been found that the m_{bb} variation is accompanied by a complementary variation on the
 1659 other variable used to compute the extrapolation uncertainty (m_{top}) which goes in the opposite direction
 1660 w.r.t. the cut defining the WCR and therefore the two effects partly compensate. **This is currently under**
 1661 **intense studies also using samples at reco level; therefore a conservative value of 10% is currently being**
 1662 **considered.**

Systematic	2j: WCR/SR	3j: WCR/SR
MCstat. 21: ckkw15	$\pm 3.0\%$	$\pm 1.7\%$
MCstat. 21: ckkw30	$\pm 4.0\%$	$\pm 2.7\%$
MCstat. 21: qsf025	$\pm 7.1\%$	$\pm 2.1\%$
MCstat. 21: qsf4	$\pm 4.0\%$	$\pm 2.3\%$
MCstat. 221: nomin	$\pm 1.8\%$	$\pm 1.1\%$
MCstat. MG Ht	$\pm 2.1\%$	$\pm 1.9\%$
2.1: ckkw	$\mp 0.8\%$	$\mp 2.3\%$
2.1: qsf	$\mp 4.4\%$	$\pm 1.2\%$
221: Ren	$+0.1 / +0.4\%$	$-1.1 / +0.7\%$
221: Fact	$+0.1 / +0.4\%$	$+0.1 / -0.7\%$
221: RenFact	$+0.6 / +0.2\%$	$-0.8 / -0.4\%$
PDF13000	$\pm 1.4\%$	$\mp 0.1\%$
PDF25300	$\pm 1.3\%$	$\pm 0.1\%$
PDFmax	$\pm 1.4\%$	$\pm 0.1\%$
Sherpa VS MG	$\mp 3.1\%$	$\pm 1.8\%$
TOTAL	$\pm 5.6\%$	$\pm 3.3\%$

Table 65: Systematic uncertainties on WCR/SR extrapolation for W+hf in 1lepton channel. The MCstat. terms for the various generators are only shown for completeness and not included in the TOTAL.

1663 F.1.3. 0Lepton-1Lepton extrapolation

1664 Table 66 contains the full breakdown of the uncertainty on the yields prediction between 0lepton and
 1665 1lepton channels; for the 1lepton channel, the sum of the WCR and the SR has been considered. A value
 1666 of 5% is assigned to both 0lepton and 1lepton region.

Systematic	2j: 0l/1l	3j: 0l/1l
MCstat. 21: ckkw15	$\pm 3.8\%$	$\pm 2.1\%$
MCstat. 21: ckkw30	$\pm 4.4\%$	$\pm 3.7\%$
MCstat. 21: qsf025	$\pm 4.1\%$	$\pm 2.6\%$
MCstat. 21: qsf4	$\pm 3.9\%$	$\pm 3.6\%$
MCstat. 221: nomin	$\pm 1.4\%$	$\pm 0.8\%$
MCstat. MG Ht	$\pm 1.9\%$	$\pm 1.7\%$
2.1: ckkw	$\pm 1.6\%$	$\pm 1.0\%$
2.1: qsf	$\pm 2.0\%$	$\mp 0.5\%$
221: Ren	$+0.8 / -1.0\%$	$-1.2 / +2.1\%$
221: Fact	$-0.5 / -0.4\%$	$+0.2 / -0.0\%$
221: RenFact	$+1.2 / -0.8\%$	$-1.4 / +1.7\%$
PDF13000	$\pm 0.1\%$	$\pm 0.4\%$
PDF25300	$\pm 0.0\%$	$\pm 0.1\%$
PDFmax	$\pm 0.1\%$	$\pm 0.4\%$
Sherpa VS MG	$\mp 4.5\%$	$\mp 3.7\%$
TOTAL	$\pm 5.3\%$	$\pm 4.2\%$

Table 66: Systematic uncertainties on 0L/1L extrapolation for W+hf. The MCstat. terms for the various generators are only shown for completeness and not included in the TOTAL.

1667 F.1.4. flavour composition

Tables 67,68,69 contains the full breakdown of the uncertainty on the flavour composition for the bc/bb, bl/bb and cc/bb ratios respectively. For each of the three components the largest of the total uncertainty in each region has been considered as common systematic uncertainty. The procedure has been considered separately for the 1lepton and the 0lepton channel, leading to different priors in the two channels but the variations will be treated as correlated. While the approach is probably conservative, the very high purity of bb events in analysis regions significantly reduces the impact of the flavour composition uncertainties.

Systematic	II: WCR 2j	II: SR 2j	II: SR+WCR 2j	0I: 2j	II: WCR 3j	II: SR 3j	II: SR+WCR 3j	0I: 3j
MCstat. 21: ckkw15	$\pm 6.9\%$	$\pm 1.9\%$	$\pm 1.8\%$	$\pm 6.8\%$	$\pm 5.3\%$	$\pm 1.4\%$	$\pm 1.3\%$	$\pm 8.1\%$
MCstat. 21: ckkw30	$\pm 8.1\%$	$\pm 2.1\%$	$\pm 2.0\%$	$\pm 10.9\%$	$\pm 15.9\%$	$\pm 1.8\%$	$\pm 1.8\%$	$\pm 5.4\%$
MCstat. 21: qsf025	$\pm 9.7\%$	$\pm 2.5\%$	$\pm 2.4\%$	$\pm 8.4\%$	$\pm 8.1\%$	$\pm 1.5\%$	$\pm 1.4\%$	$\pm 4.6\%$
MCstat. 21: qsf4	$\pm 8.9\%$	$\pm 2.4\%$	$\pm 2.3\%$	$\pm 9.9\%$	$\pm 6.3\%$	$\pm 1.6\%$	$\pm 1.6\%$	$\pm 8.8\%$
MCstat. 221: nomin	$\pm 3.3\%$	$\pm 1.4\%$	$\pm 1.2\%$	$\pm 2.1\%$	$\pm 3.4\%$	$\pm 0.9\%$	$\pm 0.8\%$	$\pm 1.8\%$
MCstat. MG Ht	$\pm 6.2\%$	$\pm 1.6\%$	$\pm 1.5\%$	$\pm 4.0\%$	$\pm 7.0\%$	$\pm 1.7\%$	$\pm 1.7\%$	$\pm 3.8\%$
2.1: ckkw	$\pm 2.4\%$	$\pm 4.1\%$	$\pm 4.1\%$	$\pm 3.6\%$	$\pm 2.8\%$	$\pm 0.5\%$	$\pm 0.6\%$	$\pm 2.0\%$
2.1: qsf	$\pm 13.9\%$	$\pm 0.6\%$	$\pm 0.5\%$	$\pm 12.9\%$	$\pm 6.0\%$	$\pm 1.0\%$	$\pm 0.6\%$	$\pm 2.5\%$
Ren	$+2.1 / -0.7\%$	$+4.0 / -2.5\%$	$+3.8 / -2.5\%$	$\pm 0.6\%$	$+1.3 / +0.5\%$	$+2.6 / -1.9\%$	$+2.7 / -1.9\%$	$+2.2 / -1.4\%$
Fact	$-0.6 / -0.1\%$	$-0.3 / +0.5\%$	$-0.4 / +0.5\%$	$+0.3 / +0.3\%$	$+0.4 / +2.3\%$	$-0.1 / -0.2\%$	$-0.1 / +0.0\%$	$+0.1 / -0.3\%$
RenFact	$-1.9 / +2.8\%$	$-2.3 / +4.2\%$	$-2.2 / +4.1\%$	$-0.1 / +0.9\%$	$+1.6 / +1.0\%$	$-1.8 / +2.5\%$	$-1.6 / +2.5\%$	$-2.0 / +2.5\%$
PDF13000	$\pm 2.7\%$	$\pm 3.2\%$	$\pm 3.0\%$	$\pm 0.5\%$	$\pm 2.6\%$	$\pm 2.0\%$	$\pm 2.0\%$	$\pm 1.2\%$
PDF25300	$\pm 1.1\%$	$\pm 1.0\%$	$\pm 0.9\%$	$\pm 1.1\%$	$\pm 0.4\%$	$\pm 0.5\%$	$\pm 0.4\%$	$\pm 2.3\%$
PDFmax	$\pm 2.7\%$	$\pm 3.2\%$	$\pm 3.0\%$	$\pm 0.5\%$	$\pm 2.6\%$	$\pm 2.0\%$	$\pm 2.0\%$	$\pm 1.2\%$
Sherpa VS MG	$\pm 24.9\%$	$\pm 3.6\%$	$\pm 4.4\%$	$\pm 9.6\%$	$\pm 20.2\%$	$\pm 14.8\%$	$\pm 15.2\%$	$\pm 14.5\%$
TOTAL	$\pm 28.8\%$	$\pm 7.2\%$	$\pm 7.5\%$	$\pm 16.5\%$	$\pm 21.6\%$	$\pm 15.1\%$	$\pm 15.5\%$	$\pm 15.0\%$

Table 67: Systematic uncertainties on bc/bb extrapolation in $W+hf$ events. The MCstat. terms for the various generators are only shown for completeness and not included in the TOTAL.

Systematic	II: WCR 2j	II: SR 2j	II: SR+WCR 2j	0I: 2j	II: WCR 3j	II: SR 3j	II: SR+WCR 3j	0I: 3j
MCstat. 21: ckkw15	$\pm 3.9\%$	$\pm 1.4\%$	$\pm 1.3\%$	$\pm 4.4\%$	$\pm 2.5\%$	$\pm 1.0\%$	$\pm 0.9\%$	$\pm 2.5\%$
MCstat. 21: ckkw30	$\pm 4.9\%$	$\pm 1.6\%$	$\pm 1.5\%$	$\pm 4.8\%$	$\pm 4.2\%$	$\pm 1.4\%$	$\pm 1.3\%$	$\pm 4.2\%$
MCstat. 21: qsf025	$\pm 14.1\%$	$\pm 3.5\%$	$\pm 3.4\%$	$\pm 4.3\%$	$\pm 3.3\%$	$\pm 1.2\%$	$\pm 1.1\%$	$\pm 3.9\%$
MCstat. 21: qsf4	$\pm 5.4\%$	$\pm 2.2\%$	$\pm 2.0\%$	$\pm 4.1\%$	$\pm 3.5\%$	$\pm 1.1\%$	$\pm 1.0\%$	$\pm 4.1\%$
MCstat. 221: nomin	$\pm 2.0\%$	$\pm 1.2\%$	$\pm 1.0\%$	$\pm 1.4\%$	$\pm 1.6\%$	$\pm 0.5\%$	$\pm 0.5\%$	$\pm 0.9\%$
MCstat. MG Ht	$\pm 3.0\%$	$\pm 1.0\%$	$\pm 1.0\%$	$\pm 2.1\%$	$\pm 3.0\%$	$\pm 1.0\%$	$\pm 0.9\%$	$\pm 1.9\%$
2.1: ckkw	$\pm 1.5\%$	$\pm 0.5\%$	$\pm 0.5\%$	$\pm 0.4\%$	$\pm 2.5\%$	$\pm 2.7\%$	$\pm 2.2\%$	$\pm 2.0\%$
2.1: qsf	$\pm 9.5\%$	$\pm 1.4\%$	$\pm 1.2\%$	$\pm 1.2\%$	$\pm 5.0\%$	$\pm 0.7\%$	$\pm 0.7\%$	$\pm 1.1\%$
Ren	$+2.2 / -2.7\%$	$+3.2 / -2.2\%$	$+3.1 / -2.3\%$	$+2.5 / -1.0\%$	$+1.2 / +0.8\%$	$+3.0 / -1.9\%$	$+3.0 / -1.9\%$	$+2.1 / -1.4\%$
Fact	$-0.4 / -0.8\%$	$+0.2 / +0.1\%$	$+0.2 / -0.0\%$	$+0.7 / -0.1\%$	$+0.6 / +0.5\%$	$\pm 0.2\%$	$+0.2 / -0.1\%$	$+0.2 / -0.1\%$
RenFact	$-2.6 / +1.7\%$	$-2.4 / +4.1\%$	$-2.4 / +3.9\%$	$-1.2 / +2.6\%$	$+0.7 / +0.8\%$	$-2.0 / +2.9\%$	$-1.8 / +2.9\%$	$-1.5 / +2.5\%$
PDF13000	$\pm 1.9\%$	$\pm 0.4\%$	$\pm 0.7\%$	$\pm 0.2\%$	$\pm 0.5\%$	$\pm 0.5\%$	$\pm 0.4\%$	$\pm 0.6\%$
PDF25300	$\pm 1.8\%$	$\pm 0.6\%$	$\pm 0.8\%$	$\pm 0.1\%$	$\pm 0.1\%$	$\pm 0.5\%$	$\pm 0.5\%$	$\pm 0.7\%$
PDFmax	$\pm 1.8\%$	$\pm 0.4\%$	$\pm 0.7\%$	$\pm 0.2\%$	$\pm 0.5\%$	$\pm 0.5\%$	$\pm 0.4\%$	$\pm 0.6\%$
Sherpa VS MG	$\pm 27.7\%$	$\pm 2.4\%$	$\pm 1.1\%$	$\pm 4.6\%$	$\pm 19.4\%$	$\pm 5.2\%$	$\pm 6.0\%$	$\pm 3.5\%$
TOTAL	$\pm 29.5\%$	$\pm 3.9\%$	$\pm 3.3\%$	$\pm 5.1\%$	$\pm 20.3\%$	$\pm 6.4\%$	$\pm 6.9\%$	$\pm 4.6\%$

Table 68: Systematic uncertainties on bl/bb extrapolation in $W+hf$ events. The MCstat. terms for the various generators are only shown for completeness and not included in the TOTAL.

Systematic	I1: WCR 2j	I1: SR 2j	I1: SR+WCR 2j	0l: 2j	I1: WCR 3j	I1: SR 3j	I1: SR+WCR 3j	0l: 3j
MCstat. 21: ckkw15	$\pm 8.5\%$	$\pm 2.8\%$	$\pm 2.7\%$	$\pm 16.4\%$	$\pm 6.7\%$	$\pm 2.5\%$	$\pm 2.3\%$	$\pm 6.8\%$
MCstat. 21: ckkw30	$\pm 8.0\%$	$\pm 3.0\%$	$\pm 2.8\%$	$\pm 11.0\%$	$\pm 7.3\%$	$\pm 2.8\%$	$\pm 2.6\%$	$\pm 8.6\%$
MCstat. 21: qsf025	$\pm 17.6\%$	$\pm 3.3\%$	$\pm 3.6\%$	$\pm 9.9\%$	$\pm 7.7\%$	$\pm 2.7\%$	$\pm 2.5\%$	$\pm 7.5\%$
MCstat. 21: qsf4	$\pm 11.1\%$	$\pm 3.8\%$	$\pm 3.6\%$	$\pm 10.1\%$	$\pm 7.2\%$	$\pm 2.7\%$	$\pm 2.5\%$	$\pm 8.3\%$
MCstat. 221: nomin	$\pm 3.3\%$	$\pm 1.6\%$	$\pm 1.5\%$	$\pm 3.8\%$	$\pm 2.8\%$	$\pm 1.1\%$	$\pm 1.0\%$	$\pm 4.0\%$
MCstat. MG Ht	$\pm 4.1\%$	$\pm 1.5\%$	$\pm 1.4\%$	$\pm 3.0\%$	$\pm 4.6\%$	$\pm 1.6\%$	$\pm 1.5\%$	$\pm 3.1\%$
2.1: ckkw	$\mp 9.2\%$	$\pm 2.1\%$	$\pm 0.9\%$	$\mp 11.0\%$	$\pm 7.3\%$	$\mp 0.9\%$	$\pm 0.2\%$	$\pm 5.5\%$
2.1: qsf	$\pm 16.4\%$	$\pm 0.7\%$	$\pm 2.7\%$	$\mp 1.9\%$	$\mp 4.5\%$	$\mp 0.4\%$	$\mp 1.0\%$	$\pm 0.1\%$
Ren	$+0.9 / -2.2\%$	$+1.5 / -3.9\%$	$+1.4 / -3.7\%$	$+3.1 / -18.3\%$	$-0.2 / -3.0\%$	$+1.4 / -1.5\%$	$+1.2 / -1.7\%$	$+5.6 / -12.1\%$
Fact	$-1.8 / -1.2\%$	$-1.7 / -1.5\%$	$-1.8 / -1.5\%$	$-1.4 / -13.6\%$	$-2.0 / -2.3\%$	$-0.4 / -1.1\%$	$-0.6 / -1.2\%$	$+2.4 / -7.7\%$
RenFact	$-0.9 / +0.8\%$	$-1.5 / +2.2\%$	$-1.4 / +2.0\%$	$-4.6 / -0.3\%$	$-1.0 / +0.0\%$	$-0.0 / +0.5\%$	$-0.1 / +0.5\%$	$-0.5 / +2.3\%$
Sherpa VS MG	$\pm 13.0\%$	$\pm 20.7\%$	$\pm 19.8\%$	$\pm 15.7\%$	$\mp 15.1\%$	$\pm 7.5\%$	$\pm 4.2\%$	$\pm 14.7\%$
TOTAL	$\pm 23.0\%$	$\pm 21.0\%$	$\pm 20.3\%$	$\pm 25.9\%$	$\pm 17.8\%$	$\pm 7.8\%$	$\pm 4.7\%$	$\pm 18.8\%$

Table 69: Systematic uncertainties on cc/bb extrapolation in $W+hf$ events. The MCstat. terms for the various generators are only shown for completeness and not included in the TOTAL. The variation due to different PDF sets are currently being debugged.

1674 **F.2. Single variation shape fit**

1675 The following figures display the fit to the individual shape variations in the various analysis regions.
 1676 The leading shape source (**SHERPA 2.2.1** and **MADGRAPH**) is shown as well as the effect of varying the
 1677 renormalisation scale in **SHERPA 2.2.1**. Other variation of Sherpa internal weight do not lead to a significant
 1678 shape effect.

Not reviewed, for internal circulation only

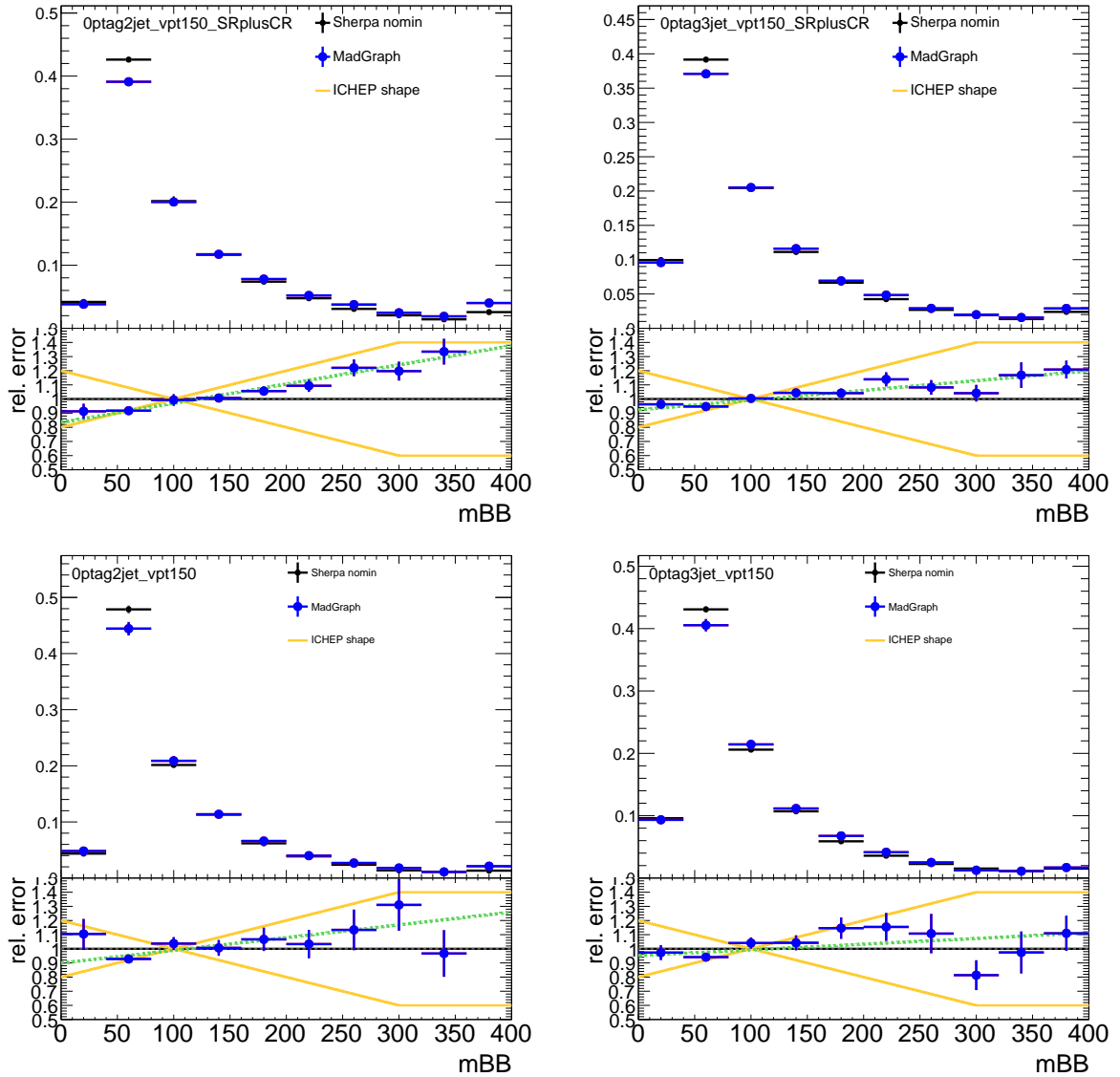


Figure 71: Comparison of normalised m_{bb} shape distributions between **SHERPA 2.2.1** and **MADGRAPH** in all the analysis regions; a linear fit (green line) is performed to the ratio. The effect of the shape used for ICHEP is also reported. 1lepton (top), 0lepton (bottom), 2jet (left), 3jet (right).

Not reviewed, for internal circulation only

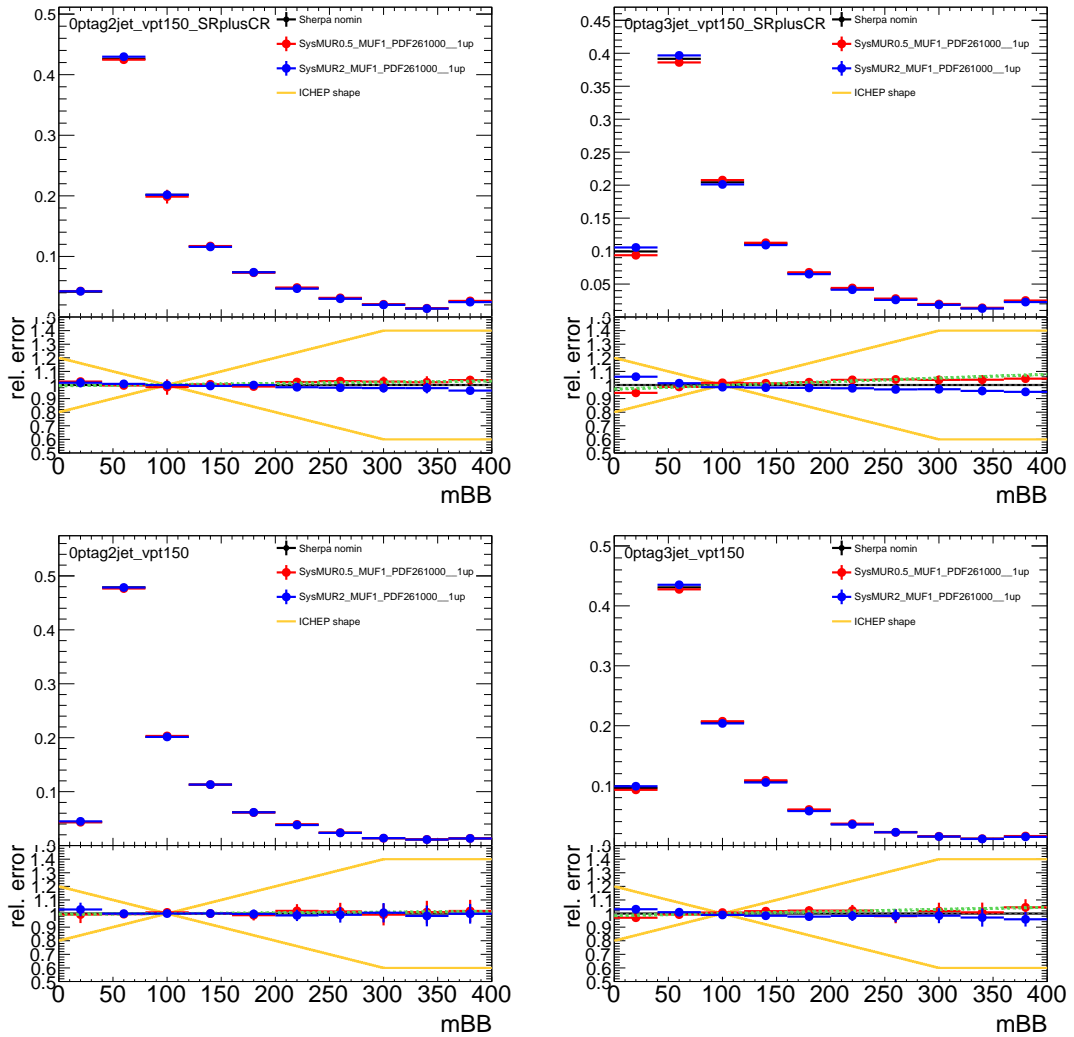


Figure 72: Comparison of normalised m_{bb} shape distributions between the nominal SHERPA 2.2.1 and the variation of the renormalisation scale in all the analysis regions; a linear fit (green line) is performed to the ratio. The effect of the shape used for ICHEP is also reported. 1lepton (top), 0lepton (bottom), 2jet (left), 3jet (right).

Not reviewed, for internal circulation only

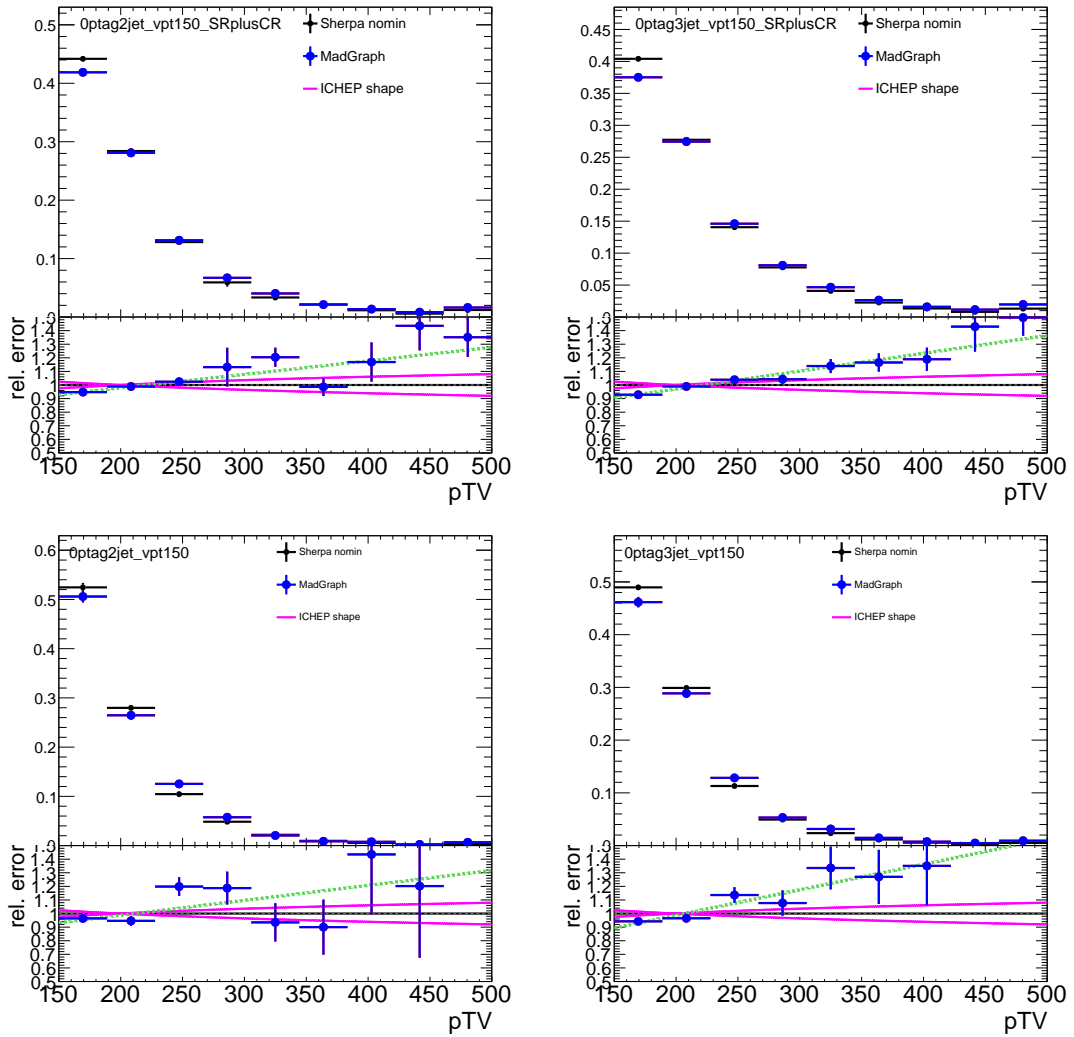


Figure 73: Comparison of normalised V_{PT} shape distributions between SHERPA 2.2.1 and MADGRAPH in all the analysis regions; a linear fit (green line) is performed to the ratio. The effect of the shape used for ICHEP is also reported. 1lepton (top), 0lepton (bottom), 2jet (left), 3jet (right).

Not reviewed, for internal circulation only

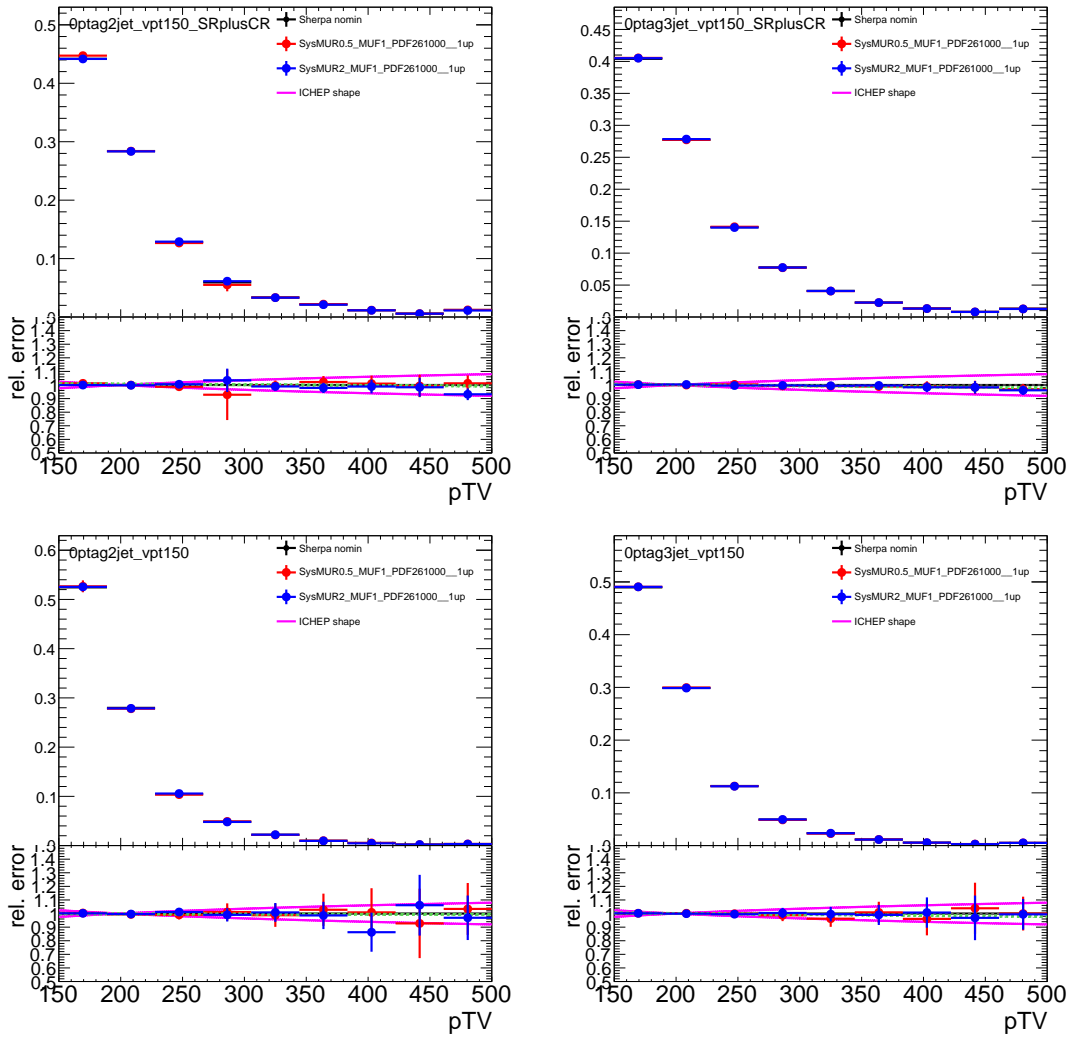


Figure 74: Comparison of normalised V_{pT} shape distributions between the nominal SHERPA 2.2.1 and the variation of the renormalisation scale in all the analysis regions; a linear fit (green line) is performed to the ratio. The effect of the shape used for ICHEP is also reported. 1lepton (top), 0lepton (bottom), 2jet (left), 3jet (right).

1679 F.3. Residual shape effects across regions

1680 A single shape variation for m_{bb} and $V p_T$ is currently be implemented. Additional uncertainties could be
 1681 computed by comparing residual effects across analysis regions; this is obtained by computing the ratio
 1682 of the shape variation between different analysis regions.

1683 Figure 75 shows the shape of residual $V p_T$ uncertainties for different channel and jet multiplicity. Residual
 1684 effects between 2 and 3jet regions are half the size of the total uncertainty and very consistent in Olepton and
 1685 1lepton region; residual effects between Olepton and 1lepton in a given jet multiplicity bin are subdominant
 1686 with respect to the total uncertainty.

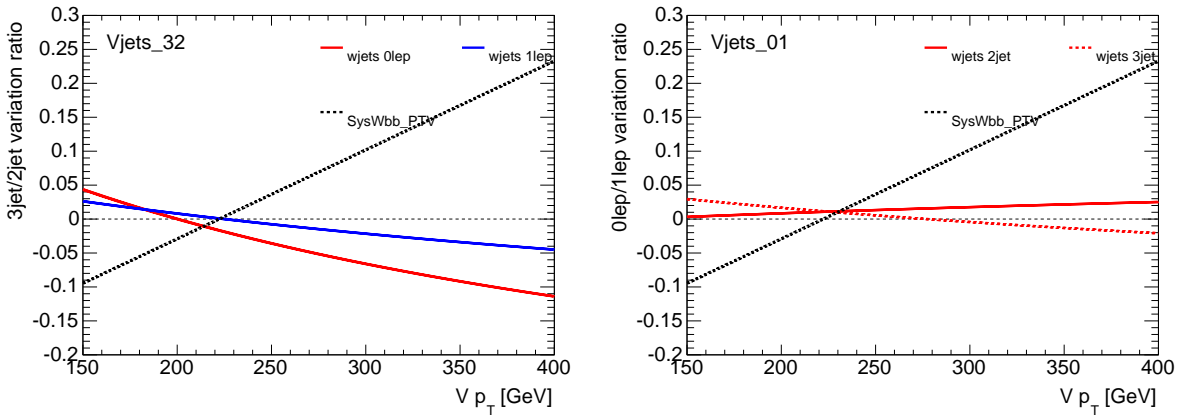


Figure 75: Residual shape uncertainties $V p_T$ between different jet multiplicities (left) and lepton channel (right). The effect of the total common shape uncertainty is also reported for completeness.

1687 Figure 76 shows the shape of residual m_{bb} uncertainties for different channel and jet multiplicity. Residual
 1688 effects between 2 and 3jet regions are half the size of the total uncertainty and very consistent in Olepton and
 1689 1lepton region; residual effects between Olepton and 1lepton in a given jet multiplicity bin are subdominant
 1690 with respect to the total uncertainty.

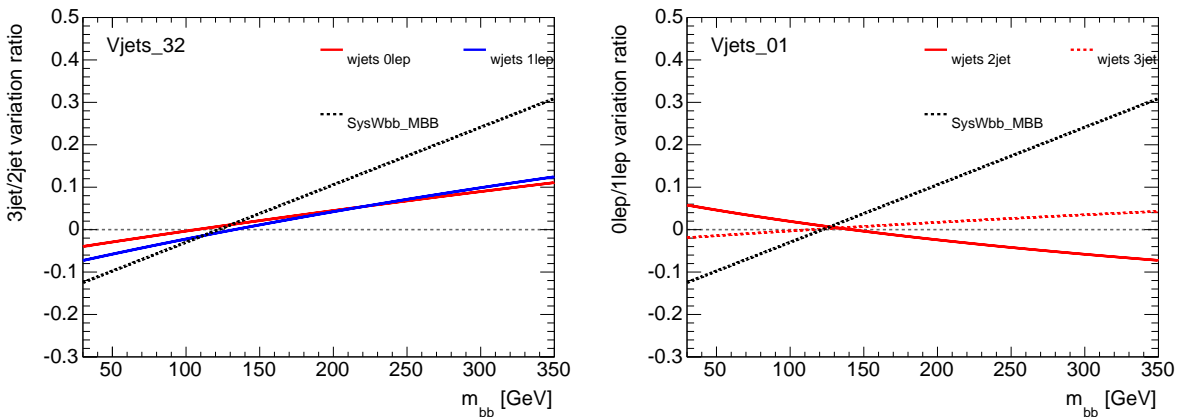


Figure 76: Residual shape uncertainties m_{bb} between different jet multiplicities (left) and lepton channel (right). The effect of the total common shape uncertainty is also reported for completeness.

¹⁶⁹¹ **F.4. Rivet-Reco comparison**

¹⁶⁹² To be added.

¹⁶⁹³ **F.5. Data/MC plots**

¹⁶⁹⁴ Data/MC plots on high statistics 1-tag regions are being prepared.

Not reviewed, for internal circulation only

1695 G. Additional material for Z+jets modeling systematics

1696 This appendix describes detailed information on the modelling uncertainties for the Z+jets background
 1697 described in Section 3.1.6.

1698 **G.1. Breakdown of normalisation/extrapolation uncertainties**

1699 Due to technical reasons the break are presented in ugly slides snapshot. Proper latex tables are in
 1700 preparation.

1701 **G.1.1. 2-3 jet extrapolation**

1702 Detailed breakdown of the 2-to-3 jet extrapolation uncertainty for the normalisation in the 0-lepton channel
 1703 is reported in 77. Detailed breakdown of the 2-to- ≥ 3 jet extrapolation uncertainty for the normalisation
 1704 in the 2-lepton channel is reported in 78; the contribution to the uncertainty is not significantly different
 1705 between the low and high V p_T regions, therefore in the baseline scenario, a conservative 30% uncertainty
 1706 will be consider in both reason in a correlated way. Altenatively an additional 10% uncertainty could be
 1707 applied in the high V p_T region region to take into account residual difference.

rel. variation	0L
muR1 muF0.5	0.002
muR1 muF2	0.00
muR0.5 muF1	0.14
muR2 muF1	-0.10
muR2 muF2	-0.11
muR0.5 muF0.5	0.15
ckkw	0.05
qsf	-0.03
madgraph	-0.05
Combination	0.17

Figure 77: Breakdown of the 2-to-3 jets Z+hf normalisation uncertainty in the 0-lepton channel.

1708 **G.1.2. 0 to 2 Lepton extrapolation**

1709 Detailed breakdown of the 0-lepton to 2-lepton extrapolation uncertainty is reported in 79.

Not reviewed, for internal circulation only

rel. variation	2L-PT1	2L-PT2
muR1 muF0.5	0.001	-0.001
muR1 muF2	-0.001	-0.003
muR0.5 muF1	0.23	0.22
muR2 muF1	-0.14	-0.15
muR2 muF2	-0.15	-0.15
muR0.5 muF0.5	0.22	0.21
ckkw	0.04	0.04
qsf	-0.002	-0.01
madgraph	-0.19	-0.10
Combination	0.30	0.24

Figure 78: Breakdown of the 2-to- ≥ 3 jets $Z+hf$ normalisation uncertainty in the 2-lepton channel. The ‘PT1’ column corresponds to the low $V p_T$ region while the ‘PT2’ column represents the high $V p_T$ region.

rel. variation	PT2
muR1 muF0.5	0.005
muR1 muF2	-0.002
muR0.5 muF1	-0.057
muR2 muF1	0.048
muR2 muF2	-0.011
muR0.5 muF0.5	-0.057
ckkw	-0.002
qsf	-0.004
madgraph	0.04
Combination	0.07

Figure 79: Breakdown of the 2-lepton to 0-lepton $Z+hf$ normalisation uncertainty. For the 2-lepton channel, only the high $V p_T$ region has been considered. The ‘PT1’ column corresponds to the low $V p_T$ region while the ‘PT2’ column represents the high $V p_T$ region

1710 G.1.3. flavour composition

1711 Tables 80,81,82 contains the full breakdown of the uncertainty on the flavour composition for the bc/bb,
 1712 bl/bb and cc/bb ratios respectively. Different normalisation priors have been considered for the 0-lepton,
 1713 2-lepton 2-jet and 2-lepton ≥ 3 -jet regions.

Not reviewed, for internal circulation only

rel. variation	2-Lepton							
	0-Lepton		2-J			3-J		
	0L-2J	0L-3J	PT0	PT1	PT2	PT0	PT1	PT2
muR1 muF0.5	-0.012	-0.010		-0.006	-0.015		-0.004	-0.007
muR1 muF2	0.01	0.01		0.00	0.01		0.00	0.01
muR0.5 muF1	-0.01	0.00		-0.02	-0.01		-0.02	-0.01
muR2 muF1	0.01	0.00		0.01	0.01		0.02	0.01
muR2 muF2	0.02	0.01		0.02	0.02		0.02	0.02
muR0.5 muF0.5	-0.02	-0.01		-0.01	-0.02		-0.02	-0.02
madgraph	-0.39	-0.34		-0.40	-0.36		-0.27	-0.27
ckkw	-0.02	-0.03		-0.04	-0.02		0.01	0.01
qsf	-0.06	-0.04		-0.01	0.00		-0.03	0.00
Combination	0.40	0.34		0.40	0.36		0.28	0.27

Figure 80: Breakdown of the $Z+bc/Z+bb$ normalisation uncertainty in all the 2-lepton and 0-lepton analysis regions.

rel. variation	2-Lepton							
	0-Lepton		2-J			3-J		
	0L-2J	0L-3J	PT0	PT1	PT2	PT0	PT1	PT2
muR1 muF0.5	-0.011	-0.005		0.000	-0.012		-0.004	-0.005
muR1 muF2	0.01	0.01		0.00	0.01		0.00	0.00
muR0.5 muF1	-0.01	0.00		-0.02	-0.01		-0.02	-0.01
muR2 muF1	0.01	0.00		0.01	0.01		0.02	0.01
muR2 muF2	0.02	0.01		0.02	0.02		0.02	0.02
muR0.5 muF0.5	-0.02	0.00		-0.01	-0.02		-0.02	-0.01
madgraph	-0.24	-0.21		-0.27	-0.24		-0.20	-0.17
ckkw	-0.02	0.02		0.04	-0.01		0.01	0.02
qsf	-0.03	-0.01		0.01	-0.01		-0.03	-0.01
Combination	0.25	0.21		0.28	0.24		0.20	0.17

Figure 81: Breakdown of the $Z+bl/Z+bb$ normalisation uncertainty in all the 2-lepton and 0-lepton analysis regions.



2-Lepton								
rel. variation	0-Lepton		2-J			3-J		
	0L-2J	0L-3J	PT0	PT1	PT2	PT0	PT1	PT2
muR1 muF0.5	-0.004	0.002		0.014	0.001		0.018	0.005
muR1 muF2	-0.01	-0.01		0.00	0.00		0.00	0.00
muR0.5 muF1	-0.01	-0.01		0.01	-0.01		-0.02	-0.03
muR2 muF1	0.01	0.01		0.00	0.01		0.04	0.03
muR2 muF2	0.01	0.01		-0.01	0.01		0.04	0.03
muR0.5 muF0.5	-0.03	-0.01		0.01	-0.01		-0.01	-0.03
madgraph	-0.14	-0.11		-0.16	-0.16		-0.08	-0.13
ckkw	0.02	0.22		0.04	0.01		0.01	0.04
qsf	-0.04	0.00		-0.03	0.00		-0.04	0.00
Combination	0.15	0.24		0.16	0.16		0.09	0.13

Figure 82: Breakdown of the $Z+cc/Z+bb$ normalisation uncertainty in all the 2-lepton and 0-lepton analysis regions.

1714 H. Additional material for 1 lepton multijet modeling

1715 This appendix describes detailed information on the fake factor method for the 1 lepton multijet back-
 1716 grounds estimation described in Section 3.5.

1717 **Fake Factor Method**

1718

1719 The fake factor method aims to determine the multijet contribution of fake leptons from photons and light
 1720 jets and from non-prompt heavy flavour decays in the signal region using a series of 3 control regions.
 1721 An estimate of the fake lepton contribution in the nominal “numerator” region is determined using a
 1722 control region with inverted lepton isolation requirements, referred to as the “denominator” region. A
 1723 comparison with the WH -signal electron requirements are summarised in Table 70. Table 71 compares the
 1724 denominator muon requirements to the WH -signal muon requirements. The reversal of the lepton isolation
 1725 requirement ensures that the selection contains a high purity of fake lepton, whilst being orthogonal to the
 1726 signal region. To obtain the pure multijet estimate, the electroweak contamination is removed from data
 1727 using MC simulated samples.

	Denominator Electron	Numerator Electron
Calorimeter Isolation	> 3.5 GeV	< 3.5 GeV

Table 70: Summary of differences between the electron denominator and numerator region definitions for the QCD fake factor method.

	Denominator Muon	Numerator Muon
Track Isolation	> 1.25 GeV	< 1.25 GeV

Table 71: Summary of differences between the muon denominator and numerator region definitions for the QCD fake factor method.

1728 The normalisation of the fake lepton contribution in the signal region is corrected using a “fake factor”, f .
 1729 High statistics di-jet events are selected by requiring containing exactly 1 signal jet, with the fake factor
 1730 the ratio of the number of events with the numerator lepton selection to the number of events with the
 1731 denominator lepton selection:

$$f = \frac{N_{\text{dijet}}^{\text{Numerator}}}{N_{\text{dijet}}^{\text{Denominator}}} \quad (3)$$

1732 where $N_{\text{dijet}}^{\text{Numerator(Denominator)}}$ is the number of di-jet events with the numerator (denominator) lepton
 1733 requirement. Therefore:

$$N_{WH}^{\text{Numerator}} = f \times N_{WH}^{\text{Denominator}} = \frac{N_{\text{dijet}}^{\text{Numerator}}}{N_{\text{dijet}}^{\text{Denominator}}} \times N_{WH}^{\text{Denominator}} \quad (4)$$

1734 where $N_{WH}^{\text{Numerator(Denominator)}}$ is the number of WH signal events with the numerator (denominator) lepton
 1735 requirement, and it is assumed that this fake factor remains constant between the di-jet selection and
 1736 nominal WH selection.

1737 The fake factor is highly sensitive to the normalisation of MC electroweak contribution. In order to
 1738 improve this agreement, the normalisation of the MC electroweak background in the di-jet control regions
 1739 is corrected by fitting to data for $150 < E_T^{\text{miss}} < 250$ GeV in this region. This procedure was found to offer
 1740 a good improvement in the modelling of the multijet background.

1741 A fake factor is derived for each corresponding m -jet region using the di-jet control regions, as a function
 1742 of $\eta(l)$ and p_T^l to ensure good modelling of the multijet background. Additionally, in the electron mode,
 1743 f is also derived as a function of E_T^{miss} .

1744 In the electron mode, dominant multijet contribution is from non-prompt heavy flavour decays. In non-
 1745 prompt electron events, hadronic activities from heavy flavor jets are around the non-prompt electron.
 1746 When their energy deposits are inside the energy window of the electron in the EM calorimeter, their
 1747 energies are added to the electron energy. In this case, since the energy scale of hadronic activities is
 1748 different from electron energy scale, they cause fake E_T^{miss} . On the other hand when they are outside,
 1749 they can be added to the calorimeter isolation value of the electron. Hence the not-isolated non-prompt
 1750 electrons (“denominator” electrons) have different E_T^{miss} distributions from well-isolated non-prompt
 1751 electrons (“numerator” electrons). The dependency on E_T^{miss} is introduced to take into account the energy
 1752 mis-calibration effect.

1753 A multijet template is derived for each m -jet region using the denominator lepton selection. The normal-
 1754 izations of $t\bar{t}$ and W+HF contamination in m -jet region are corrected using $t\bar{t}$ CR and W+HF CR.

1755 An additional consideration of this procedure is that the light jet fakes and non-prompt electron may have
 1756 a different fake factor. This is checked by studying the electron σ_{d_0} distributions, where non-prompt
 1757 electrons are expected to have a wider σ_{d_0} distribution. It was observed that after applying b -tagging,
 1758 the distribution of σ_{d_0} was unchanged, indicating that the fake electron contribution is dominated by
 1759 non-prompt electrons. Therefore, it is not necessary to consider separately non-prompt and light electrons
 1760 in the fake factor method.

1761 The effect of the energy mis-calibration is better solved by additional correction. When the calorimeter
 1762 isolation value is removed from E_T^{miss} in the “denominator” region, this region has very similar energy
 1763 mis-calibration effect as the “numerator” region. Figure 83 compares BDT distributions in multijet events
 1764 between the “numerator” region and the “denominator” region after applying the “fake factor” using bb-
 1765 filtered di-jet MC samples. Here “CR-FF IsoSub”, which is corresponding to estimated the multijet shape
 1766 with the fake factor method and the E_T^{miss} correction, has a very similar BDT shape as the “numerator”
 1767 region.

1768 Figure 84 shows the data and EW contribution as a function of E_T^{miss} and m_T^W for the 2- and 3-jet e channel
 1769 for $p_T^W > 150$ GeV, including the multijet estimate, shown in purple. After a cut on the E_T^{miss} distributions
 1770 of 30 GeV, the multijet contamination is very much suppressed in the 2 tag regions, but still consistent in the
 1771 1 tag region. Small discrepancies can be seen between data/BG in 1-tag regions. Here the normalization
 1772 scale factors estimated in W+hf CR and ttbar CR, where 2-tag is required, are applied to W+hf and ttbar
 1773 MC. The 1-tag regions can have different correction factor from the 2-tag regions due to MC modeling
 1774 uncertainties. In this case, incorrect correction factors are applied to the 1-tag regions, thus W+hf and
 1775 ttbar are mismodeled in these regions. Table 72 compares the expected electron multijet acceptance and

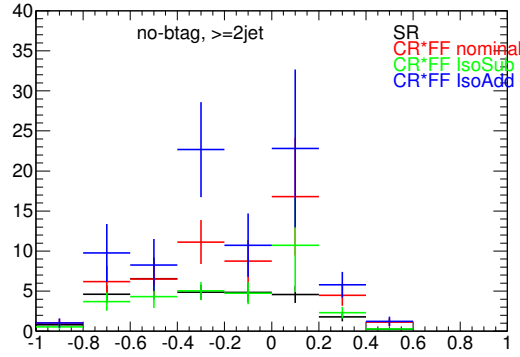


Figure 83: BDT shapes in multijet events. In order to increase statistics, b-tagging is not applied, and jet multiplicity requirement is at least 2-jet. ‘‘CR-FF’’ multijet shapes estimated with the fake factor method. ‘‘IsoSub’’ is corresponding to a BDT shape with the E_T^{miss} correction for the energy mis-calibration effect.

1776 signal acceptance after applying the $E_T^{\text{miss}} > 30$ GeV cut requirement. Templates to describe the multijet
 1777 background in the multi-variate and statistical procedures are used.

1778 Figure 85 shows the data and EW contribution as a function of E_T^{miss} and m_T^W for the 2- and 3-jet μ channel
 1779 for $p_T^W > 150$ GeV, including the multijet estimate, shown in purple.

	2 jet		3 jet	
	1 tag	2 tag	1 tag	2 tag
Signal passing $E_T^{\text{miss}} > 30$ GeV	90%	91%	93%	91%
Multijet passing $E_T^{\text{miss}} > 30$ GeV	33%	33%	42%	42%

Table 72: The expected electron multijet acceptance and signal acceptance in the $p_T^V > 150$ GeV region, from applying the $E_T^{\text{miss}} > 30$ GeV cut. It can be seen that the requirement of this cut results in a significant decrease in the single fake electron contribution, whilst maintaining a high signal acceptance [ICHEP analysis].

Not reviewed, for internal circulation only

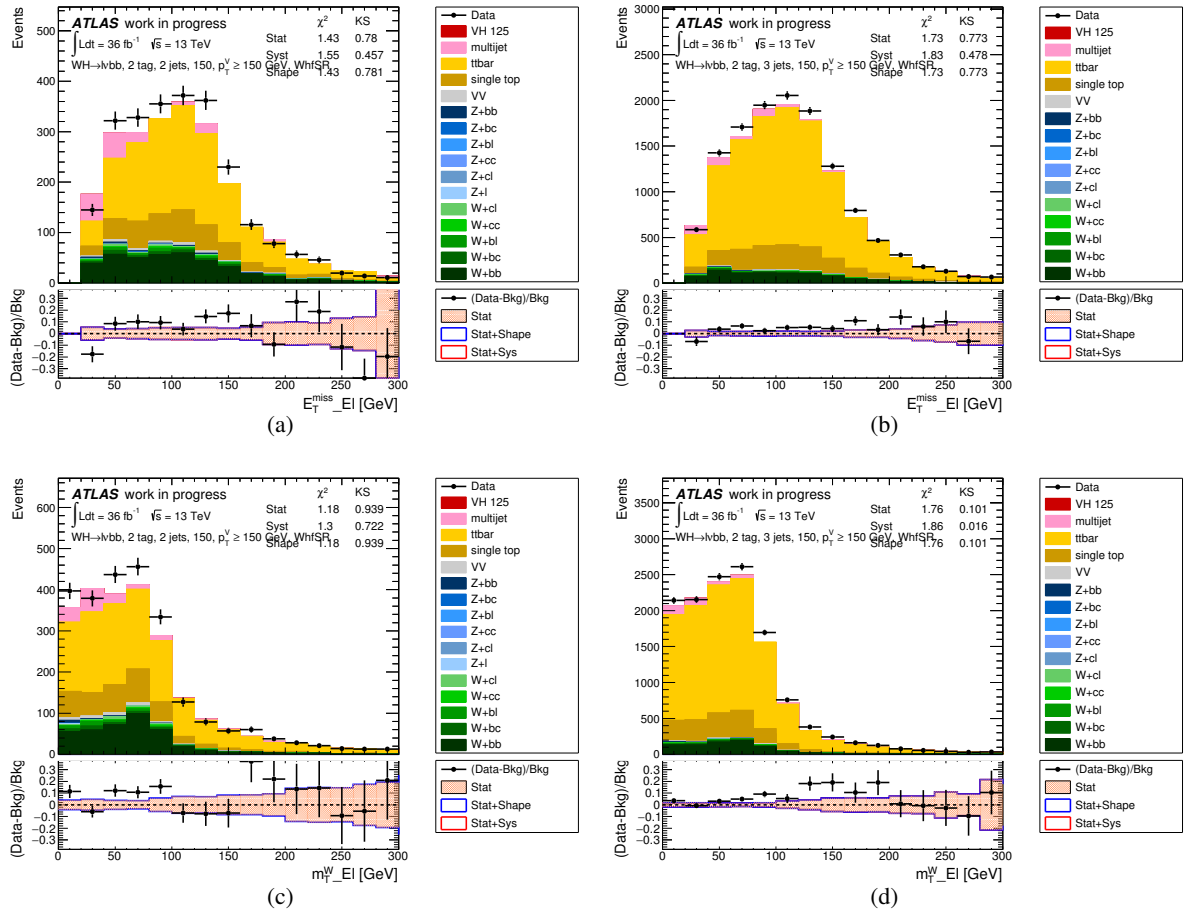


Figure 84: The pre-fit E_T^{miss} distribution in the 1-lepton $p_T^W > 150$ GeV e only channel requiring exactly 2 b -tags with 2 signal jets (a), 3 signal jets (b) and m_T^W requiring exactly 2 b -tags and exactly 2 signal jets (c) and 3 signal jets (d) [ICHEP analysis].

Not reviewed, for internal circulation only

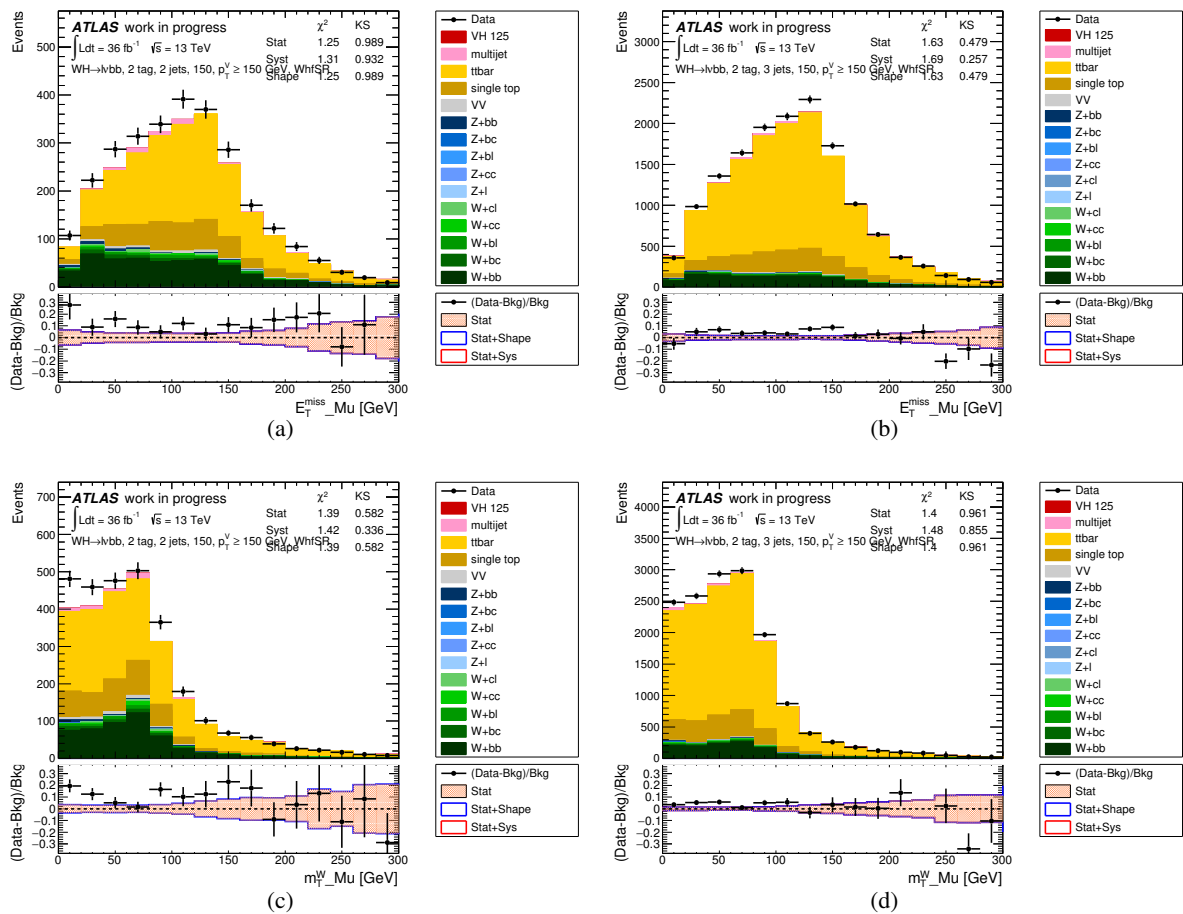


Figure 85: The pre-fit E_T^{miss} distribution in the 1-lepton $p_T^W > 150$ GeV μ only channel requiring exactly 2 b -tags with 2 signal jets (a), 3 signal jets (b) and m_T^W requiring exactly 2 b -tags and exactly 2 signal jets (c) and 3 signal jets (d) [ICHEP analysis].

1780 In both the electron and muon modes, sources of systematic uncertainty are considered in the multijet
1781 estimation:

- 1782 • **In both the electron and muon modes**, as described above, the fake factor is derived using di-jet
1783 control regions. In these di-jet control regions, the nominal case is taken after scaling the electroweak
1784 background to data, using the region $150 < E_T^{\text{miss}} < 250$ GeV. A two sided systematic uncertainty
1785 is then generated by considering the case where the scaling of the electroweak background to data
1786 is shifted by $\pm 1\sigma$ error.
- 1787 • **In both the electron and muon modes**, the normalizations of $t\bar{t}$ and W+HF contamination in m -jet
1788 region are corrected using $t\bar{t}$ CR and W+HF CR. The statistical error in the CRs are propagated to
1789 the uncertainties of the scaling.
- 1790 • **In the electron mode**, the impact of fake electrons on the E_T^{miss} calculation is considered. As
1791 fake electrons have different energy scale from real electrons, the energy scale depends on isolation
1792 value, with a mis-calibration of energy scale affecting E_T^{miss} as described above. The systematic
1793 uncertainty is therefore considered by subtracting isolation value from E_T^{miss} calculation in the
1794 denominator region.
- 1795 • **In the electron mode**, the effect of fake electrons originating from either light or heavy decays
1796 is considered. Common fake factors are used in different b-tag regions, yet the fake electron
1797 contribution from light jets faking electrons may be non-negligible, the fake electron contamination
1798 may change with in the different b-tag regions. The fake factor derived in the di-jet control regions
1799 is then evaluated before b-tagging, and after b-tagging, with a resulting 22% uncertainty on the fake
1800 factor.

Not reviewed, for internal circulation only

1801 **References**

- [1] G. Luisoni et al., *HW ±HZ + 0 and 1 jet at NLO with the POWHEG BOX interfaced to GoSam and their merging within MiNLO*, Journal of High Energy Physics **2013**.10 (2013) 83, ISSN: 1029-8479, URL: [http://dx.doi.org/10.1007/JHEP10\(2013\)083](http://dx.doi.org/10.1007/JHEP10(2013)083).
- [2] T. Sjostrand, S. Mrenna and P. Skands, *A brief introduction to {PYTHIA} 8.1*, Computer Physics Communications **178**.11 (2008) 852 –867, ISSN: 0010-4655, URL: <http://www.sciencedirect.com/science/article/pii/S0010465508000441>.
- [3] G. Aad et al., *Measurement of the Z/γ^* boson transverse momentum distribution in pp collisions at $\sqrt{s} = 7$ TeV with the ATLAS detector*, JHEP **09** (2014) 145, arXiv: [1406.3660 \[hep-ex\]](https://arxiv.org/abs/1406.3660).
- [4] R. D. Ball et al., *Parton distributions for the LHC Run II*, JHEP **04** (2015) 040, arXiv: [1410.8849 \[hep-ph\]](https://arxiv.org/abs/1410.8849).
- [5] R. D. Ball et al., *Parton distributions with LHC data*, Nucl. Phys. **B867** (2013) 244–289, arXiv: [1207.1303 \[hep-ph\]](https://arxiv.org/abs/1207.1303).
- [6] ‘ATLAS Run 1 Pythia8 tunes’, tech. rep. ATL-PHYS-PUB-2014-021, CERN, 2014, URL: <https://cds.cern.ch/record/1966419>.
- [7] J. Alwall et al., *The automated computation of tree-level and next-to-leading order differential cross sections, and their matching to parton shower simulations*, JHEP **07** (2014) 079, arXiv: [1405.0301 \[hep-ph\]](https://arxiv.org/abs/1405.0301).
- [8] M. Botje et al., *The PDF4LHC Working Group Interim Recommendations* (2011), arXiv: [1101.0538 \[hep-ph\]](https://arxiv.org/abs/1101.0538).
- [9] J. Butterworth et al., *PDF4LHC recommendations for LHC Run II*, J. Phys. **G43** (2016) 023001, arXiv: [1510.03865 \[hep-ph\]](https://arxiv.org/abs/1510.03865).
- [10] L. A. Harland-Lang et al., *Parton distributions in the LHC era: MMHT 2014 PDFs*, Eur. Phys. J. **C75**.5 (2015) 204, arXiv: [1412.3989 \[hep-ph\]](https://arxiv.org/abs/1412.3989).
- [11] S. Dulat et al., *New parton distribution functions from a global analysis of quantum chromodynamics*, Phys. Rev. **D93**.3 (2016) 033006, arXiv: [1506.07443 \[hep-ph\]](https://arxiv.org/abs/1506.07443).
- [12] J. Gao and P. Nadolsky, *A meta-analysis of parton distribution functions*, JHEP **07** (2014) 035, arXiv: [1401.0013 \[hep-ph\]](https://arxiv.org/abs/1401.0013).
- [13] S. Carrazza et al., *An Unbiased Hessian Representation for Monte Carlo PDFs*, Eur. Phys. J. **C75**.8 (2015) 369, arXiv: [1505.06736 \[hep-ph\]](https://arxiv.org/abs/1505.06736).
- [14] G. Watt and R. S. Thorne, *Study of Monte Carlo approach to experimental uncertainty propagation with MSTW 2008 PDFs*, JHEP **08** (2012) 052, arXiv: [1205.4024 \[hep-ph\]](https://arxiv.org/abs/1205.4024).
- [15] O. Brein, A. Djouadi and R. Harlander, *NNLO QCD corrections to the Higgs-strahlung processes at hadron colliders*, Phys. Lett. **B579** (2004) 149–156, arXiv: [hep-ph/0307206 \[hep-ph\]](https://arxiv.org/abs/hep-ph/0307206).
- [16] O. Brein et al., *Top-Quark Mediated Effects in Hadronic Higgs-Strahlung*, Eur. Phys. J. **C72** (2012) 1868, arXiv: [1111.0761 \[hep-ph\]](https://arxiv.org/abs/1111.0761).

- 1840 [17] A. Denner et al.,
 1841 *Electroweak corrections to Higgs-strahlung off W/Z bosons at the Tevatron and LHC with HAWK*,
 1842 *JHEP* **03** (2012) 075, arXiv: [1211.5142 \[hep-ph\]](https://arxiv.org/abs/1211.5142).
- 1843 [18] L. Altenkamp et al., *Gluon-induced Higgs-strahlung at next-to-leading order QCD*,
 1844 *JHEP* **02** (2013) 078, arXiv: [1211.5015 \[hep-ph\]](https://arxiv.org/abs/1211.5015).
- 1845 [19] S Heinemeyer et al., ‘Handbook of LHC Higgs Cross Sections: 3. Higgs Properties: Report of the
 1846 LHC Higgs Cross Section Working Group’, tech. rep. arXiv:1307.1347. CERN-2013-004,
 1847 Comments: 404 pages, 139 figures, to be submitted to CERN Report. Working Group web page:
 1848 <https://twiki.cern.ch/twiki/bin/view/LHCPhysics/CrossSections>, 2013,
 1849 URL: <https://cds.cern.ch/record/1559921>.
- 1850 [20] B. Mellado Garcia et al., ‘CERN Report 4: Part I Standard Model Predictions’,
 1851 tech. rep. LHCHXSWG-DRAFT-INT-2016-008, CERN, 2016,
 1852 URL: <https://cds.cern.ch/record/2150771>.
- 1853 [21] I. W. Stewart and F. J. Tackmann,
 1854 *Theory uncertainties for Higgs mass and other searches using jet bins*,
 1855 *Phys. Rev. D* **85** (3 2012) 034011,
 1856 URL: <http://link.aps.org/doi/10.1103/PhysRevD.85.034011>.
- 1857 [22] ‘Monte Carlo Generators for the Production of a W or Z/γ^* Boson in Association with Jets at
 1858 ATLAS in Run 2’, tech. rep. ATL-PHYS-PUB-2016-003, CERN, 2016,
 1859 URL: <https://cds.cern.ch/record/2120133>.
- 1860 [23] T. Gleisberg et al., *Event generation with SHERPA 1.1*,
 1861 *Journal of High Energy Physics* **2009**.02 (2009) 007,
 1862 URL: <http://stacks.iop.org/1126-6708/2009/i=02/a=007>.
- 1863 [24] L. Lonnblad, *Correcting the color dipole cascade model with fixed order matrix elements*,
 1864 *JHEP* **05** (2002) 046, arXiv: [hep-ph/0112284 \[hep-ph\]](https://arxiv.org/abs/hep-ph/0112284).
- 1865 [25] N. Lavesson and L. Lonnblad, *$W+jets$ matrix elements and the dipole cascade*,
 1866 *JHEP* **07** (2005) 054, arXiv: [hep-ph/0503293 \[hep-ph\]](https://arxiv.org/abs/hep-ph/0503293).
- 1867 [26] J. Alwall et al., *The automated computation of tree-level and next-to-leading order differential
 1868 cross sections, and their matching to parton shower simulations*, English,
 1869 *Journal of High Energy Physics* **2014**.7, 79 (2014),
 1870 URL: <http://dx.doi.org/10.1007/JHEP07\%282014\%29079>.
- 1871 [27] J Butterworth et al.,
 1872 ‘Single Boson and Diboson Production Cross Sections in pp Collisions at $\sqrt{s}=7$ TeV’,
 1873 tech. rep. ATL-COM-PHYS-2010-695, CERN, 2010,
 1874 URL: <https://cds.cern.ch/record/1287902>.
- 1875 [28] T. Masubuchi, C. Maiani and A. S. Bell, ‘Search for a Standard Model Higgs boson produced in
 1876 association with a vector boson and decaying to a pair of b -quarks’,
 1877 tech. rep. ATL-COM-PHYS-2016-429, CERN, 2016,
 1878 URL: <https://cds.cern.ch/record/2150252>.
- 1879 [29] S. F. et al.,
 1880 *A positive-weight next-to-leading-order Monte Carlo for heavy flavour hadro-production*,
 1881 *JHEP* **09** (2007) 126.

- [30] P. Nason, *A New method for combining NLO QCD with shower Monte Carlo algorithms*, JHEP **11** (2004) 040, arXiv: [0409146 \[hep-ph\]](#).
- [31] T. S. et al., *An Introduction to PYTHIA 8.2*, Comput. Phys. Commun. **191** (2015) 159, arXiv: [1410.3012 \[hep-ph\]](#).
- [32] ‘Studies on top-quark Monte Carlo Modelling for Top 2016’, tech. rep. ATL-PHYS-PUB-2016-020, CERN, 2016, URL: <https://cds.cern.ch/record/2216168>.
- [33] M. Beneke et al., *Hadronic top-quark pair production with {NNLL} threshold resummation*, Nuclear Physics B **855.3** (2012) 695 – 741, ISSN: 0550-3213, URL: <http://www.sciencedirect.com/science/article/pii/S0550321311005803>.
- [34] M. Cacciari et al., *Top-pair production at hadron colliders with next-to-next-to-leading logarithmic soft-gluon resummation*, Physics Letters B **710.4–5** (2012) 612 – 622, ISSN: 0370-2693, URL: <http://www.sciencedirect.com/science/article/pii/S0370269312002766>.
- [35] P. Bärnreuther, M. Czakon and A. Mitov, *Percent-Level-Precision Physics at the Tevatron: Next-to-Next-to-Leading Order QCD Corrections to $q\bar{q} \rightarrow t\bar{t} + X$* , Phys. Rev. Lett. **109** (13 2012) 132001, URL: <http://link.aps.org/doi/10.1103/PhysRevLett.109.132001>.
- [36] M. Czakon and A. Mitov, *NNLO corrections to top-pair production at hadron colliders: the all-fermionic scattering channels*, English, Journal of High Energy Physics **2012.12**, 54 (2012), URL: <http://dx.doi.org/10.1007/JHEP12%282012%29054>.
- [37] M. Czakon and A. Mitov, *NNLO corrections to top pair production at hadron colliders: the quark-gluon reaction*, English, Journal of High Energy Physics **2013.1**, 80 (2013), URL: <http://dx.doi.org/10.1007/JHEP01%282013%29080>.
- [38] M. Czakon, P. Fiedler and A. Mitov, *Total Top-Quark Pair-Production Cross Section at Hadron Colliders Through $O(\alpha_S^4)$* , Phys. Rev. Lett. **110** (25 2013) 252004, URL: <http://link.aps.org/doi/10.1103/PhysRevLett.110.252004>.
- [39] M. Czakon and A. Mitov, *Top++: A Program for the Calculation of the Top-Pair Cross-Section at Hadron Colliders*, Comput. Phys. Commun. **185** (2014) 2930, arXiv: [1112.5675 \[hep-ph\]](#).
- [40] A. Martin et al., *Parton distributions for the LHC*, English, The European Physical Journal C **63.2** (2009) 189–285, ISSN: 1434-6044, URL: <http://dx.doi.org/10.1140/epjc/s10052-009-1072-5>.
- [41] A. Martin et al., *Uncertainties on α_S in global PDF analyses and implications for predicted hadronic cross sections*, English, The European Physical Journal C **64.4** (2009) 653–680, ISSN: 1434-6044, URL: <http://dx.doi.org/10.1140/epjc/s10052-009-1164-2>.
- [42] H.-L. Lai et al., *New parton distributions for collider physics*, Phys. Rev. D **82** (7 2010) 074024, URL: <http://link.aps.org/doi/10.1103/PhysRevD.82.074024>.
- [43] J. Gao et al., *CT10 next-to-next-to-leading order global analysis of QCD*, Phys. Rev. D **89** (3 2014) 033009, URL: <http://link.aps.org/doi/10.1103/PhysRevD.89.033009>.

- 1925 [44] M. Bahr et al., *Herwig++ physics and manual*, English,
 1926 The European Physical Journal C **58**.4 (2008) 639–707, ISSN: 1434-6044,
 1927 URL: <http://dx.doi.org/10.1140/epjc/s10052-008-0798-9>.
- 1928 [45] J. B. et al., *Herwig 7.0/Herwig++3.0 release note*, Eur. Phys. J. C **76** (2016) 196,
 1929 arXiv: [1512.01178 \[hep-ph\]](https://arxiv.org/abs/1512.01178).
- 1930 [46] E. S. Paul Thompson,
 1931 ‘Theoretical studies for the Standard Model VH,H to bbbar and related searches’,
 1932 tech. rep. ATL-COM-PHYS-2016-475, CERN, 2016,
 1933 URL: <https://cds.cern.ch/record/2151835>.
- 1934 [47] S.-M. Wang et al., ‘Supporting Note for the 2HDM Higgs $A \rightarrow Zh, h \rightarrow b\bar{b}$ searches’,
 1935 tech. rep. ATL-COM-PHYS-2016-030, CERN, 2016,
 1936 URL: <https://cds.cern.ch/record/2121287>.
- 1937 [48] M. Aliev et al., *{HATHOR} – {HAdronic} Top and Heavy quarks crOss section calculatoR*,
 1938 Computer Physics Communications **182**.4 (2011) 1034 –1046, ISSN: 0010-4655,
 1939 URL: <http://www.sciencedirect.com/science/article/pii/S0010465510005333>.
- 1940 [49] P. Kant et al., *HatHor for single top-quark production: Updated predictions and uncertainty*
 1941 *estimates for single top-quark production in hadronic collisions*,
 1942 Computer Physics Communications **191** (2015) 74 –89, ISSN: 0010-4655,
 1943 URL: <http://www.sciencedirect.com/science/article/pii/S0010465515000454>.
- 1944 [50] ‘Simulation of top quark production for the ATLAS experiment at $\sqrt{s} = 13$ TeV’,
 1945 tech. rep. ATL-PHYS-PUB-2016-004, CERN, 2016,
 1946 URL: <https://cds.cern.ch/record/2120417>.
- 1947 [51] ‘Multi-Boson Simulation for 13 TeV ATLAS Analyses’, tech. rep. ATL-PHYS-PUB-2017-005,
 1948 CERN, 2017, URL: <https://cds.cern.ch/record/2261933>.
- 1949 [52] M. Seymour and A. Siódmiok, *Constraining MPI models using σ_{eff} and recent Tevatron and LHC*
 1950 *Underlying Event data*, English, Journal of High Energy Physics **2013**.10, 113 (2013),
 1951 URL: <http://dx.doi.org/10.1007/JHEP10%282013%29113>.

List of contributions

Not reviewed, for internal circulation only

1952	Ahmadov, Faig Argyropoulos, Spyridon Arnold, Hannah Amaral Coutinho, Yara Sanchez Pineda, Arturo Rodolfo Bell, Andrew Stuart Benitez, Jose Buzatu, Adrian	MC contact, CxAOD framework CxAOD framework jet resolution studies CxAOD framework 1-lepton analyzer, Main support note editor, BG modeling 0-lepton analyzer, Main support note editor dijet mass reconstruction, CxAOD framework, Objects support note editor Supervision, BG modeling None Supervision Supervision BG modelling, CxAOD framework, statistical analysis 0-lepton analyzer, b-tagging studies VH boosted studies, statistical analysis Supervision
	Calderini, Giovanni Chan, Stephen Kam-wah Chen, Chunhui Buckley, Andrew Buscher, Daniel Delporte, Charles De Lorenzi, Francesco De Vivie De Regie, Jean-Baptiste Dao, Valerio Enari, Yuji Francavilla, Paolo Gargiulo, Simona Gaycken, Goetz Gray, Chloe Grivaz, Jean-Francois Hays, Jonathan Michael Hesketh, Gavin Grant Hobbs, John Huth, John Ishijima, Naoki Kado, Marumi Kato, Chikuma Li, Changqiao Li, Haifeng Liu, Yanwen Marchiori, Giovanni Ma, Lianliang Ma, Yanhui Mario Jose da Cunha Sargedas de Sousa Masubuchi, Tatsuya Mallik, Usha Mehta, Andrew Montalbano, Alyssa Morange, Nicolas Moser, Brian	Coordination of modelling studies, statistical analysis Supervision BG modeling, Statistical analysis, paper editor W+jets modelling uncertainties Supervision Signal modelling uncertainties Supervision, analysis review CxAOD framework coordinator Supervision Supervision Supervision 1-lepton analyzer, multijet studies Supervision dijet mass reconstruction, CxAOD production 0-lepton analyzer, CxAOD production, statistical analysis Diboson modelling uncertainties, statistical analysis Supervision Egamma contact, Supervision Supervision 1-lepton analyzer, CxAOD framework, multijet studies Statistical analysis
1953	Pandini, Carlo Emanuele Piacquadio, Giacinto Prell, Soeren Robson, Aidan Scanlon, Tim Schopf, Elisabeth	2-lepton analyzer, Main supporting note editor Supervision 2-lepton analyzer, BG modelling 1-lepton analyzer, multijet studies Coordination BG modelling 0-lepton analyzer, BG and signal modelling Paper editor, coordination of multijet studies Supervision Single-top modelling uncertainties Coordination Modelling support note editor, background modelling studies, stat

